# INVESTIGATION OF THE POTENTIAL TSUNAMI HAZARD ON THE NORTH COAST OF PUERTO RICO DUE TO SUBMARINE LANDSLIDES ALONG THE PUERTO RICO TRENCH

by

Aurelio Mercado Irizarry
Department of Marine Sciences, RUM/UPR
Coastal Hazards Specialists, University of Puerto Rico Sea Grant College Program

Nancy Grindlay
Department of Earth Sciences, University of North Carolina at Wilmington
(Landslide study; Appendix 3)

Patrick Lynett
Ph.D. Candidate, Department of Civil and Environmental Engineering
Cornell University (Wave modeling; Appendix 4)

Philip L.-F. Liu
Department of Civil and Environmental Engineering, Cornell University
(Wave modeling; Appendix 4)

submitted to

Puerto Rico State Emergency Management Agency
and
Sea Grant College Program, University of Puerto Rico

February, 2002

## TABLE OF CONTENTS

## INDEX OF TABLES

# TABLE OF FIGURES

# EXECUTIVE SUMMARY

Submarine landslides are becoming more and more a cause of great concern to specialists, hazard mitigation officials, and state and federal agencies dealing with natural hazards due to their potential for generating tsunamis. These tsunamis can vary from catastrophic events, for which there is evidence pre-historic evidence, down to smaller scale, but still very dangerous, events. They are of great concern not only for their magnitude, but also because they may have no detectable precursors (unlike earthquake tsunamis), and can be generated locally, implying a few minutes before they can reach a populated area.

Since the studies in which the amphitheater shaped scar at the south slope of the Puerto Rico Trench was first identified as the result of a submarine landslide, there has been concern about what could be the implications for Puerto Rico if all the slope material went down as a single event. In this study we make a first attempt to quantify what could happen if it happens again, using an Extended Boussinesq wave model developed at Cornell University. The model, called COULWAVE, is still under development, and its progress can be followed by assessing its WEB page at http://ceeserver.cee.cornell.edu/pjl2/research_web/COULWAVE/ .

Five landslide time scales (time of duration of the slide) were investigated: 1000, 1500, 2000, 3600, and 7200 seconds. They all give extensive flooding all along the north coast of Puerto Rico, extending many miles inland and highlighting the seriousness of the latent threat existing all along the Puerto Rico Trench as far as we in Puerto Rico are concerned. Much has been said and written in national news and press about the threat that submarine landslides offer both the western and eastern seaboard of the United States of America. But nothing has come out about the same threat here in Puerto Rico and the U.S. Virgin Islands. It is the goal of this study to raise the awareness of the stakeholders in Puerto Rico about this threat

# INVESTIGATION OF THE POTENTIAL TSUNAMI HAZARD ON THE NORTH COAST OF PUERTO RICO DUE TO SUBMARINE LANDSLIDES ALONG THE PUERTO RICO TRENCH

Aurelio Mercado Irizarry, Department of Marine Sciences, RUM/UPR
Coastal Hazards Specialists, University of Puerto Rico Sea Grant College Program
Nancy Grindlay, Department of Earth Sciences, University of North Carolina at Wilmington (Landslide study; Appendix 3)
Patrick Lynett, Ph.D. Candidate, Department of Civil and Environmental Engineering, Cornell University (Wave modeling: Appendix 4)
Philip L.-F. Liu, Department of Civil and Environmental Engineering, Cornell University (Wave modeling; Appendix 4)

Sponsors: Puerto Rico State Emergency Management Agency and Sea Grant College Program UPR

## INTRODUCTION

There is unequivocal evidence of a pre-historical gigantic submarine slope failure with a displaced volume that has been estimated at approximately 1500 $km^3$ by Schwab et al. (1991) and approximately 910-1050 $km^3$ by Grindlay (1998). Its location is the southern slope of the Puerto Rico Trench, about 37 kilometers off the north coast of Puerto Rico (see Figure 1). It is approximately 55 km across (east-west), has a crown in a water depth of approximately 3000 m, and extends to a water depth of approximately 6000 m (images of the scarp can be seen in Figure 6 in Appendix 1 and the figures in Appendix 3). The trench is the surface trace of a southward-dipping Benioff zone (Grindlay et al., 1997), and it includes the deepest part of the Atlantic Ocean with depths up to 8.4 km. Because of the obvious concern by the Puerto Rico emergency managers, the Puerto Rico State Emergency Management Agency (PRSEMA) (previously known as the Civil Defense) and the University of Puerto Rico Sea Grant College Program (UPRSG), sponsored a research project with the purpose of ascertaining what could be expected along the north coast of Puerto Rico if a submarine slope failure of this same magnitude were to occur again as a catastrophic event, i.e., the entire mass disintegrating rapidly. A contract (C-99-02) was signed between PRSEMA and the Center for Research and Development of the University of Puerto Rico in which funds were supplied to the University of Puerto Rico in order to subcontract Dr. Nancy Grindlay, of the University of North Carolina at Wilmington, N.C., to estimate the amount of material involved in the slope failure using new ocean bottom data, and to make an estimate of the density of the material. An additional contract was signed with the company HydroMath LLC, in which Dr. Philip Liu and Mr. Patrick Lynett, Ph.D. candidate, of Cornell University, were to apply a new wave model (COULWAVE), together with a simple slump model, in order to estimate the expected coastal flooding under various slumping time scale scenarios.

In this report we will put together Grindlay's 1998 report and the recent modeling results obtained by the Cornell Ph.D. graduate student, Mr. Patrick Lynett, who has been the developer

Figure 1

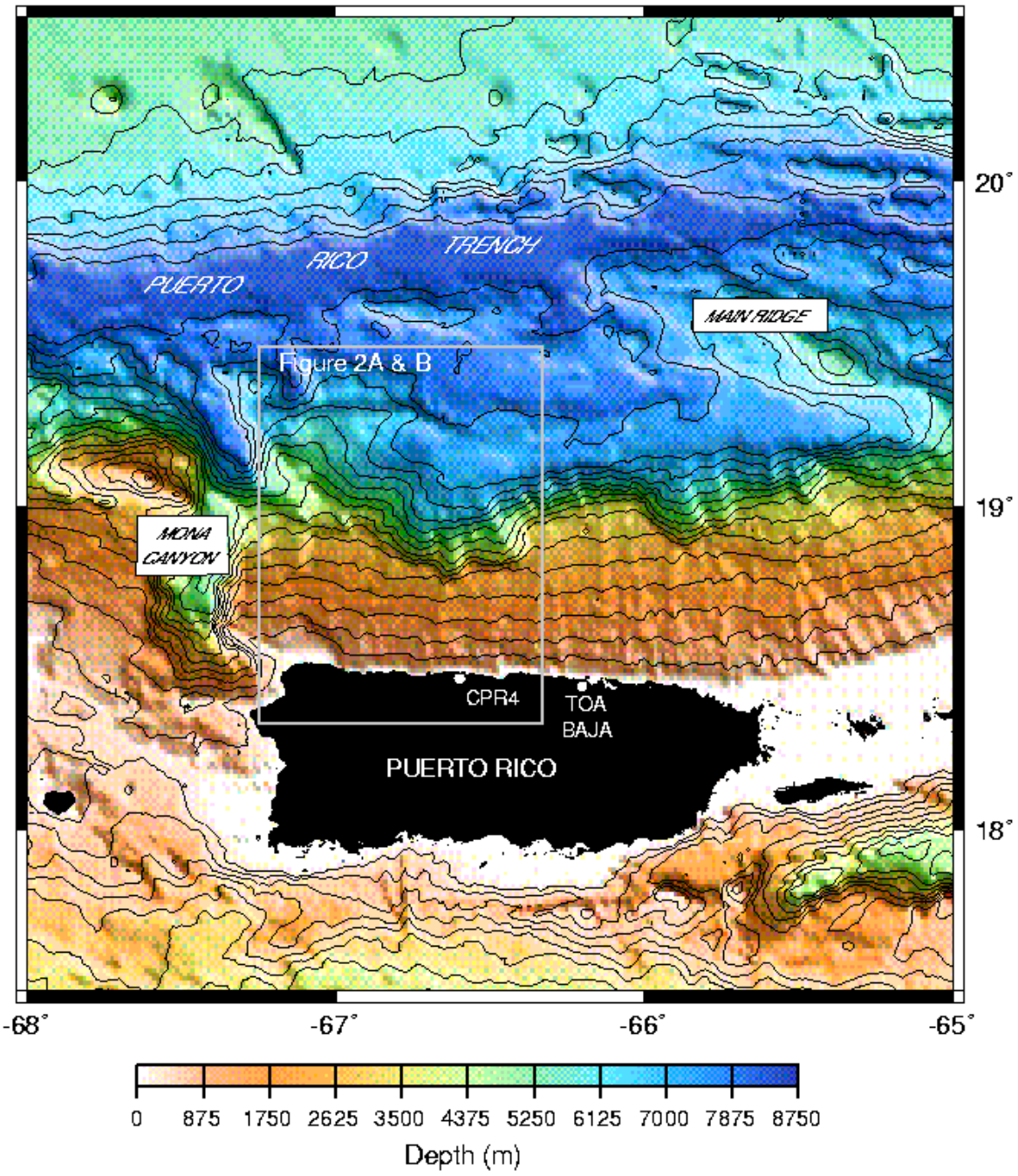


Figure 1 – Location map showing the island of Puerto Rico, the Puerto Rico Trench, and the location of the scarp (taken from Figure 1 in Grindlay, 1998; see Appendix 3).

of COULWAVE as part of his dissertation. We will also include the report submitted by Liu and Lynett about the model, including the user's manual. Finally, flood maps will be presented based on the results obtained by Lynett.

## SUBMARINE SLOPE FAILURES AND ASSOCIATED TSUNAMIGENIC THREAT

Rapid submarine slope failures (as well as subaereal ones) can take many forms and shapes: falls, slumps, slides, debris flows, grain flows, and turbidity currents. A **fall** occurs when loose rock or sediment is dislodged and drops from very steep or vertical slopes. A **slide** occurs when a mass of rock or sediment is dislodged and moves along a plane of weakness, such as a fault, fracture, or bedding plane. A slide that separates along a concave surface is a **slump**. A flow occurs when a mass of rock fragments or sediment moves downslope as a highly viscous fluid. Figure 2 sketches these different slope failures.


Figure 2 – Sketch describing the differences between falls, slides, slumps, and flows (taken from Chernicoff and Venkatakrishnan, 1995, page 371).

A good review of the topic of submarine landslides is given by Hampton et al., 1996), and we will quote and summarize some of the material covered in the review here. The first thing they tackle is the terminology or semantics. "Submarine landslides", or just "slides", will be used to describe almost all of the above-mentioned slope failures.

Quoting from Hampton et al., 1996:

*"Landslides possess two essential features: a rupture surface (failure surface, slide surface) and a displaced mass of sediment or rock* [see Figures 3a and 3b in this report, taken from Brunsden and Prior, 1984]. *The rupture surface is where failure took place and downslope movement originated, and more than one such surface may be present in a particular landslide complex. The displace mass is the material that traveled downslope. It commonly rests partly on the rupture surface, but it might have moved completely beyond it. Moreover, the displaced mass*

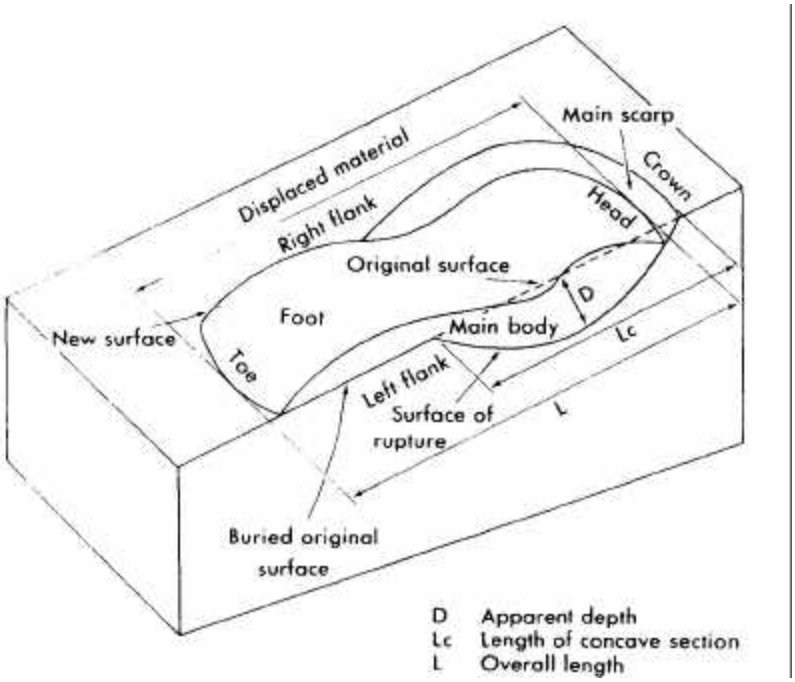


Figure 3a – Features of submarine landslides (from Brunsden and Prior, 1984)

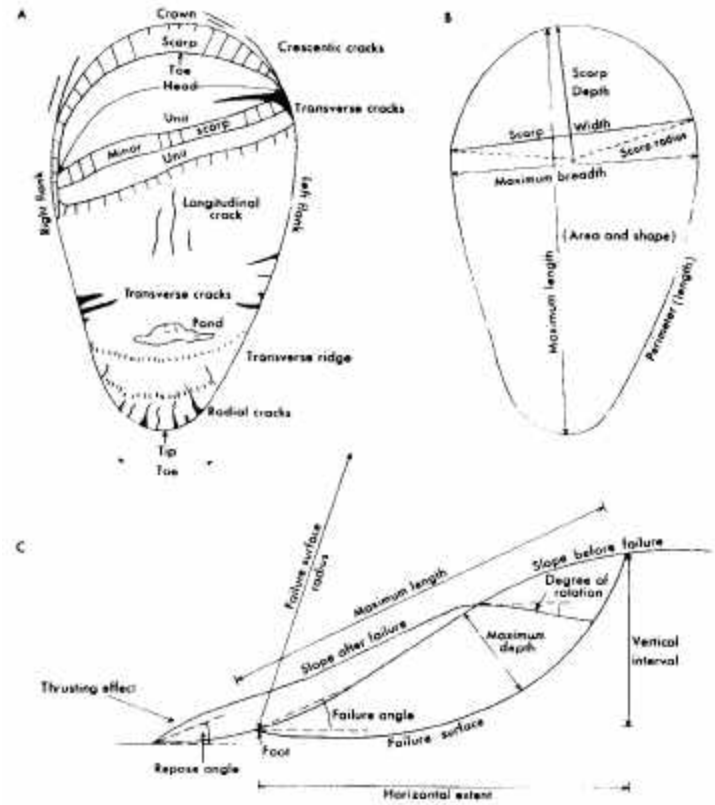


Figure 3b – Morphometry of slump movement systems (from Brunsden and Prior, 1984).

*might remain intact, slightly to highly deformed, or it might break up into distinct slide blocks. In some slides, all or part of the mass completely disintegrates, producing a flow.*

*Following the terminology of Varnes [1978], the main scarp (or headwall scarp) is the upper part of the rupture surface vacated by the displaced mass. Crown cracks may exist within marginally stable material upslope from the main scarp, and minor scarps may exist within the displaced mass itself. The upslope terminus of the displaced mass is the head of the landslide, and the downslope terminus is the toe. The toe region of the displaced mass can have an elevated surface created by resistance to downslope movement or rotation.*

*The rupture surface, particularly in mechanically homogeneous material, commonly is concave upward and scoop-shaped. Accordingly, motion of the displaced mass is rotational, whereby the original seafloor is backtilted. Such slides are formally termed "rotational slides", or "slumps". However, if mechanical inhomogeneities such as bedding planes control failure, the rupture surface is more or less planar, movement is translational, and the landslide is called a "translational slide". Sliding that occurs serially as numerous adjacent failures that progress upslope is termed "retrogressive".*

End of quote from Hampton, et al., 1996.

They go on to state that submarine landslides can be orders of magnitude larger than subaerial landslides. While the largest known Quaternary subaerial landslide is given as the 26-$km^3$ Mount Shasta slide (Crandell et al., 1984), the largest submarine slide is the Agulhas slide off South Africa, with a volume of 20,000 $km^3$.

Very steep slopes are not required, since submarine debris flows have been documented on very gentle slopes, i.e. less than 1° (Elverhoi et. al., 2000), a Gulf of Alaska slide in a 0.5° slope (Carlson, 1978), an offshore of northern California slide in a slope of 0.25° (Field et al., 1982), and a Mississippi River delta slide in a slope of 0.01° (Prior and Coleman, 1978). Elverhoi et al. (2000) show that hydroplaning may be a reason for the near frictionless movement of some slides. Another interesting result is that it has been found that some of them act as if the water were not present as far as hydrodynamic-drag forces (both at the front and on the top of the moving mass) are concerned (Hampton et al., 1996).

The stratification into the above categories (slump vs. slide vs. flows) is not straightforward, since typically the slope failure may start as one, say as a slide (basal failure of topography that moves downslope in coherent blocks), and along the way it may disintegrate, changing into debris or grain flow, and possibly changing further downslope into a turbidity current (a dense turbid slurry of sediment and water).

According to Grindlay (1998), the big amphitheater-shaped scarp along the south slope of the Puerto Rico Trench is the result of a landslide with the characteristics of a debris flow. This is according to the terminology of Hampton et al. (1996) in which they state that "slumps consist of relatively undisturbed masses that slid along curved rupture surfaces, with the bulk of the material not traveling beyond the flank of the volcano. …… In contrast to slumps, debris

avalanches have a well-defined headwall scarp (amphitheater), and the transported rock and sediment are broken into numerous discrete blocks, some of which move great distances (> 200 km)." The figures in Grindlay's report show a curved rupture surface, a headwall scarp, or amphitheater, and accumulated debris at the bottom of the slope. Time-sequence profiles of the landslide model used to generate the tsunami in this report can be seen in Figure 9, page 45 in the manuscript titled *"A numerical study of submarine landslide generated waves and runup"*, by Lynett and Liu, Appendix 4. The sequence of events shown in the figure mimic better the definition of a debris flow than of a slump. No unique concave slip surface is seen, but instead a sequence of bottom profiles representing the progressive erosion of bottom material as the debris flow progresses. Though it is also possible that the failure started as a slump and then degenerated into a debris flow. This happens when loss of shear strength (shear strength is a measure of the soil's ability to resist the driving forces that tend to push the mass downslope) occurs during failure, and the resulting strength becomes smaller than the downslope gravitational shear stress (shear stress, a driving force, pushes soil downslope). The failed sediment mass will then accelerate downslope and tend to disintegrate and flow (Hampton et al., 1996).

A good layman's description of the difference between a "slump" and a "slide" (or landslide) is given by Smith (2000), quoting from P. Watts (a submarine landslide and tsunami specialist). It all depends on the shear strength of the bottom material. For stiff material the slope failure tends to mode downslope as a slump, not a landslide. Quoting Watts: *"A slump is like a couch potato. When the slump fails, its butt slides a little farther forward on the sofa cushion, and its head sinks a little lower"*. Continuing to quote from Smith (2000), and using his figure shown here as Figure 3c:

*"That is, the slump's center of mass moves down and forward in a short arc. This motion is modeled by rotating a cylinder that lies on its side on the seabed like one of the fallen columns*

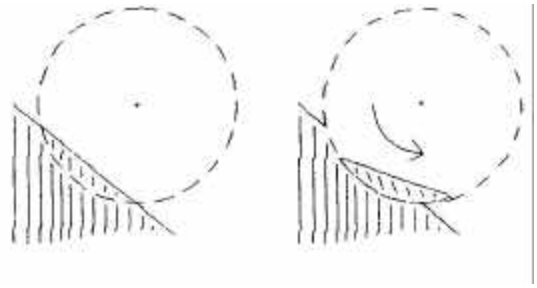

Figure 3c – A cross-section of a slump (from Smith, 2000).

*of Atlantis. The cylinder penetrates the hillside (shaded) to a depth equal to the maximum thickness of the slump, and the buried portion of the cylinder's curved surface is the failure plane along which the slump will move. If you rotate the cylinder maybe six degrees, the embedded portion travels downslope a ways, and that's the slump. The degree and speed of rotation, the diameter of the cylinder, and the depth to which it is embedded, all depend on the clay's shear strength."*

Says Watts, *"The key difference between a landslide and a slump is the center-of-mass motion. A slump starts and stops – if you plot position as a function of time. It accelerates, achieves some maximum velocity, and then decelerates. Whereas a landslide is like your umbrella getting whipped away by the wind and carried down the street – there's nothing to stop it. It experiences a relatively rapid acceleration and then just keeps in going. Nothing stops s landslide".*

Landslide generated tsunamis remain one of the least studied of the causes of tsunamis, in part because their occurrence is often concealed and in part because of the complicated dynamics involved in failure, center of mass motion, and deformation. Underwater landslides also pose difficulties for tsunami warning systems as they often occur on coastal margins near shorelines, can not be predicted as of yet, and may strike within minutes following a moderate earthquake. On the other hand, tsunamis generated by underwater landslides often cause limited damage outside of some range of influence.

Wave generation by landslides depends primarily upon the volume of material moved, the depth of submergence, and the speed of downslope motion (Ward, 2000). As the slide speed increases (and becomes closer in magnitude to the tsunami wave velocity) the sea surface response increases. If the slide's duration is too long (slide time scale = $\vartheta >> L/(gh)^{1/2}$, where L is the horizontal dimension of the slide, and h is the water depth) then long waves would propagate away from the source area in much less time than it takes for the initial "doming" of the surface to form. In this case, no significant waves could be generated (Kulikov et al., 1996). An interesting result that comes out from this study is that as the slide time scale is increased from the shortest (16.7 min) to the longest (2 hours) the observed runup first decreases – as expected from the discussion above – but then it reaches a minimum and starts to increase again for the longer time scales.

Other facts about tsunamis due to submarine landslides are that the larger the slide volume, the higher the sea surface response. Also, the deeper the slide the smaller the sea surface response. While many failure events may not be tsunamigenic, recent events and simulations both corroborate new understanding that underwater landslides and slumps are responsible for the largest tsunamis besides meteor strikes (http://rccg03.usc.edu/la2000/).

The wavelength and periods of landslide-generated tsunamis range between 1 and 10 km and 1 and 5 minutes respectively (Bryant, 2001). These values are much shorter than those produced by earthquakes. The wave period and wavelength increases as the size of the slide increases and the slope decreases (Ward, 2000).

The way a submarine slope failure causes a tsunami is that a slope failure on the move leaves a void behind itself that the ocean instantly fills, creating a wave. If the mass movement is away from the coast then the void created behind (or wave trough, or sea surface depression) points towards land. This is the case for the slope failure we are dealing with since it occurred along the south slope of the Puerto Rico Trench. Therefore, the first manifestation of the tsunami along the north coast of Puerto Rico will be a withdrawal of the sea at the coastline. According to the models, when the wave trough arrives first (versus the wave crest arriving first) the runup (highest elevation reached by the water at a given inland point) tends to be higher than when the

crest arrives first (Smith, 2000). On the positive side, the withdrawal of the sea offers a warning to the coastal population.

In general, this type of tsunami tends to be much more compact than earthquake tsunamis, sometimes being described as "pocket tsunamis" (Smith, 2000). Examples of the compactness of these tsunamis are the Papua-New Guinea tsunami of 1998, and the Vanuatu (formerly New Hebrides) tsunami of 1999. But there is ample geological evidence that there are exceptions to the characterization of submarine slope failure tsunamis as "pocket tsunamis". This is the case of the hypothesized giant tsunamis generated by pre-historic slope failures like the ones in the Hawaiian islands (Lipman et al., 1988; Moore and Moore, 1988; Moore et al., 1994; Masson et al., 1996), the Canary Islands (Masson, 1996; Carracedo et al., 1998), the Storegga Slide (Dawson et al., 1988; Dawson, 1994; Long et al., 1989; Hansom and Briggs, 1991; Harbitz, 1992; Henry and Murty, 1992; Bondevik et al., 1997a,b), and the Oregon Cascadia Margin (Goldfinger et al., 2000).

Scientists are currently unable to accurately assess underwater landslide risks, predict their occurrence following a nearby earthquake, evaluate their tsunamigenic potential, and warn coastal communities of imminent danger. (Workshop on the Prediction of Underwater Landslide and Slump Occurrence and Tsunami Hazards Off of Southern California, WEB page http://rccg03.usc.edu/la2000/. The results presented in this report present a first attempt at quantifying Puerto Rico's risk to this newly recognized hazard.

## PREVIOUS STUDIES OF THE PUERTO RICO TRENCH LANDSLIDE

Schwab et al. (1991) investigated the Puerto Rico Trench scarp and found the following:

1) They estimated that the volume displaced was of the order of 1,500 $km^3$.

2) The insular slope above the amphitheater-shaped scarp in the Puerto Rico Trench (depths less than 3000 m) has a regional slope of 4.5°. The average declivity of the scarp is 8.5°.

3) It is 55 km across (east-west), has a crown at a water depth of 3500 m, and extends to a water depth of 3000 m.

4) Concluded that the scarp formed principally as a result of slope failure and subsequent mass movement. They based this conclusion on four pieces of evidence:

   a) the tectonic setting of the study area, a plate boundary and a region of high seismicity
   b) the general morphology of the scarp, a distinct embayment having a radius of a circle fitting the failure surface
   c) the presence of shallow-water carbonate debris downslope and near the base of the slope
   d) the analysis of seismic-reflection data showed truncation of sedimentary strata by faults

5) They could not determine if failure was catastrophic or took place over a substantial

period of time.

6) They add that recent data has shown that submarine slope failures of this magnitude (~ 1500 $km^3$) are not unusual. Among the factors that increase the danger that an scenario like this could happen again they mention that the declivity of the insular slope north of Puerto Rico and therefore the downslope gravitational shear stress has been steadily increasing due to the northward tilting (tectonic oversteepening) of the Arecibo basin since Pliocene time. In addition, pre-existing faults that lead into the headwall of the scarp could also significantly reduce the shear strength of the strata. All this could lead to slope failure when shaken by an earthquake, as has been observed all over the world (see Figure 6). As a matter of fact, further east, at 66° W, just offshore of San Juan, Scanlon et al. (1988) and Schwab et al. (1991) found evidence of another, though smaller, slump, with an amphitheater-shaped scarp. They conclude that all this put together suggests that the entire northern margin of the Arecibo basin is falling due to the present tectonic regime. Further studies are required in order to document well this smaller slump.

7) Evidence of the gradual decrease in the stability of the northern insular slope off Puerto Rico is the presence of several smaller downslope-facing scarps seen on the insular slope in water depths less than 3000 m. They conclude that these smaller scarps may represent incipient slope failures and they may indicate that the scarp is retrogressive upslope, and that it continues to be active.

8) Finally, and quoting from the last paragraph in Schwab et al. (1991*): "Because the condition of slope instability that allowed an extremely large landslide continues to develop north of Puerto Rico (assuming the mass slid as a single event), and because the seismic risk remains the same as when the slide took place, a repetition of the event is quite possible, with a potential for the generation of a catastrophic tsunami."*

Therefore, it is not surprising that the evidence of this landslide has worried scientists and hazard mitigation personnel in Puerto Rico and in some federal agencies. Recent experience has shown that landslide generated tsunamis could be much more common than previously thought. These can occur many minutes after an earthquake has been felt, and even more worrisome, can be triggered even by earthquakes smaller than the lower earthquake magnitude threshold of 6.5 for tsunami generation. There is even the documented case of submarine landslides being triggered by hurricane waves in water depths greater than 100 m (Henkel, 1979; Bea et al., 1983). Thus they can become what Ward (2000) has called "surprise tsunami". They can be generated far outside the earthquake epicenter, or be far larger than expected given the earthquake magnitude. And they may arrive without any precursory seismic warning at all.

Thus north of Puerto Rico we have all the conditions needed in order to start worrying about the possibility of future submarine landslides, and the accompanying tsunami: steep slopes close to shore, history of previous landslides (including a very large one), gradual decrease in the slope stability due to tectonic oversteepening and continuous overloading due to sediments discharged by the major rivers in Puerto Rico (almost all of which discharge along the north coast; not only river discharge can lead to local oversteepening but if the sedimentation rate is fast enough then high pore water pressure may be retained, producing unconsolidated

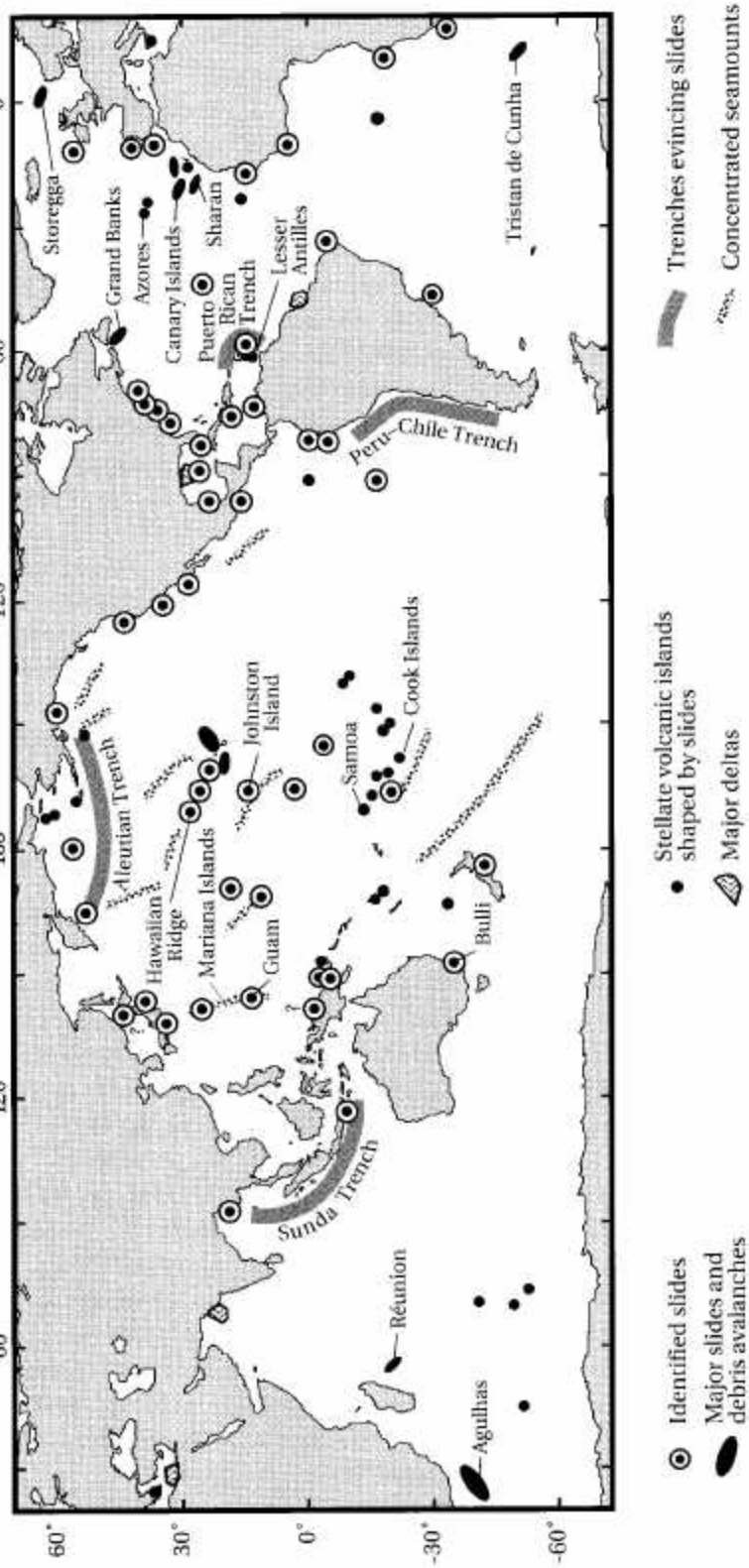


**6.2** Location of major submarine slides and debris flows. Those parts of the oceans with topography susceptible to underwater landslides are also marked (based on Moore, 1978, Keating et al., 1987, and Holcomb and Searle, 1991).

Figure 4 – Location of major submarine slides and debris flows (from Bryant, 2001).

sediments), the presence of many submarine canyons (some coming very close to the coast), the presence of many faults and high seismicity, and the annual occurrence of large waves due to winter extra-tropical storms (occurring as long period swell which can penetrate to relatively large depth; according to Bea, 1971, wavelength can be more significant than wave height in destabilizing sediments along slopes) and due to hurricanes.

This led the PRSEMA and the Sea Grant Program of the University of Puerto Rico to sponsor this study. The potential for another similar one is there since at the same location active faults are present, bringing into mind a scenario like the 1998 Papua-New Guinea deadly tsunami, whose 7 to 14 meters high waves have been blamed on a submarine landslide on the steeply sloping bottom off the affected area. The PNG event has raised much concern in hazard mitigation officials, emergency response personnel, and tsunami experts because, quoting from an article in Science News (Vol. 154, October 3, 1988), "The main lesson is that small, local faults have a much greater potential for tsunami generation than we had thought earlier". The educational message from the Papua-New Guinea tsunami adopted by the western seaboard states of the USA is that "it can happen here and we need to deal with this problem now". This has led the National Science Foundation to sponsor a "Workshop on the Prediction of Underwater Landslide and Slump Occurrence and Tsunami Hazards off the Southern California Coast", held in March of 2000, and was also the main topic in a "NATO Advanced Research Workshop on Underwater Ground Failures on Tsunami Generation, Modeling, Risk and Management", held in May 23-26, 2001, in Turkey. Also, in January of 2001, the National Oceanic and Atmospheric Administration (NOAA), together with the Washington State Military Department, sponsored a workshop titled "Puget Sound Tsunami/Landslide Workshop". Recently the landslide-generated tsunami threat to both the west and east coasts of the United States has been addressed in the national press, like the article in the San Francisco Chronicle, December 18, 2000, titled "Underwater landslides threaten California coast", and the paper by Driscoll et al. (2000), on the threat to the Atlantic coast of the USA.

## RECENT STUDIES OF THE LANDSLIDE AREA

Grindlay et al., 1997, report on a 1996 survey in which the landslide evidence was corroborated. And as part of the present study, she re-examined the data obtained in the survey and came out with a more recent estimate of the volume of material involved in the slide and the average sediment density. The most important conclusions from Grindlay's report, as far as the modeling of the slide is concerned is that the new mass failure volume estimate was revised down to 910-1050 $km^3$, and that the average density of the material is approximately 2.2 $g/cm^3$.This is all reported in her report titled *"Volume and Density Approximations of Material Involved in a Debris Avalanche on the South Slope of the Puerto Rico Trench"*. Appendix 2 shows the publication that describes the 1996 survey from which Grindlay obtained the data used to prepare her report. Grindlay's report is given in Appendix 3. In the tsunami model it will be assumed that the volume displaced was 900 $km^3$.

Grindlay concludes that the landslide that generated the amphitheater-shaped scarp on the south slope of Puerto Rico Trench was most likely a debris avalanche. The bathymetric and sidescan imagery clearly show a giant amphitheater-shaped scarp that is approximately 57 km

across. The crown of the headwall scarp lies at depths of 2500 m to 3500 m. The debris deposit extends more than 25 km down the slope to depths of approximately 7000 m.

## LANDSLIDE AND TSUNAMI GENERATION, PROPAGATION AND RUNUP STUDY FOR THE PUERTO RICO TRENCH DEBRIS FLOW

Recognizing the potential threat of another landslide along the Puerto Rico Trench, this research project was started in order to estimate what could be expected along Puerto Rico's north coast if an event like the one mentioned above in the Puerto Rico Trench were to be repeated again. The modeling of landslide tsunamis is much more difficult than the modeling of earthquakes tsunamis since the time scale of the bottom displacement is much longer than the time scale of the bottom displacement due to a tsunamigenic earthquake. This couples the dynamics of the tsunami generation and propagation with the dynamics of the deforming bottom. In addition, the length scale of landslide tsunamis tends to be much smaller than that due to earthquake tsunamis, making the shallow water approximation (e.g., non dispersion) an unreliable approximation. Also, wave heights can become very large when in shallow water. This requires the use of a system of fully nonlinear wave equations that retain both frequency and amplitude dispersion. And this is the task that the newly developed Cornell model (COULWAVE) is supposed to accomplish.

## LANDSLIDE TSUNAMI MODEL

For this problem a mathematical model has been developed to describe the generation and propagation of water waves by a submarine landslide. The general model consists of depth-integrated continuity and momentum equations, in which the ground movement is a forcing function. These equations include full nonlinear, but weakly dispersive effects. The model allows larger waves than those appropriate for traditional Boussinesq equations. Thus it is described as an Extended Boussinesq Model because of the inclusion of fully nonlinear effects. The model has been applied up to now with a simple bottom deformation algorithm mimicking the gross shape and volume of the Puerto Rico Trench landslide, which seems to have occurred mainly as a debris flow (Grindlay, 1998). An important, unknown, parameter is the landslide time scale since the dynamics of the slide itself is not modeled itself. Instead the time history of the bottom deformation is assumed given. We don't know if the 900 $km^3$-plus material that was displaced went down slope as just one event, or as a sequence of smaller events. And even if we assume a worst case scenario in which we assume that it all moved down as one event, we don't know how long it may have taken. The landslide time scale has to be externally supplied. As a first study attempt, and from the emergency management point of view in which one of the first things that is wanted is to grasp the magnitude of the potential event, it was decided to use the modeling effort to assess five worst-case scenarios in which we assume that the landslide occurred as just one event under five different landslide time scales: 1000, 1500, 2000, 3600, and 7200 seconds (16.7 minutes, 25 minutes, 33.3 minutes, 1 hour, and 2 hours, respectively). In other words, we are trying to have an idea of the magnitude of the event Schwab et al (1991) mentioned at the end of their paper.

Due to the complexity of the numerical code and its large memory and CPU time requirements (even when we had available a DEC Alpha 600 MHz workstation with 2 MB of

RAM), the computational grid size was limited to 300 m, which is too gross for reliable runup calculations. A typical run takes approximately 12 days of CPU time on the DEC Alpha 600 MHz workstation. The input bathymetry is from Mercado (1994), and the input topography is from a DEM for Puerto Rico. The final runs of the model were carried out by Lynett at Cornell.

Details about the wave model and its application to the simulation of the tsunami due to the Puerto Rico Trench landslide is given in the reports by Lynett and Liu given in Appendix 4, so they will not be repeated here. Not mentioned in the reports is the fact that the model version used in the simulations is the weakly nonlinear version (WNL-EXT; see Appendix 4, page 8 in the document titled "*A numerical study of submarine landslide generated waves and runup*", by Lynett and Liu). According to Lynett (personal communication, 2001), test results for the scenarios studied showed that there was not much difference in the runup results between the fully nonlinear version (FNL-EXT) and WNL-EXT, while there was a large difference in execution time. Also, the bottom friction factor "*f*" used in the runs (see Appendix 4, page 5 in the document titled "Modeling wave runup with depth-integrated equations", by Lynett, Wu, and Liu), was taken as 0.01. According to Lynett et al. (see Appendix 4) the typical range of $f$ is $10^{-3} \# f \# 10^{-2}$. A sensitivity run was made for the 1000 s scenario using $f = 0.05$.

The friction factor "*f* " is difficult to ascertain, especially since at present, the model only allows for one constant value all over the computational domain. But even if it were given as a function of geographical position, representing the different energy dissipation sources that a runup of the magnitudes found here will encounter as it propagates inland, its determination is very difficult. And it is obvious that when the runup encounters large structures (forests with large tree trunks with dense foliage, buildings, etc.) then the problem becomes three-dimensional, and outside the capabilities of the COULWAVE model.

Lynett (personal communication, 2002) states that $f$ and the Chezy coefficient, $C$, are related by

$$f = g/C^2$$

where $g$ is the gravitational acceleration. The relationship between $C$ and Manning's coefficient, $n$, is given by

$$C = R^{1/6} / n$$

where $R$ is the hydraulic radius of the channel.

A few conversions between $C$ and $f$ are given in the table below.

**TABLE 1**
**Relationship Between C and f Coefficients**

| *C* | *f* |
|---|---|
| 10 | 0.1 |
| 14 | 0.05 |
| 31 | 0.01 |
| 99 | 0.001 |

The topic of the friction factor, *f*, still requires much further research since the ultimate goal of the modeling effort, the evaluation of the runup along the coast, will be sensitive to the values of *f* in practical applications.

RESULTS

Movies of the results show that towards the island a deep wave trough is initially generated, with a high wave crest generated away from the island. But following the propagation of the initial trough towards the north coast of Puerto Rico (at the coastline the initial manifestation of the tsunami is a withdrawal of the sea along the coast), a crest follows, which shoals up to very large heights as it reaches the north coast. Figures 5 to 9 show the maximum sea surface elevation obtained for each one of the time scales mentioned above, with friction factor $f = 0.01$. Figure 10 shows the result for the sensitivity run with $f = 0.05$ using a time scale of 1000s.

The figures show extensive flooding all along the north coast of the island (all the way from Aguadilla to Fajardo) even for the longest slide time scale. The water penetrates several miles inland, apparently being stopped only by the abrupt topography change found inland. Maximum runups are found between Arecibo and Vega Baja. It is important to emphasize that bottom frictional dissipation is represented by a single value of *f*, and that no consideration is given whatsoever of large-scale dissipation factors, or structures. Thus results will lie on the conservative side, but the state-of-the-art nowadays in the preparation of tsunami coastal flood maps is of no consideration of structures, forests, etc. The neglect of these considerations is justified as a safety factor.

Figures 8 and 9 show that the results for the two longest time scales tend to be noisy, especially so for the time scale of 2 hours. The reason for this is not clear, and is a topic of further research. The sensitivity test using $f = 0.05$ (Figure 10) shows that the maximum runup is decreased (by 6 m), but the flooding is still very extensive.

Table 2 shows the maximum sea surface elevation at the generating area and maximum runup height for the six different scenarios modeled. It is important to realize that the maximum runup given in the table is not measured at the same constant location for each simulation made.

**TABLE 2**
CHARACTERISTICS OF LANDSLIDE AND TSUNAMI SCENARIOS MODELLED

| LANDSLIDE TIME SCALE (seconds:minutes) | MAXIMUM SEA SURFACE ELEVATION AT GENERATION AREA (M) | MAXIMUM RUNUP (M) | *f* |
|---|---|---|---|
| 1000 s = 16.7 min | 19 | 55 | 0.01 |
| 1500 s = 25 min | 12 | 37 | 0.01 |
| 2000 s = 33.3 min | 8 | 30 | 0.01 |
| 3600 s = 60 min | 11 | 31 | 0.01 |
| 7200 s = 120 min | 10 | 35 | 0.01 |
| 1000 s = 16.7 min | 21 | 49 | 0.05 |

It is interesting to notice that the expected trend of decreasing runup with increasing time scale holds between 1000 and 2000 s, but that the runup actually increases between 3600 s and 7200 s (though the increase of just 1 m between 2000 and 3600 s might not significant). But between 2000 s and 7200 s the increase is of 5 m. It should be emphasized that the maximum runups listed in Table 2 do not necessarily occur at the same locations. In order to study the behavior of the runups at the same given location, three slices were taken in the north-south direction for each one of the Figures 5 to 10. These are shown in Figure 5. One of the slices passes right through the center of the offshore maximum in elevation (identified as CENTER, and it passes slightly west of the city of Barceloneta), another one passes right through the city of Arecibo (west of CENTER), and the other one passes through the San Juan metropolitan area (east of CENTER).

Figure 11 shows the plot of the three slices for each one of the slide time scales used. The figures do show consistently that the runup for the time scale of 2 hours tends to be higher than for the time scale of 1 hour. And for the CENTER slice the runup for time scale of 1 hour becomes higher than for time scale of 2000 s, with the runup for 2 hours being equal to or higher than the runup for the time scale of 1 hour. The reason for this behavior is not yet clear, and is under further investigation. But one possible reason may lie with the fact that for the two longest time scales the initial sea surface profile consists of waves smaller in height and wavelength.

In all scenarios a depression, or wave trough, is the first manifestation of the tsunami that reaches the coast. This depression is initially generated over the landslide area and propagates towards shore. This can be seen in Figure 12 which shows snapshots of the sea surface at 5 minutes after the start of the landslide with a time scale of 1 hour (left graph) and 6.7 minutes after the start of the landslide with a time scale of 2 hours (right graph), showing the leading depression moving to the south. This is corroborated by the plot of the time histories of the sea surface elevation, shown in Figures in Figures 13 and 14, which show the leading depression wave over the generation area and just offshore of San Juan, P.R. Figures 15 and 16 show the corresponding time histories of the vertically averaged velocities.

The time histories shown in Figure 13, taken right over the generation area, shows how the initial sea surface disturbance for the two longest time scales, 1 and 2 hours, differ from the shorter time scales in that they consist of much smaller height and wavelength waves. Whether

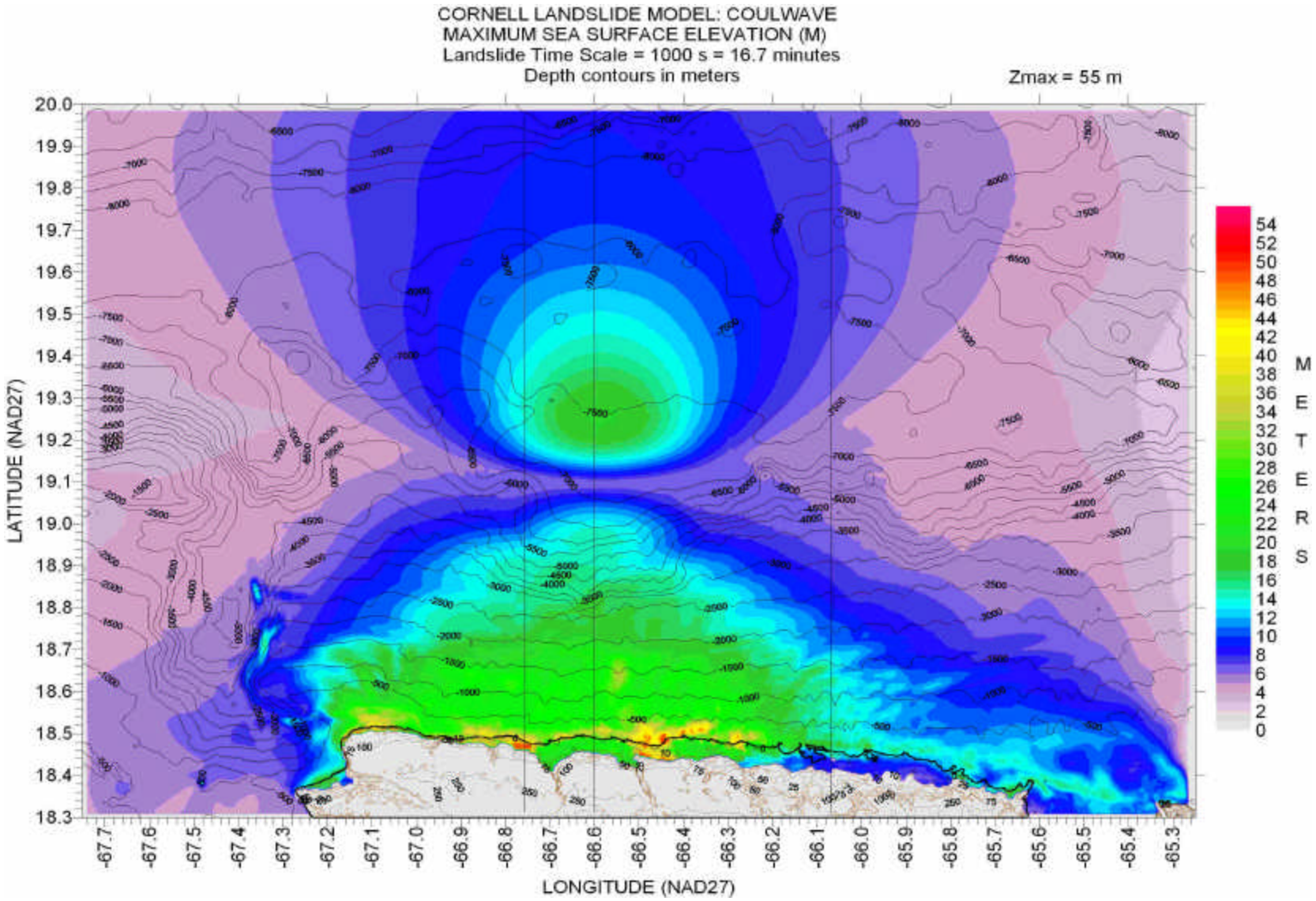


Figure 5 – Maximum sea surface heights for landslide time scale of 1000 seconds. Friction coefficient $f$ = 0.01. Maximum runup = 55 m above MSL. Slices of the sea surface elevation results shown in Figures 5 to 9 were taken along the straight lines extending north-south.

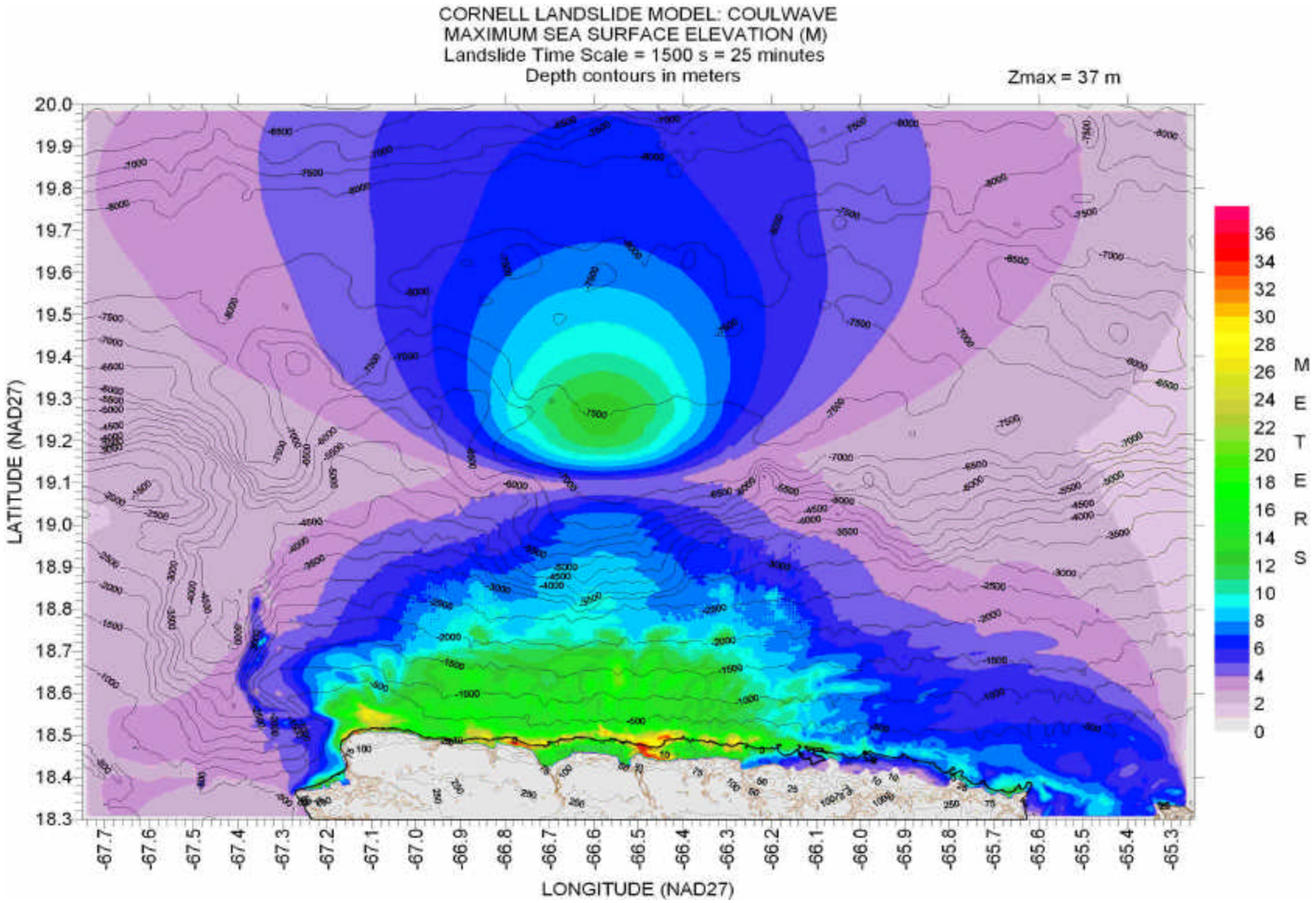


Figure 6 – Maximum sea surface heights for landslide time scale of 1500 seconds. Friction coefficient $f$ = 0.01. Maximum runup = 37 m above MSL.

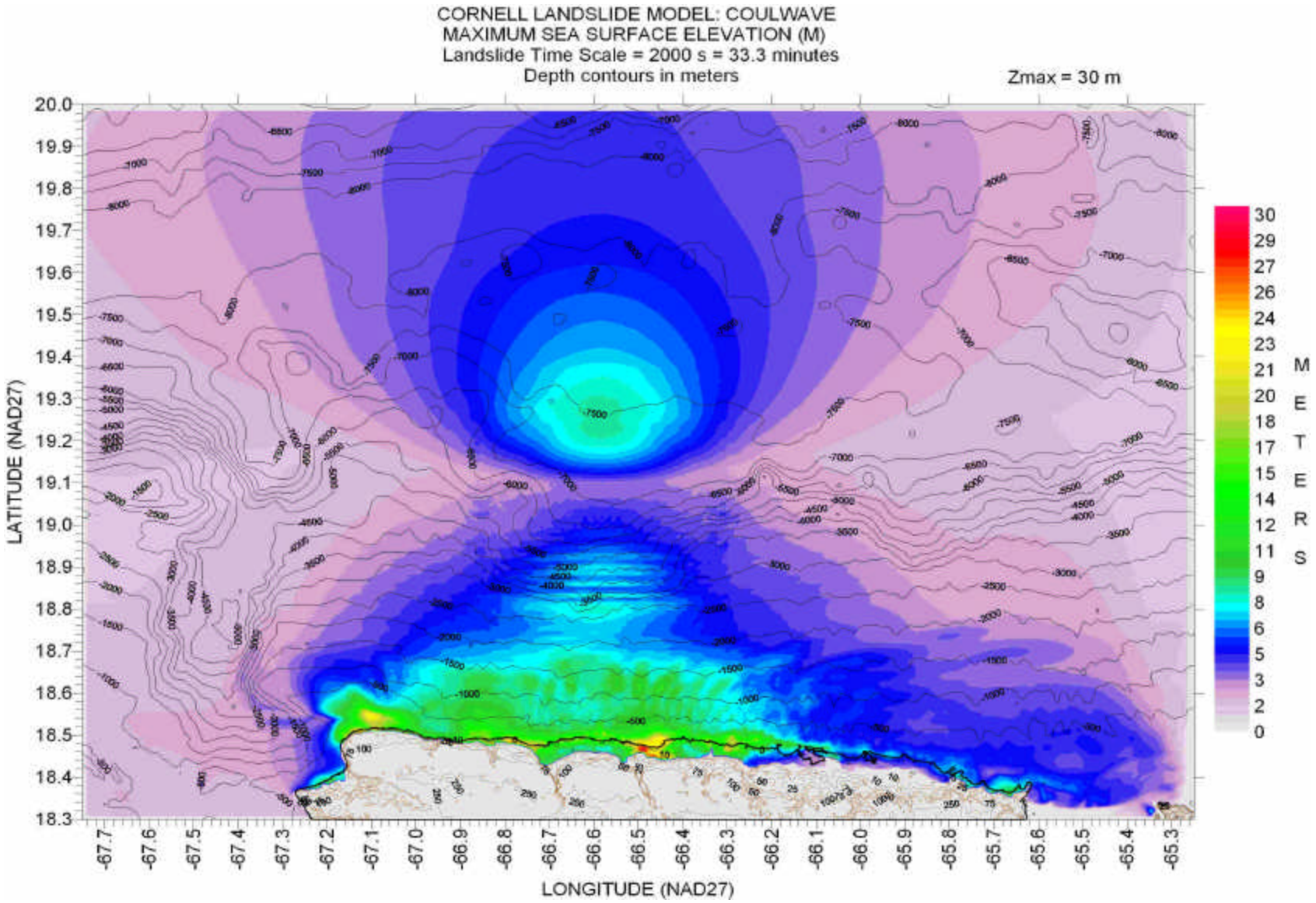


Figure 7 – Maximum sea surface heights for landslide time scale of 2000 seconds. Friction coefficient $f$ = 0.01. Maximum runup = 30 m above MSL.

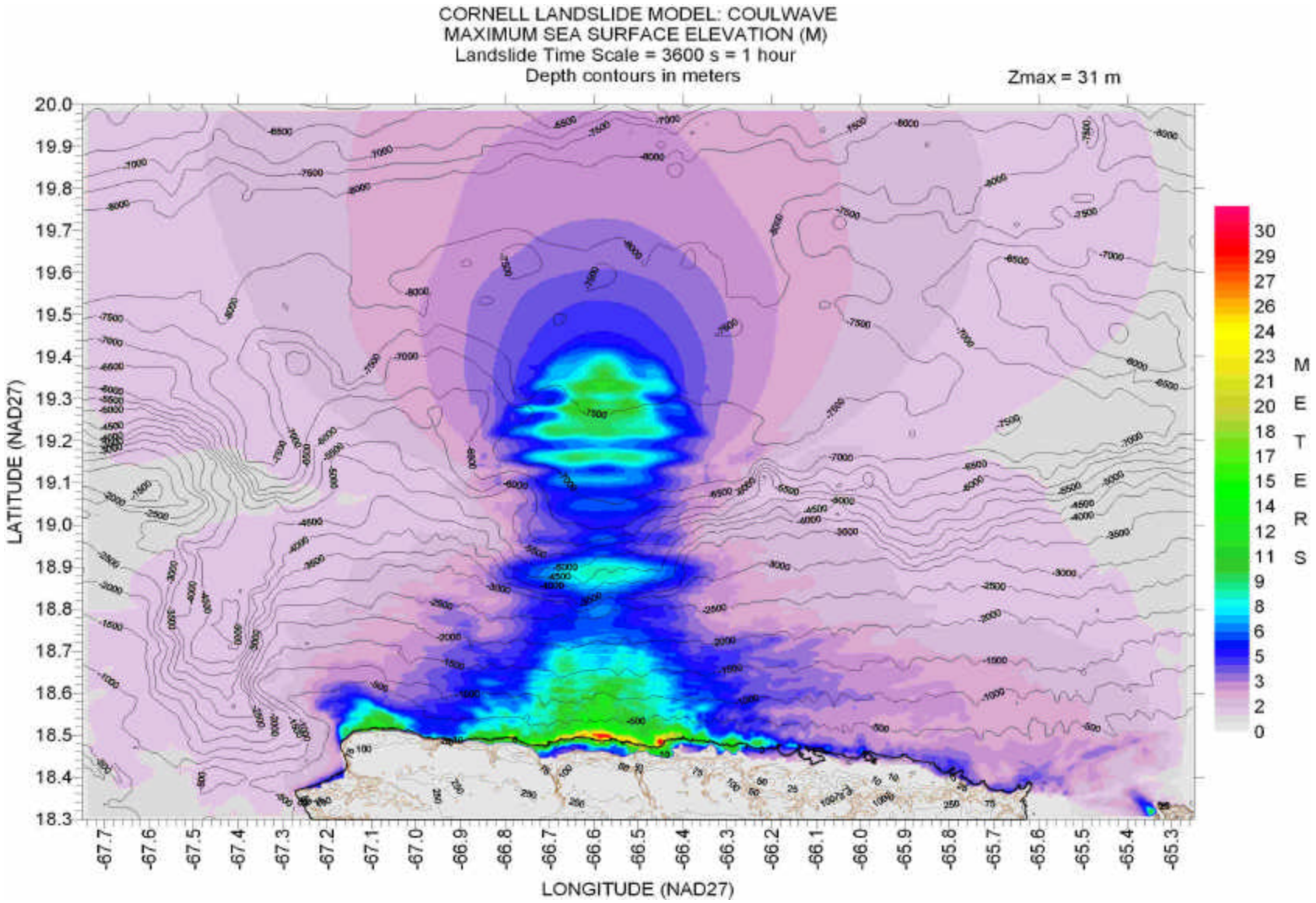


Figure 8 – Maximum sea surface heights for landslide time scale of 3600 seconds. Friction coefficient $f$ = 0.01. Maximum runup = 31 m above MSL.

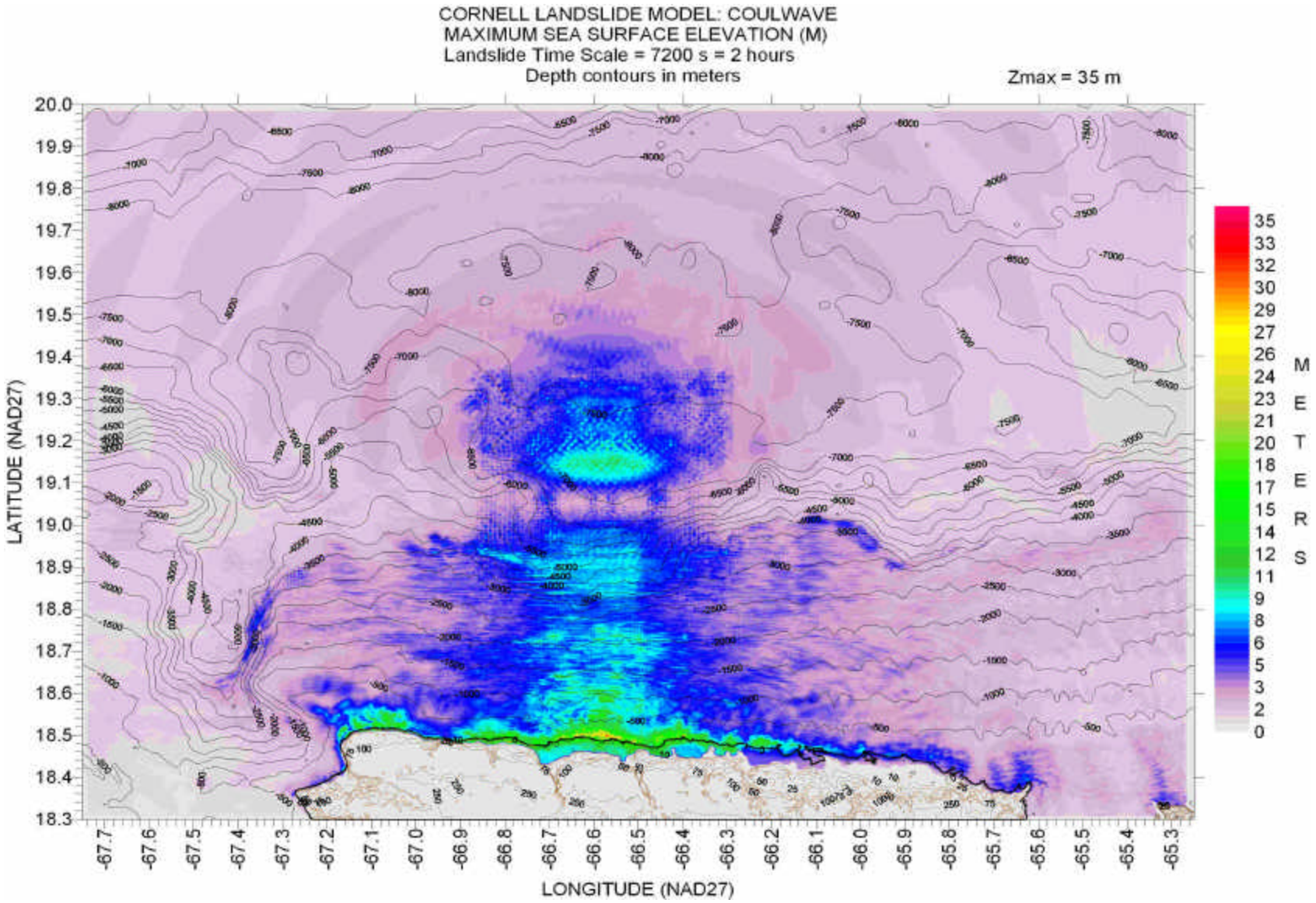


Figure 9 – Maximum sea surface heights for landslide time scale of 7200 seconds. Friction coefficient $f$ = 0.01. Maximum runup = 35 m above MSL.

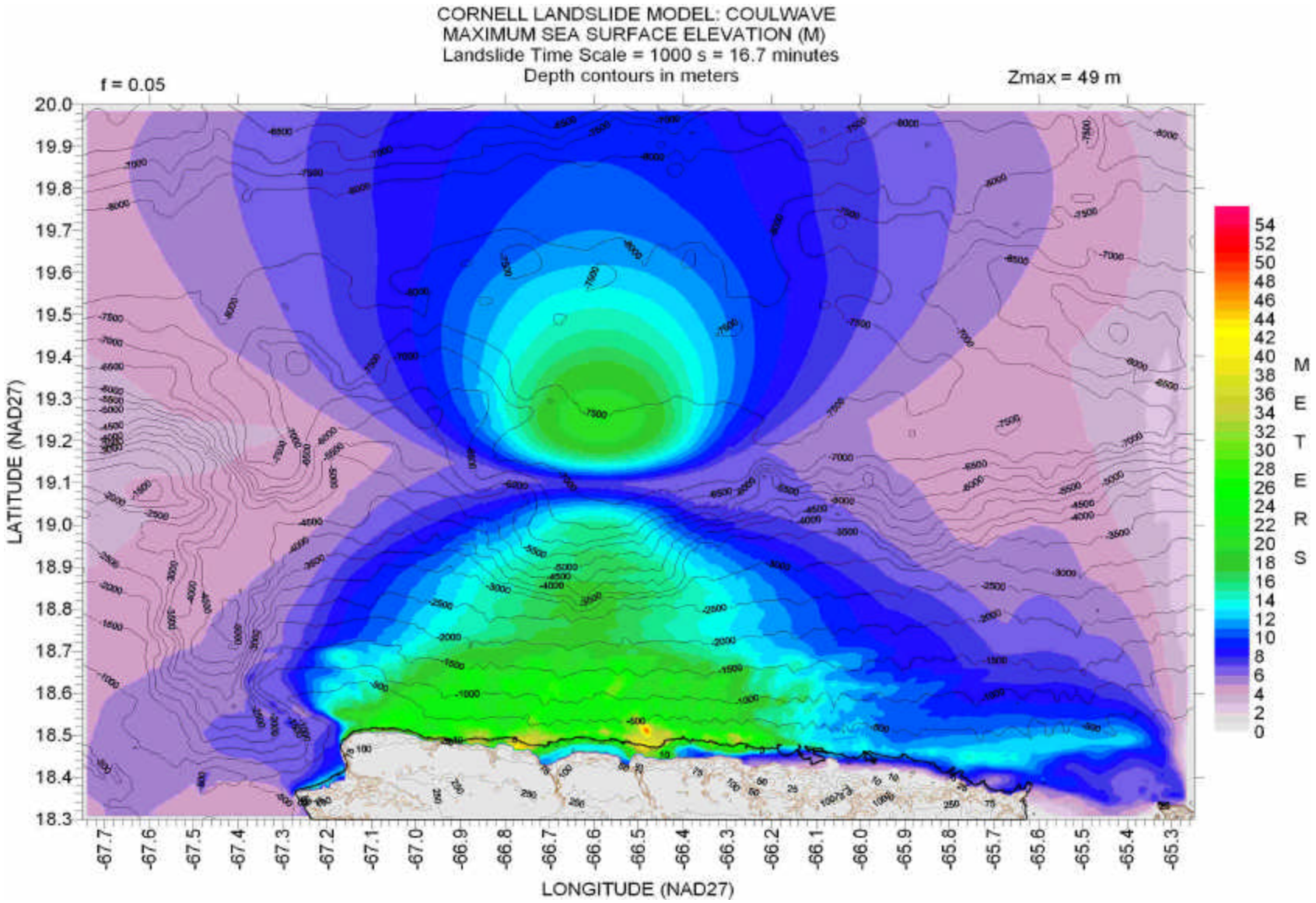


Figure 10 – Maximum sea surface heights for landslide time scale of 1000 seconds. Friction coefficient $f$ = 0.05. Maximum runup = 49 m above MSL.

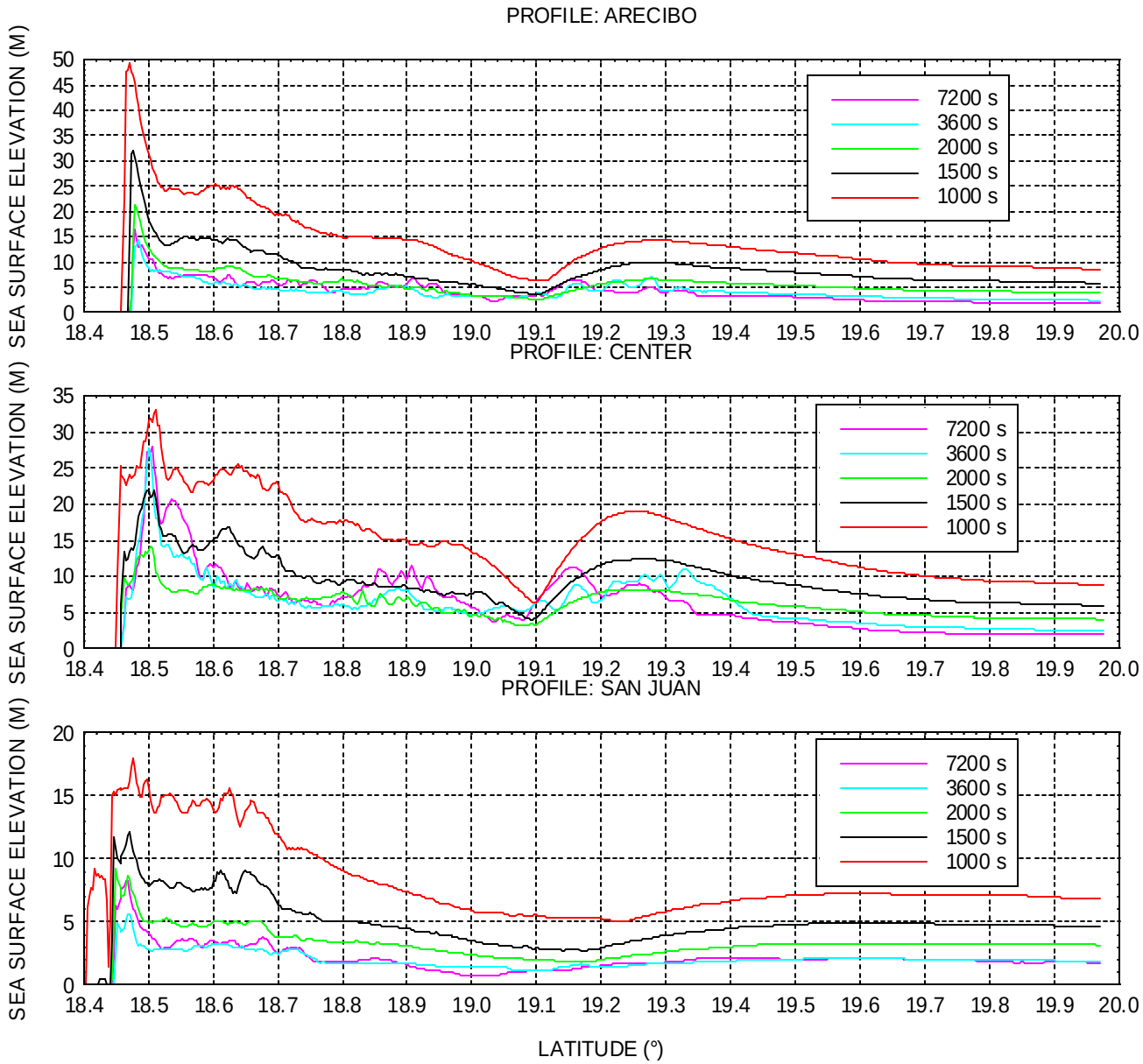


Figure 11 – Sea surface elevation along the 3 north-south slices shown in Figure 5. The top figure corresponds to the slice passing through the city of Arecibo, the middle figure to the slice passing through the center of the offshore maximum in sea surface elevation, and the bottom figure corresponds to the slice passing through the San Juan metropolitan area. Note the different vertical scales.

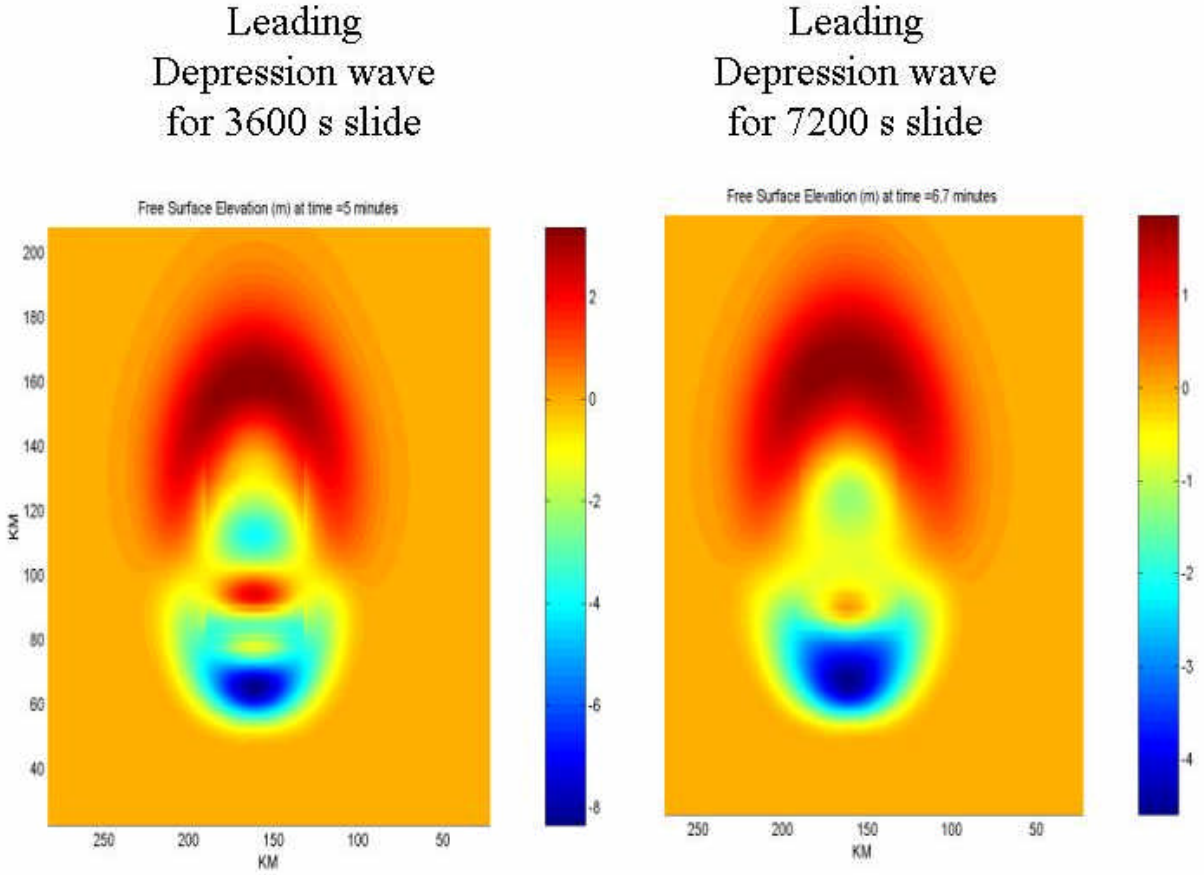


Figure 12 - Snapshots of landslide tsunami for landlside time scales of 1 and 2 hours. Puerto Rico is along the bottom boundary.

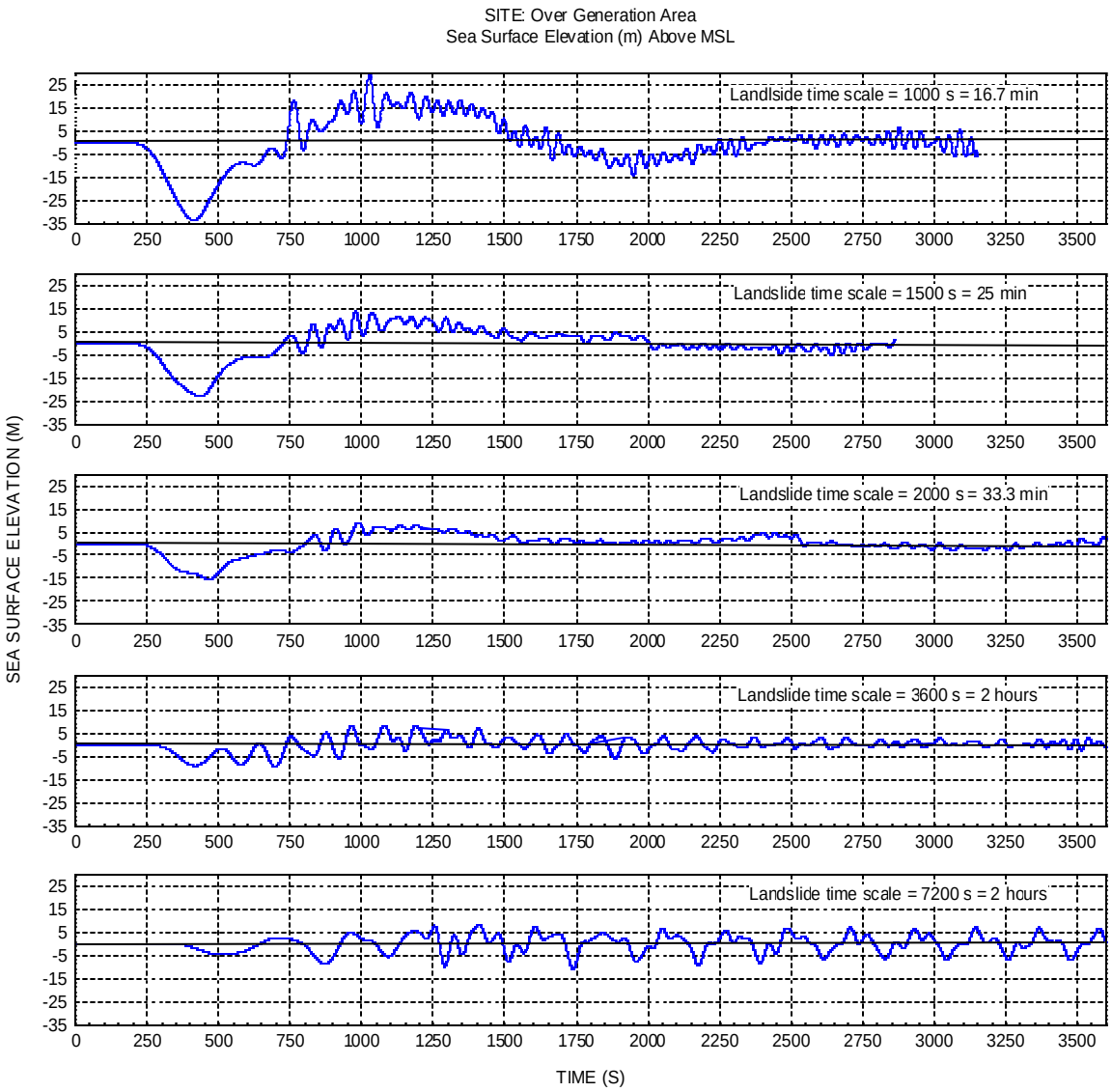


Figure 13 – Time history of sea surface elevation at generation area for the different scenarios. Friction factor $f$ = 0.01.

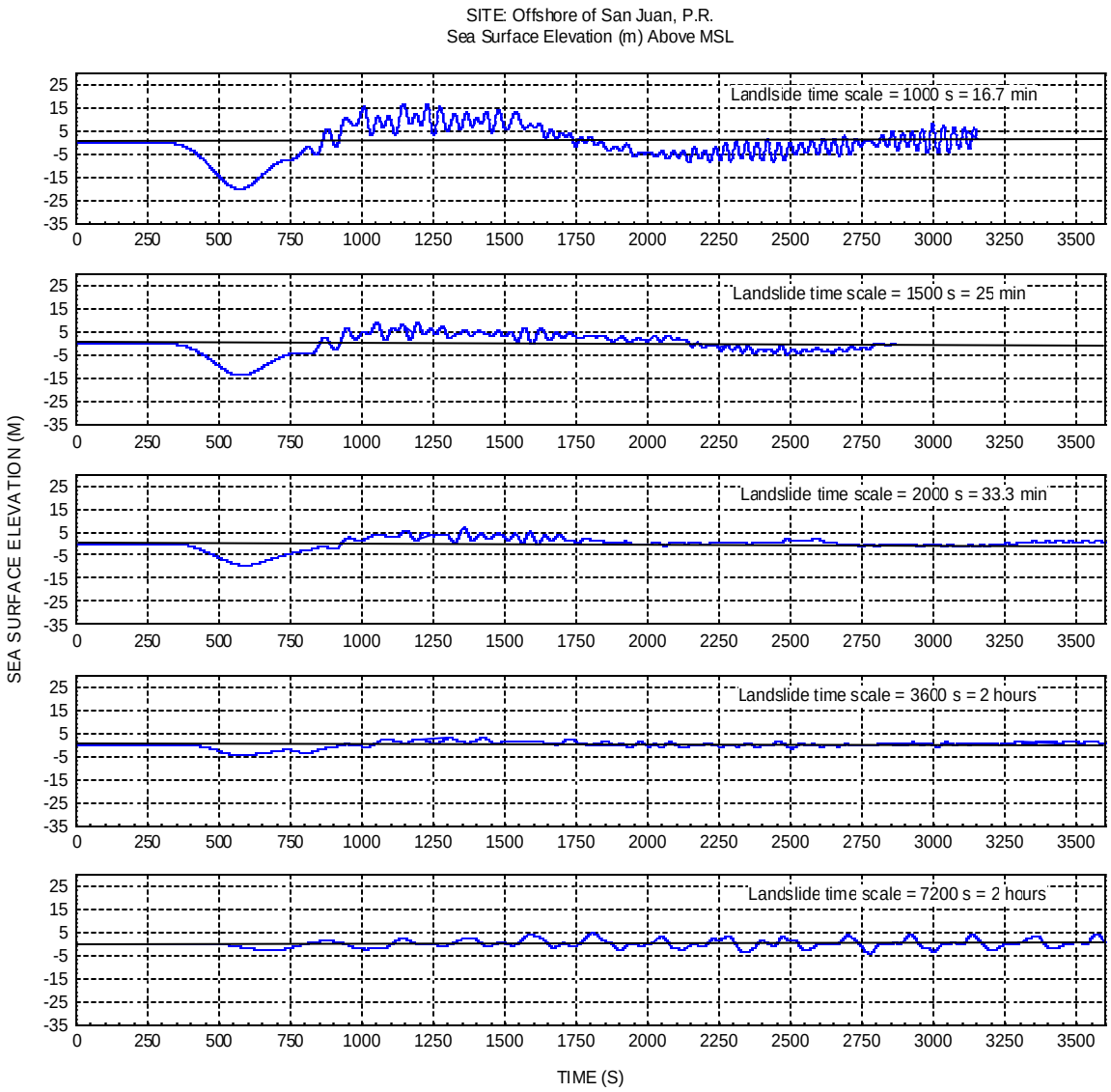


Figure 14 – Time history of sea surface elevation offshore of San Juan, P.R., for the different scenarios. Friction factor $f = 0.01$.

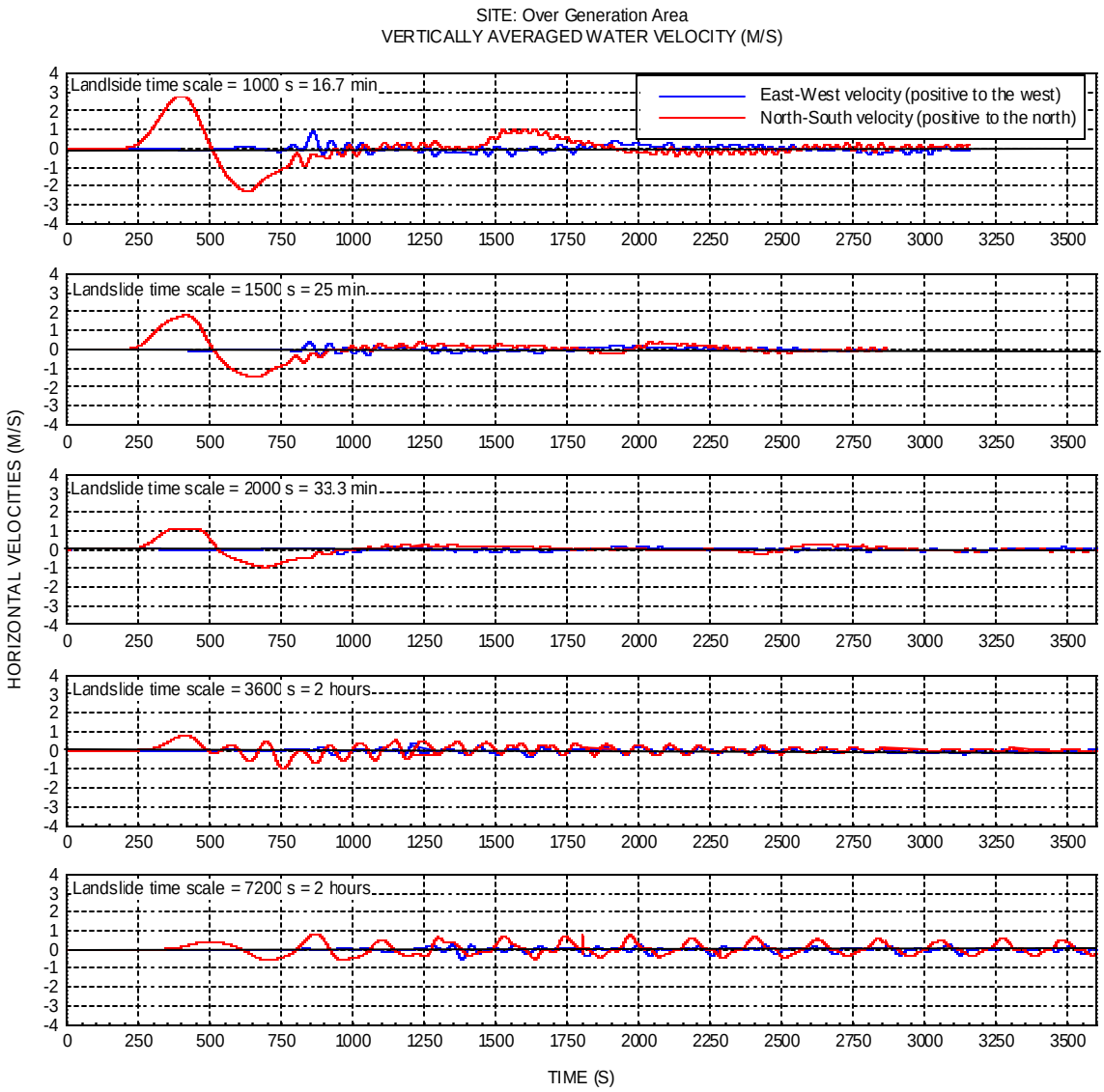


Figure 15 – Time history of vertically averaged horizontal velocities at generation area for the different scenarios. Friction factor $f = 0.01$.

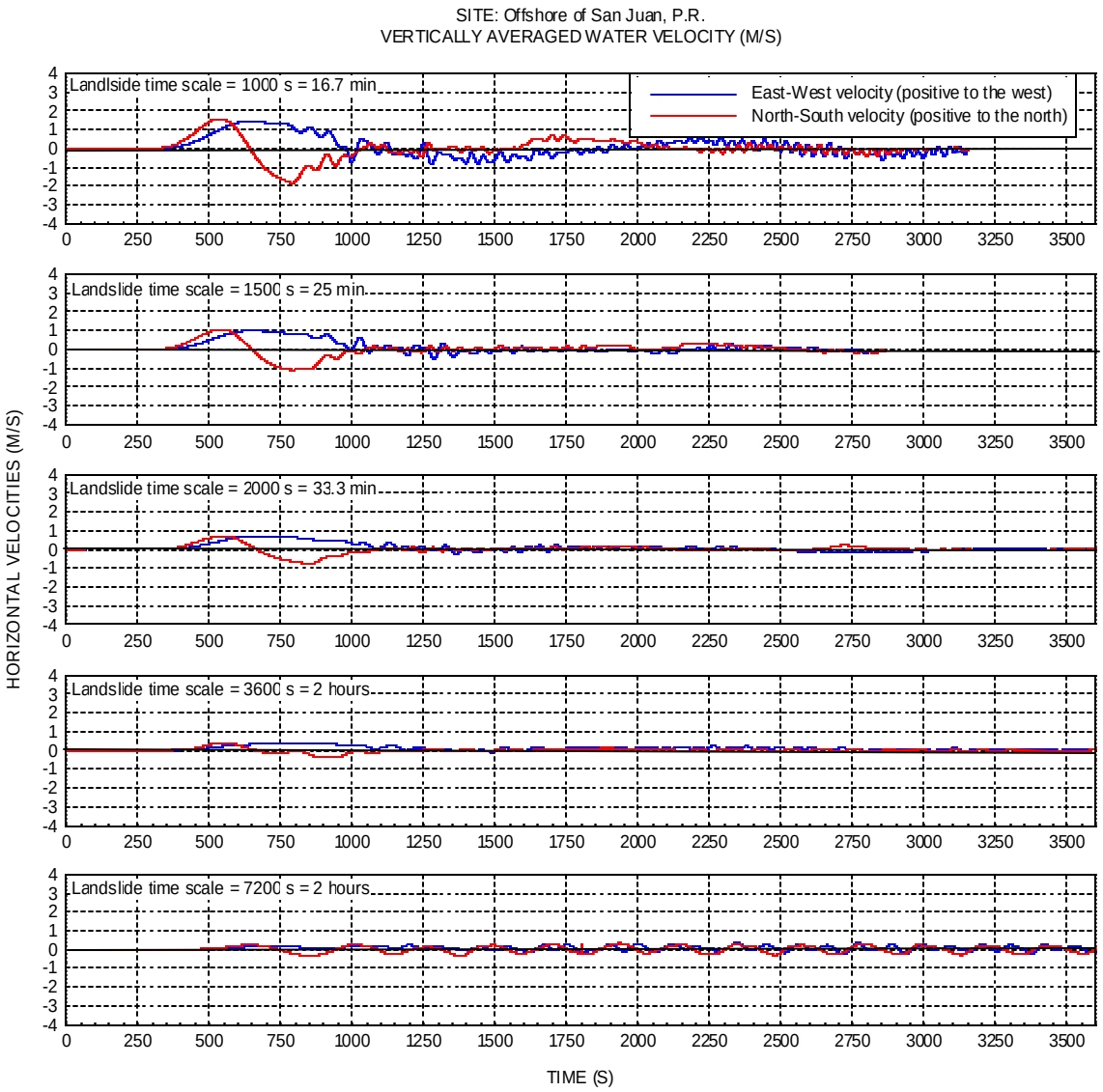


Figure 16 – Time history of vertically averaged horizontal velocities offshore of San Juan, P.R., for the different scenarios. Friction factor $f$ = 0.01.

this is the reason for the increase in runup compared to the previous shorter time scale is not clear. The observed decrease in initial wave height (Figure 13) is consistent with the statements that the slower the slide then the smaller the initial disturbance over the generation area. This trend can also be observed just offshore of San Juan (Figure 14). It is in the runup phase that this trend is violated.

Figures 17 and 18 show the results of the sensitivity test made by increasing the fiction factor, *f*, from 0.01 to 0.05. This was done only for the time scale of 1000 s. We can notice that by increasing *f* the high frequency oscillations superimposed on the lower frequency wave are decreased. But interestingly, the depth of the initial trough is slightly increased for $f = 0.05$ versus the result for $f = 0.01$. The same happens with the velocities, which initially show slightly higher values for $f = 0.05$ than for 0.01.

Another very important result to be obtained from these computer simulations is the time it takes for the coastal flooding to start once the wave is generated in deep water. This can be estimated from the sea surface time histories shown in Figures 13 and 14. In order to make this estimate we will use as our start time the moment when the leading depression wave over the generation area reaches its maximum value. That will be assumed as the start of propagation time. For the arrival time we will use the time when the sea surface elevation just offshore of San Juan rises above Mean Sea Level (MSL) once the sea first withdraws from the coastline. The table below shows the results for the six scenarios modeled in this study.

**TABLE 3**
**APPROXIMATE TRAVEL TIMES**

| Time Scale | Starting Time (s) | Arrival Time (s) | Propagation Time | Friction Factor |
|---|---|---|---|---|
| 1000 s = 16.7 min | 408 | 862 | 454 s = 7.6 min | 0.01 |
| 1500 s = 25 min | 434 | 850 | 416 s = 6.9 min | 0.01 |
| 2000 s = 33.3 min | 468 | 929 | 461 s = 7.7 min | 0.01 |
| 3600 s = 1 hour | 416 | 944 | 528 s =8.8 min | 0.01 |
| 7200 s = 2 hours | 505 | 801 | 296 s = 4.9 min | 0.01 |
| 1000 s = 16.7 min | 405 | 842 | 437 s = 7.3 min | 0.05 |

The fourth column corroborates the statement made above about the danger posed by local landslides in that in a matter of a few minutes they are affecting the local coastlines.

Finally, Figures 19 to 83 show the computed coastal flooding (friction factor $f = 0.01$) for each of the following north coast quadrangles: Aguadilla, Isabela, Qubradillas, Camuy, Arecibo, Barcelojneta, Manati, Vega Alta, Bayamon, San Juan, Carolina, Rio Grande, and Fajardo. Figures 84 to 96 show the results of the sensitivity test made for the time scale of 1000 s with $f = 0.05$. It is important to understand that the computational grid size was 300 m and, therefore, we can expect some mismatch between topographic details in the maps and the flood contour values. Also, the topographic information used for the preparation of the computational grid was obtained from a USGS DEM which is based on topographic information approximately 40 years old. This topographic information should be the same one appearing in the USGS quadrangle sheets. But at some locations the topographic information according to the DEM does not match the one appearing in the quadrangles. This

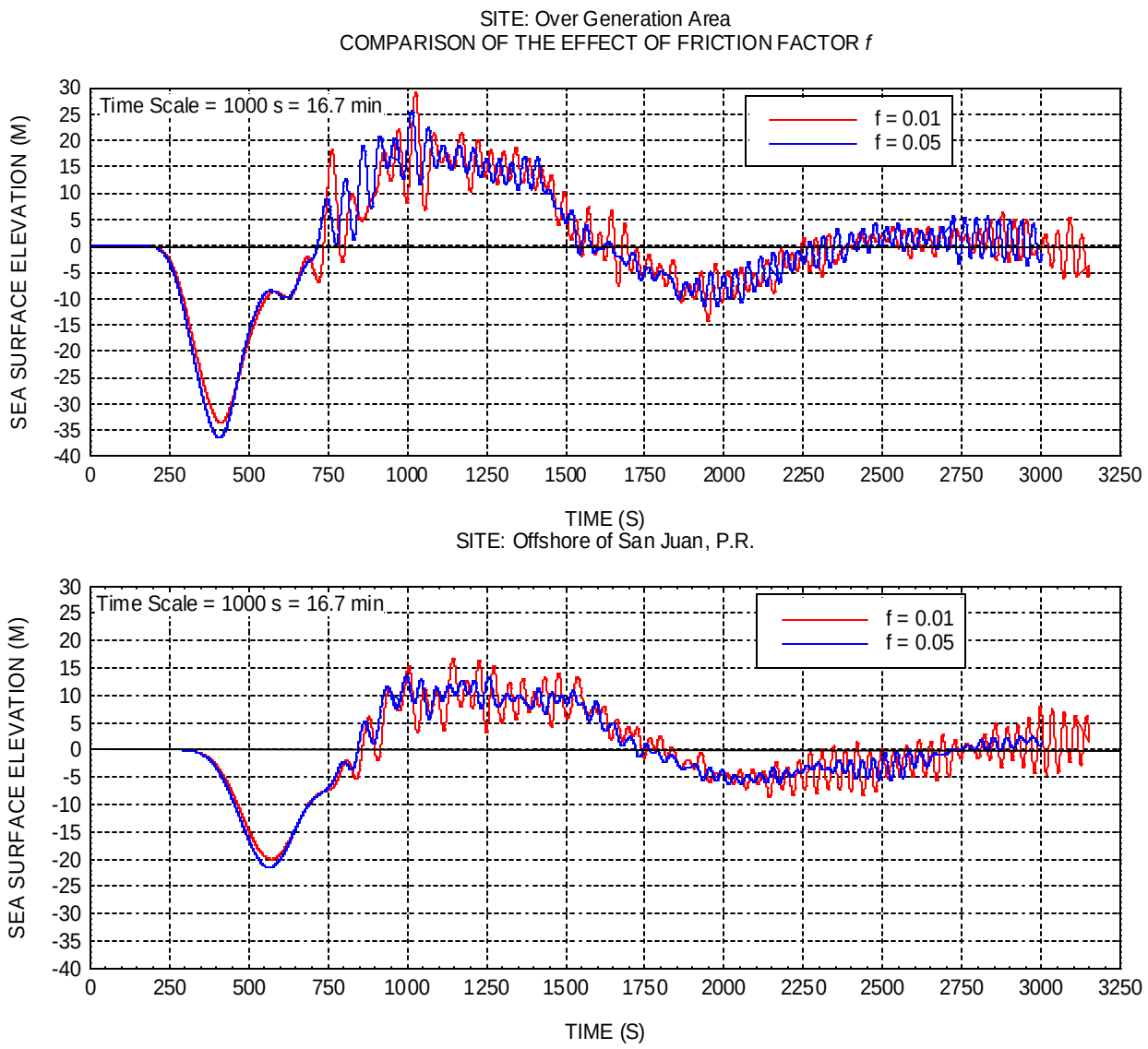


Figure 17 – Comparison of time histories of sea surface elevation at generation area (top) and offshore of San Juan, P.R., for friction factor $f$ = 0.01 and 0.05. Landslide time scale = 1000 s = 16.7 min.

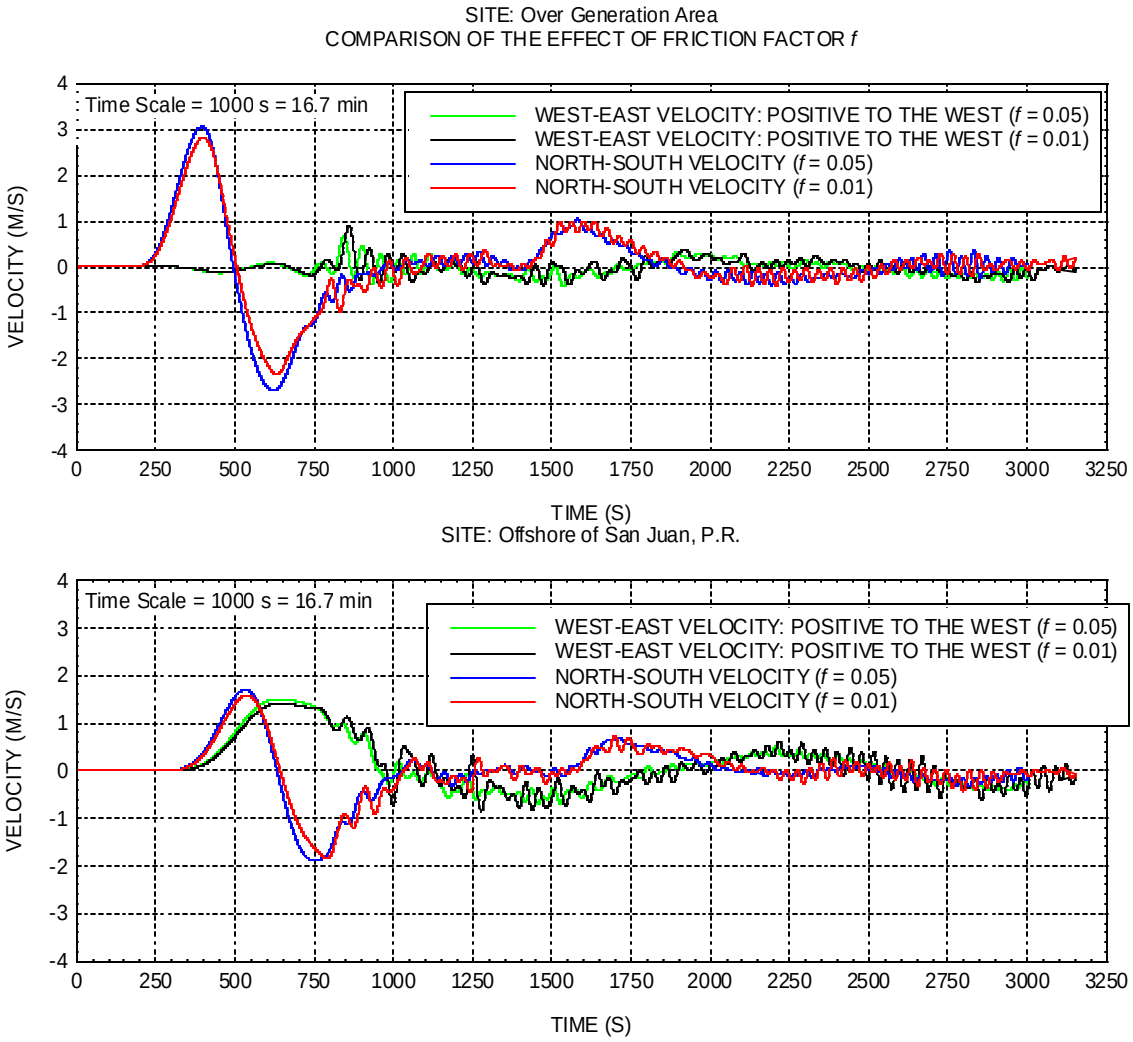


Figure 18 – Comparison of time histories of vertically averaged horizontal velocities at generation area (top) and offshore of San Juan, P.R., for friction factor $f$ = 0.01 and 0.05. Landslide time scale = 1000 s = 16.7 min

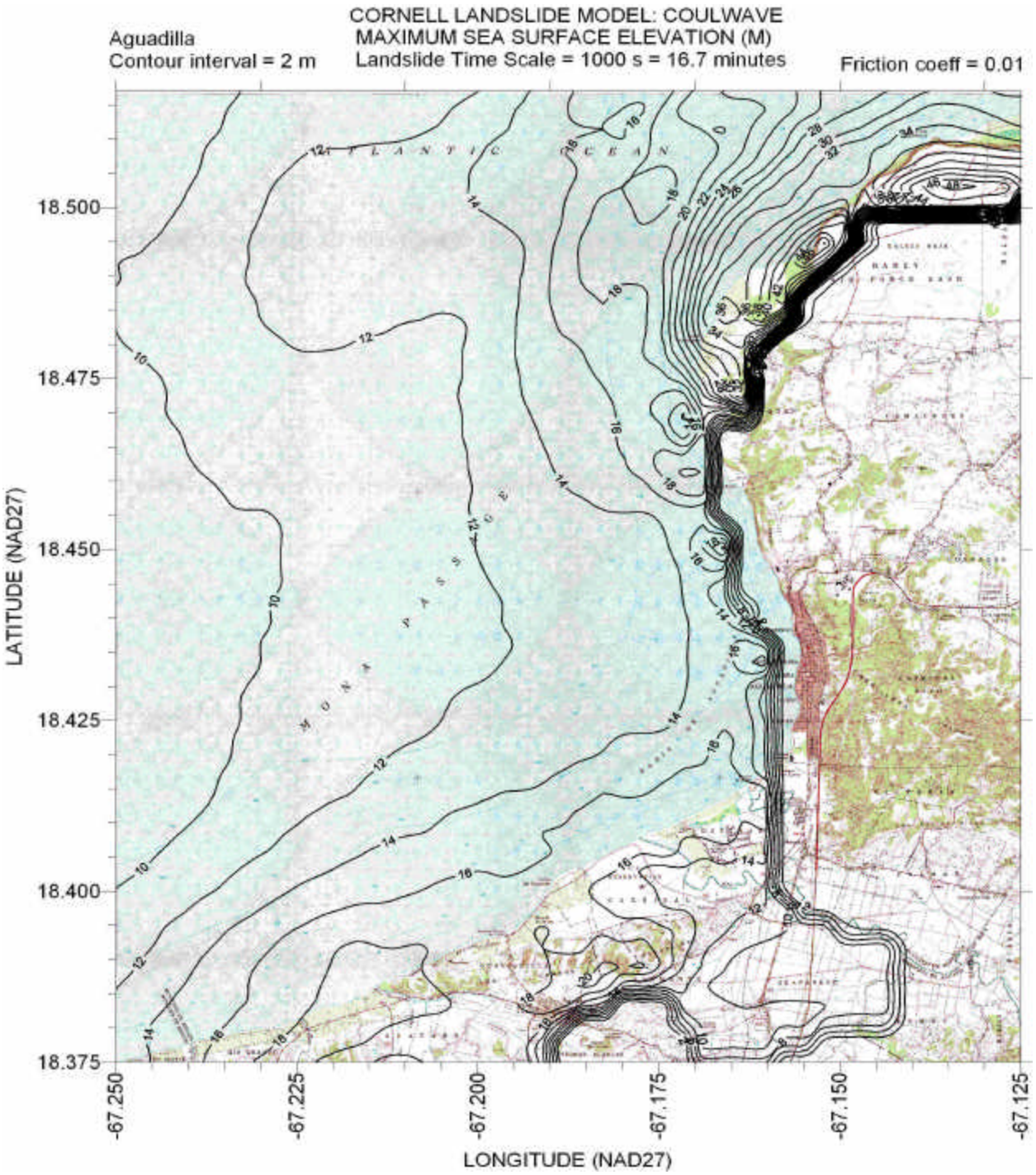


Figure 19 – Contours of maximum sea surface elevation for time scale = 1000 s for Aguadilla quadrangle. Friction factor f = 0.01.

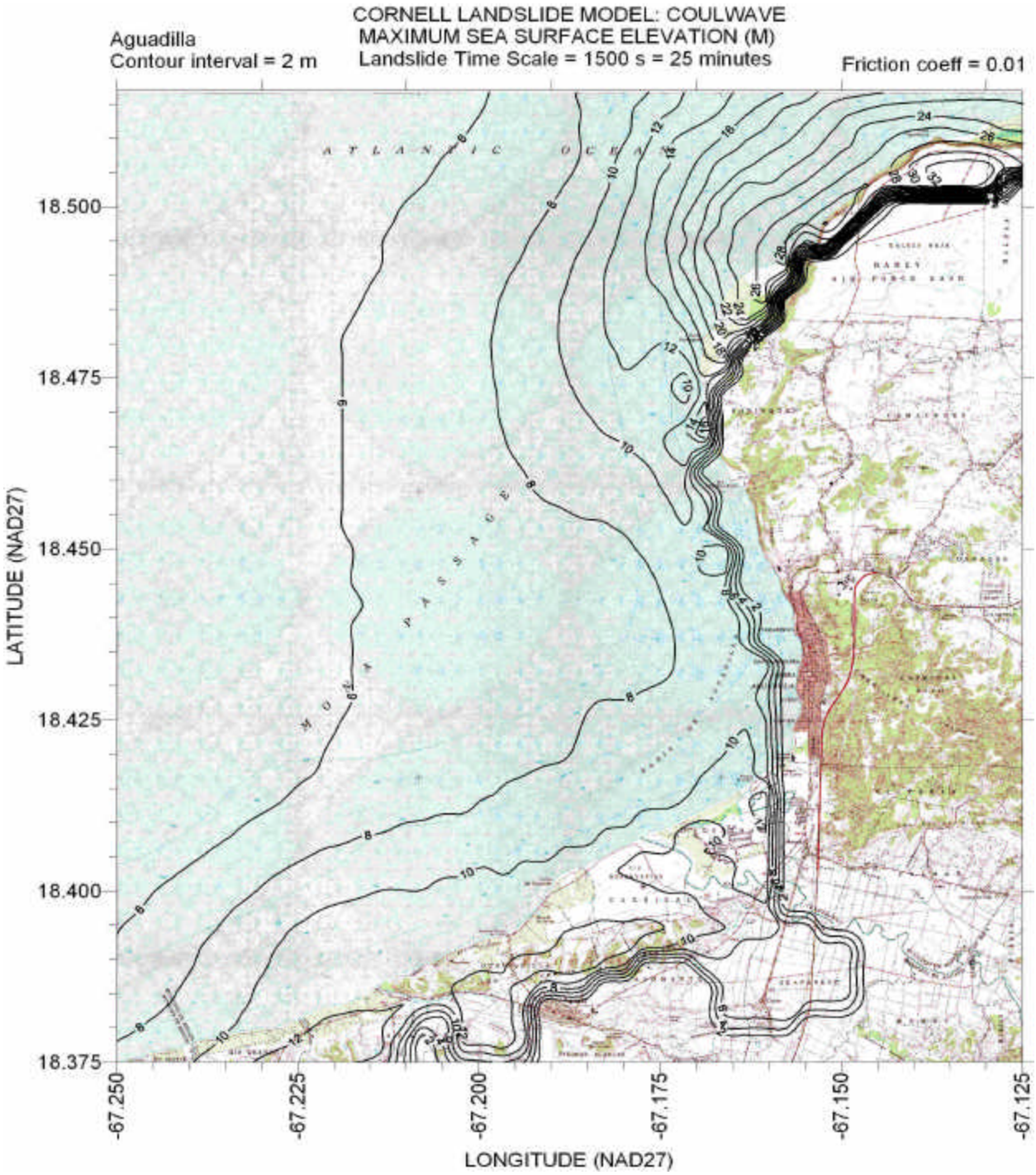


Figure 20 – Contours of maximum sea surface elevation for time scale = 1500 s for Aguadilla quadrangle. Friction factor f = 0.01.

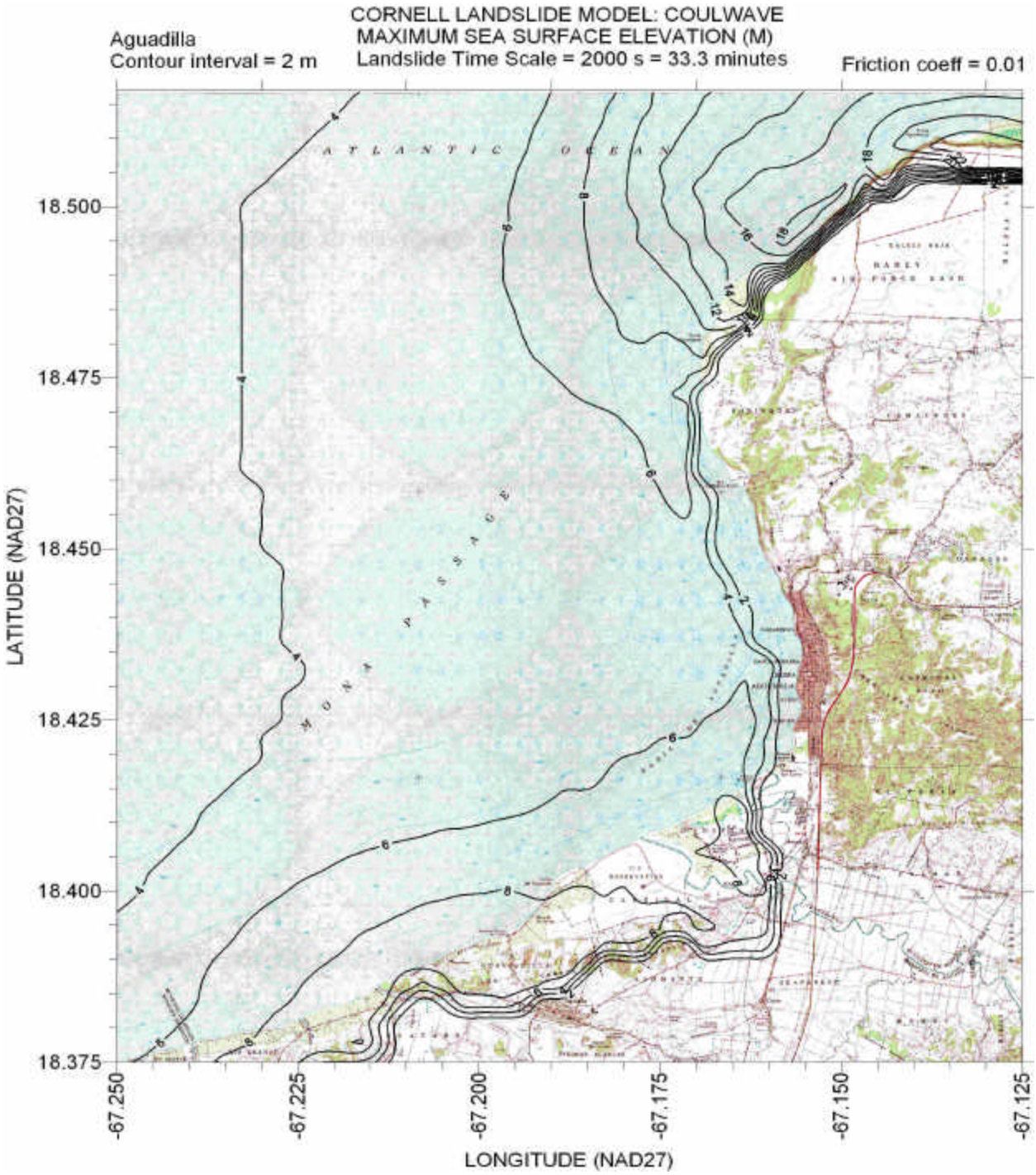


Figure 21 – Contours of maximum sea surface elevation for time scale = 2000 s for Aguadilla quadrangle. Friction factor f = 0.01.

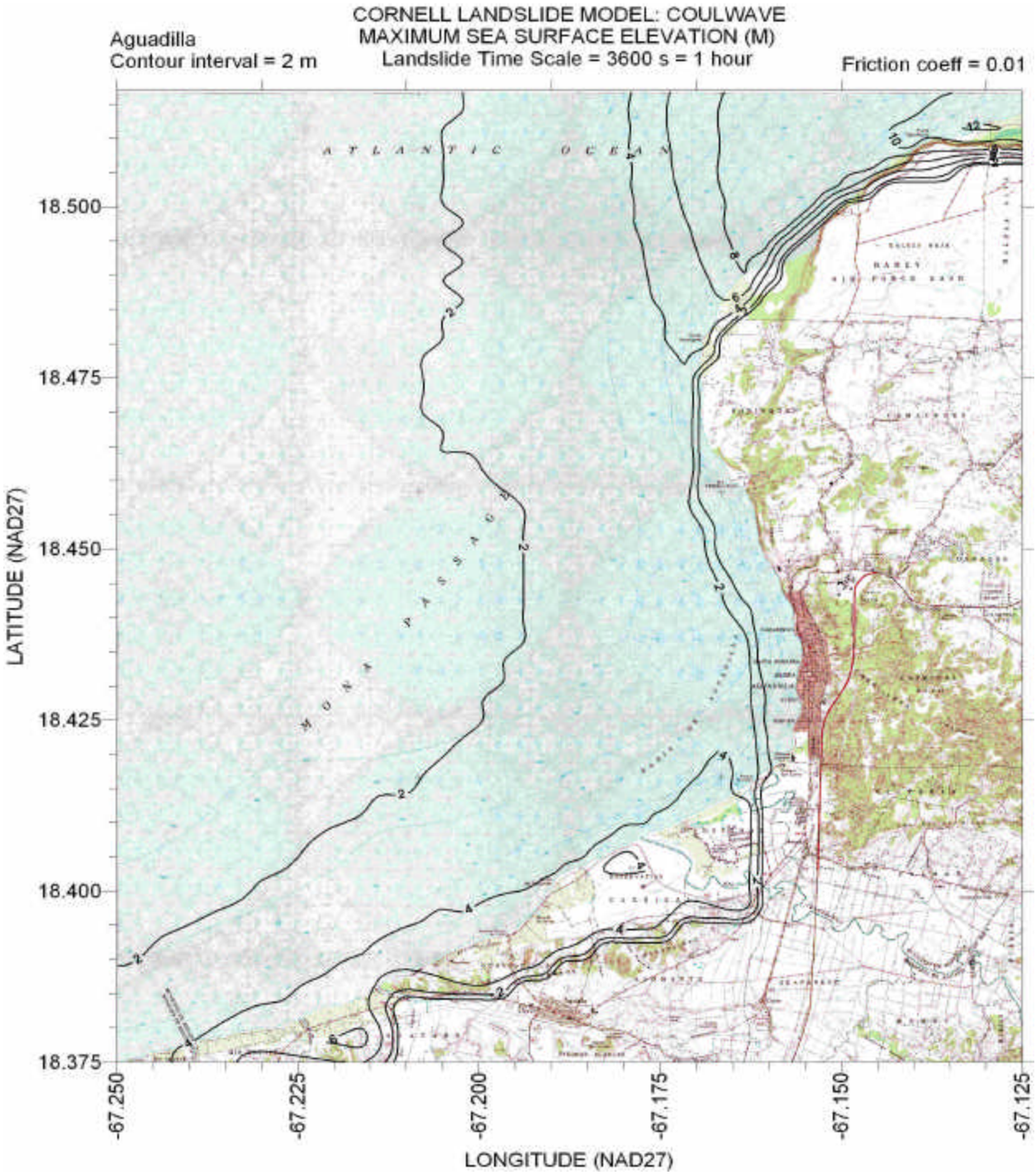


Figure 22 – Contours of maximum sea surface elevation for time scale = 3600 s for Aguadilla quadrangle. Friction factor f = 0.01.

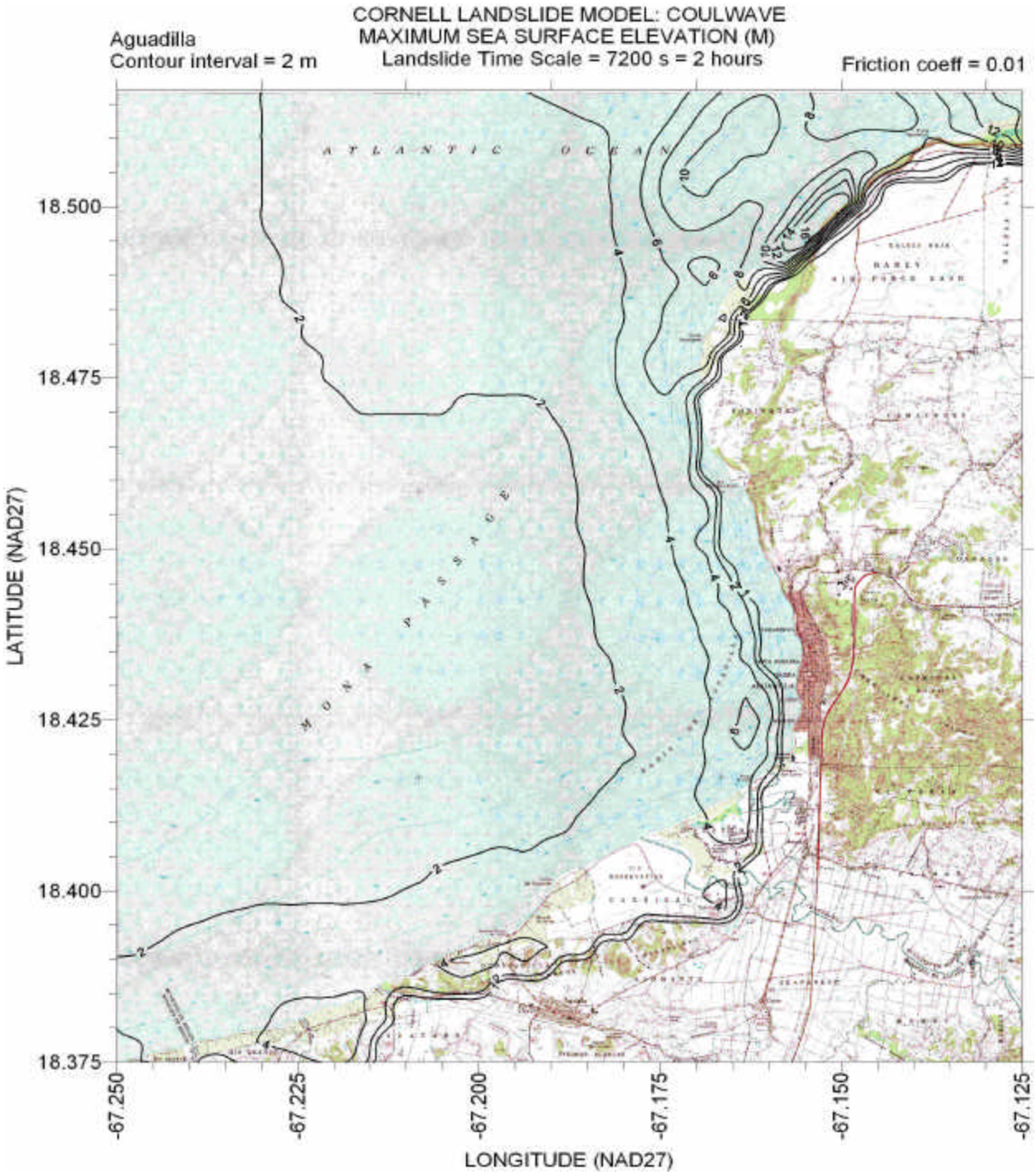


Figure 23 – Contours of maximum sea surface elevation for time scale = 7200 s for Aguadilla quadrangle. Friction factor f = 0.01.

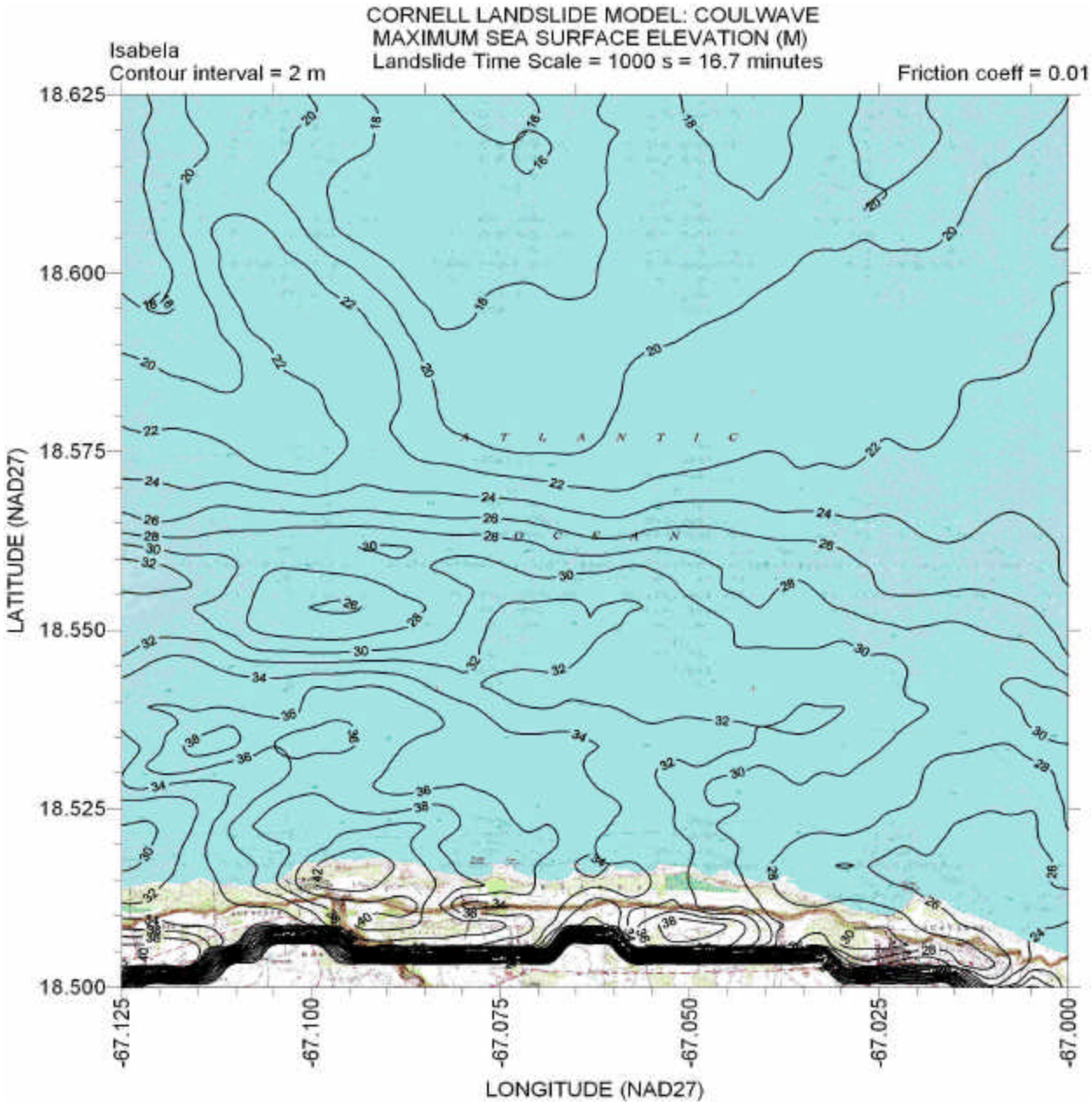


Figure 24 – Contours of maximum sea surface elevation for time scale = 1000 s for Isabela quadrangle. Friction factor f = 0.01.

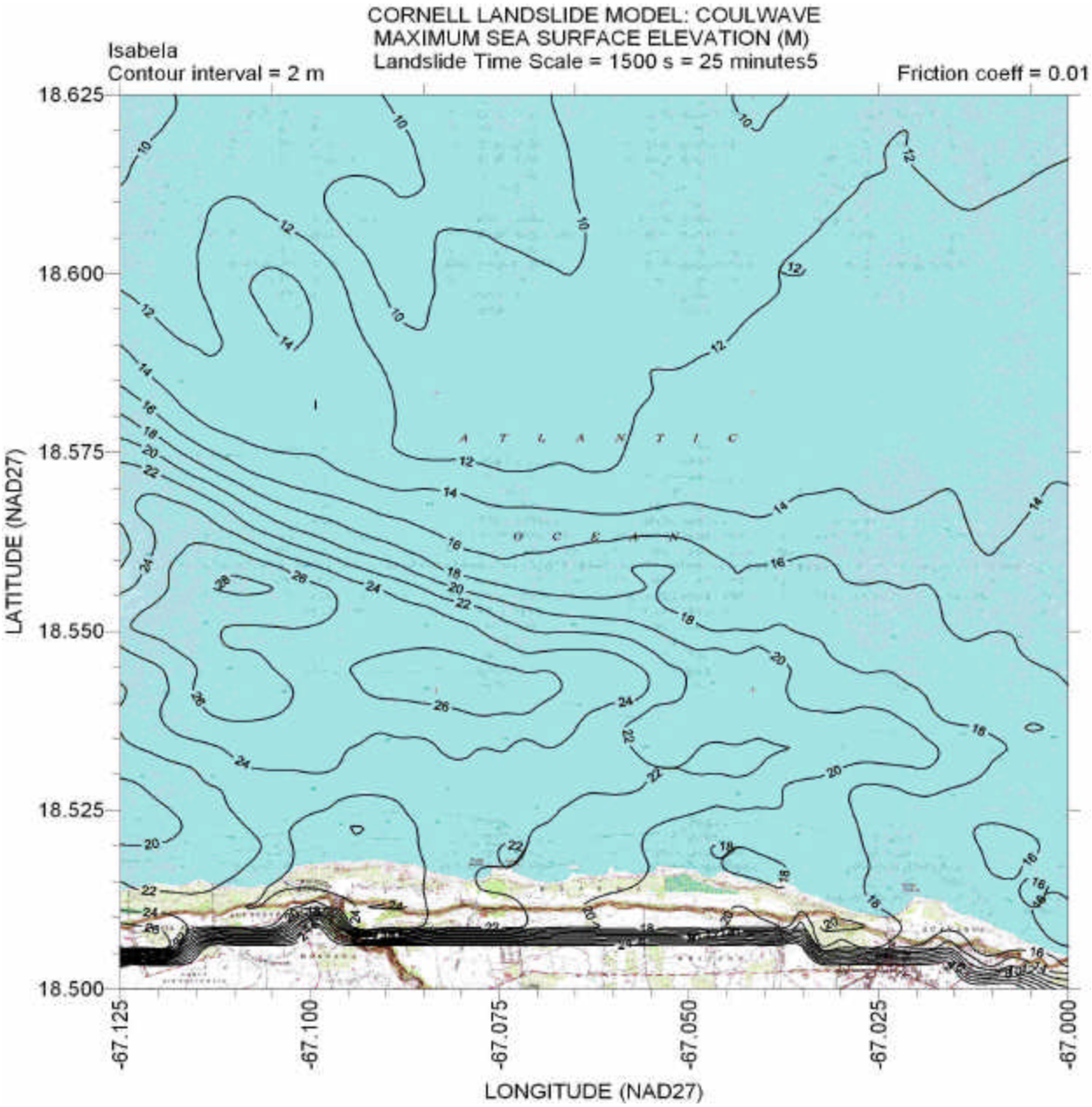


Figure 25 – Contours of maximum sea surface elevation for time scale = 1500 s for Isabela quadrangle. Friction factor f = 0.01.

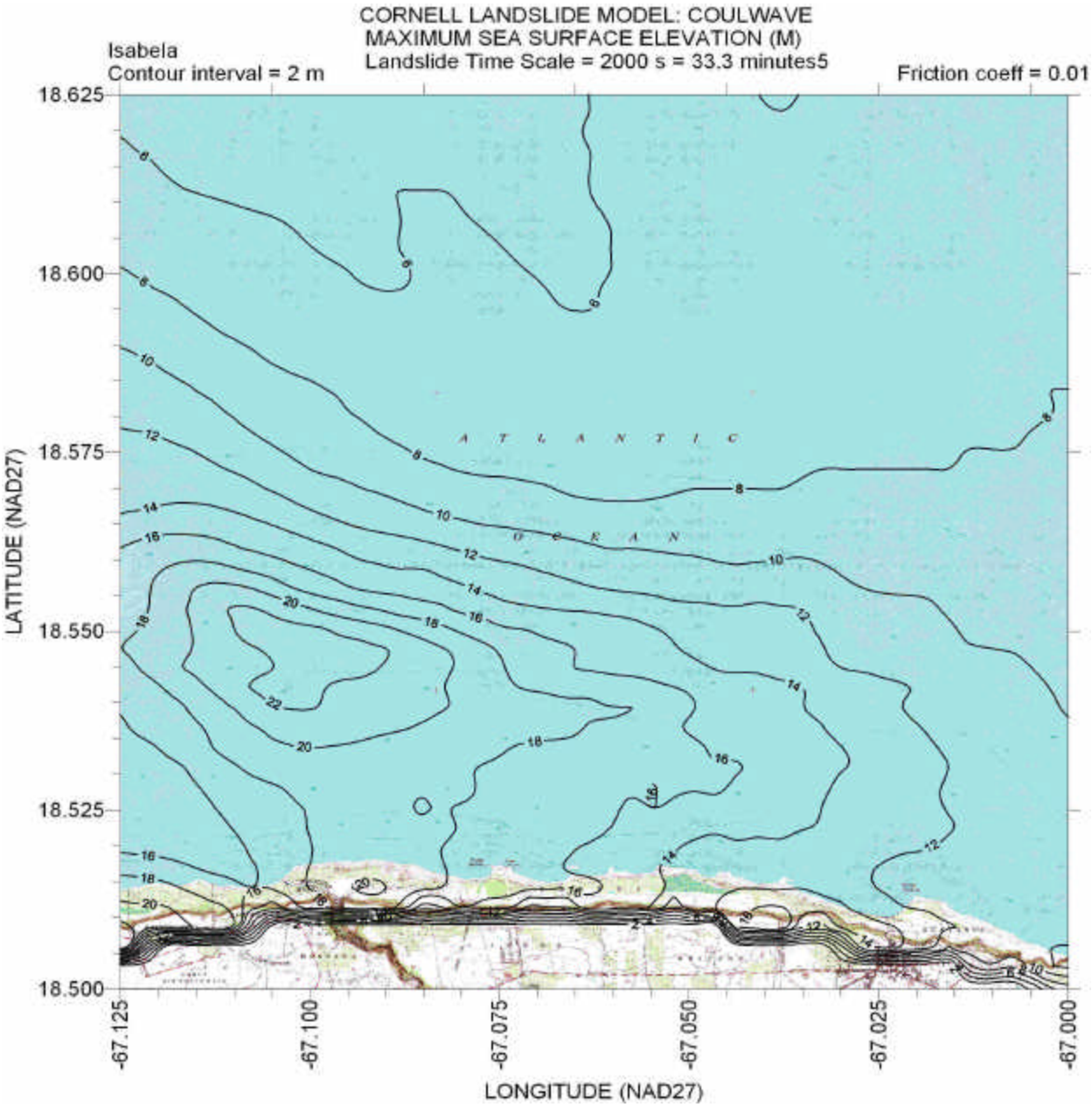


Figure 26 – Contours of maximum sea surface elevation for time scale = 2000 s for Isabela quadrangle. Friction factor f = 0.01.

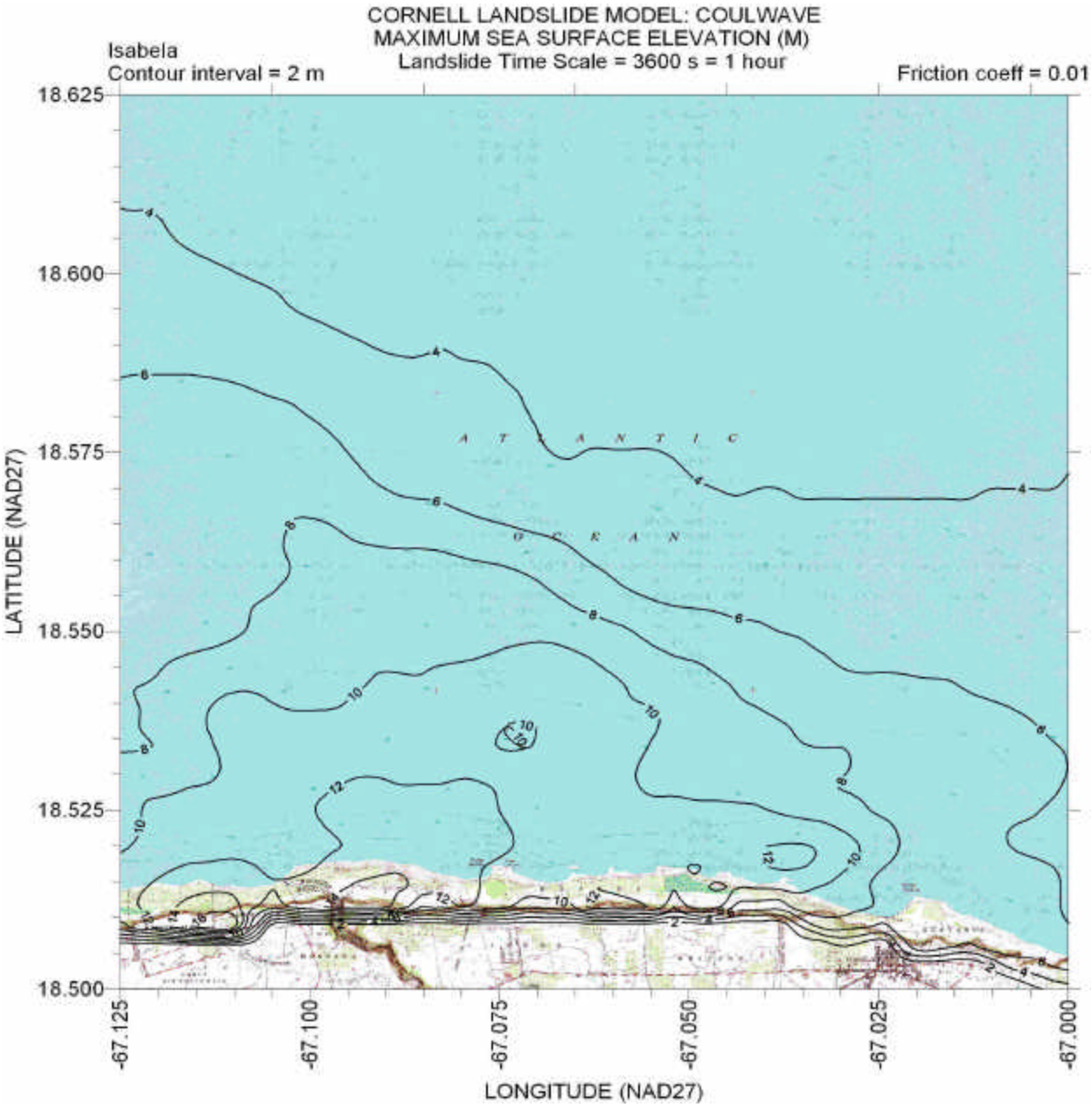


Figure 27 – Contours of maximum sea surface elevation for time scale = 3600 s for Isabela quadrangle. Friction factor f = 0.01.

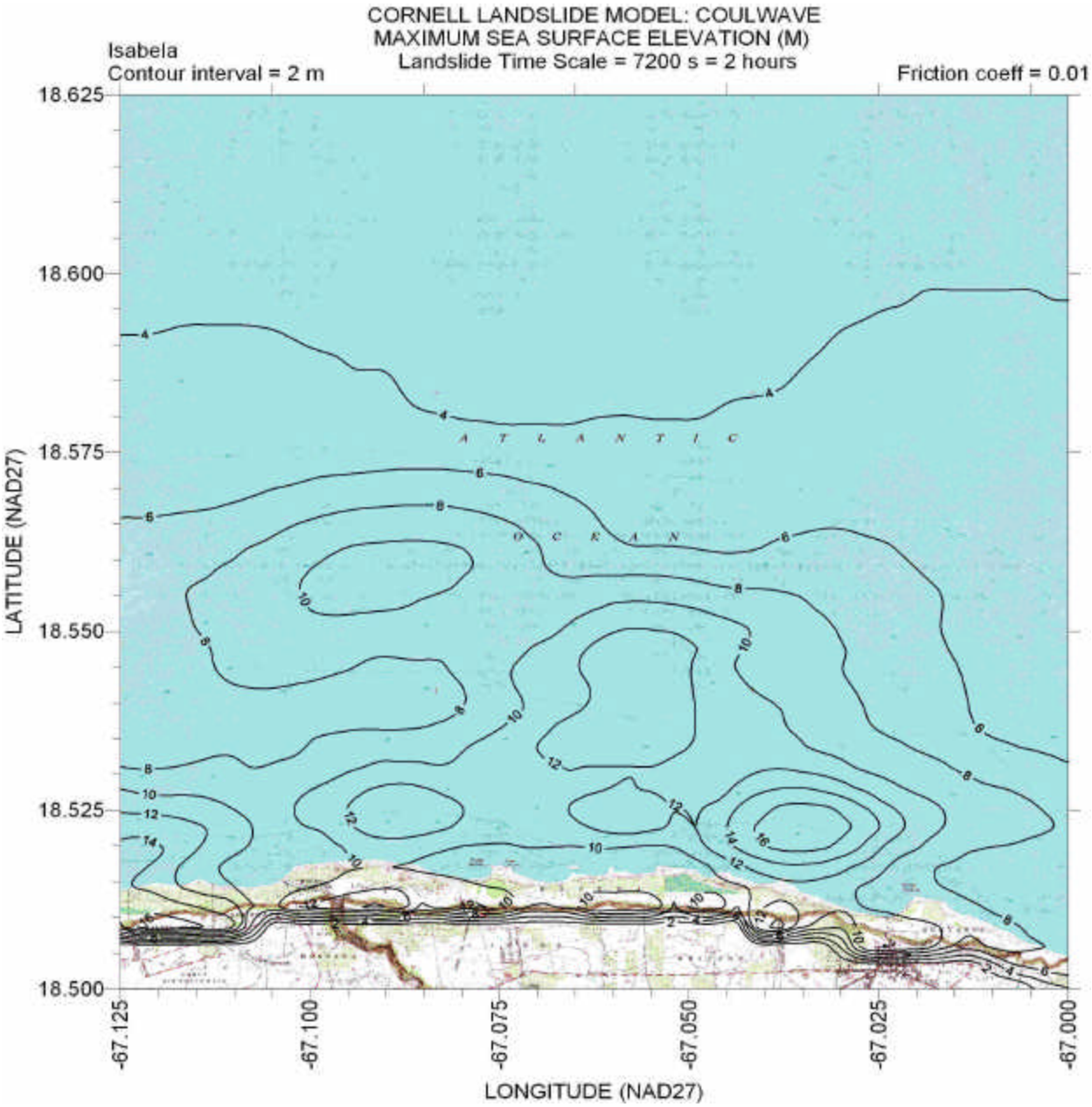


Figure 28 – Contours of maximum sea surface elevation for time scale = 7200 s for Isabela quadrangle. Friction factor f = 0.01.

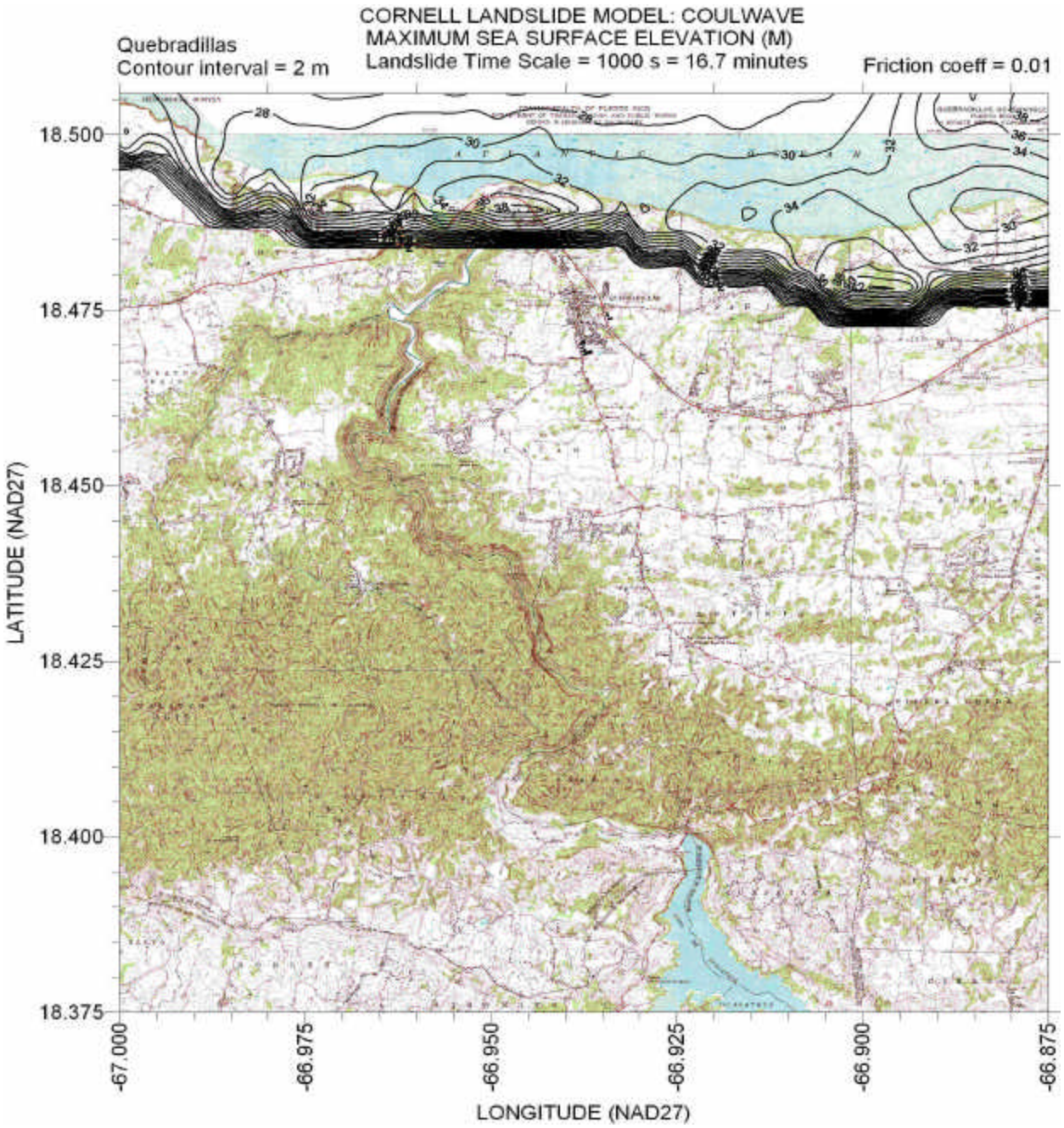


Figure 29 – Contours of maximum sea surface elevation for time scale = 1000 s for Quebradillas quadrangle. Friction factor f = 0.01.

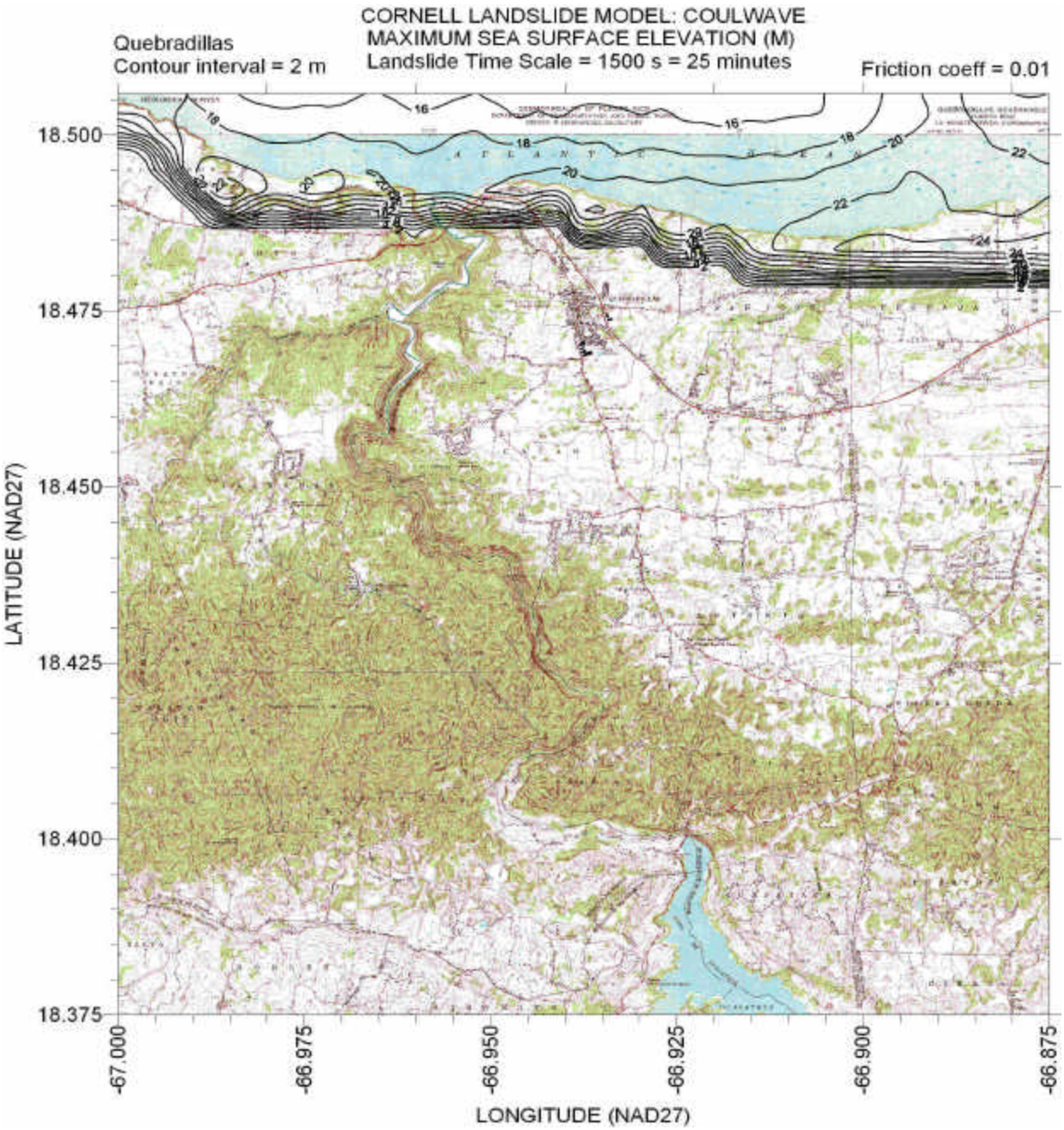


Figure 30 – Contours of maximum sea surface elevation for time scale = 1500 s for Quebradillas quadrangle. Friction factor f = 0.01.

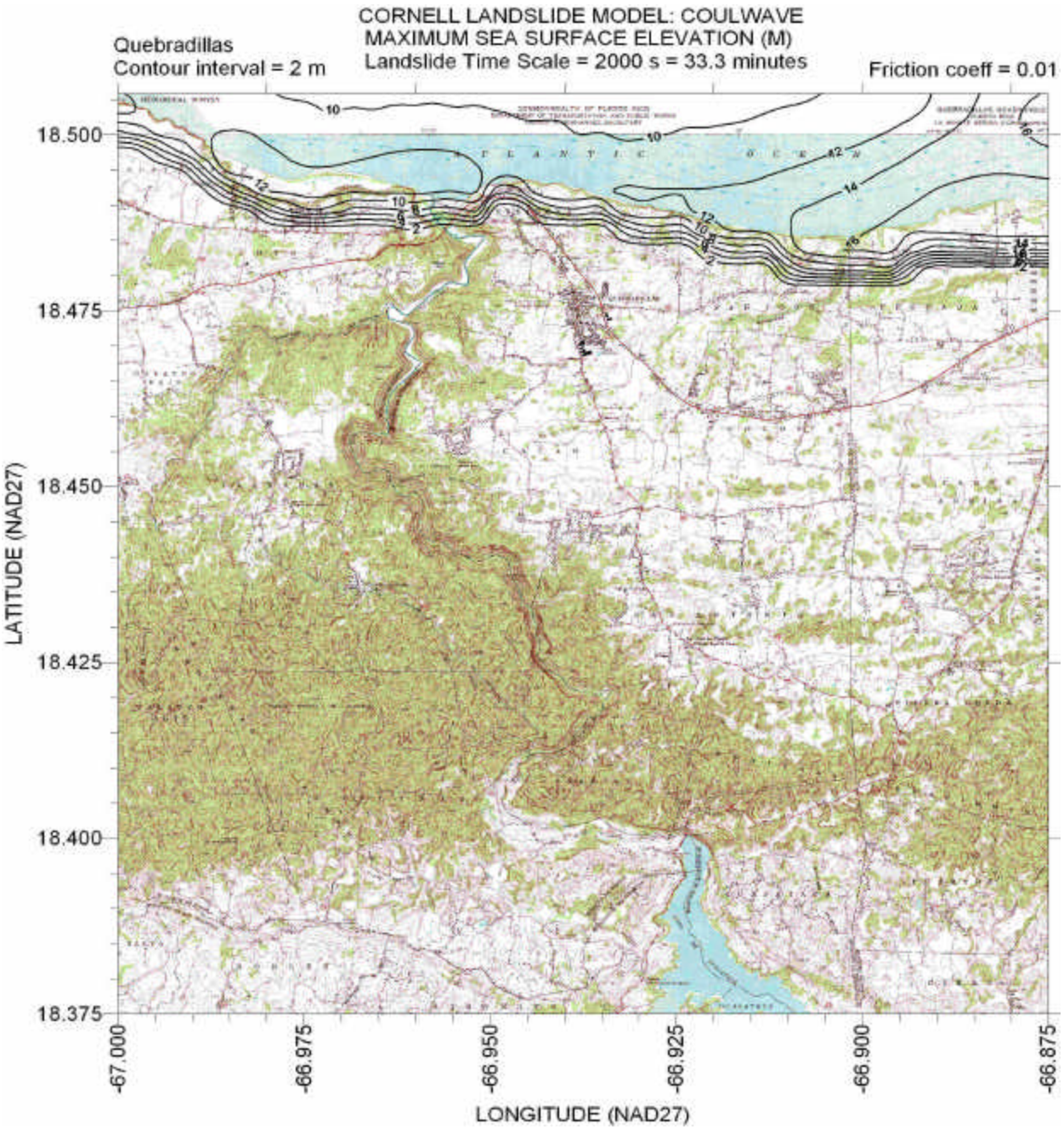


Figure 31 – Contours of maximum sea surface elevation for time scale = 2000 s for Quebradillas quadrangle. Friction factor f = 0.01.

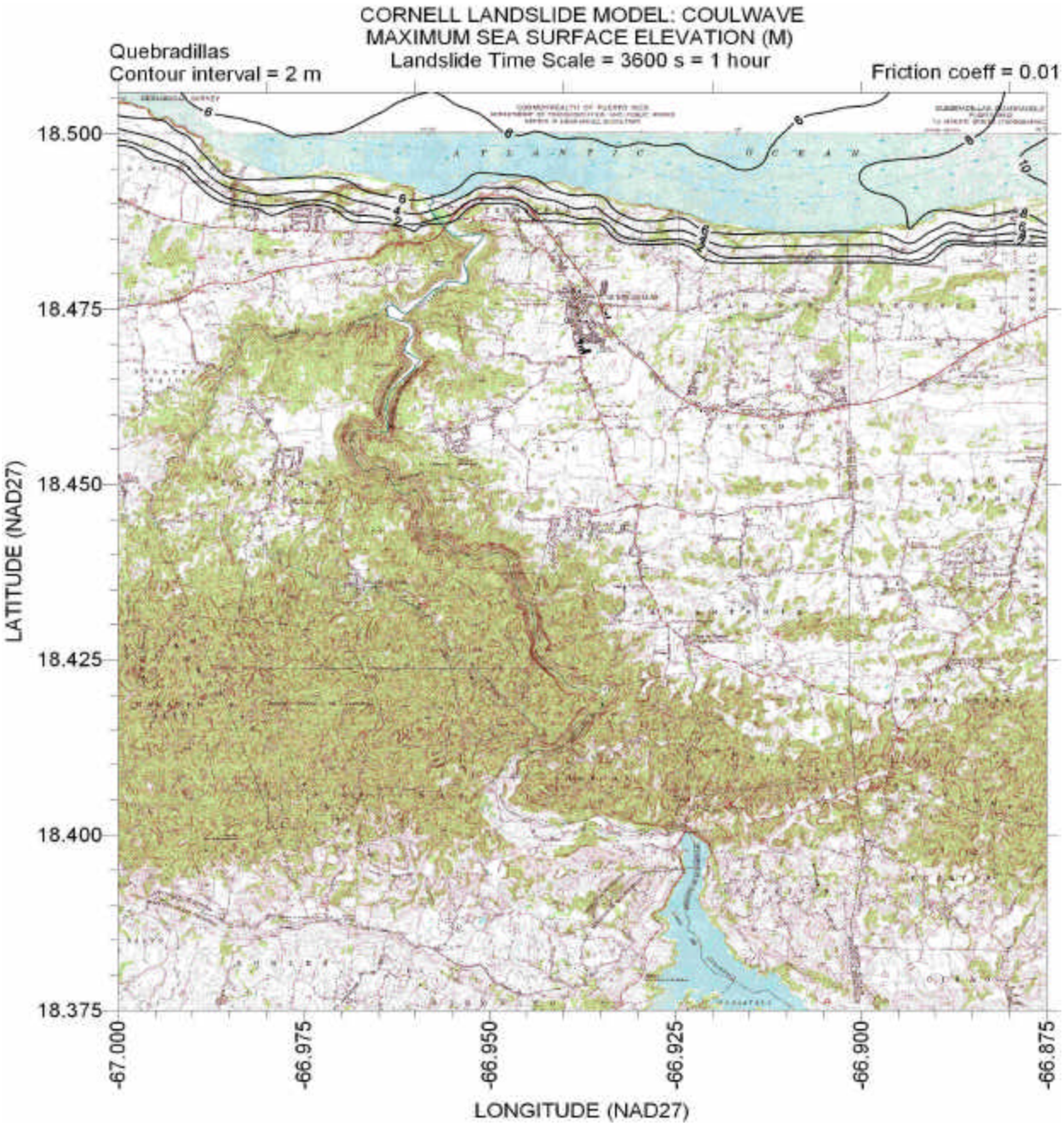


Figure 32 – Contours of maximum sea surface elevation for time scale = 3600 s for Quebradillas quadrangle. Friction factor f = 0.01.

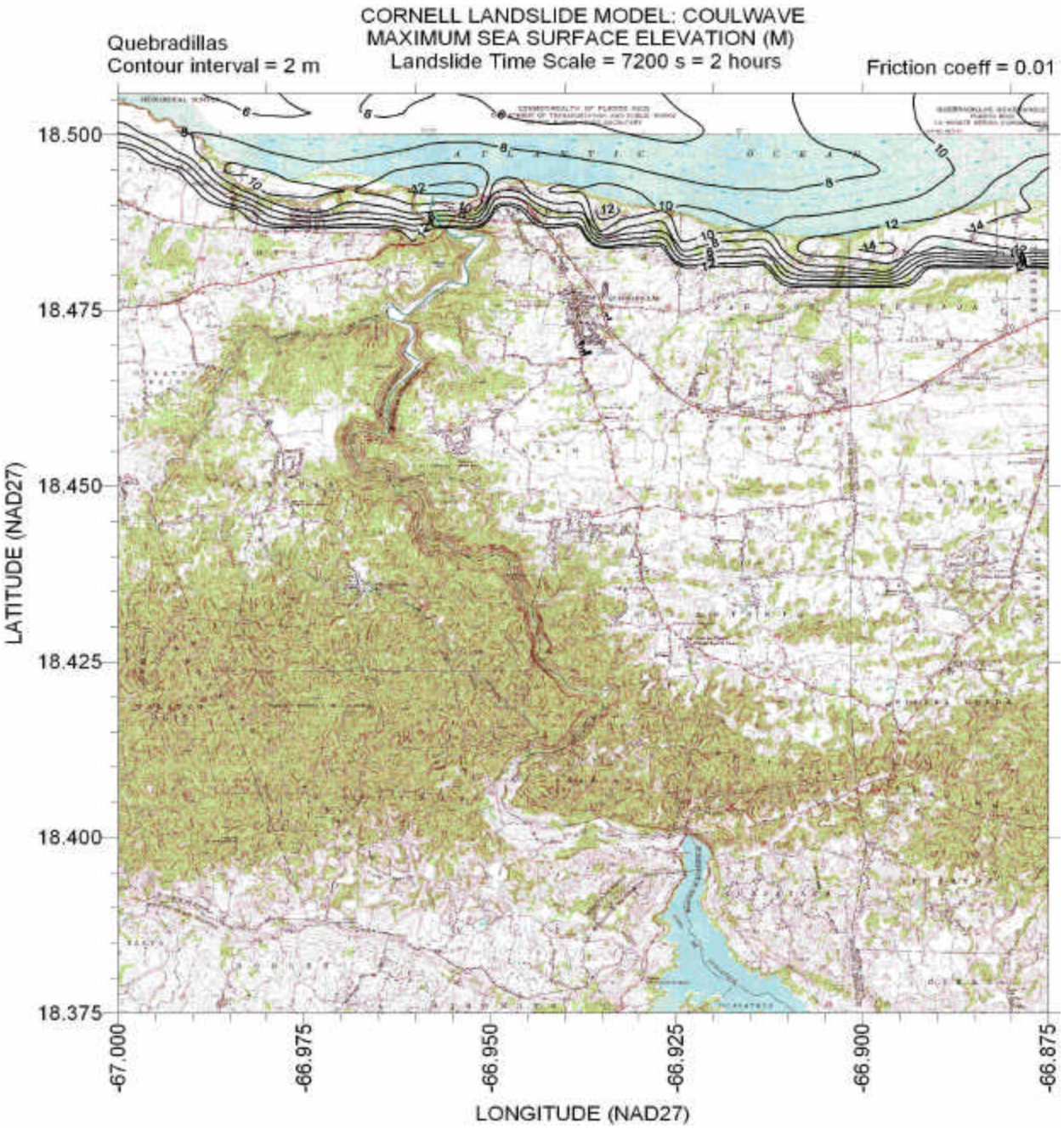


Figure 33 – Contours of maximum sea surface elevation for time scale = 7200 s for Quebradillas quadrangle. Friction factor f = 0.01.

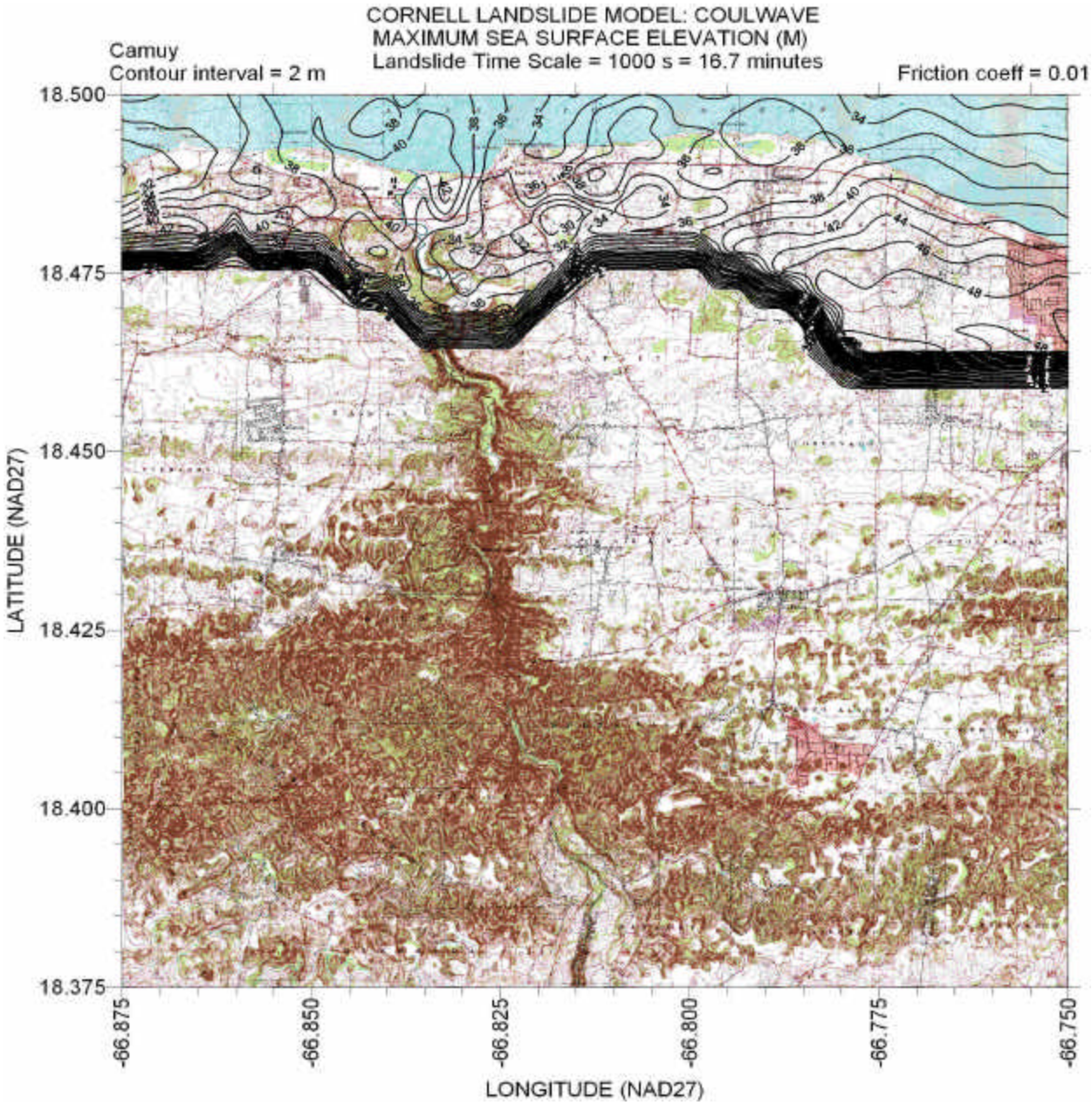


Figure 34 – Contours of maximum sea surface elevation for time scale = 1000 s for Camuy quadrangle. Friction factor f = 0.01.

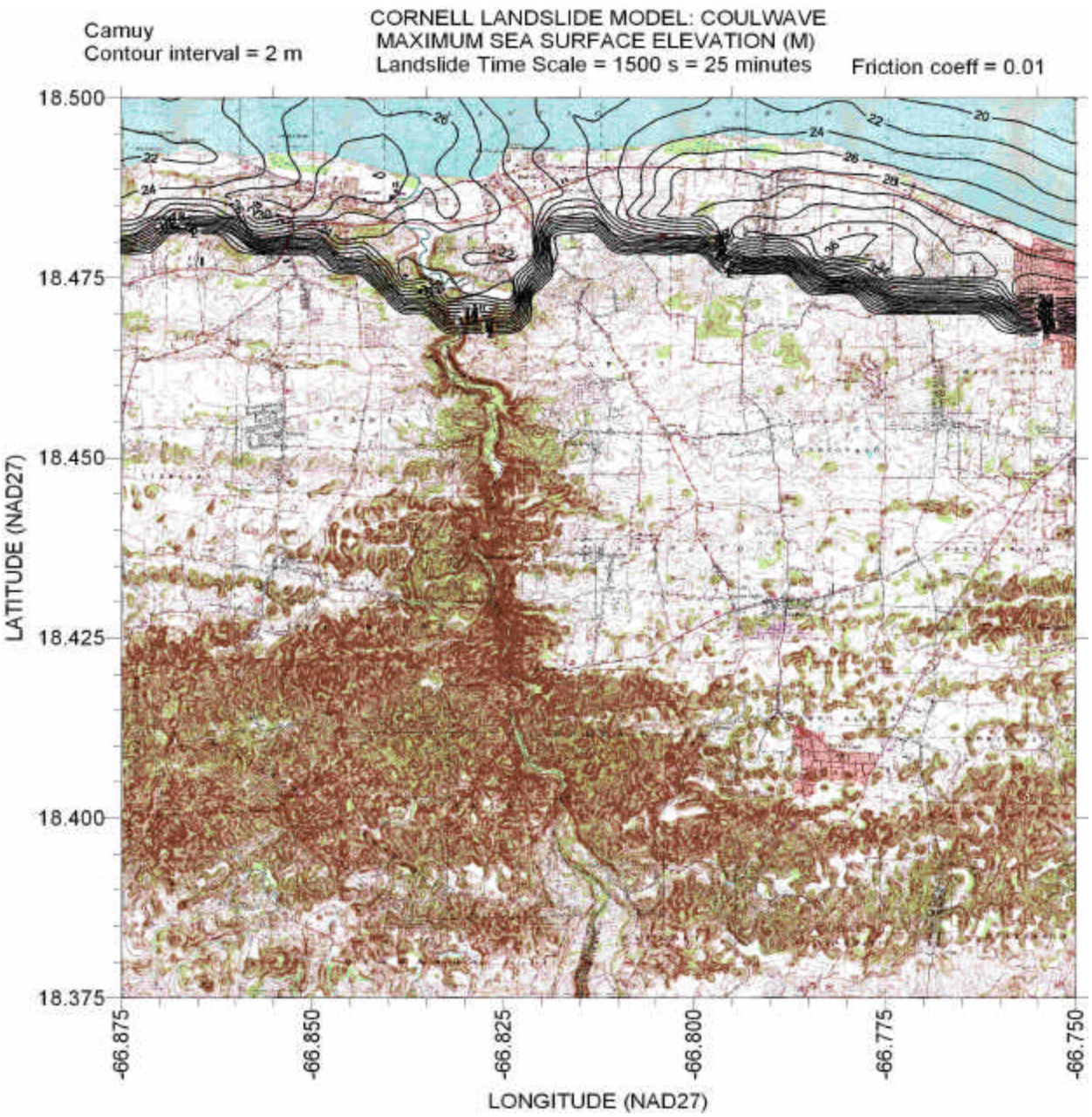


Figure 35 – Contours of maximum sea surface elevation for time scale = 1500 s for Camuy quadrangle. Friction factor f = 0.01.

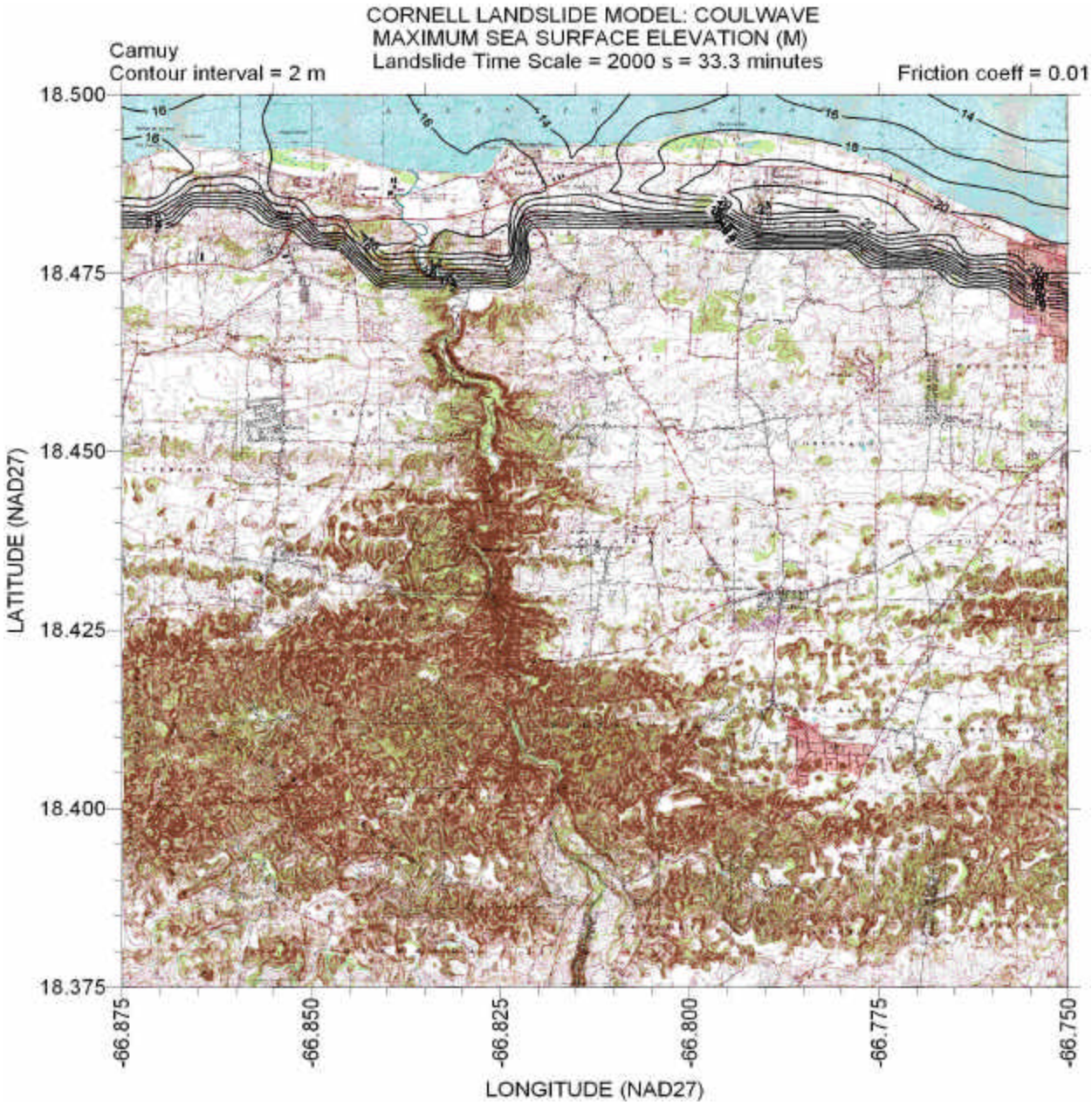


Figure 36 – Contours of maximum sea surface elevation for time scale = 2000 s for Camuy quadrangle. Friction factor f = 0.01.

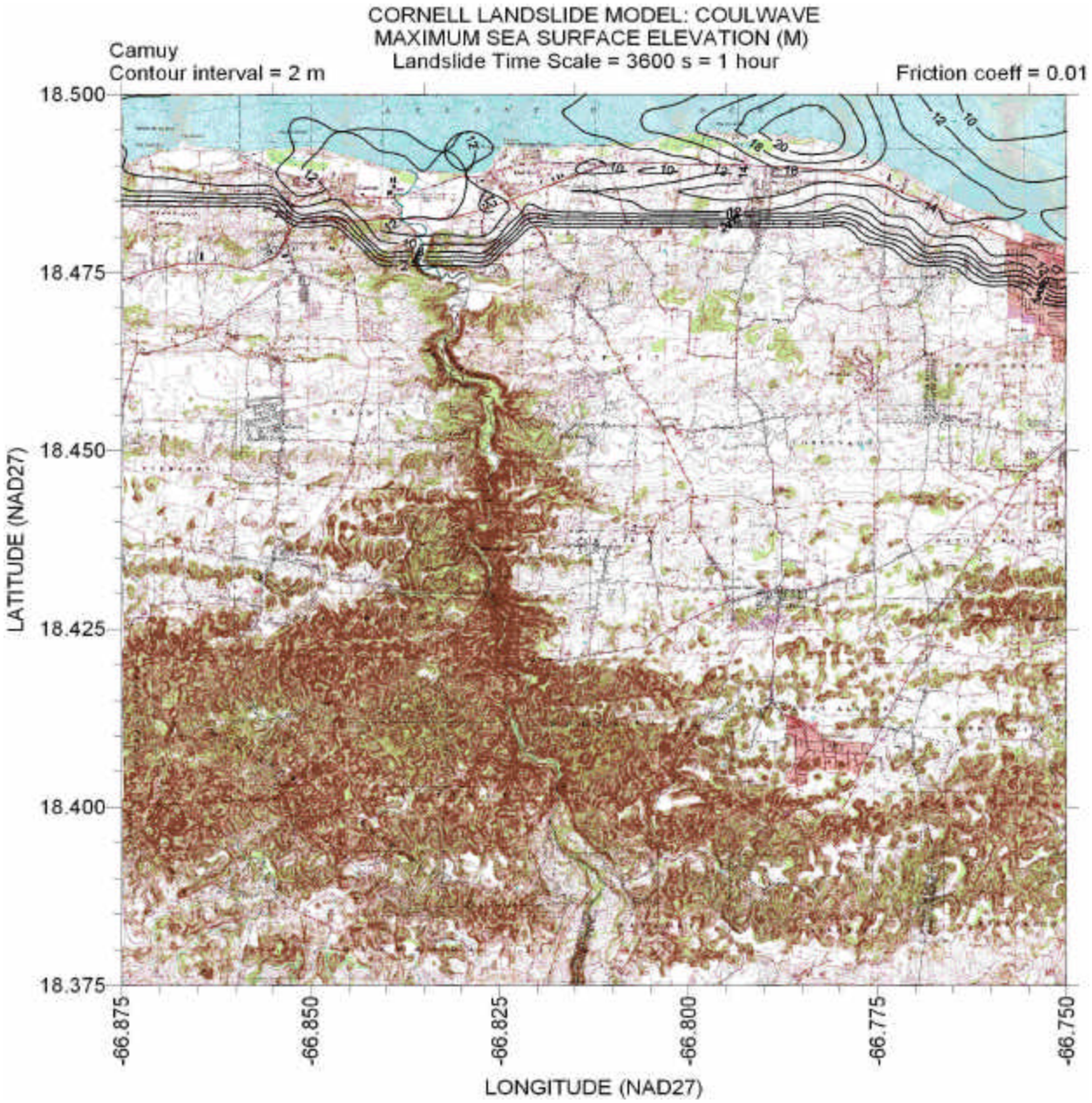


Figure 37 – Contours of maximum sea surface elevation for time scale = 3600 s for Camuy quadrangle. Friction factor f = 0.01.

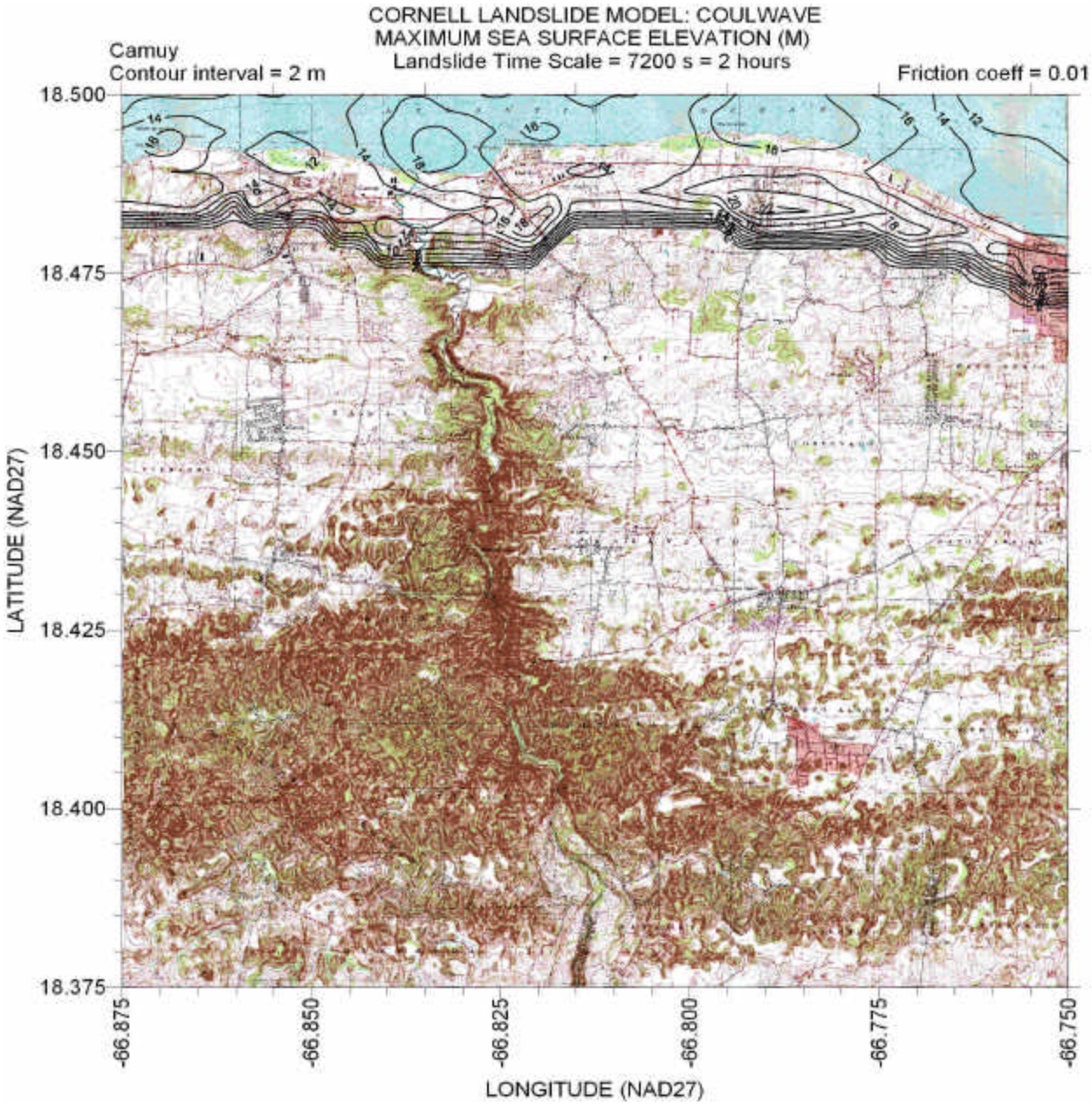


Figure 38 – Contours of maximum sea surface elevation for time scale = 7200 s for Camuy quadrangle. Friction factor f = 0.01.

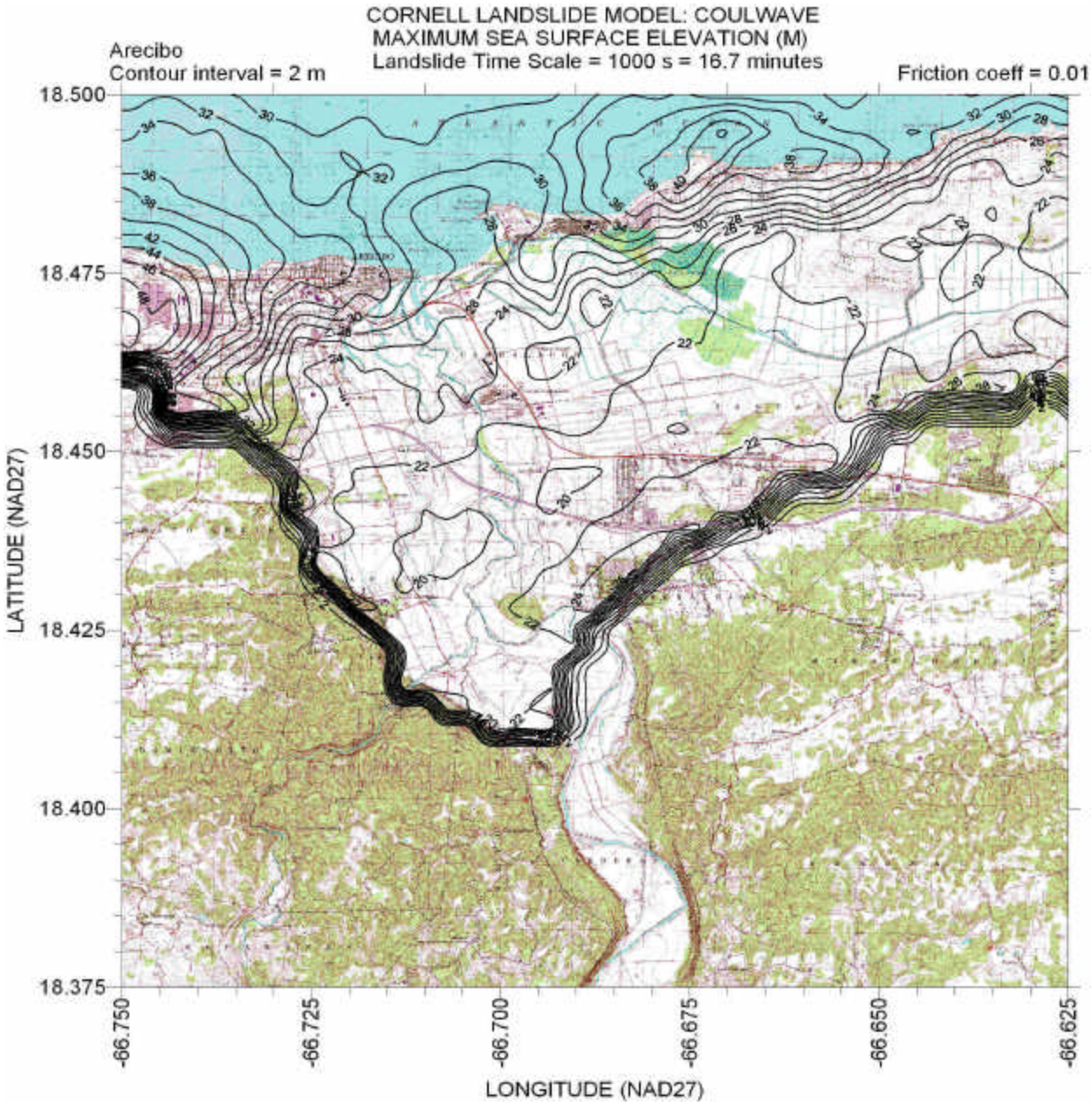


Figure 39 – Contours of maximum sea surface elevation for time scale = 1000 s for Arecibo quadrangle. Friction factor f = 0.01.

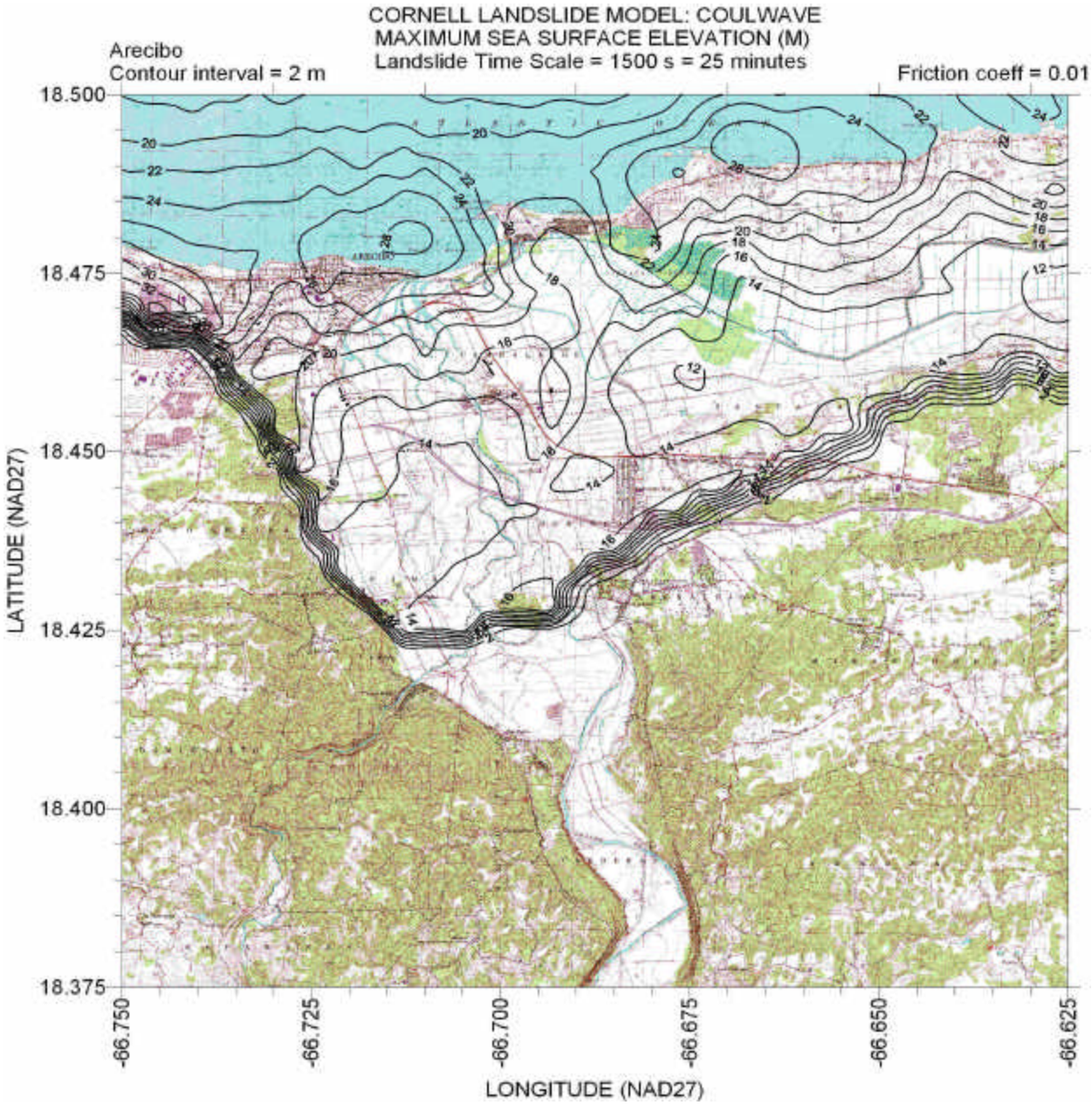


Figure 40 – Contours of maximum sea surface elevation for time scale = 1500 s for Arecibo quadrangle. Friction factor f = 0.01.

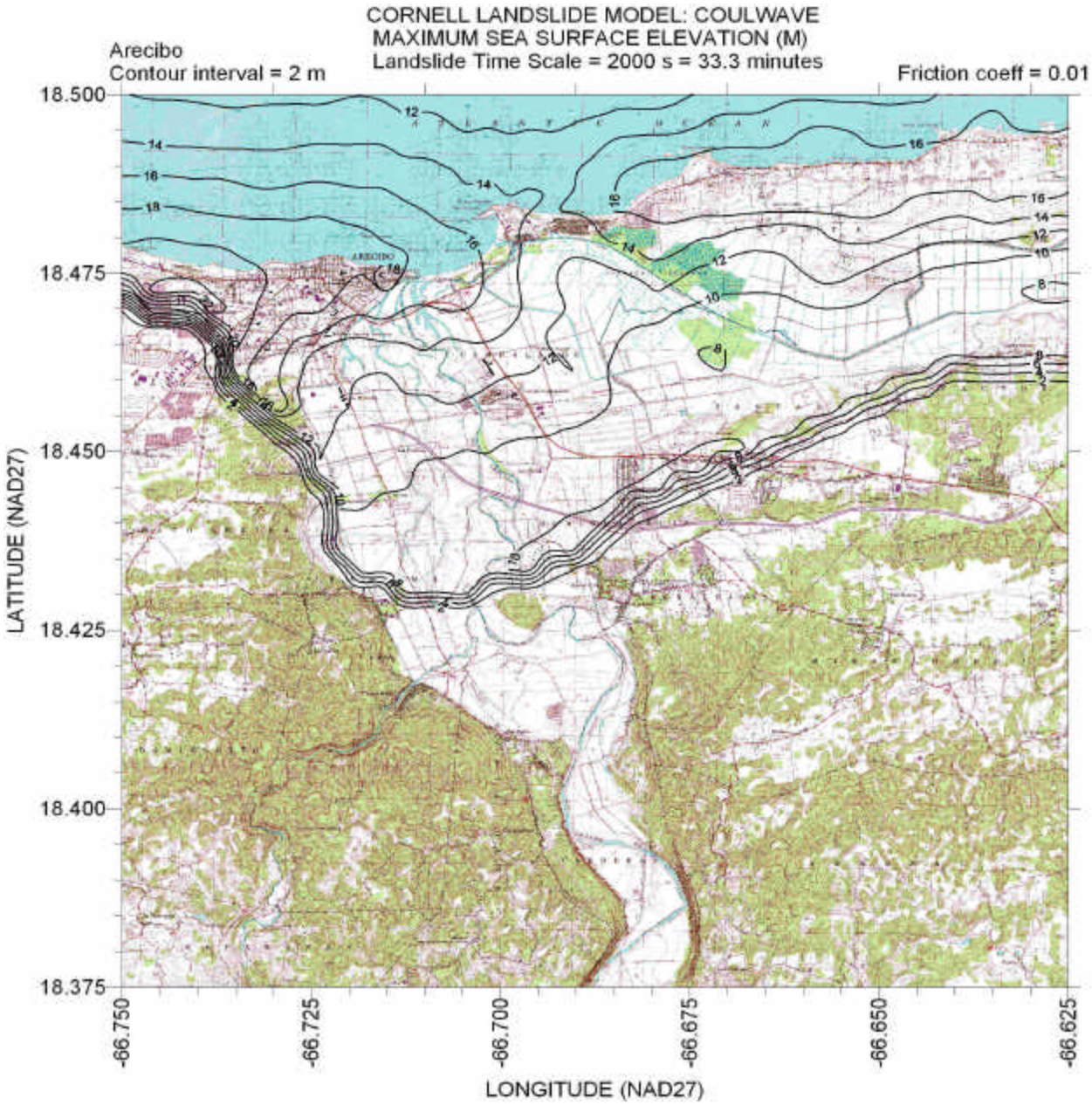


Figure 41 – Contours of maximum sea surface elevation for time scale = 2000 s for Arecibo quadrangle. Friction factor f = 0.01.

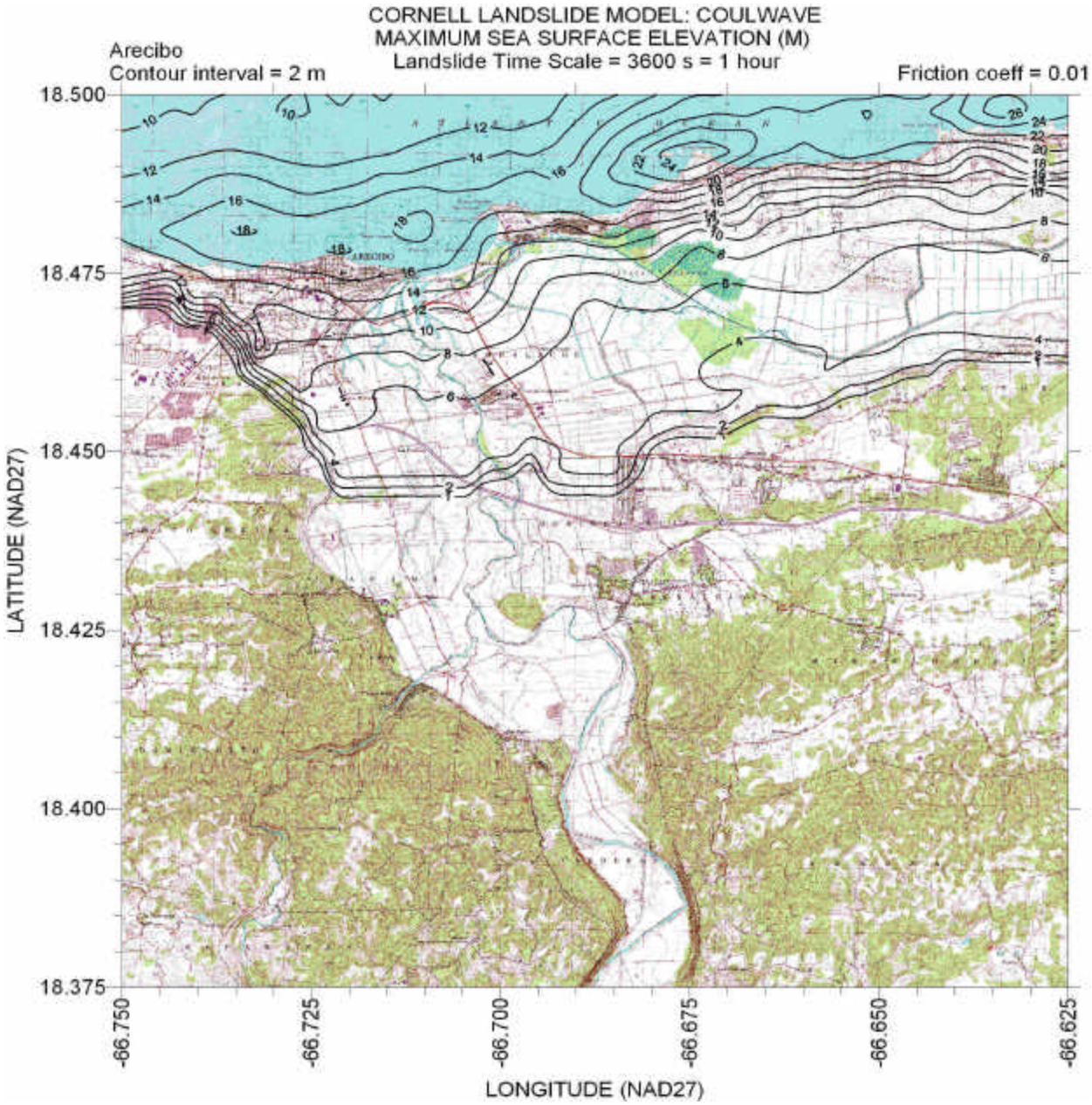


Figure 42 – Contours of maximum sea surface elevation for time scale = 3600 s for Arecibo quadrangle. Friction factor f = 0.01.

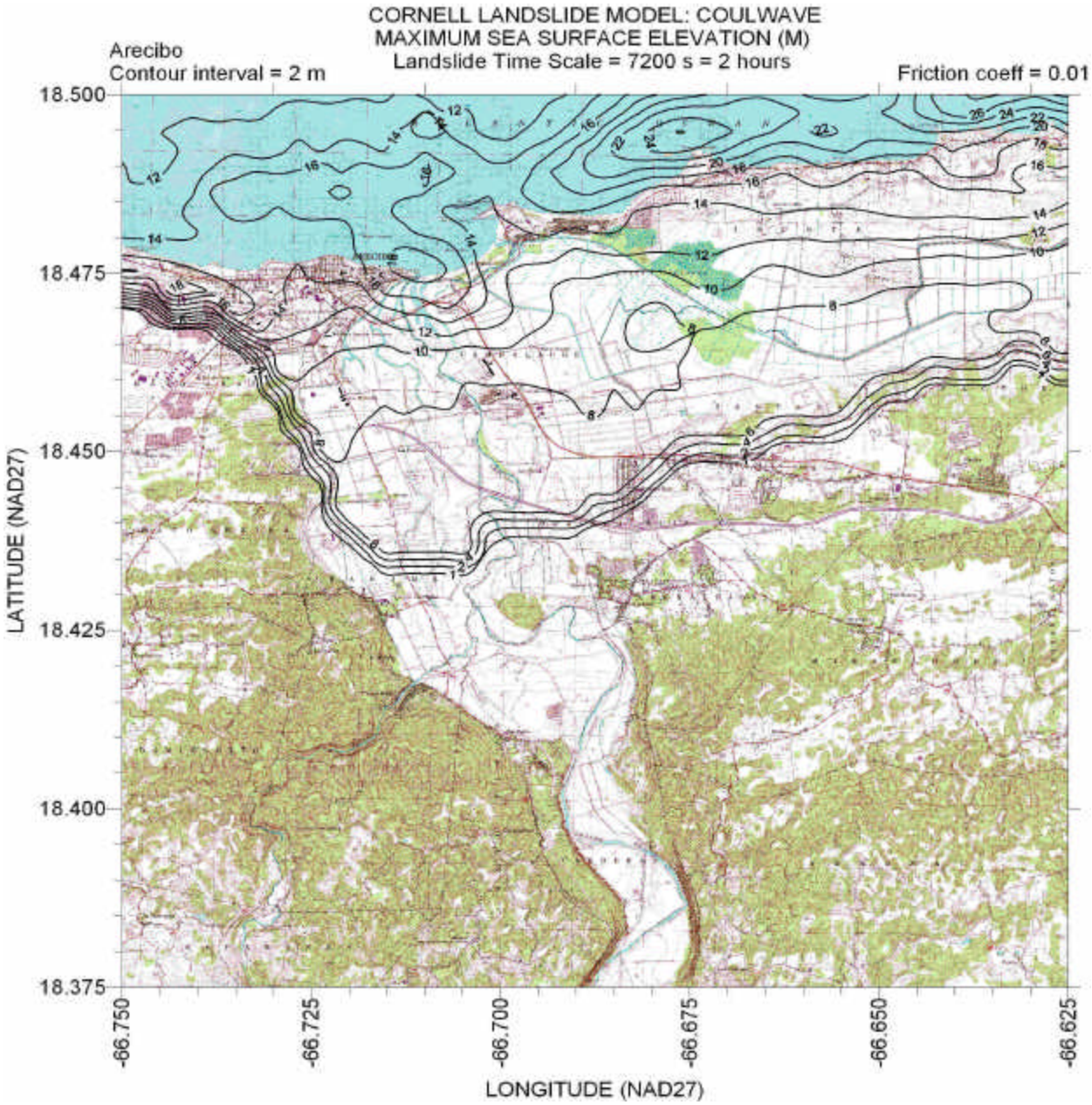


Figure 43– Contours of maximum sea surface elevation for time scale = 7200 s for Arecibo quadrangle. Friction factor f = 0.01.

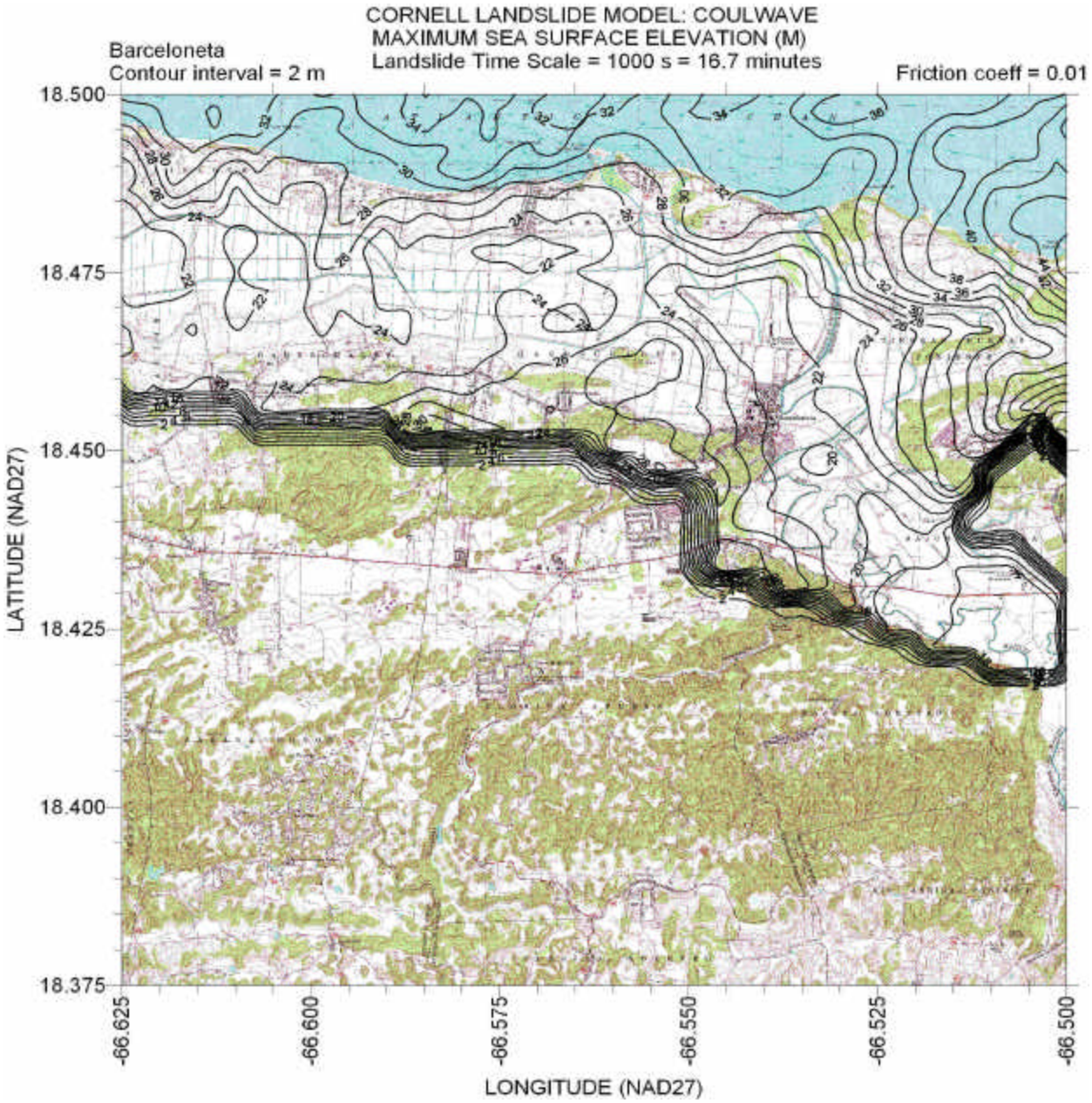


Figure 44– Contours of maximum sea surface elevation for time scale = 1000 s for Barceloneta quadrangle. Friction factor f = 0.01.

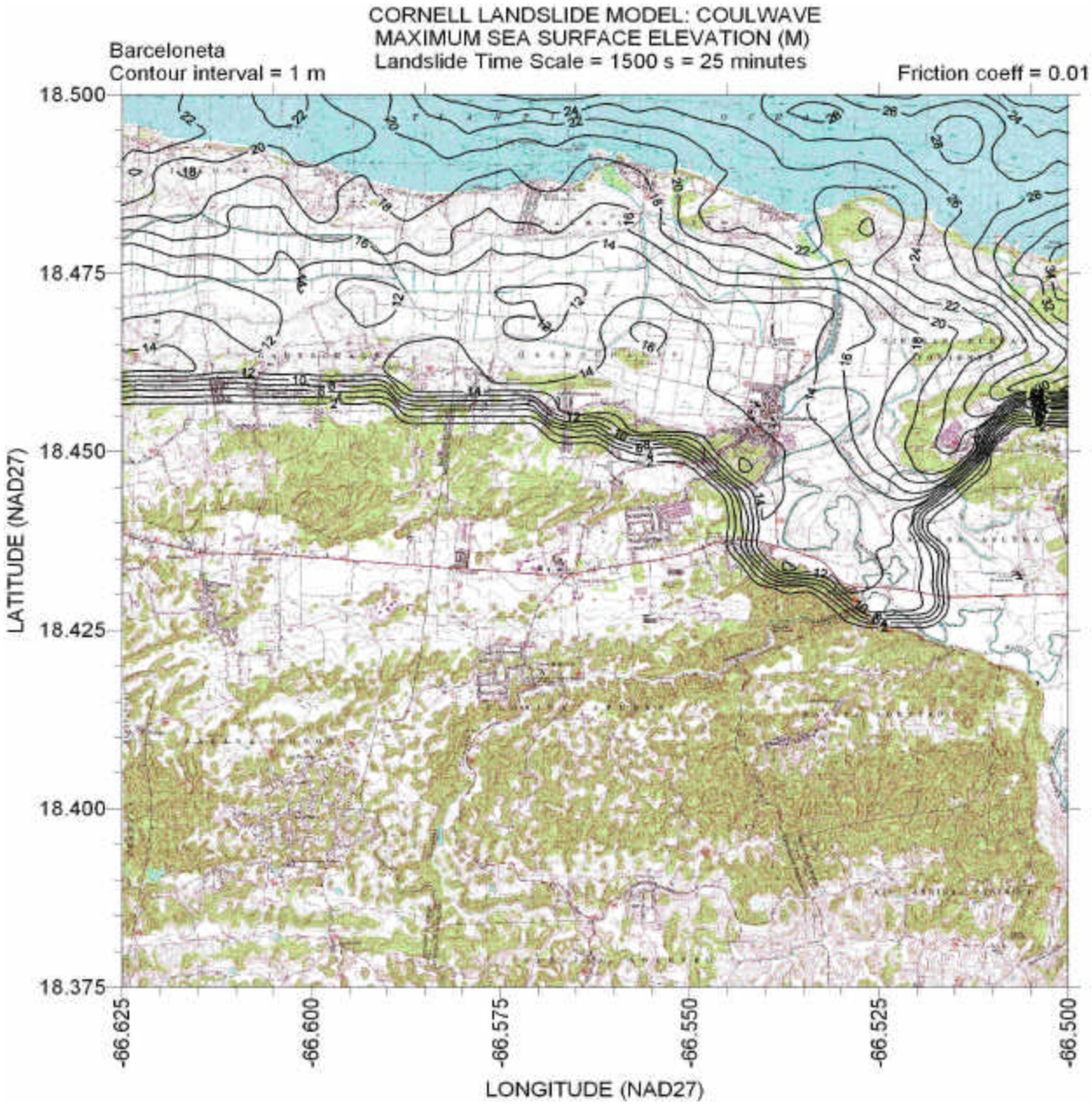


Figure 45– Contours of maximum sea surface elevation for time scale = 1500 s for Barceloneta quadrangle. Friction factor f = 0.01.

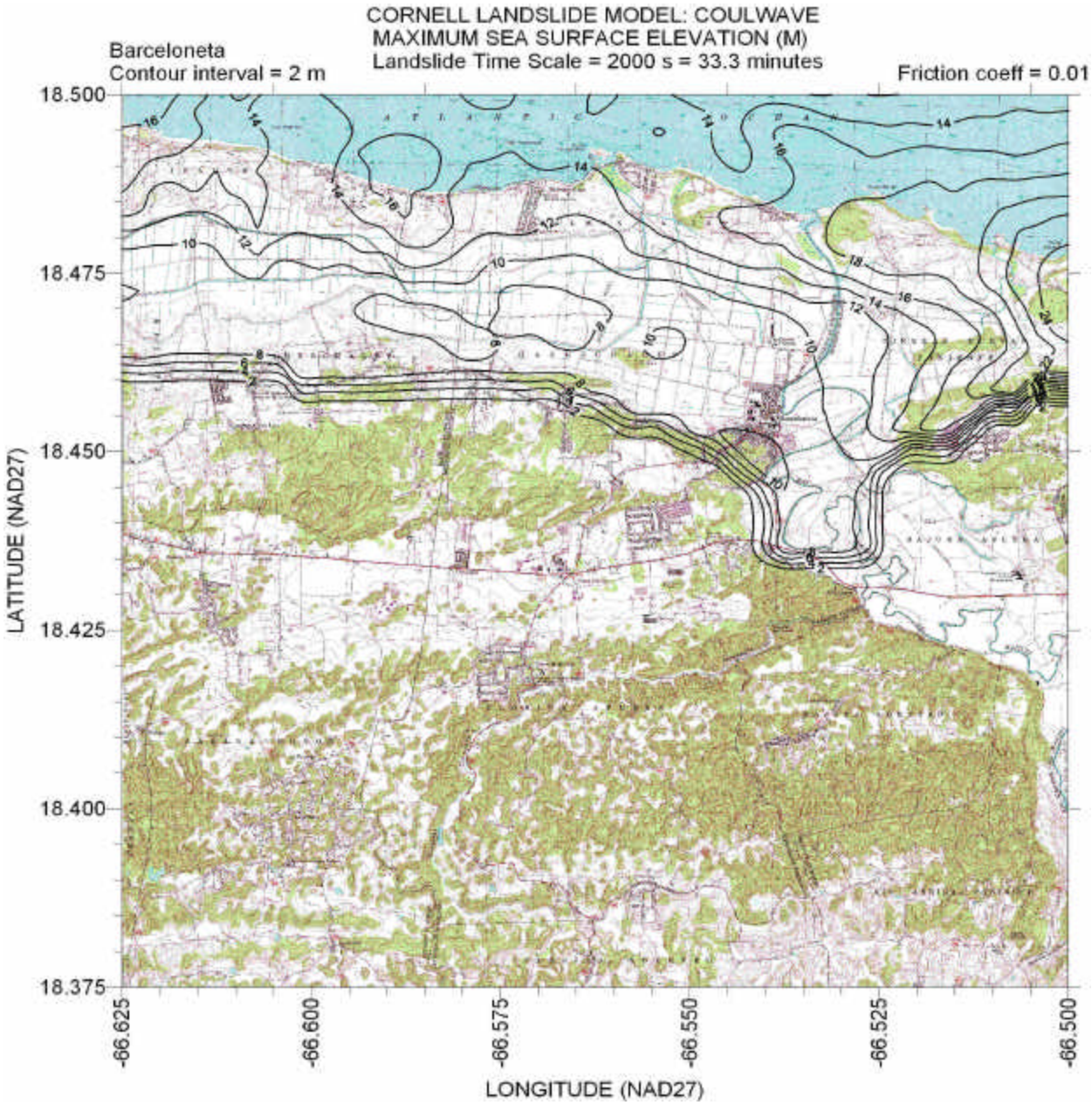


Figure 46– Contours of maximum sea surface elevation for time scale = 2000 s for Barceloneta quadrangle. Friction factor f = 0.01.

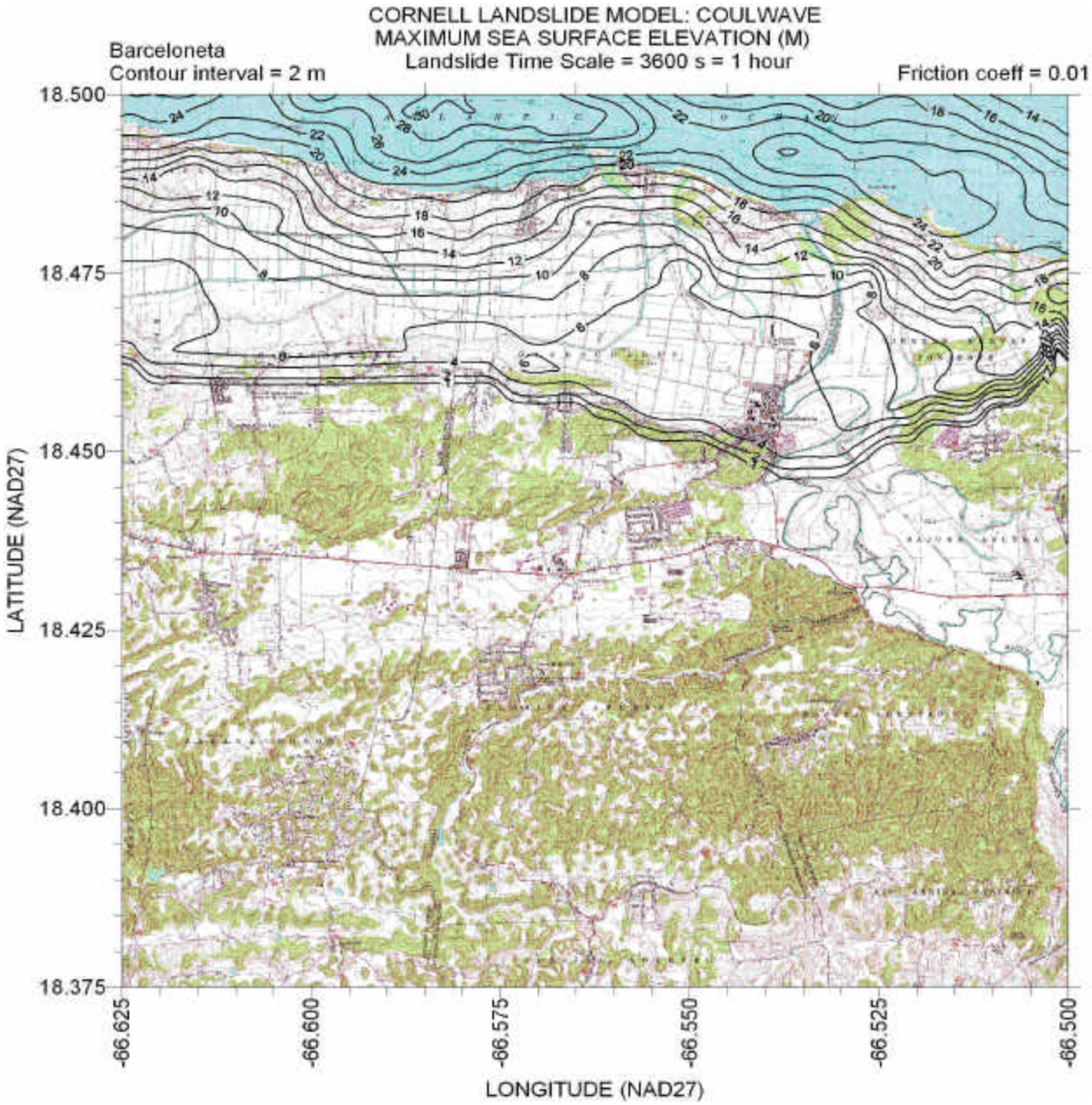


Figure 47– Contours of maximum sea surface elevation for time scale = 3600 s for Barceloneta quadrangle. Friction factor f = 0.01.

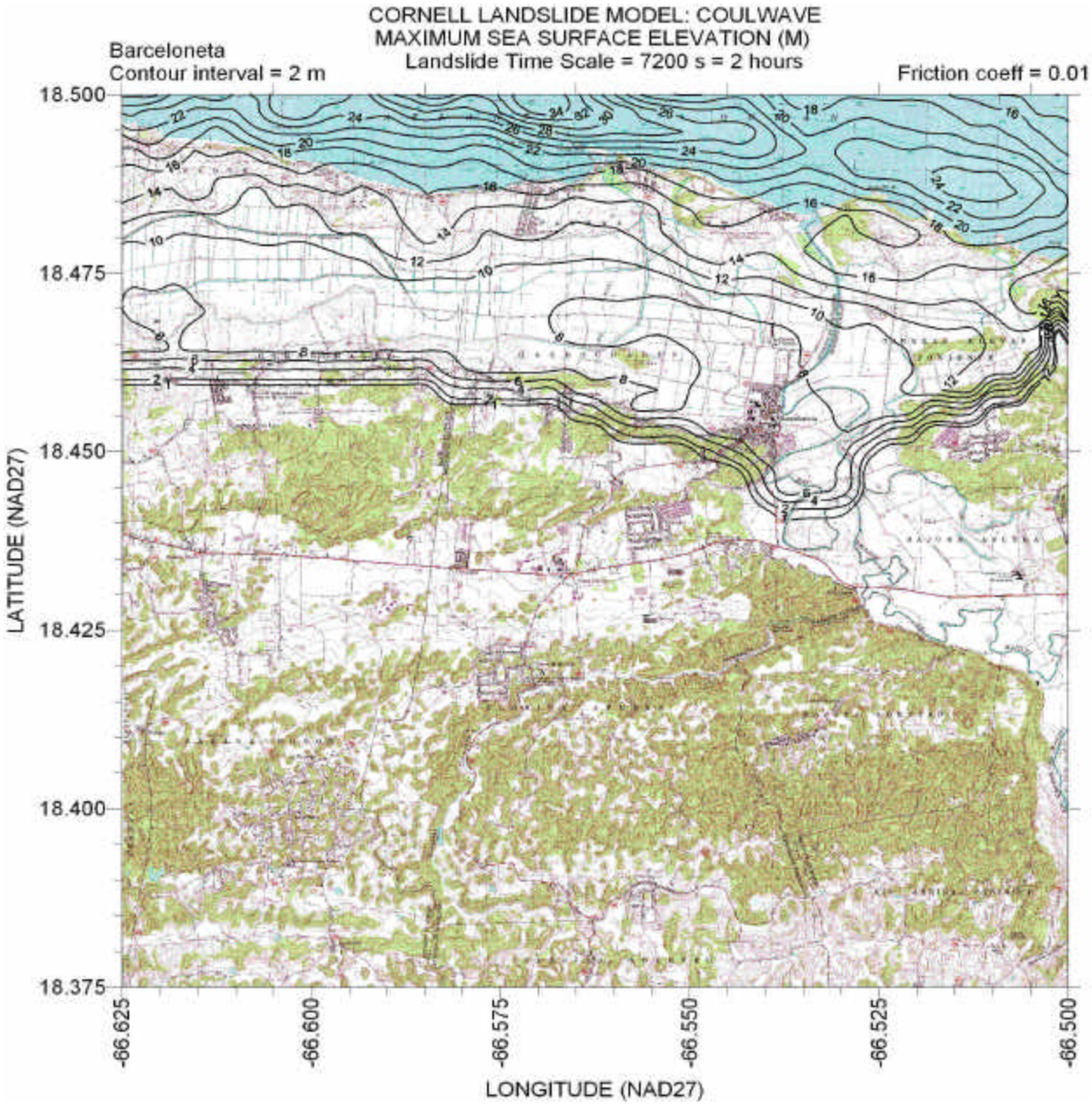


Figure 48– Contours of maximum sea surface elevation for time scale = 7200 s for Barceloneta quadrangle. Friction factor f = 0.01.

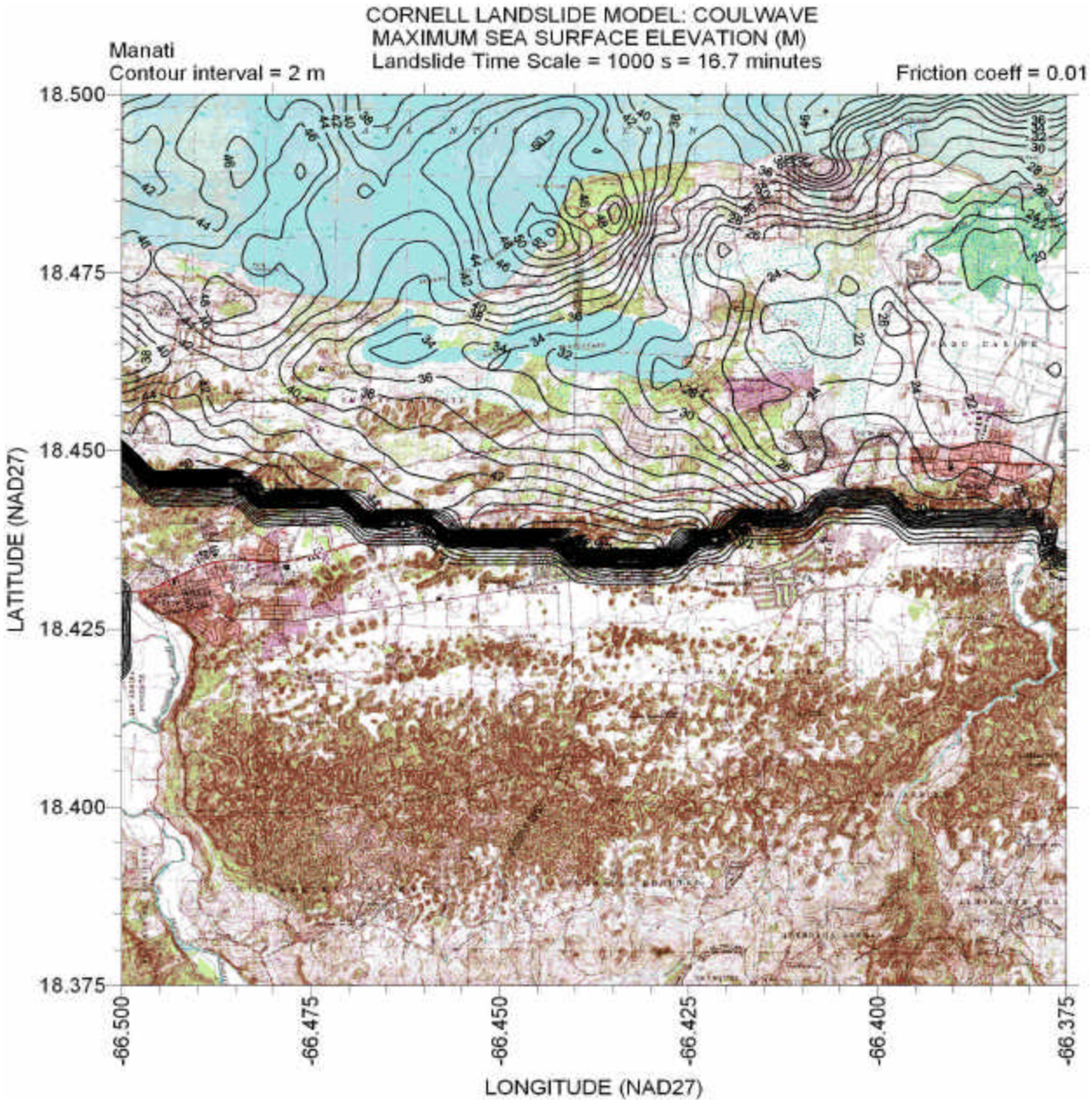


Figure 49– Contours of maximum sea surface elevation for time scale = 1000 s for Manati quadrangle. Friction factor f = 0.01.

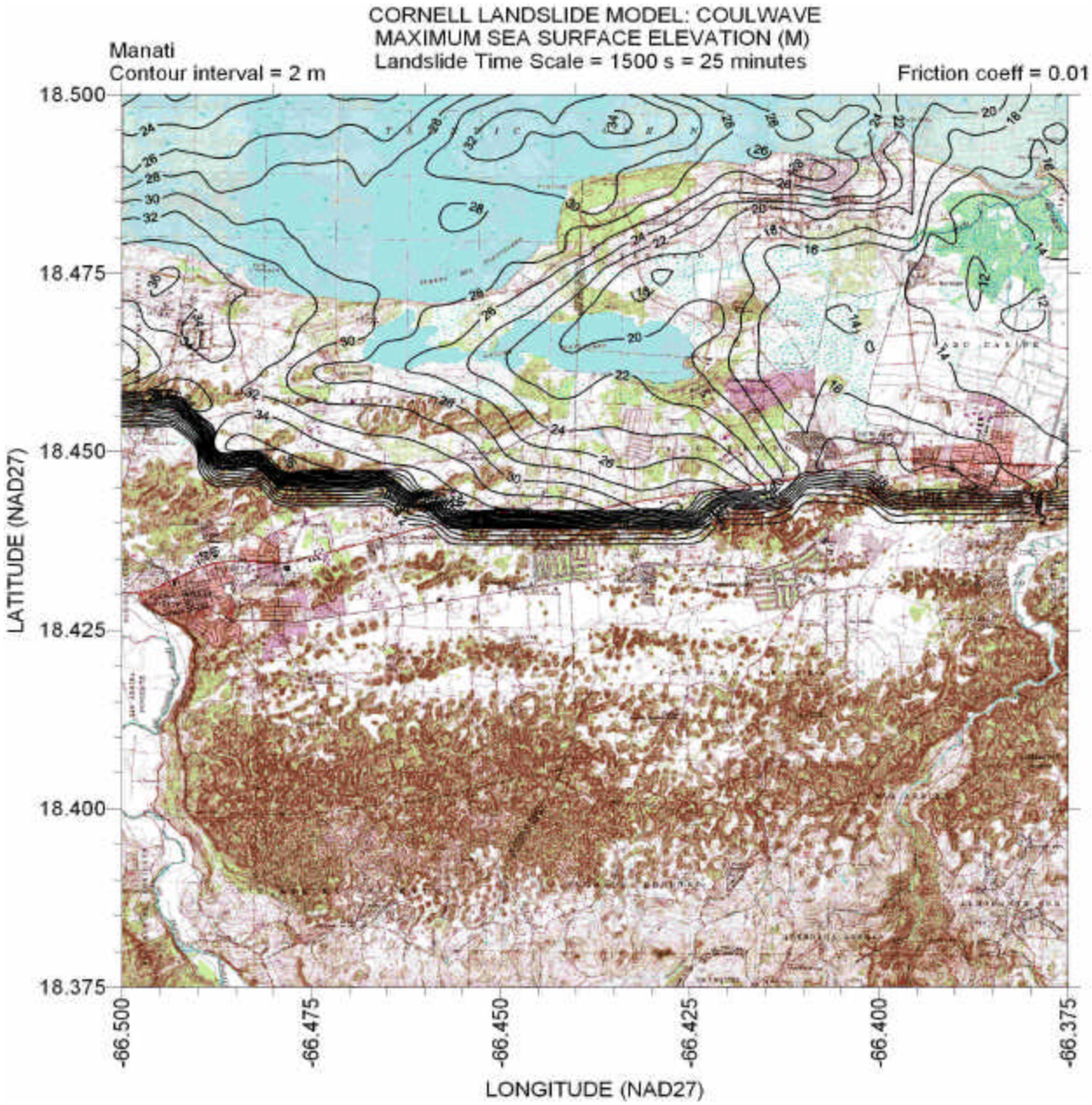


Figure 50– Contours of maximum sea surface elevation for time scale = 1500 s for Manati quadrangle. Friction factor f = 0.01.

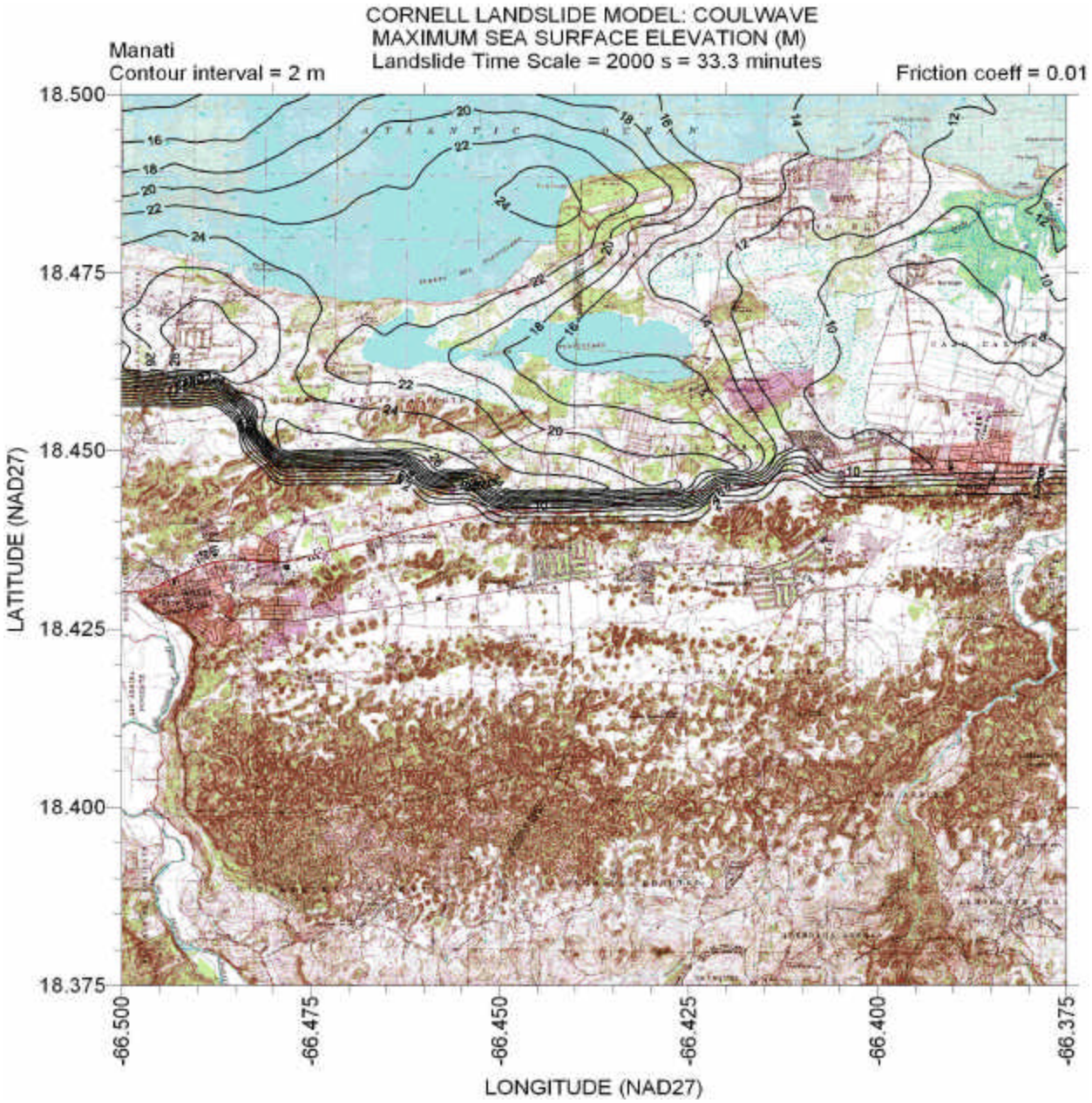


Figure 51– Contours of maximum sea surface elevation for time scale = 2000 s for Manati quadrangle. Friction factor f = 0.01.

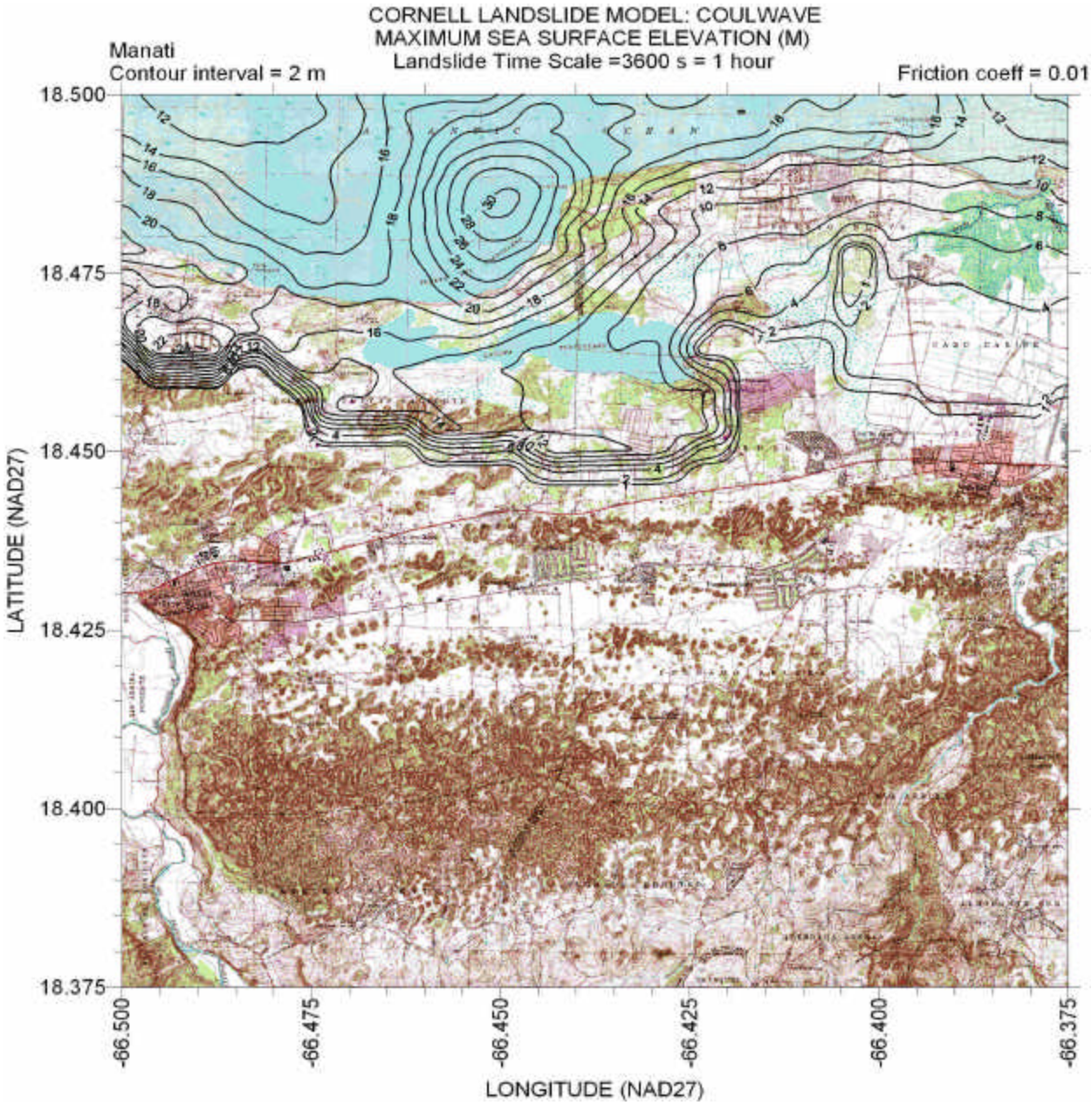


Figure 52– Contours of maximum sea surface elevation for time scale = 3600 s for Manati quadrangle. Friction factor f = 0.01.

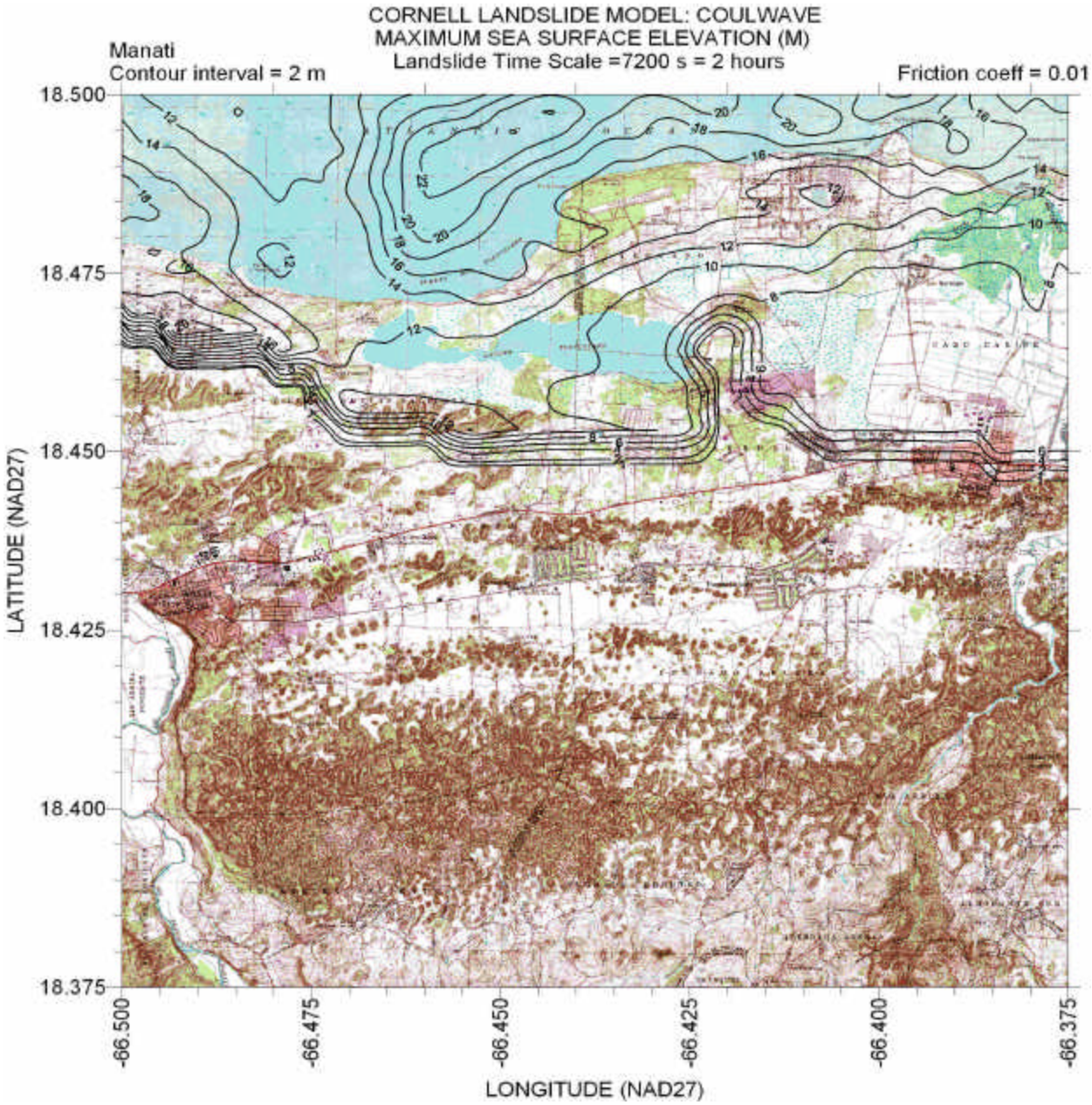


Figure 53– Contours of maximum sea surface elevation for time scale = 7200 s for Manati quadrangle. Friction factor f = 0.01.

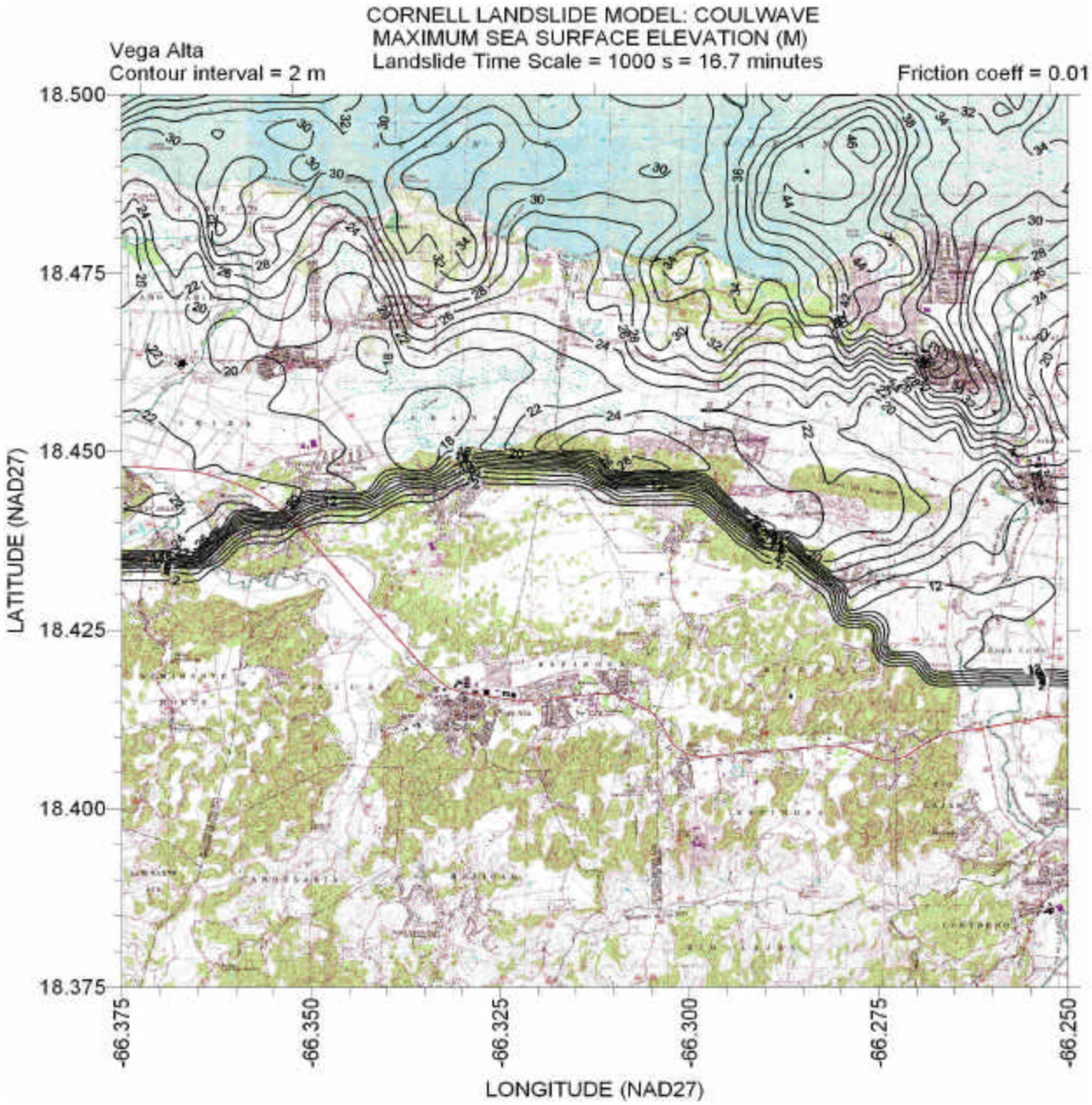


Figure 54– Contours of maximum sea surface elevation for time scale = 1000 s for Vega Alta quadrangle. Friction factor f = 0.01.

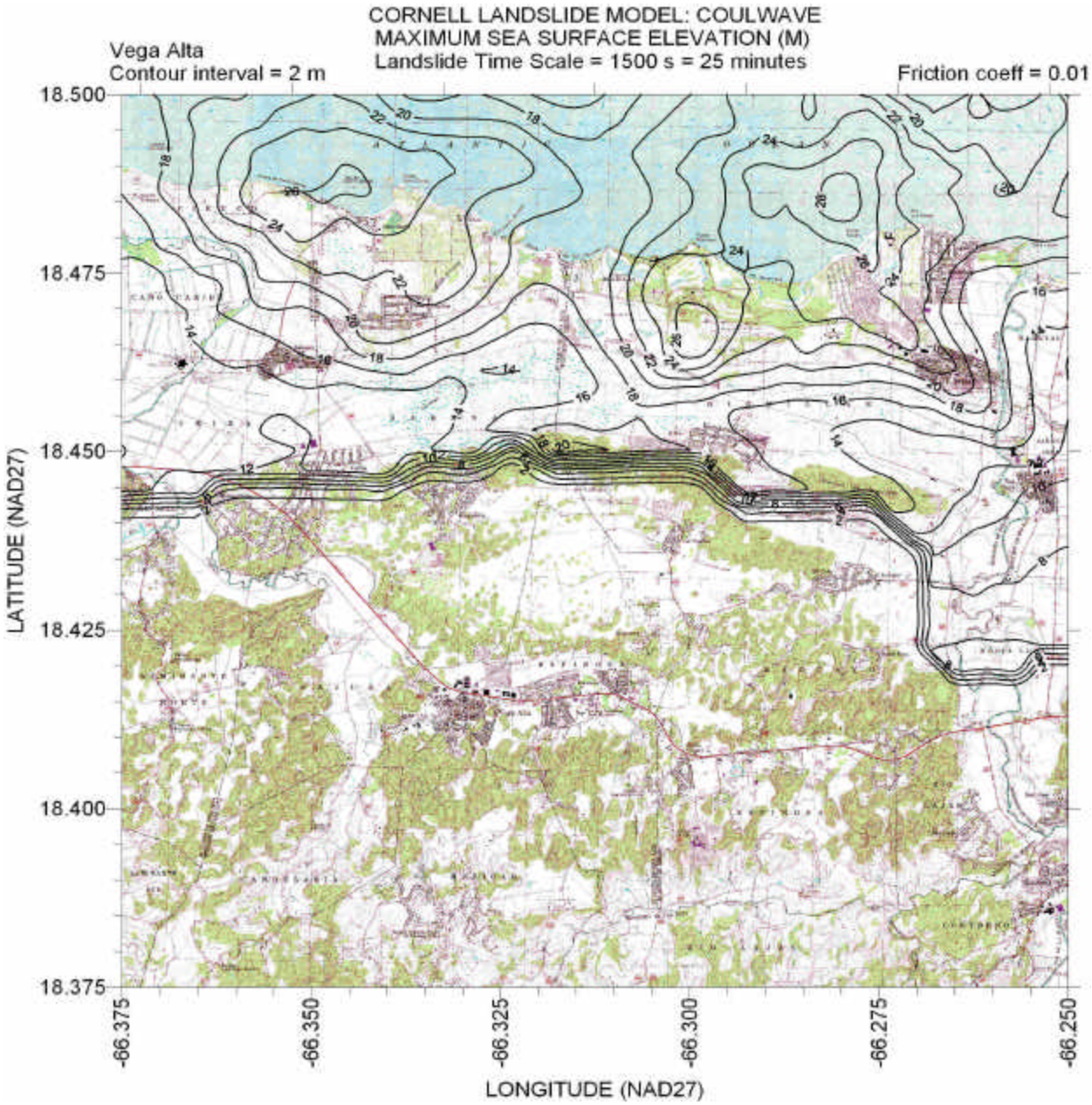


Figure 55– Contours of maximum sea surface elevation for time scale = 1500 s for Vega Alta quadrangle. Friction factor f = 0.01.

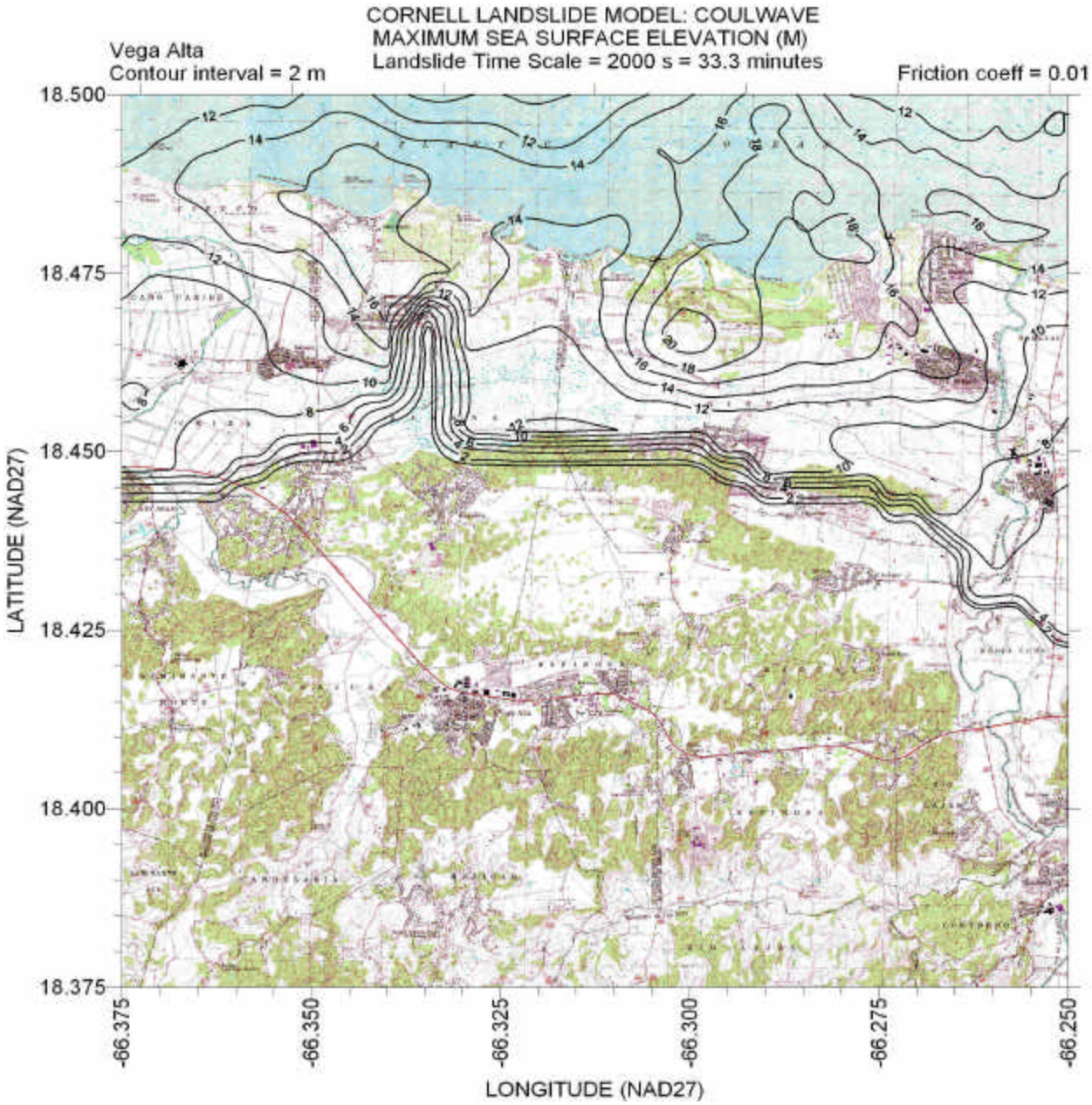


Figure 56– Contours of maximum sea surface elevation for time scale = 2000 s for Vega Alta quadrangle. Friction factor f = 0.01.

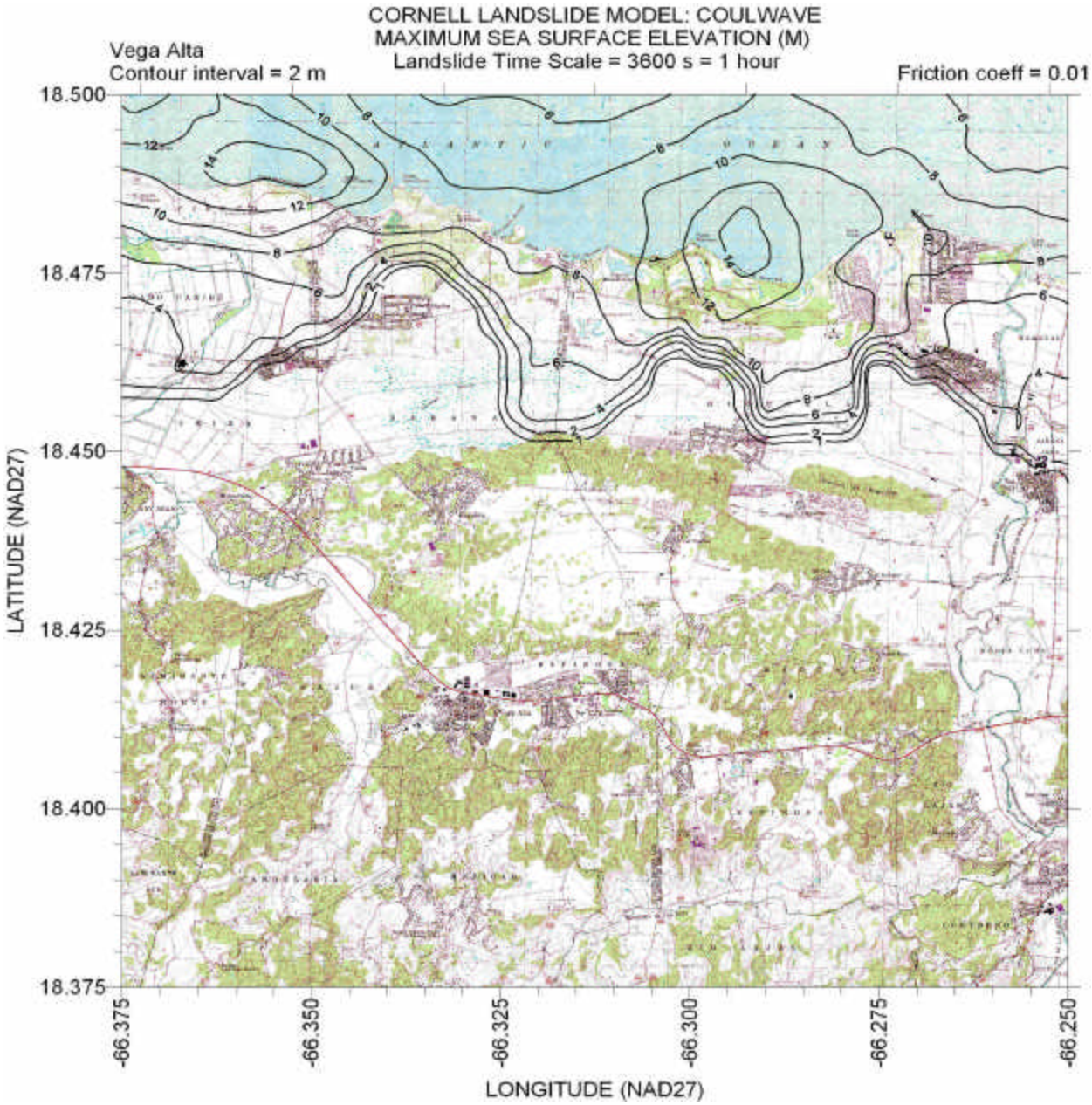


Figure 57– Contours of maximum sea surface elevation for time scale = 3600 s for Vega Alta quadrangle. Friction factor f = 0.01.

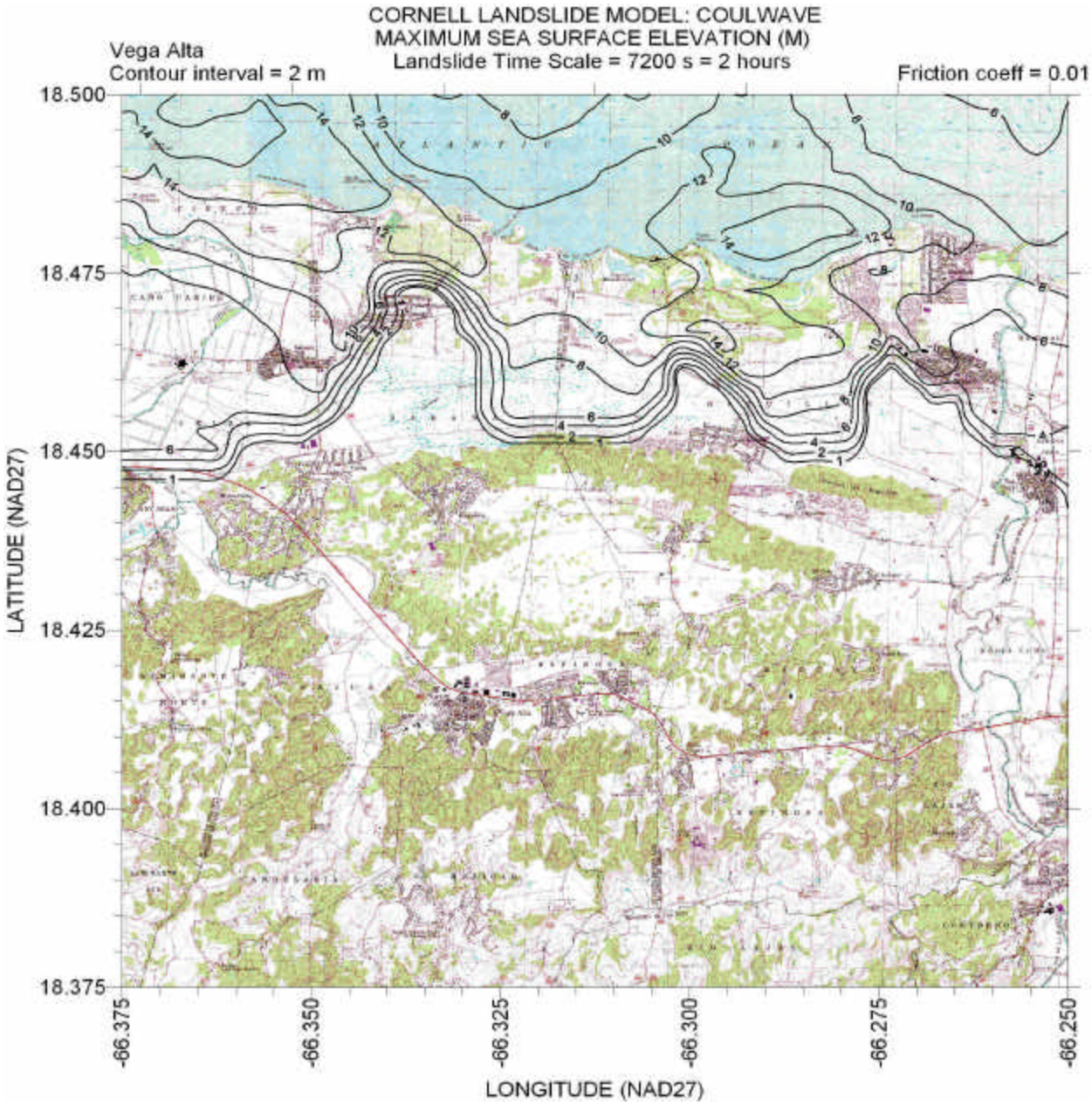


Figure 58– Contours of maximum sea surface elevation for time scale = 7200 s for Vega Alta quadrangle. Friction factor f = 0.01.

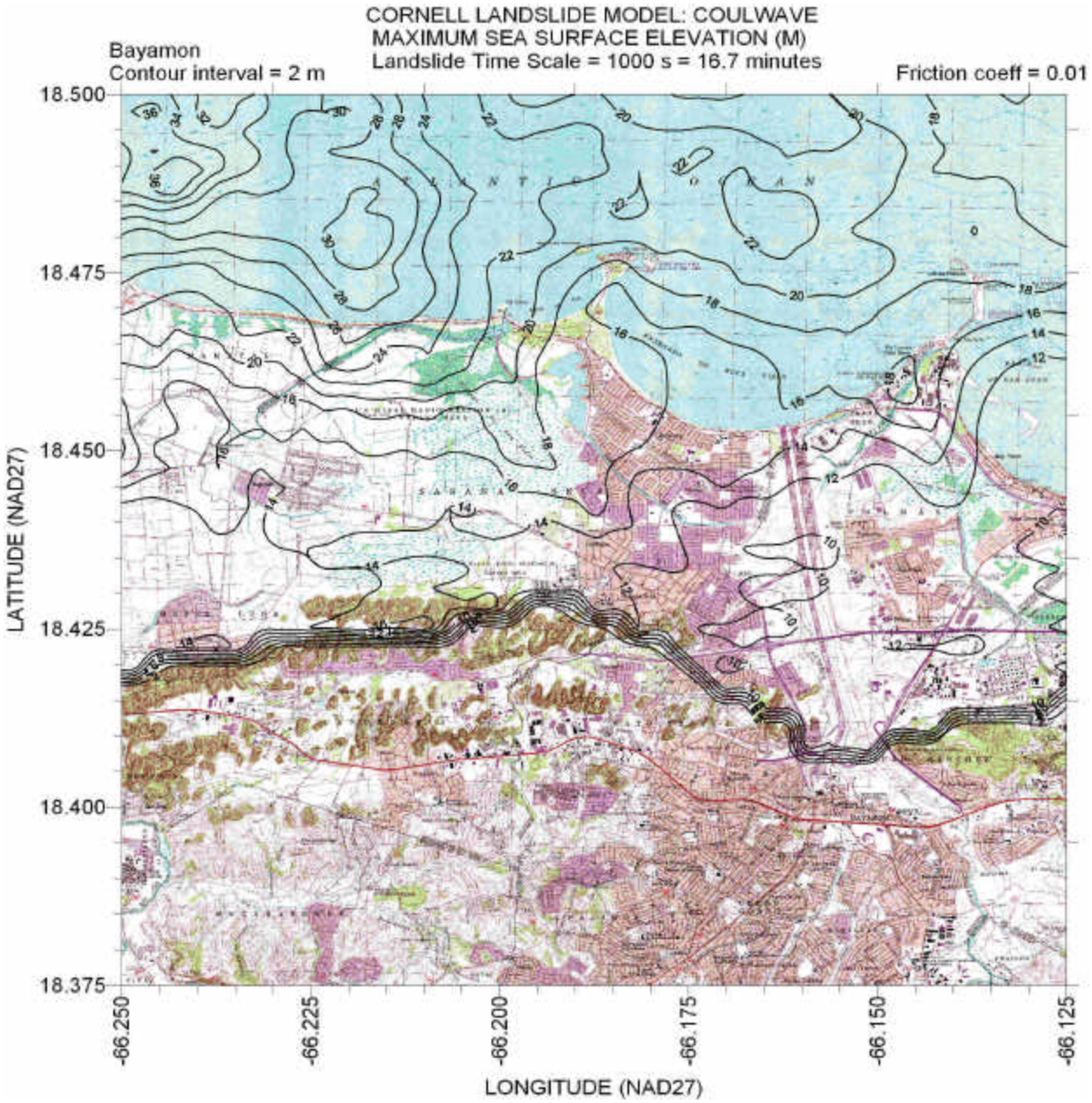


Figure 59– Contours of maximum sea surface elevation for time scale = 1000 s for Bayamon quadrangle. Friction factor f = 0.01.

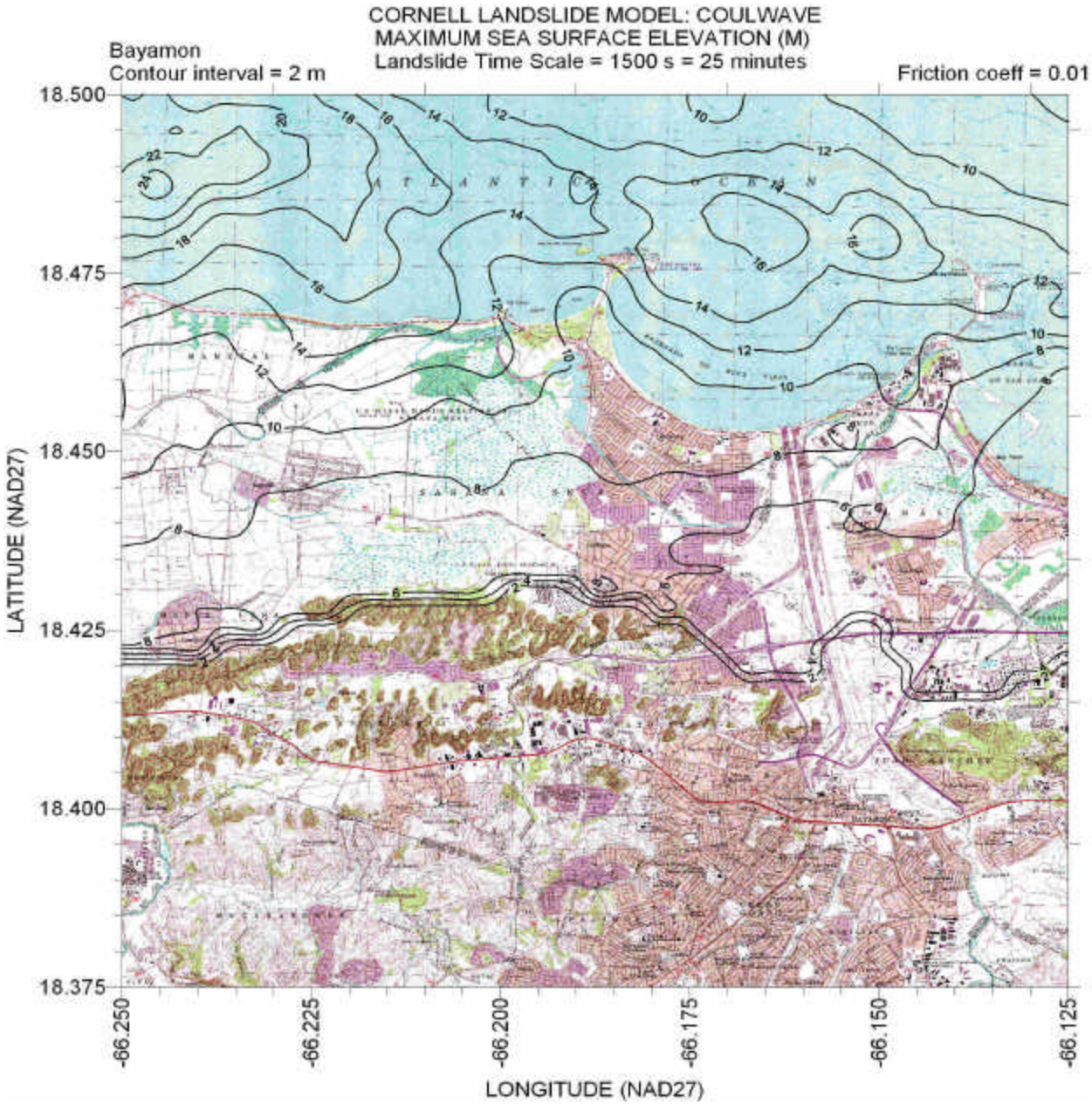


Figure 60– Contours of maximum sea surface elevation for time scale = 1500 s for Bayamon quadrangle. Friction factor f = 0.01.

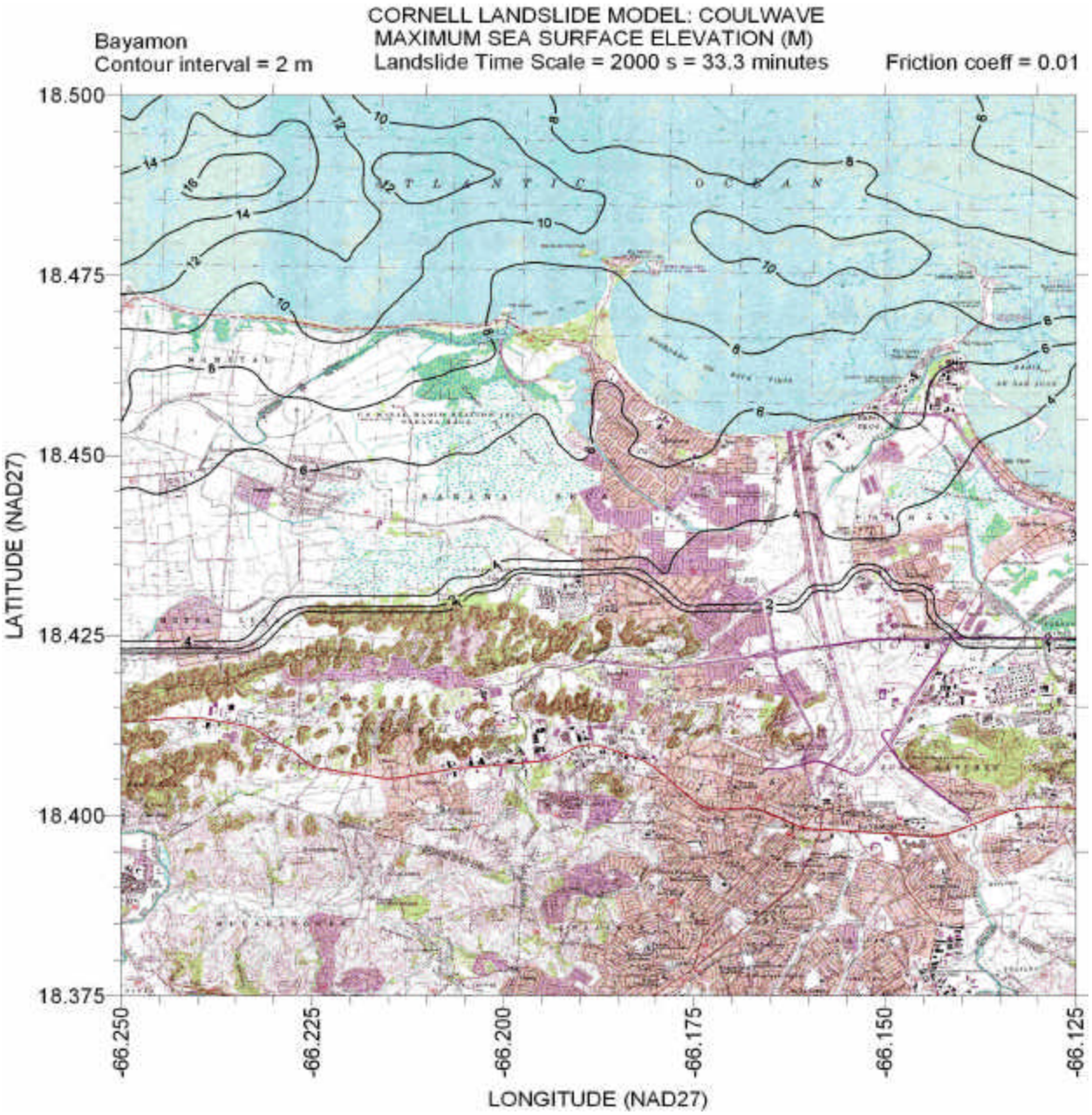


Figure 61– Contours of maximum sea surface elevation for time scale = 2000 s for Bayamon quadrangle. Friction factor f = 0.01.

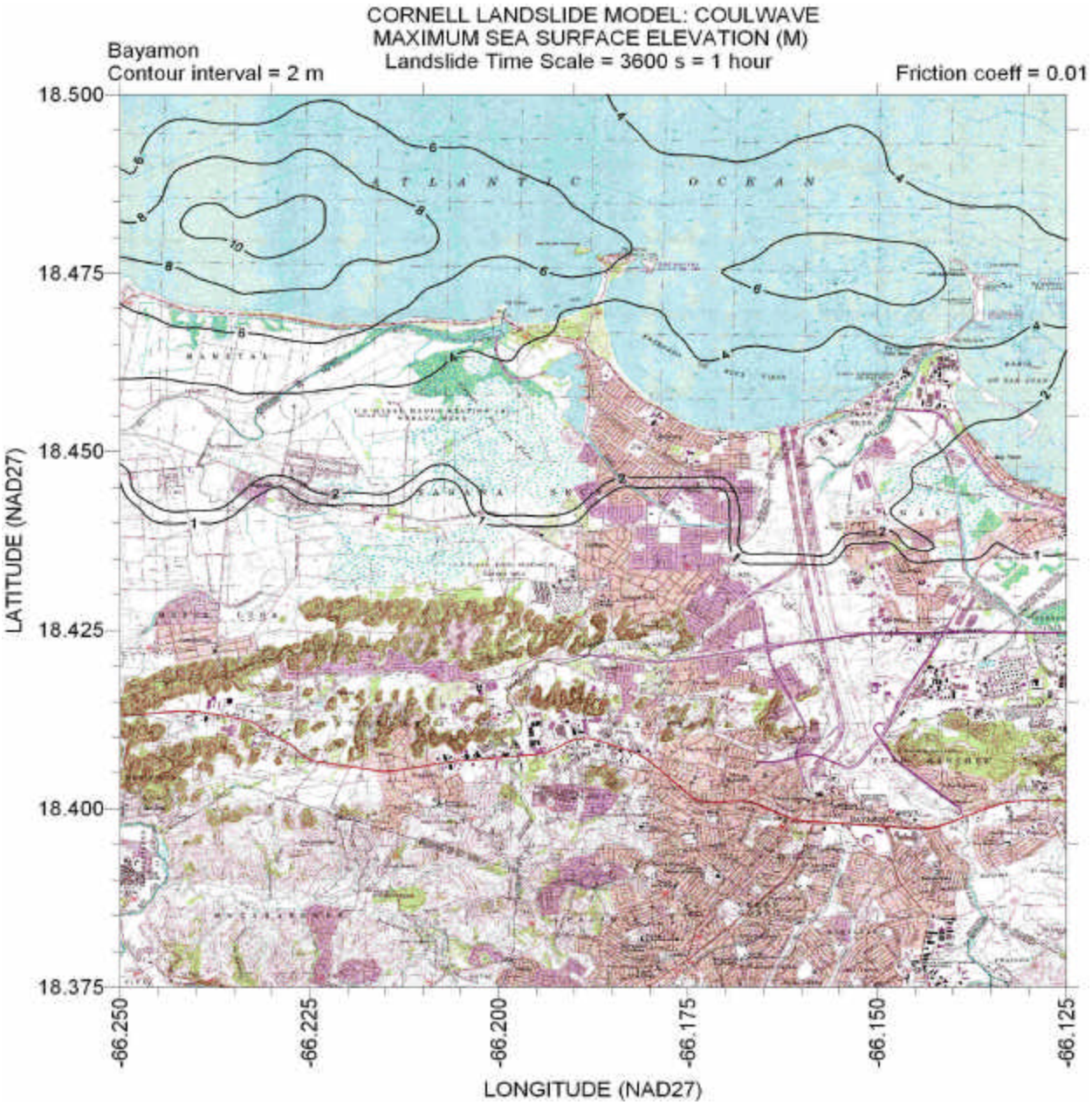


Figure 62– Contours of maximum sea surface elevation for time scale = 3600 s for Bayamon quadrangle. Friction factor f = 0.01.

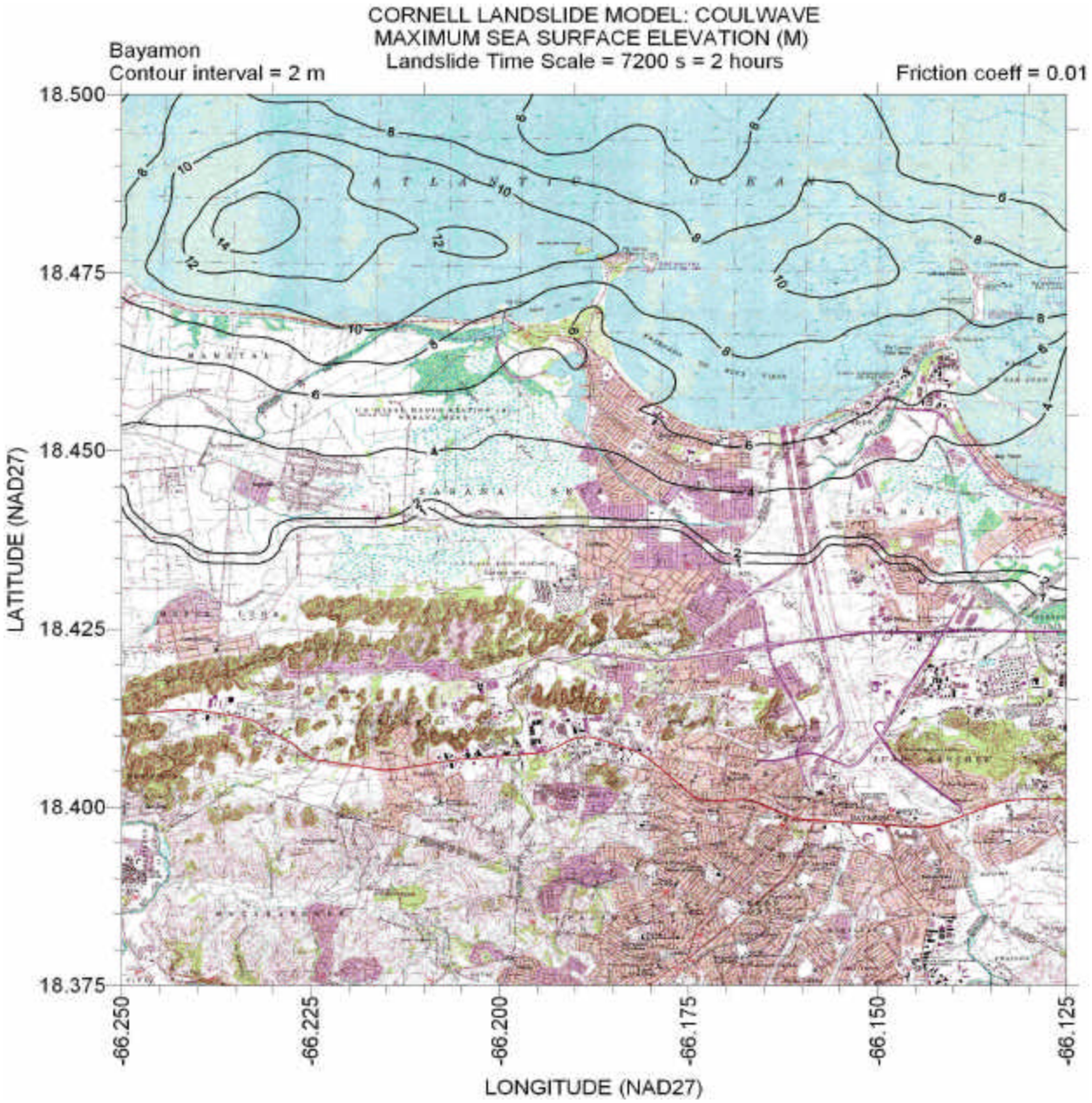


Figure 63– Contours of maximum sea surface elevation for time scale = 7200 s for Bayamon quadrangle. Friction factor f = 0.01.

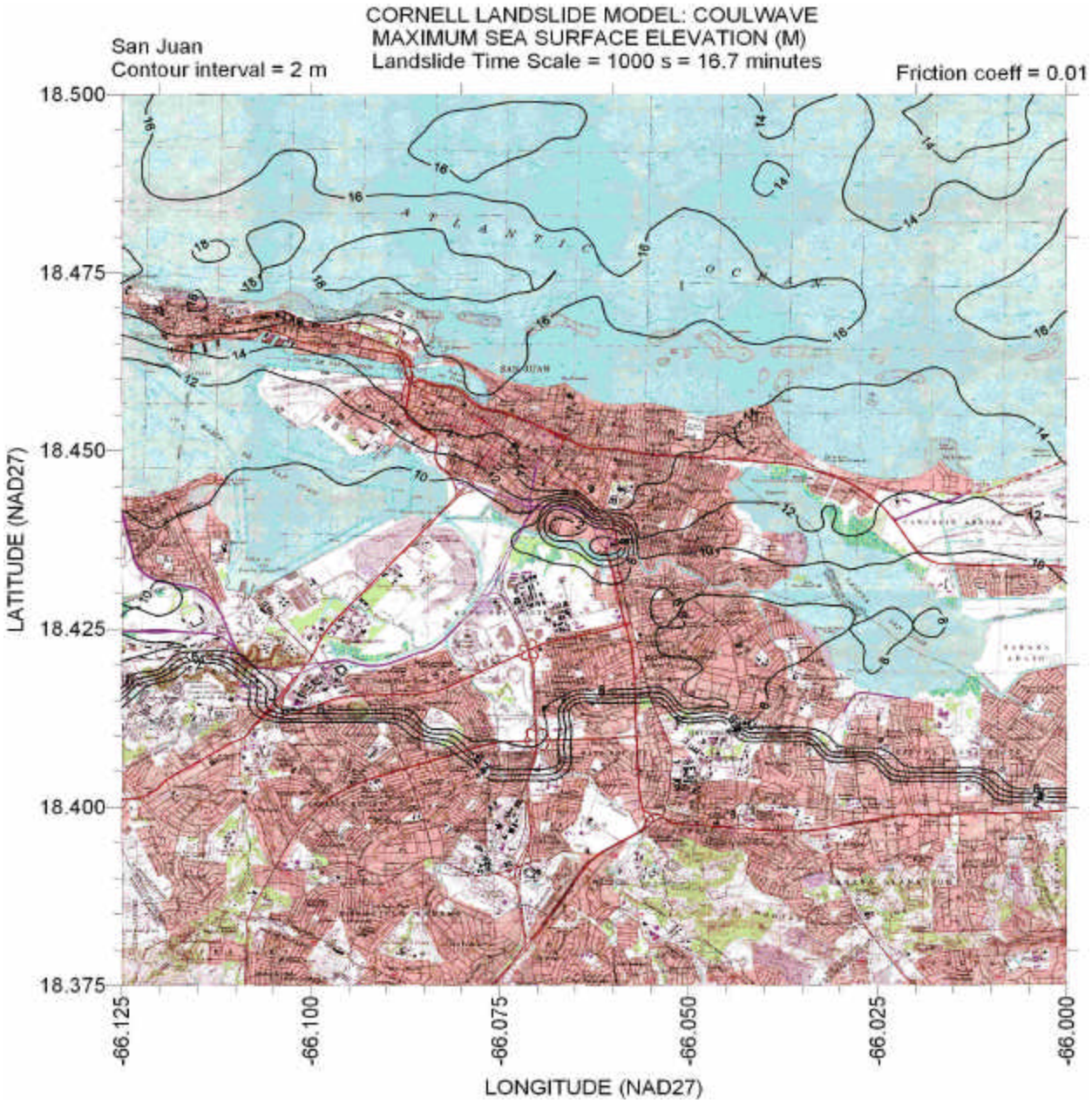


Figure 64– Contours of maximum sea surface elevation for time scale = 1000 s for San Juan quadrangle. Friction factor f = 0.01.

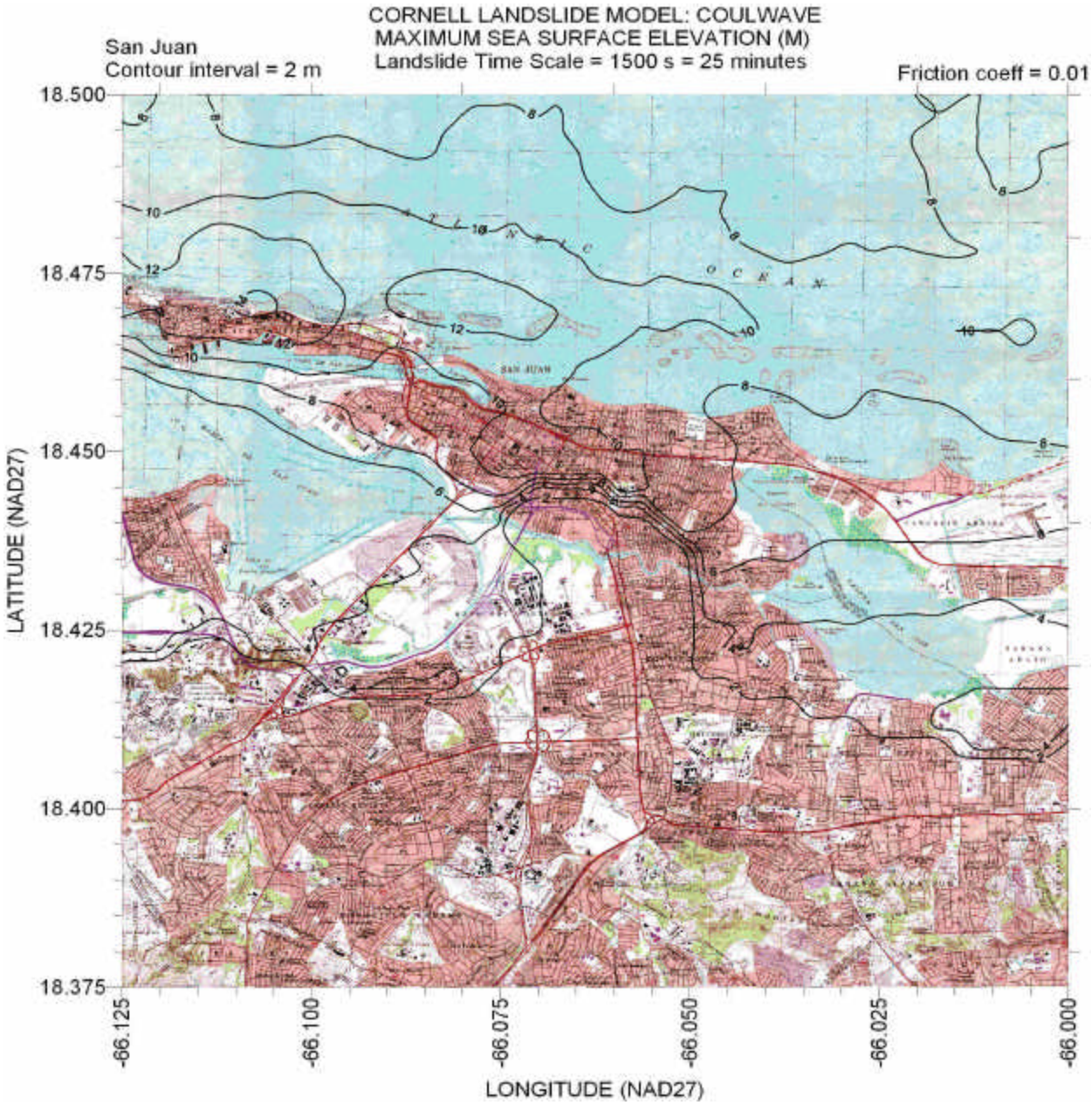


Figure 65– Contours of maximum sea surface elevation for time scale = 1500 s for San Juan quadrangle. Friction factor f = 0.01.

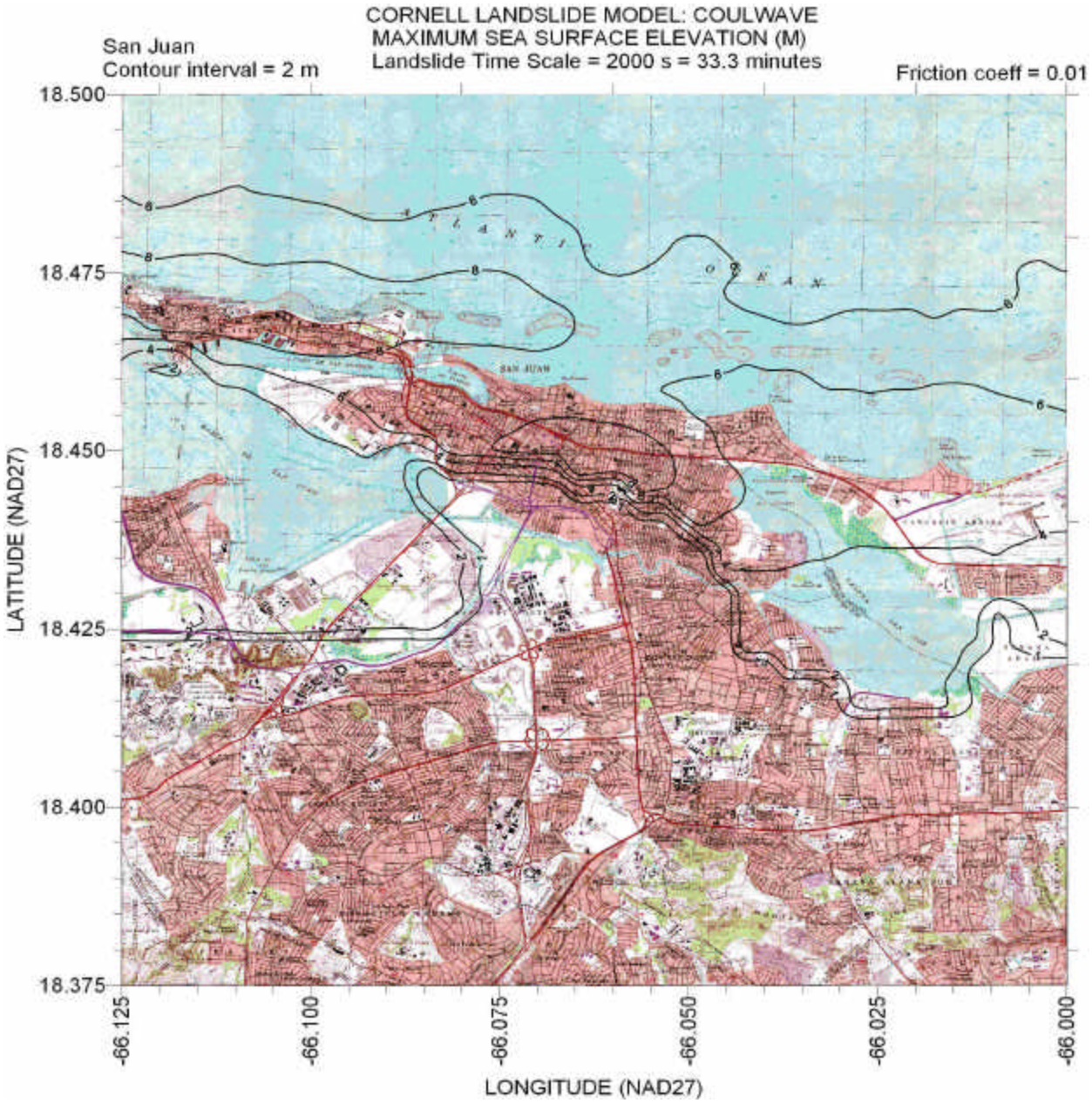


Figure 66– Contours of maximum sea surface elevation for time scale = 2000 s for San Juan quadrangle. Friction factor f = 0.01.

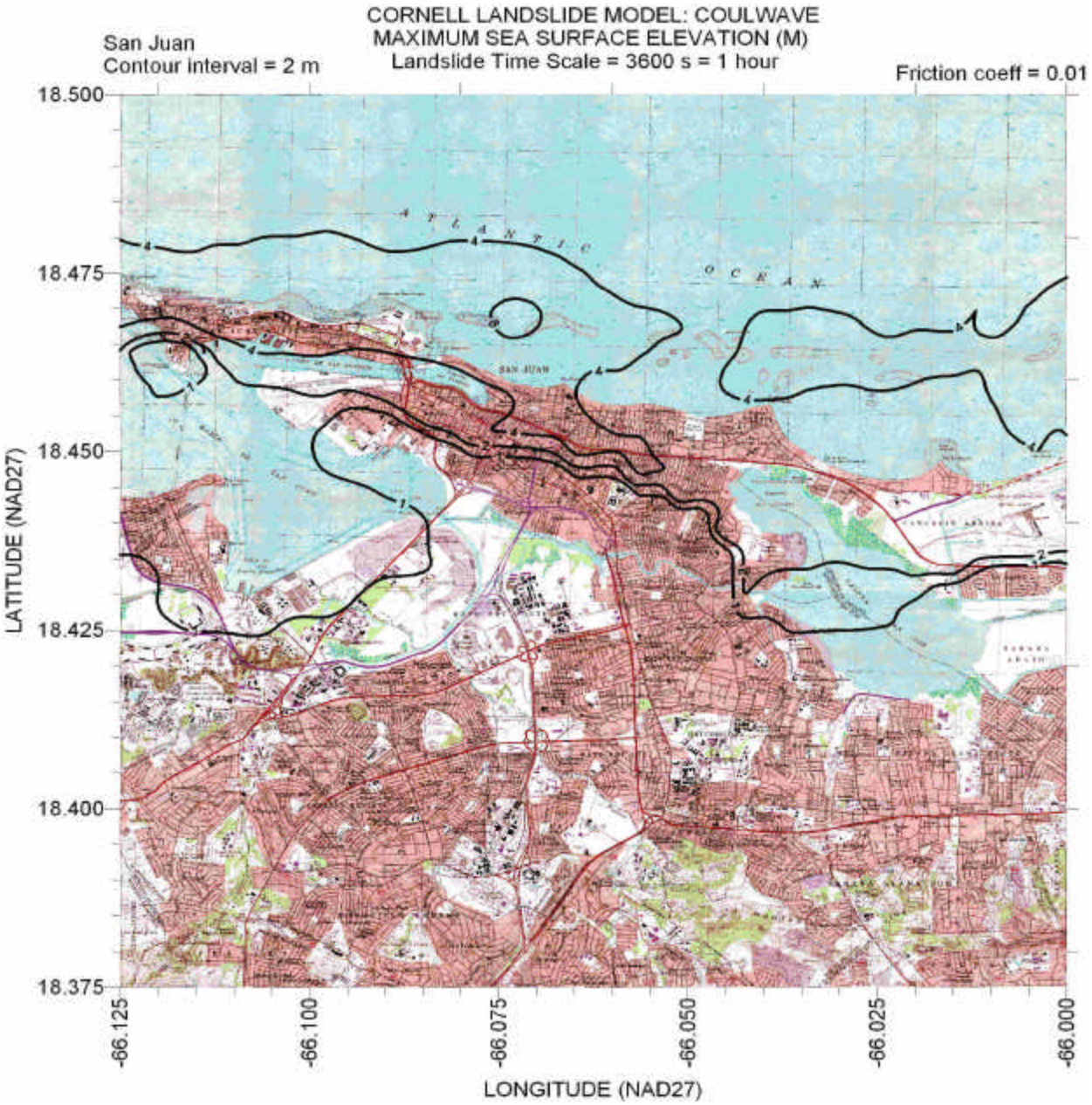


Figure 67– Contours of maximum sea surface elevation for time scale = 3600 s for San Juan quadrangle. Friction factor f = 0.01.

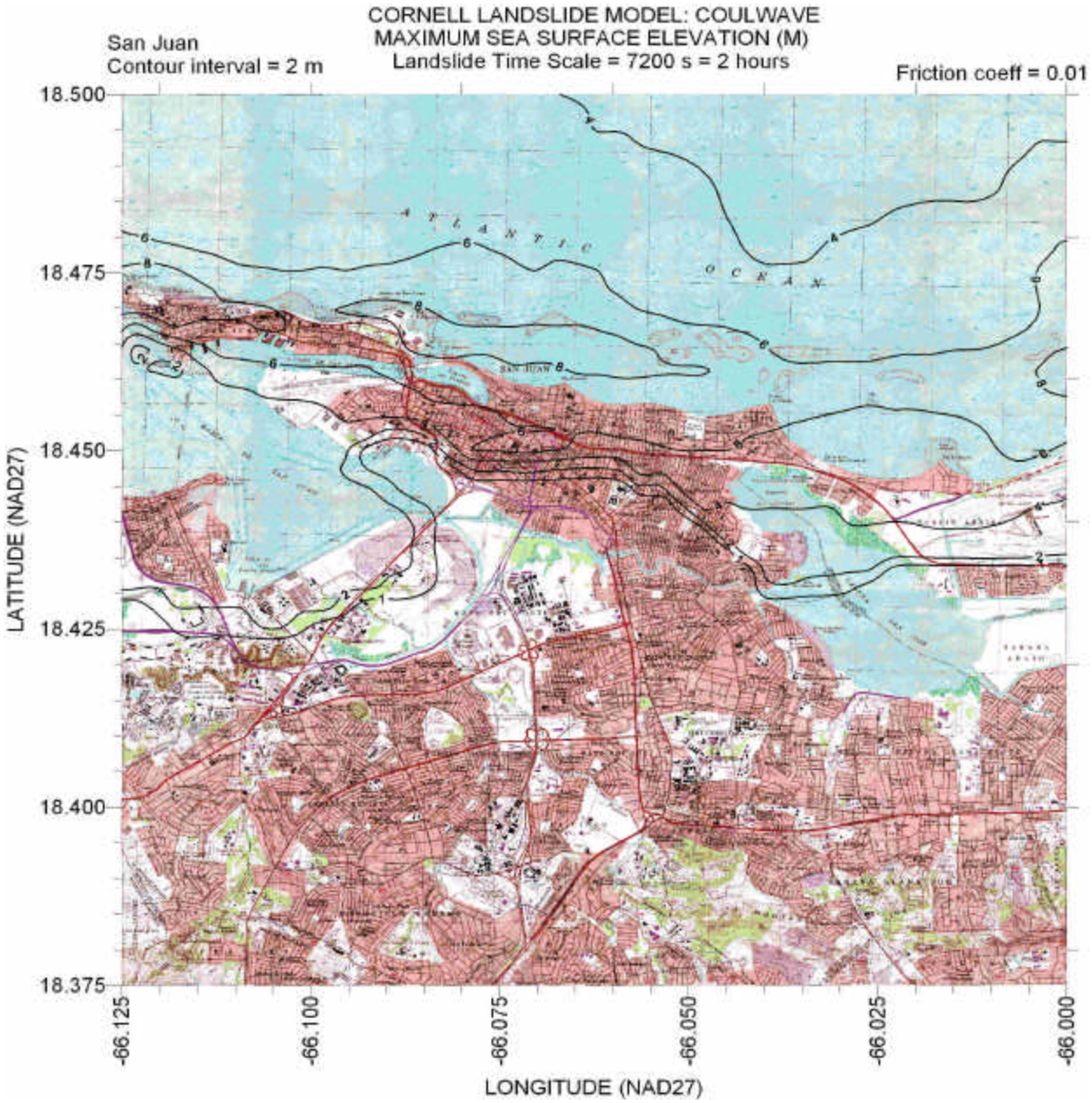


Figure 68– Contours of maximum sea surface elevation for time scale = 7200 s for San Juan quadrangle. Friction factor f = 0.01.

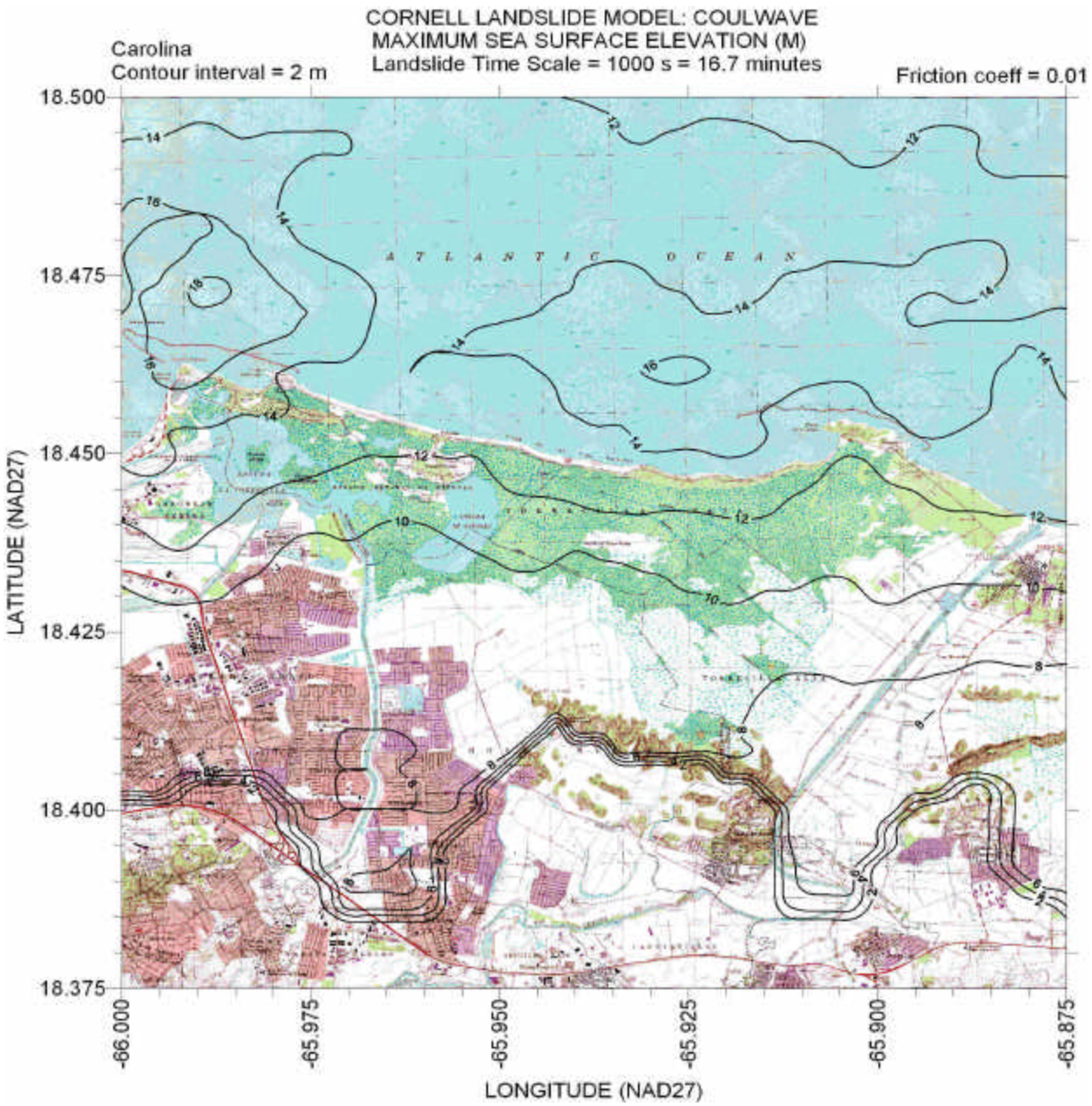


Figure 69– Contours of maximum sea surface elevation for time scale = 1000 s for Carolina quadrangle. Friction factor f = 0.01.

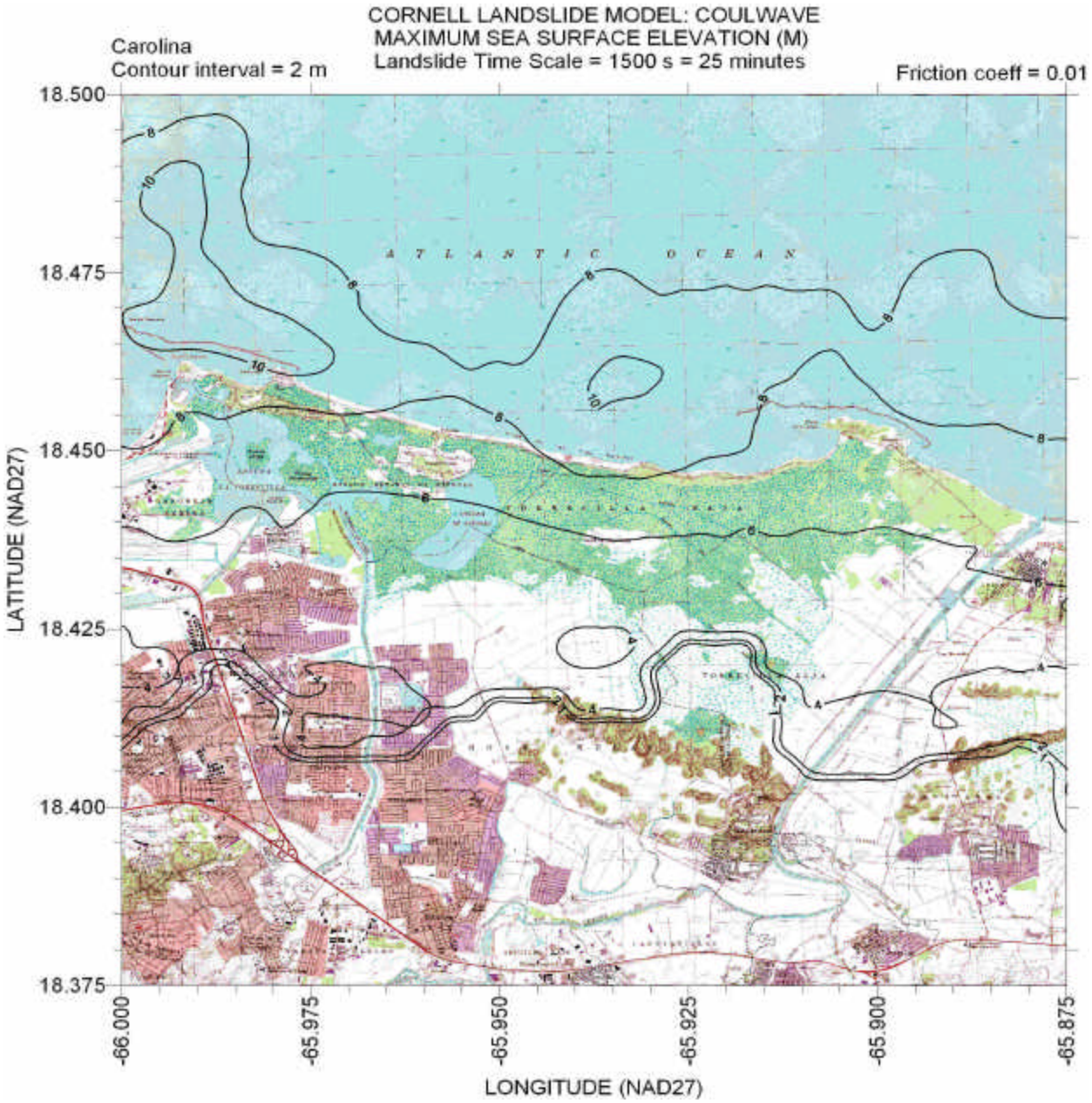


Figure 70– Contours of maximum sea surface elevation for time scale = 1500 s for Carolina quadrangle. Friction factor f = 0.01.

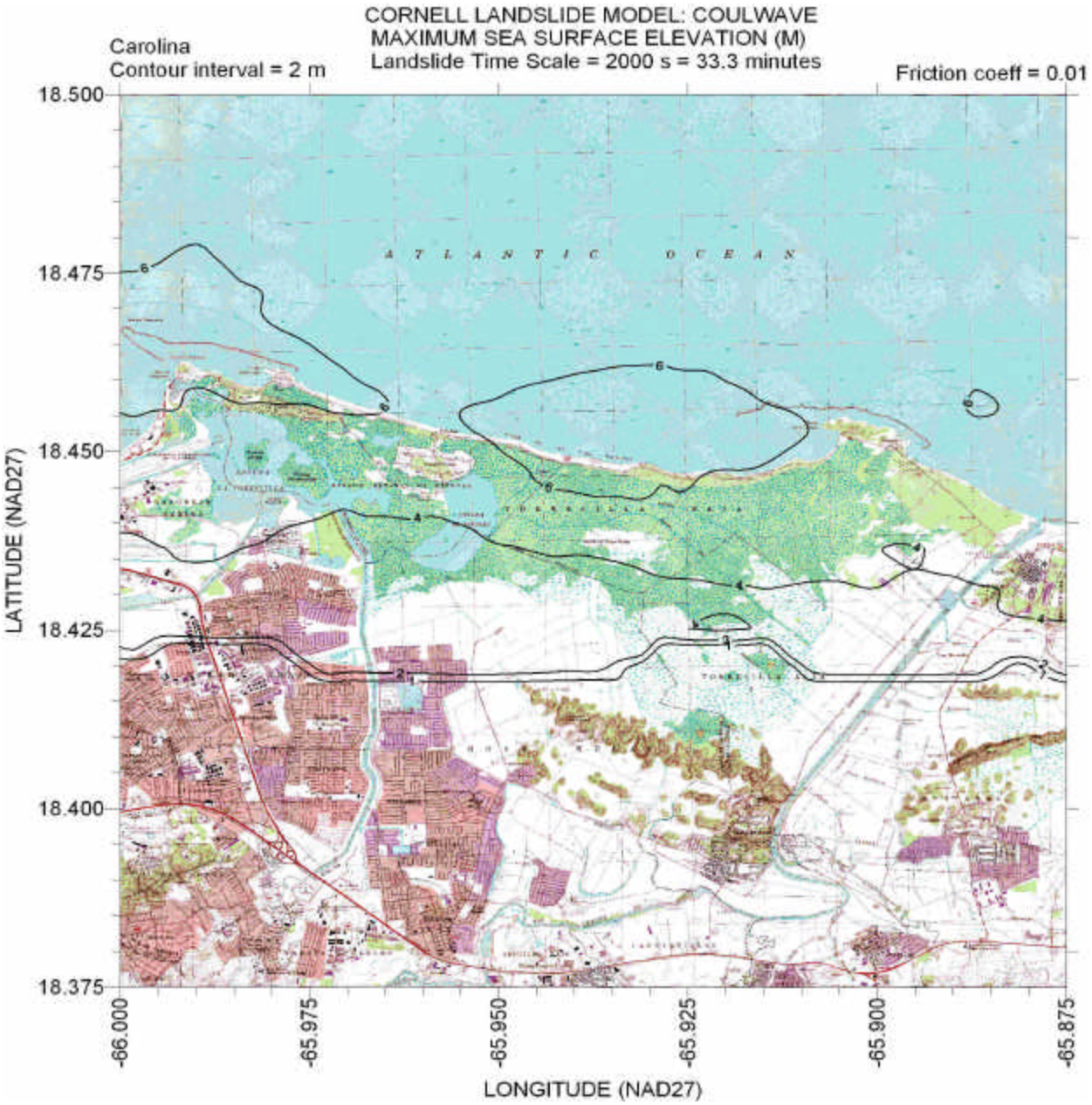


Figure 71– Contours of maximum sea surface elevation for time scale = 2000 s for Carolina quadrangle. Friction factor f = 0.01.

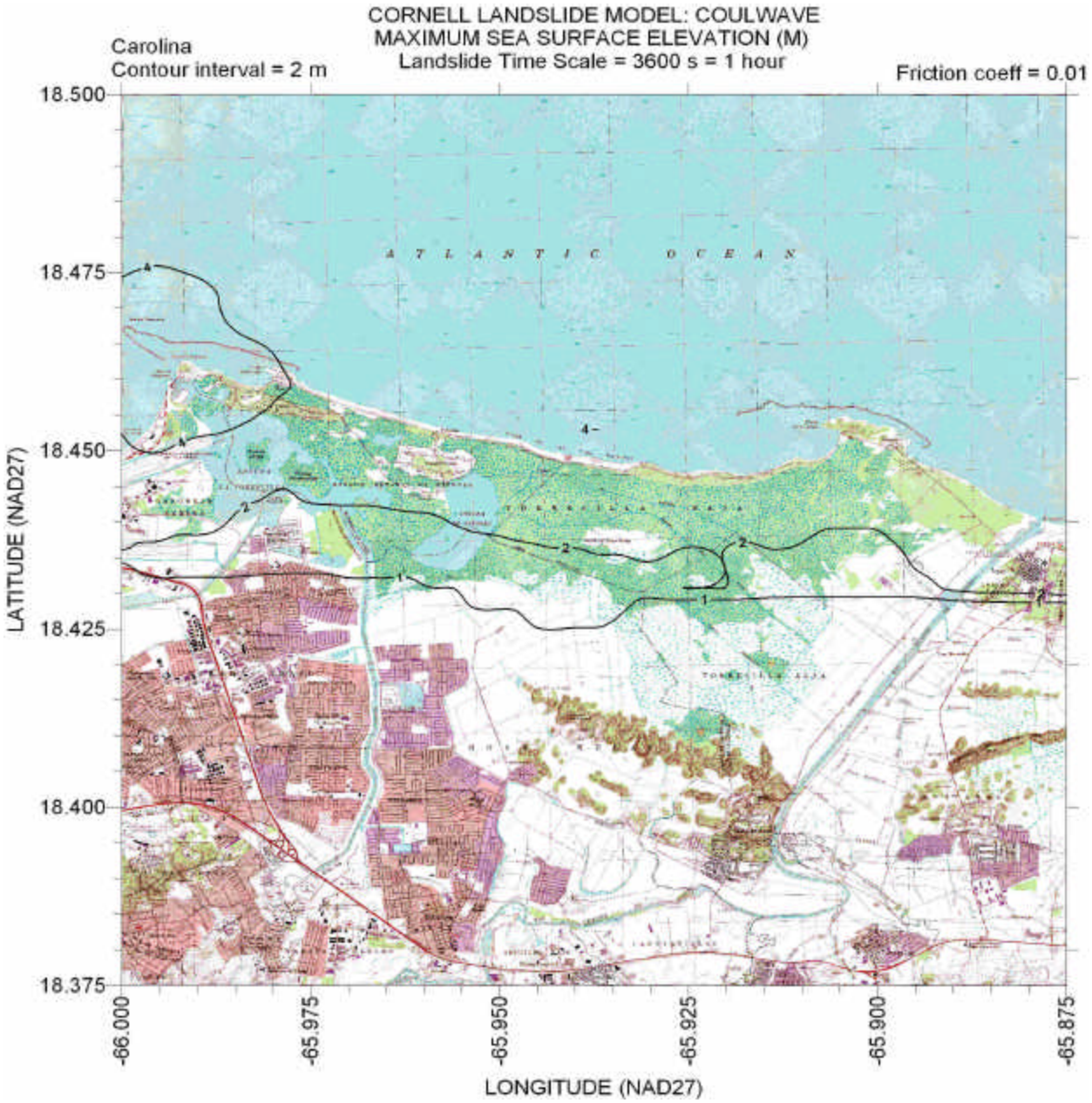


Figure 72– Contours of maximum sea surface elevation for time scale = 3600 s for Carolina quadrangle. Friction factor f = 0.01.

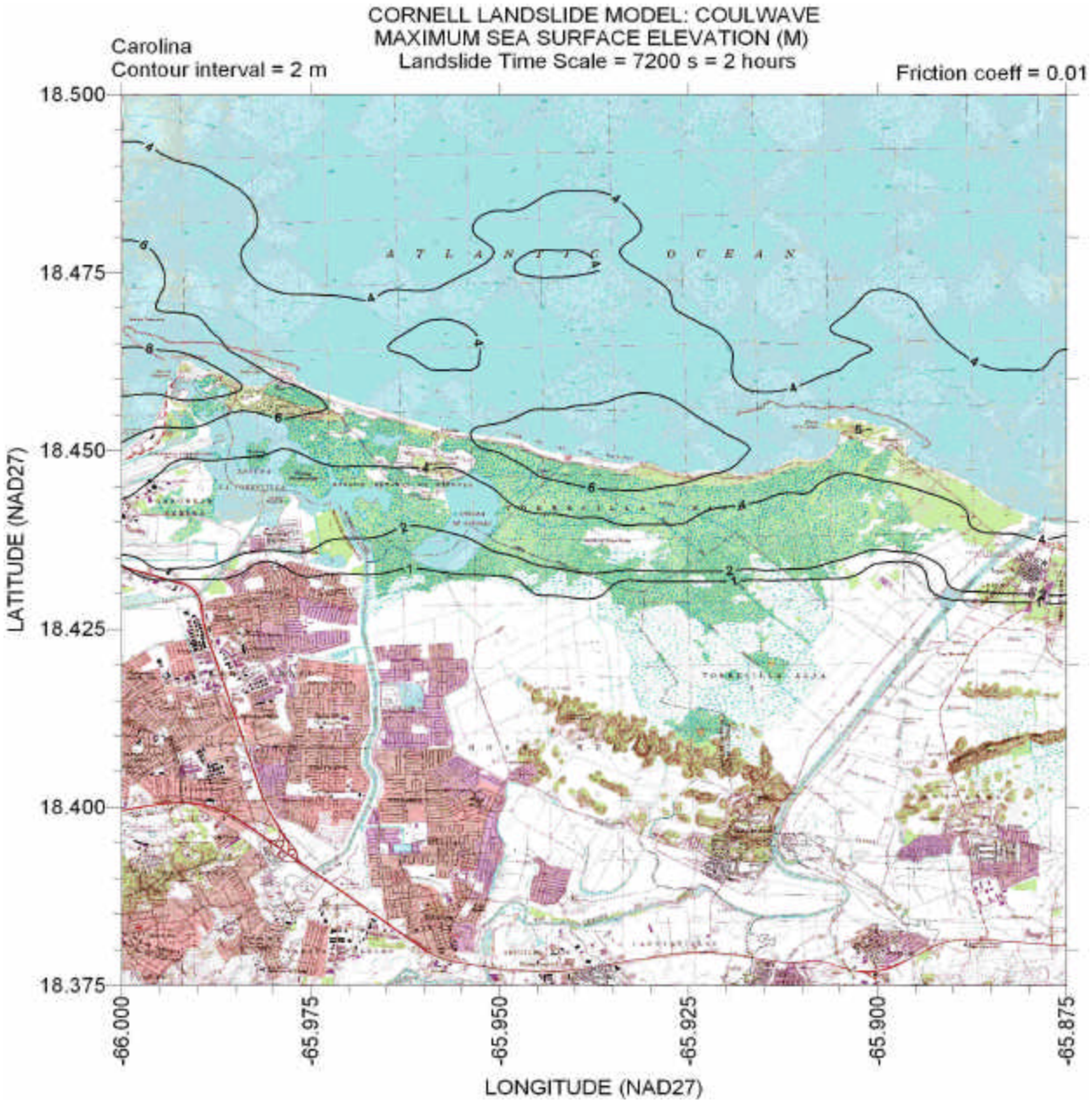


Figure 73– Contours of maximum sea surface elevation for time scale = 7200 s for Carolina quadrangle. Friction factor f = 0.01.

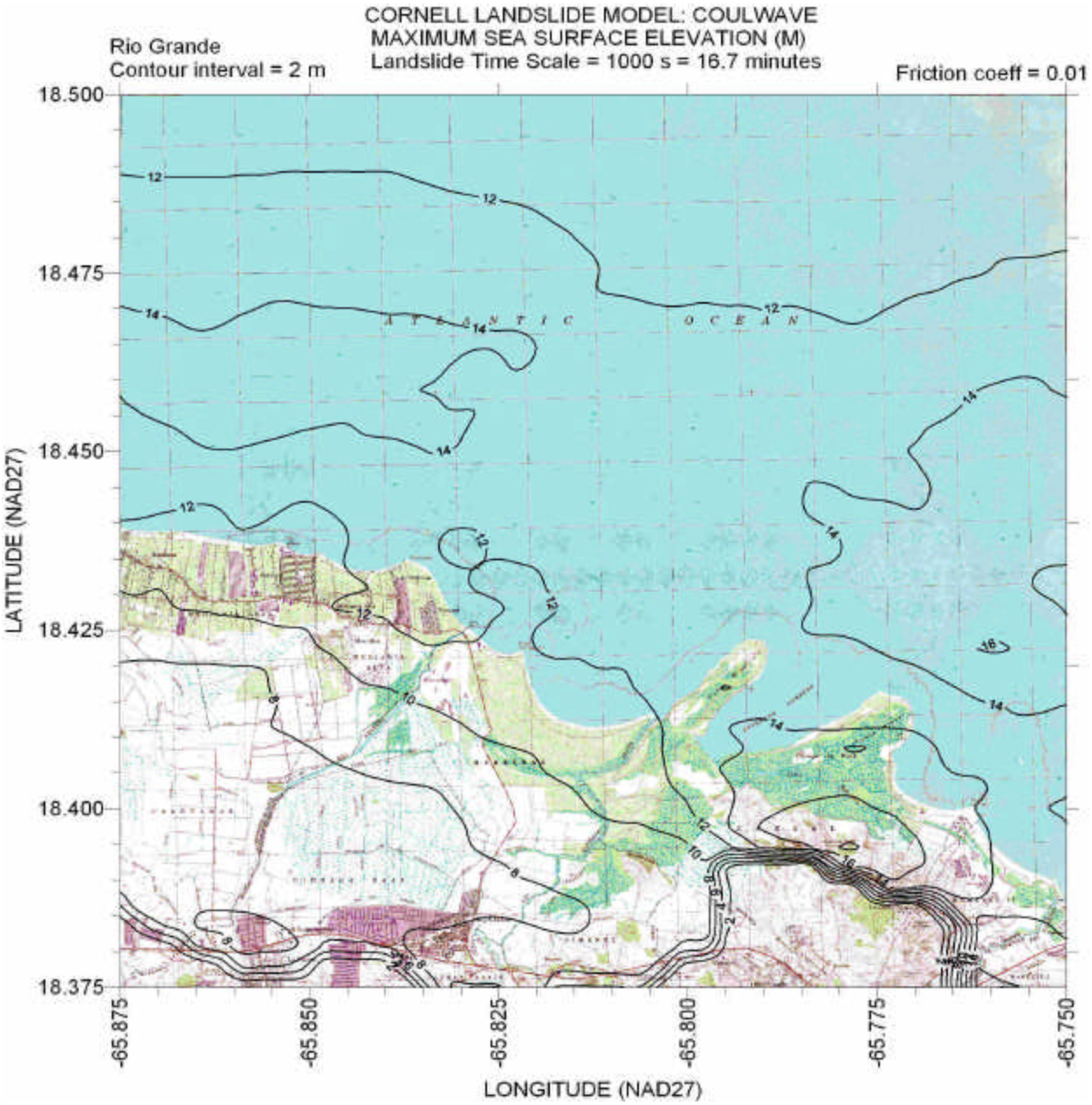


Figure 74– Contours of maximum sea surface elevation for time scale = 1000 s for Rio Grande quadrangle. Friction factor f = 0.01.

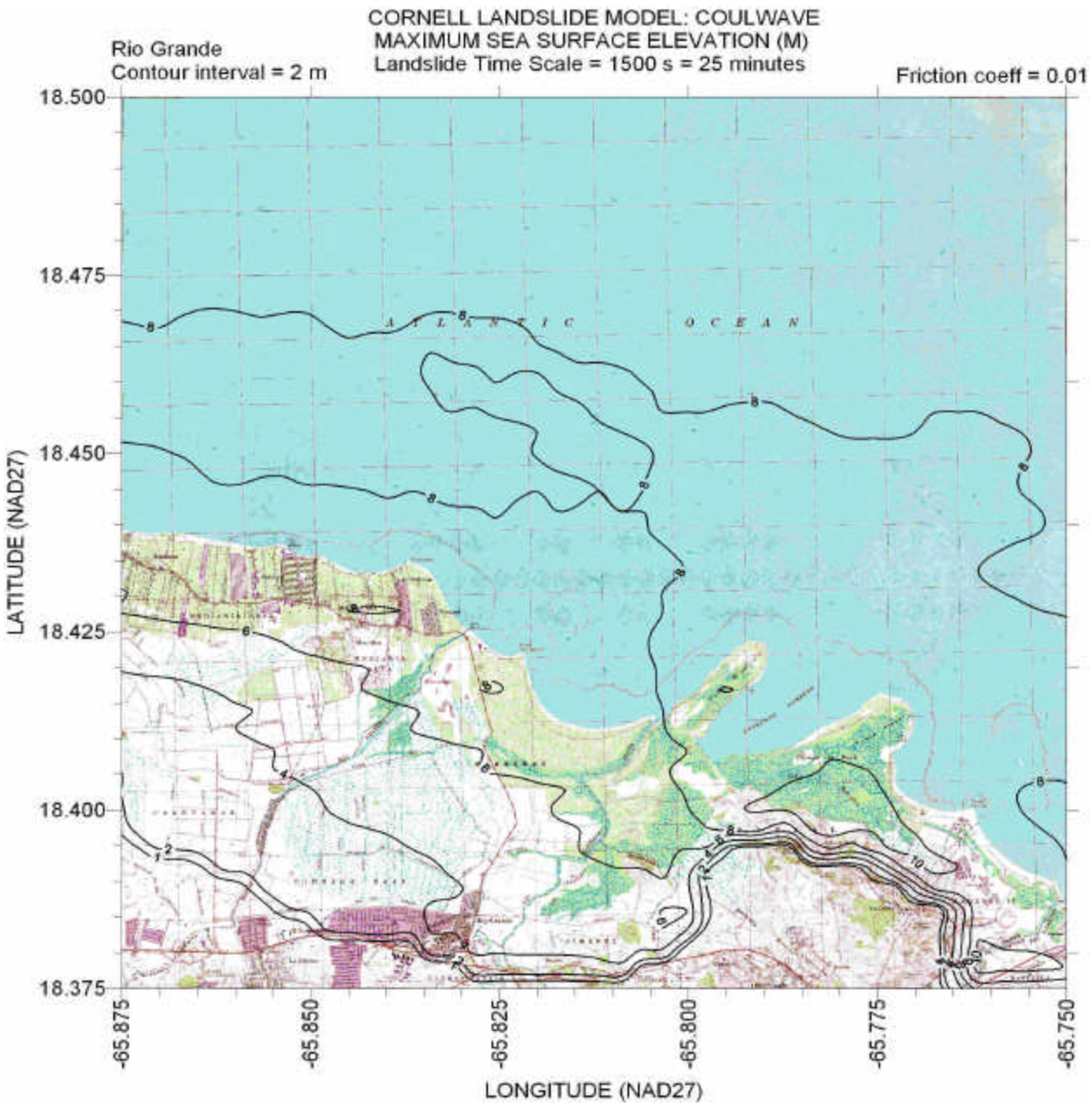


Figure 75– Contours of maximum sea surface elevation for time scale = 1500 s for Rio Grande quadrangle. Friction factor f = 0.01.

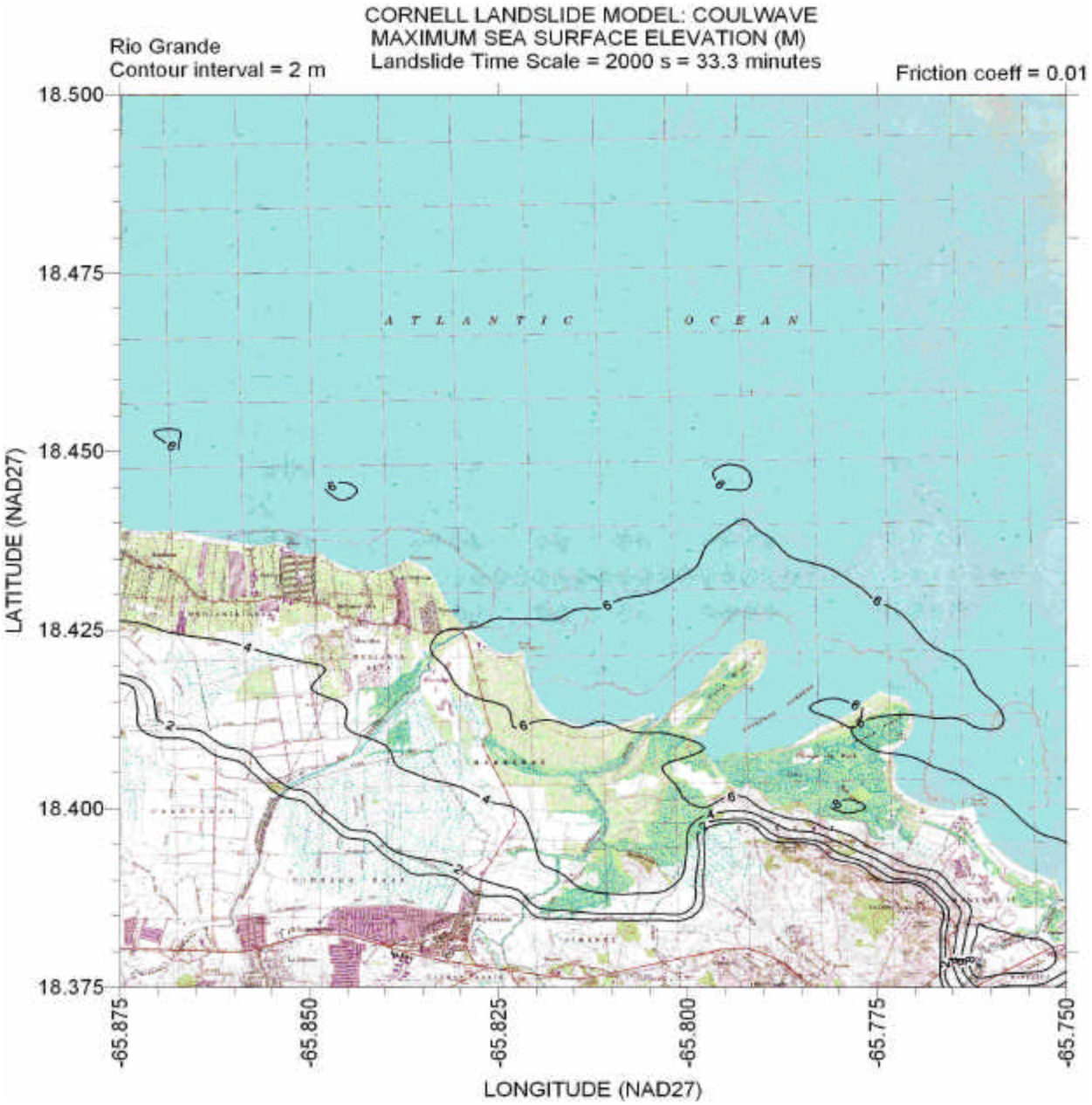


Figure 76– Contours of maximum sea surface elevation for time scale = 2000 s for Rio Grande quadrangle. Friction factor f = 0.01.

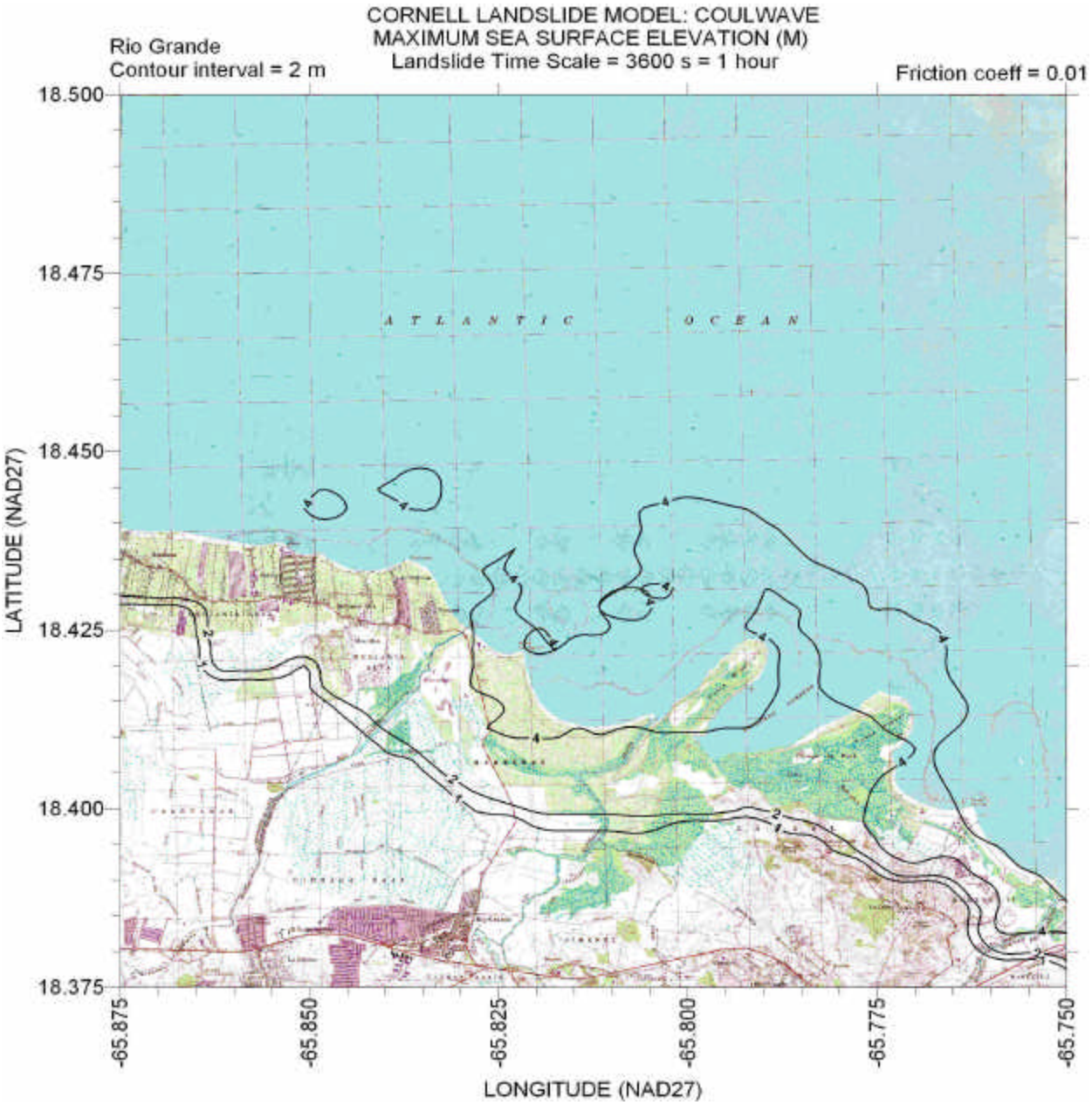


Figure 77– Contours of maximum sea surface elevation for time scale = 3600 s for Rio Grande quadrangle. Friction factor f = 0.01.

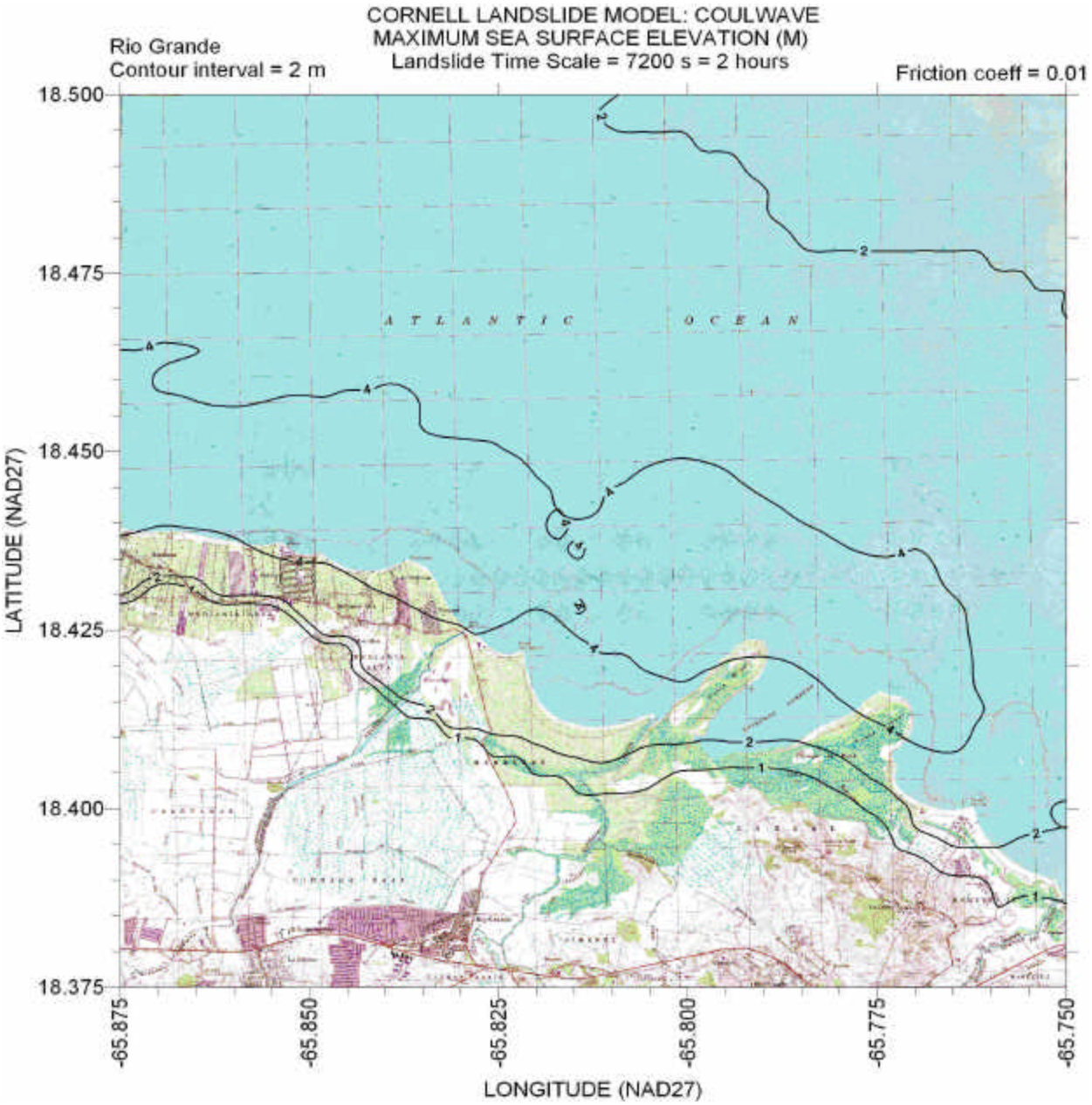


Figure 78– Contours of maximum sea surface elevation for time scale = 7200 s for Rio Grande quadrangle. Friction factor f = 0.01.

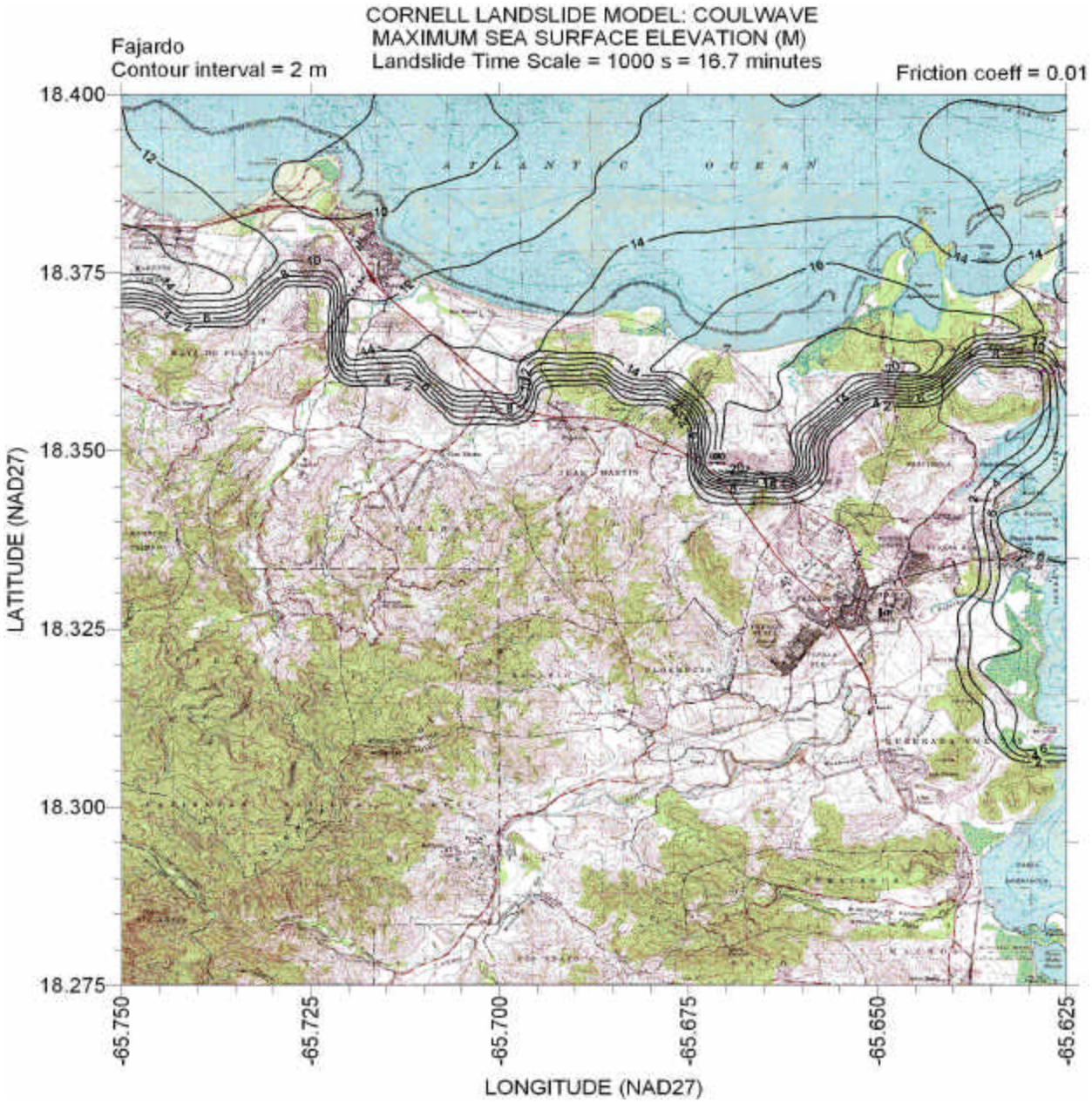


Figure 79– Contours of maximum sea surface elevation for time scale = 1000 s for Fajardo quadrangle. Friction factor f = 0.01.

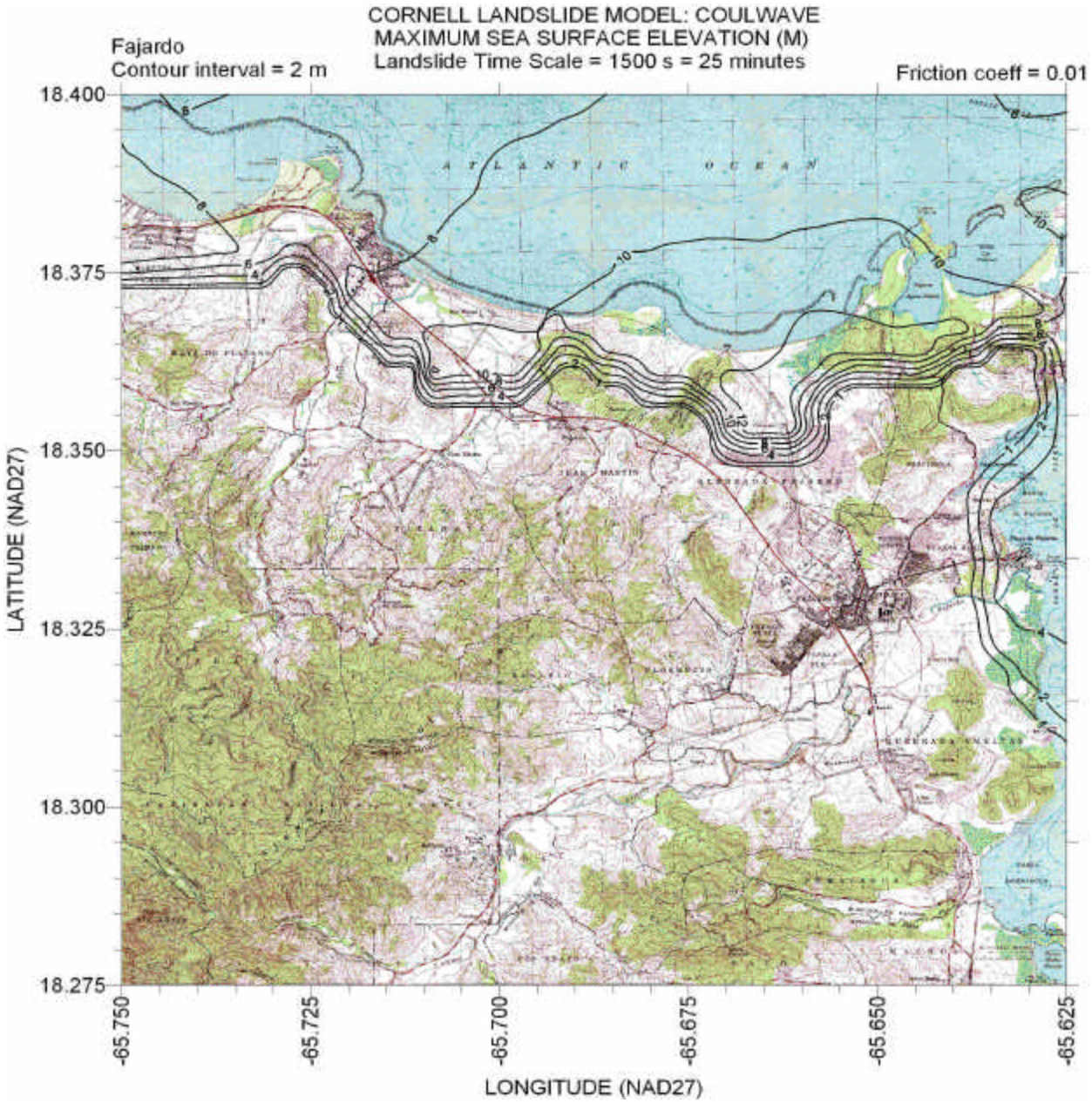


Figure 80– Contours of maximum sea surface elevation for time scale = 1500 s for Fajardo quadrangle. Friction factor f = 0.01.

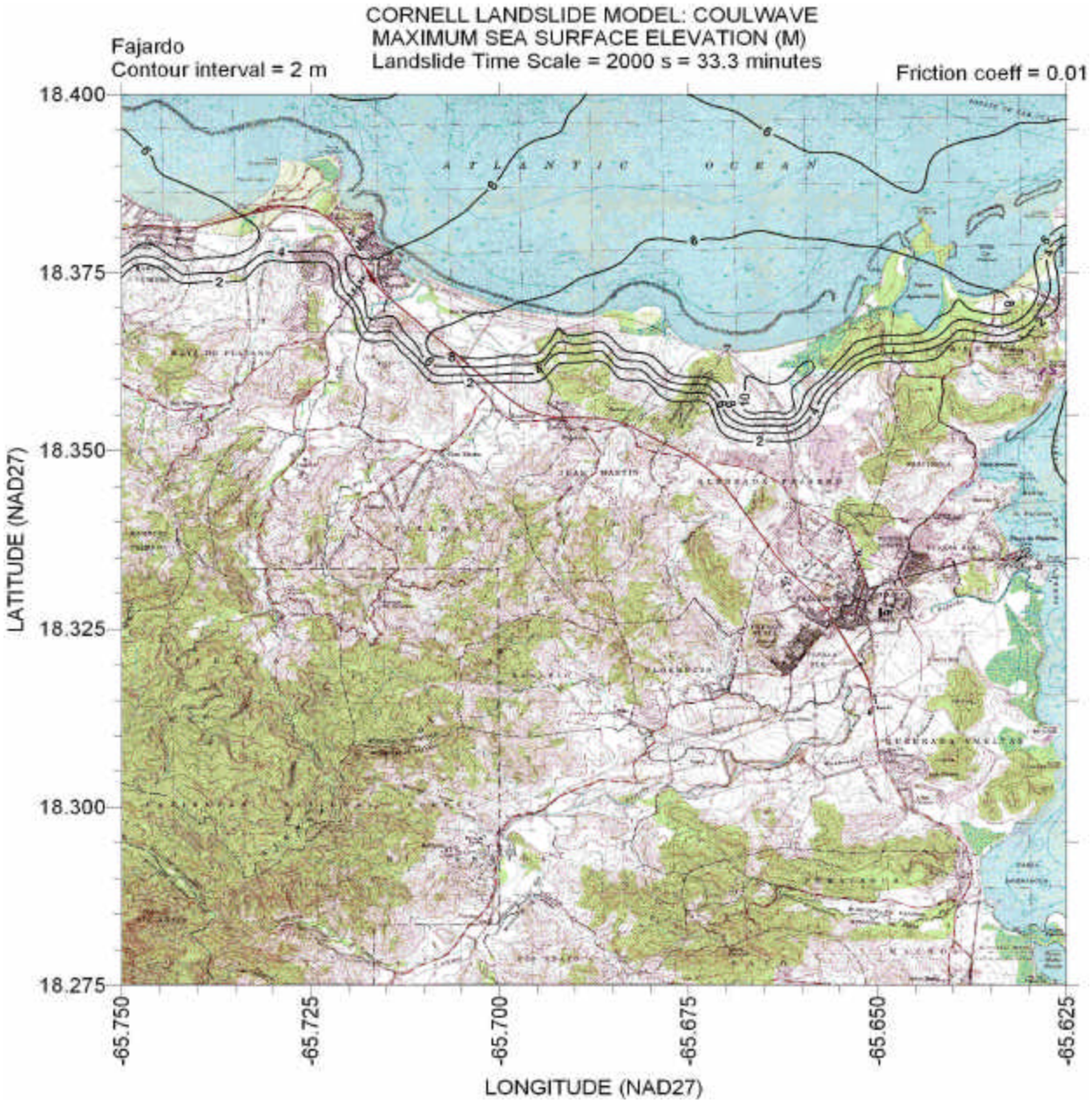


Figure 81– Contours of maximum sea surface elevation for time scale = 2000 s for Fajardo quadrangle. Friction factor f = 0.01.

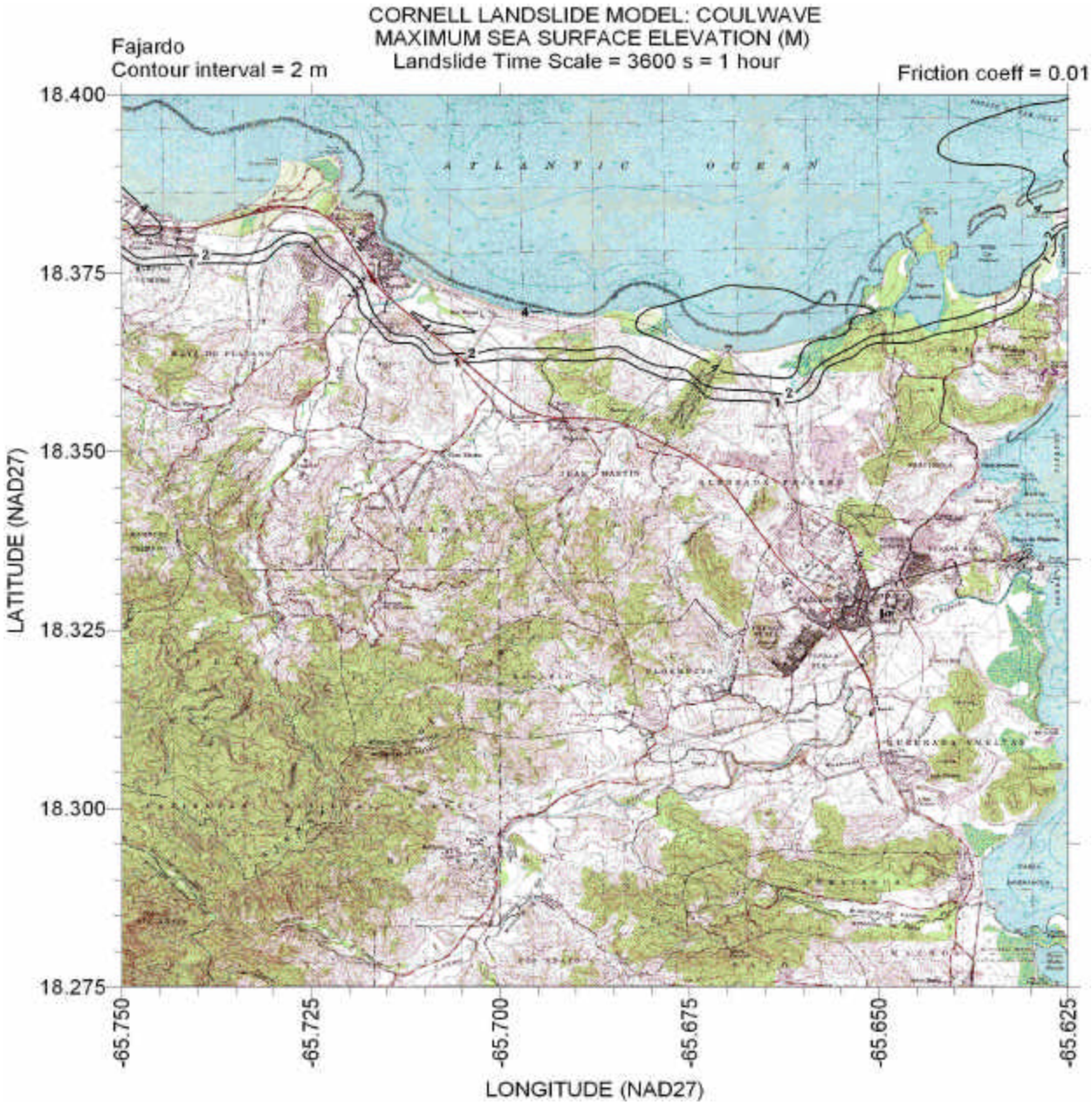


Figure 82– Contours of maximum sea surface elevation for time scale = 3600 s for Fajardo quadrangle. Friction factor f = 0.01.

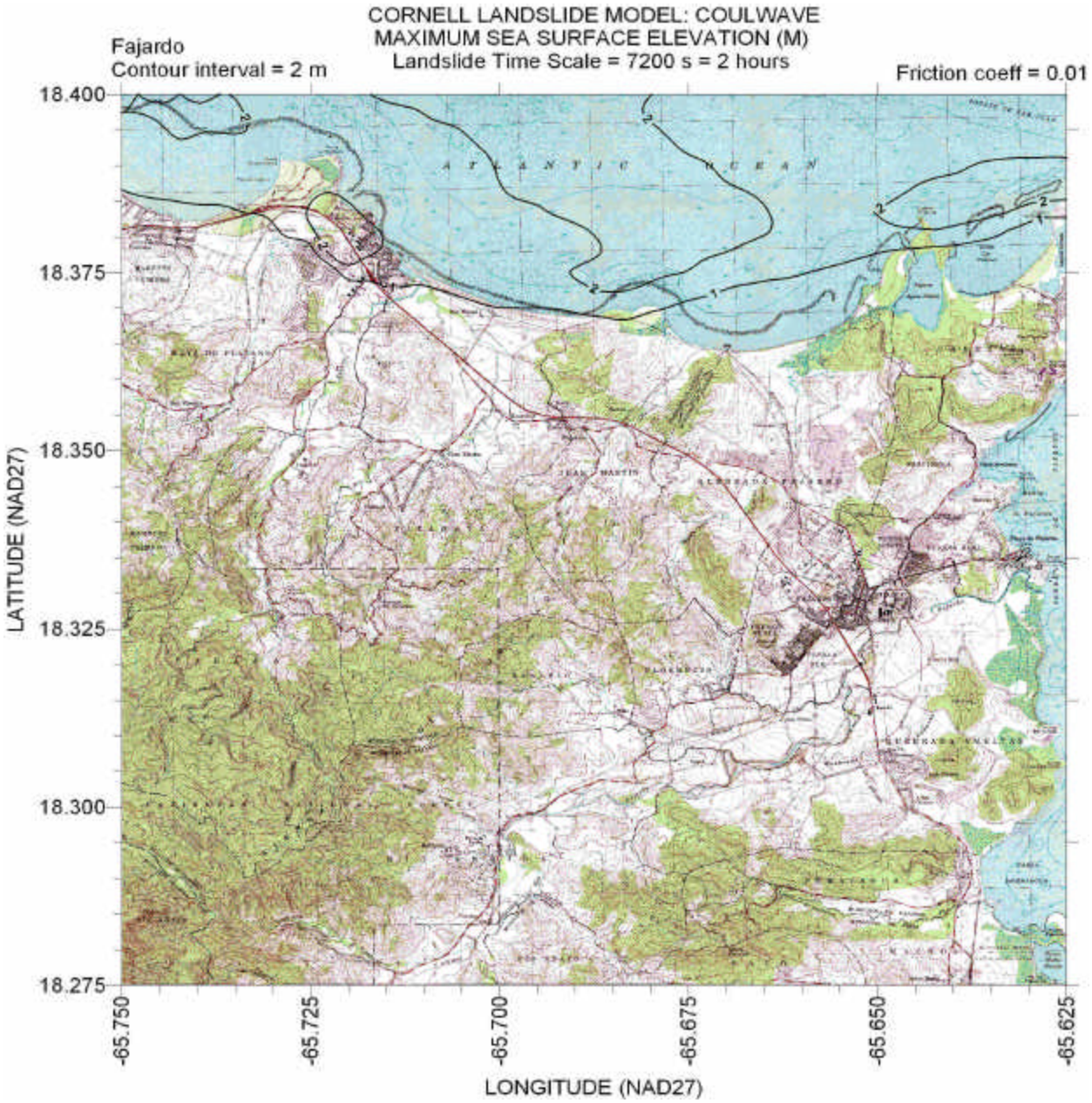


Figure 83– Contours of maximum sea surface elevation for time scale = 7200 s for Fajardo quadrangle. Friction factor f = 0.01.

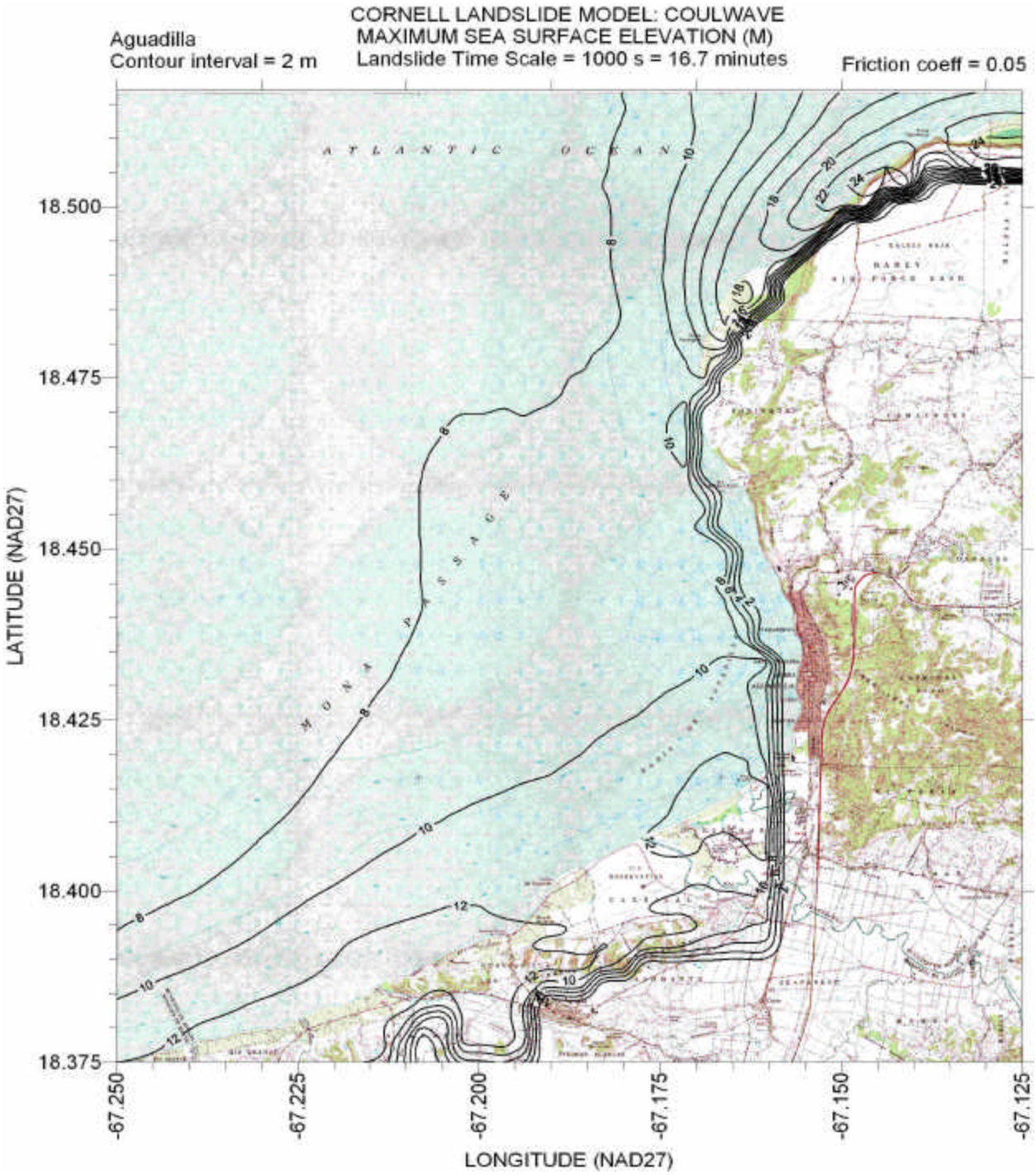


Figure 84– Contours of maximum sea surface elevation for time scale = 1000 s for Aguadilla quadrangle. Friction factor $f$ = 0.05.

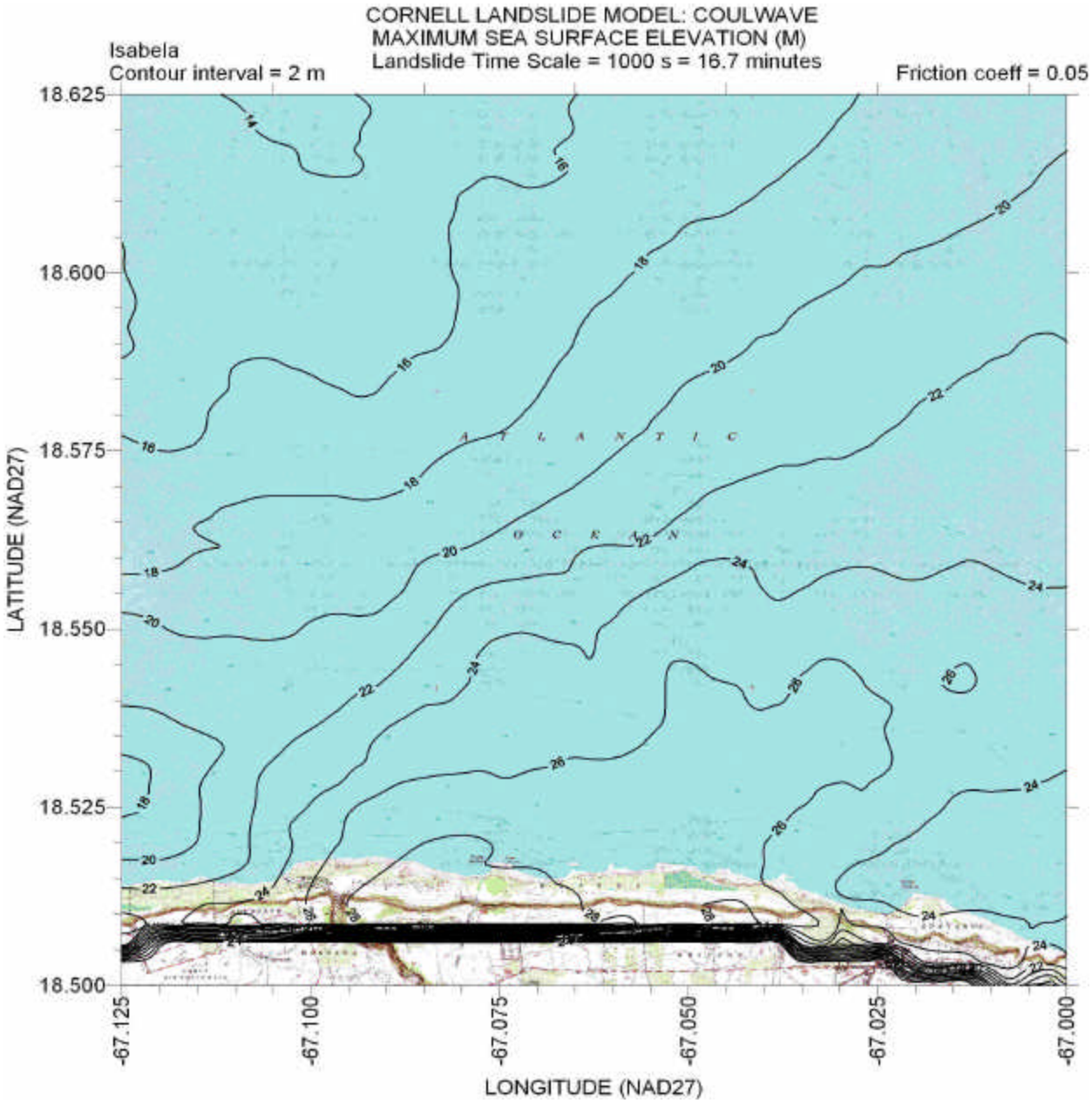


Figure 85– Contours of maximum sea surface elevation for time scale = 1000 s for Isabela quadrangle. Friction factor $f$ = 0.05.

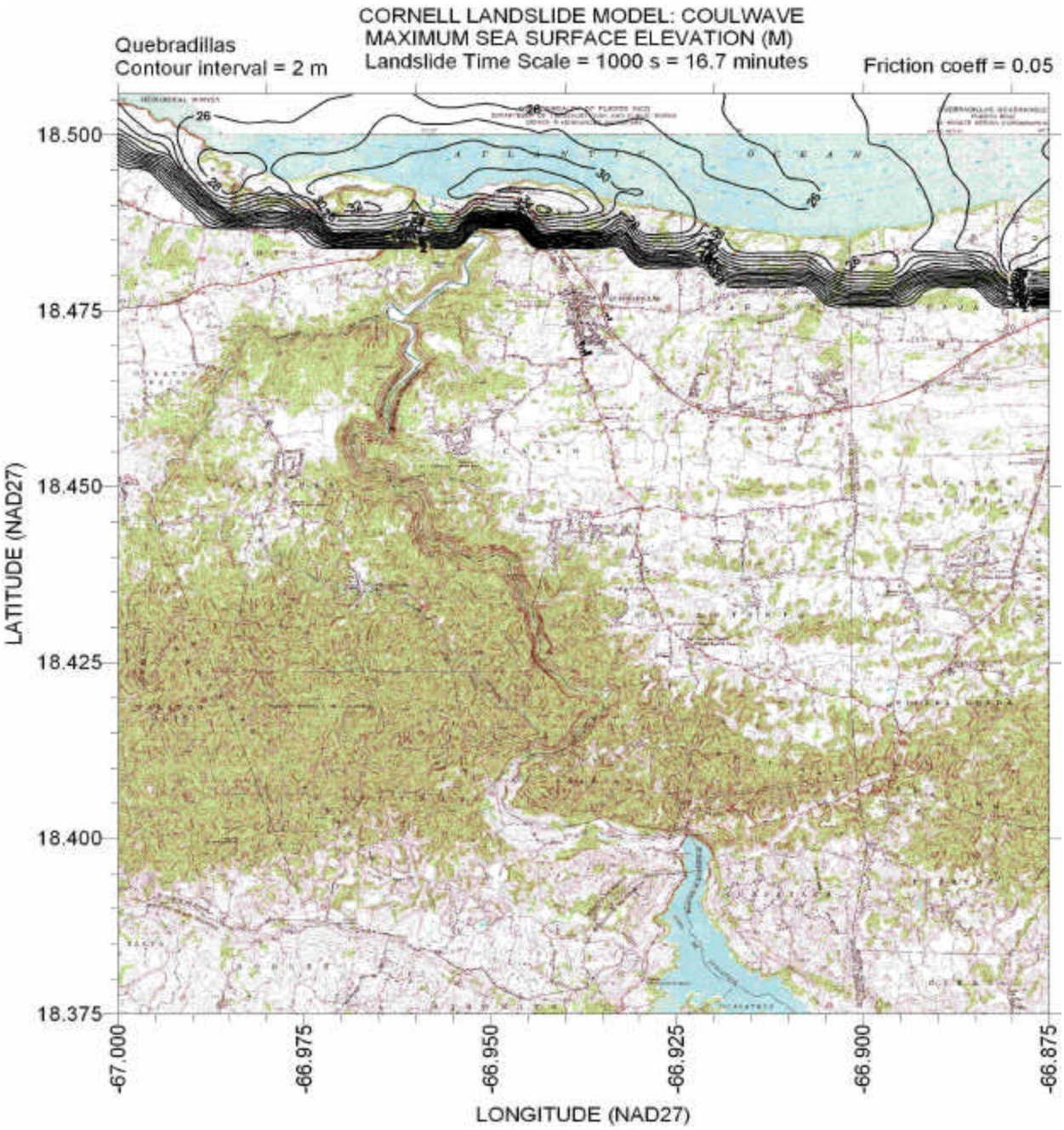


Figure 86– Contours of maximum sea surface elevation for time scale = 1000 s for Quebradillas quadrangle. Friction factor $f$ = 0.05.

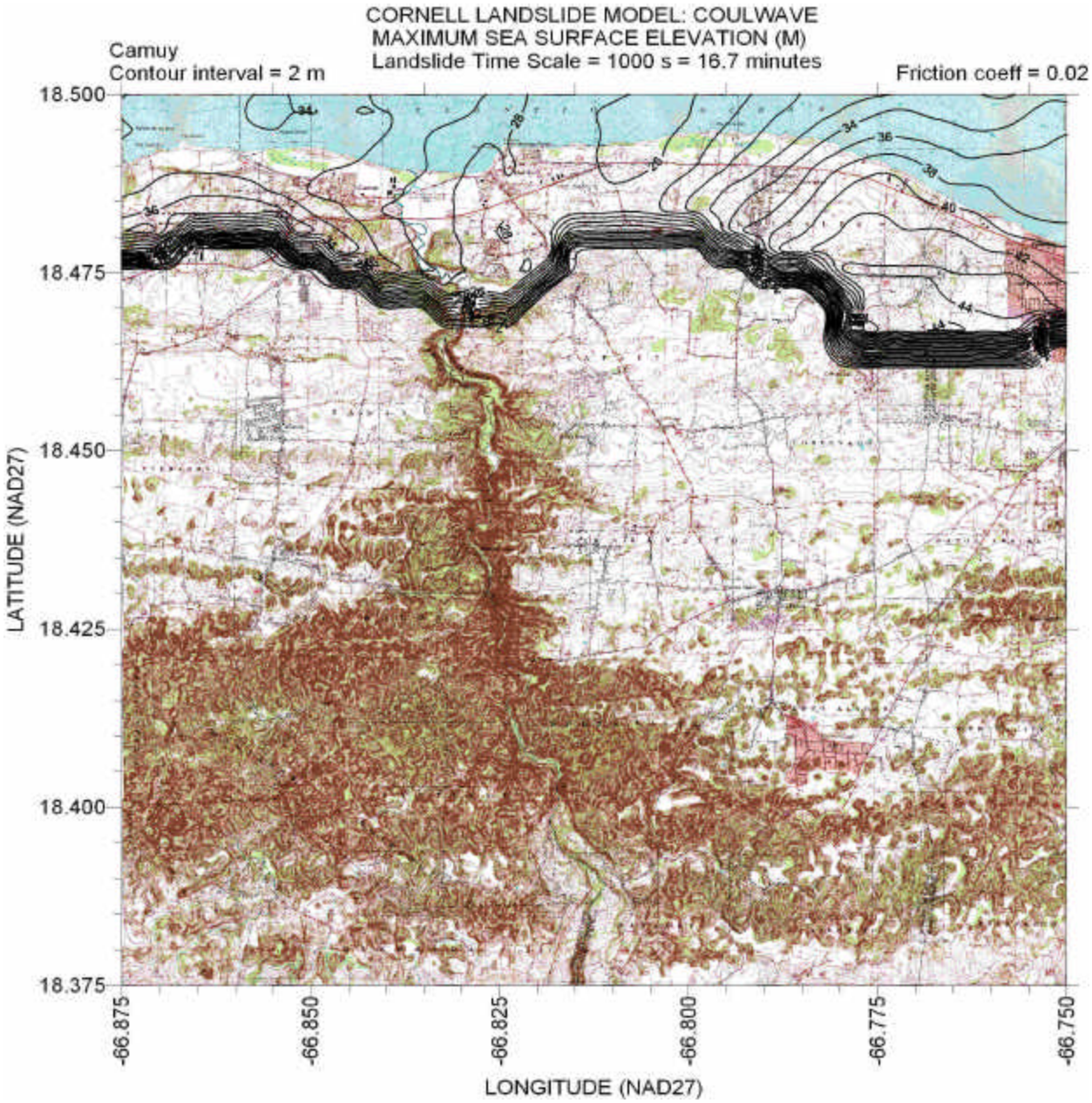


Figure 87– Contours of maximum sea surface elevation for time scale = 1000 s for Camuy quadrangle. Friction factor $f$ = 0.05.

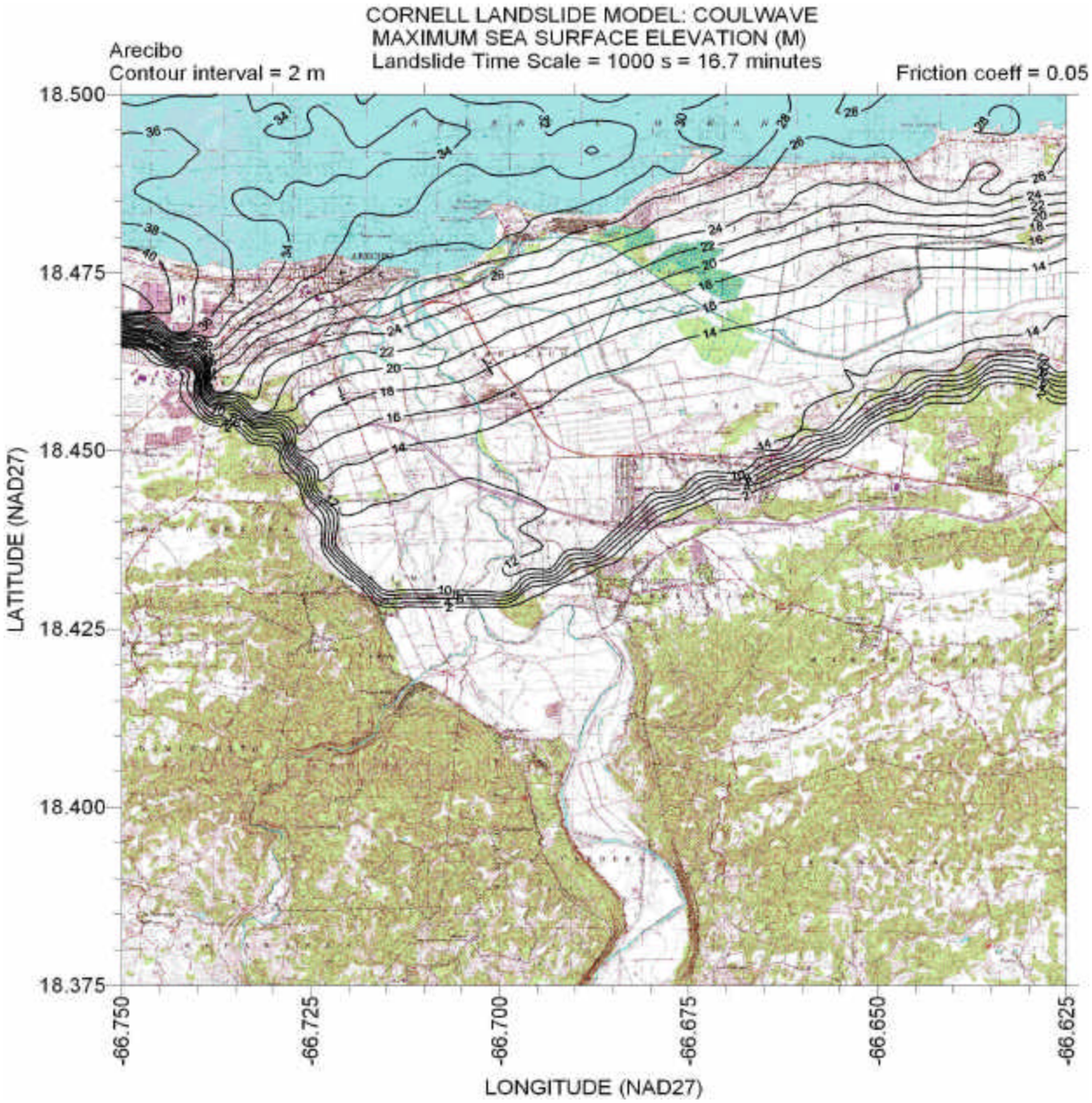


Figure 88– Contours of maximum sea surface elevation for time scale = 1000 s for Arecibo quadrangle. Friction factor $f$ = 0.05.

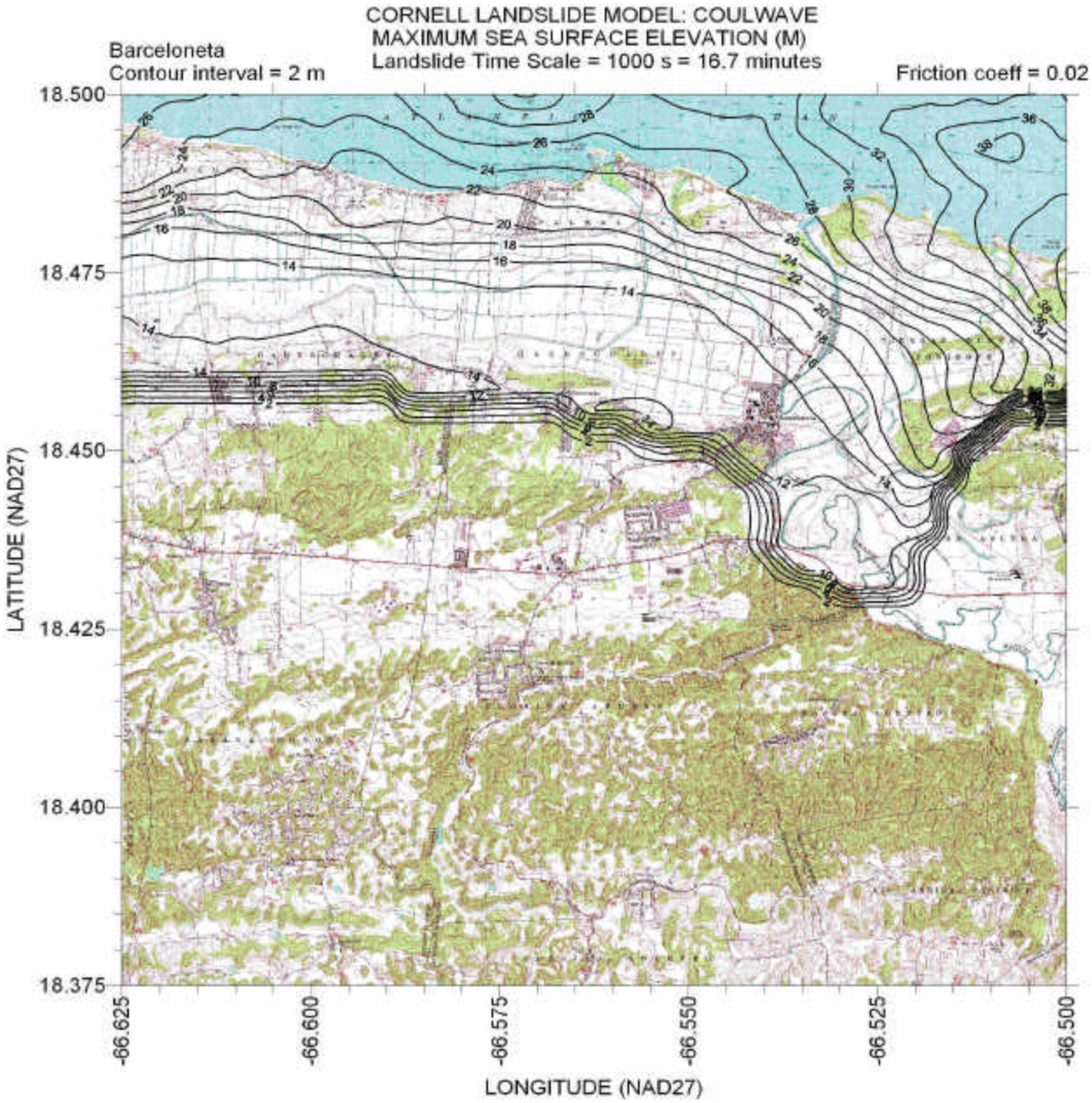


Figure 89– Contours of maximum sea surface elevation for time scale = 1000 s for Barceloneta quadrangle. Friction factor $f$ = 0.05.

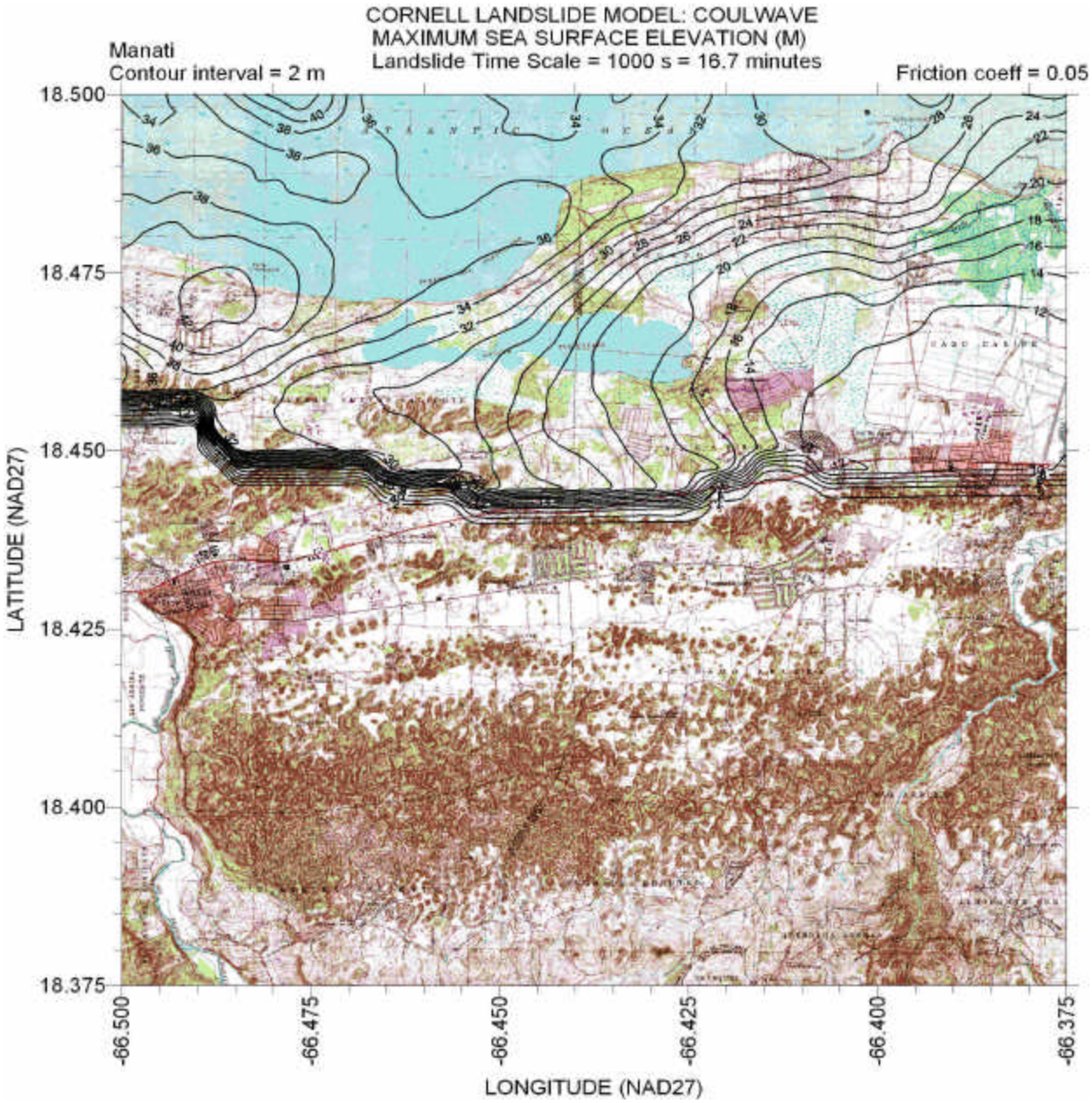


Figure 90– Contours of maximum sea surface elevation for time scale = 1000 s for Manati quadrangle. Friction factor $f$ = 0.05.

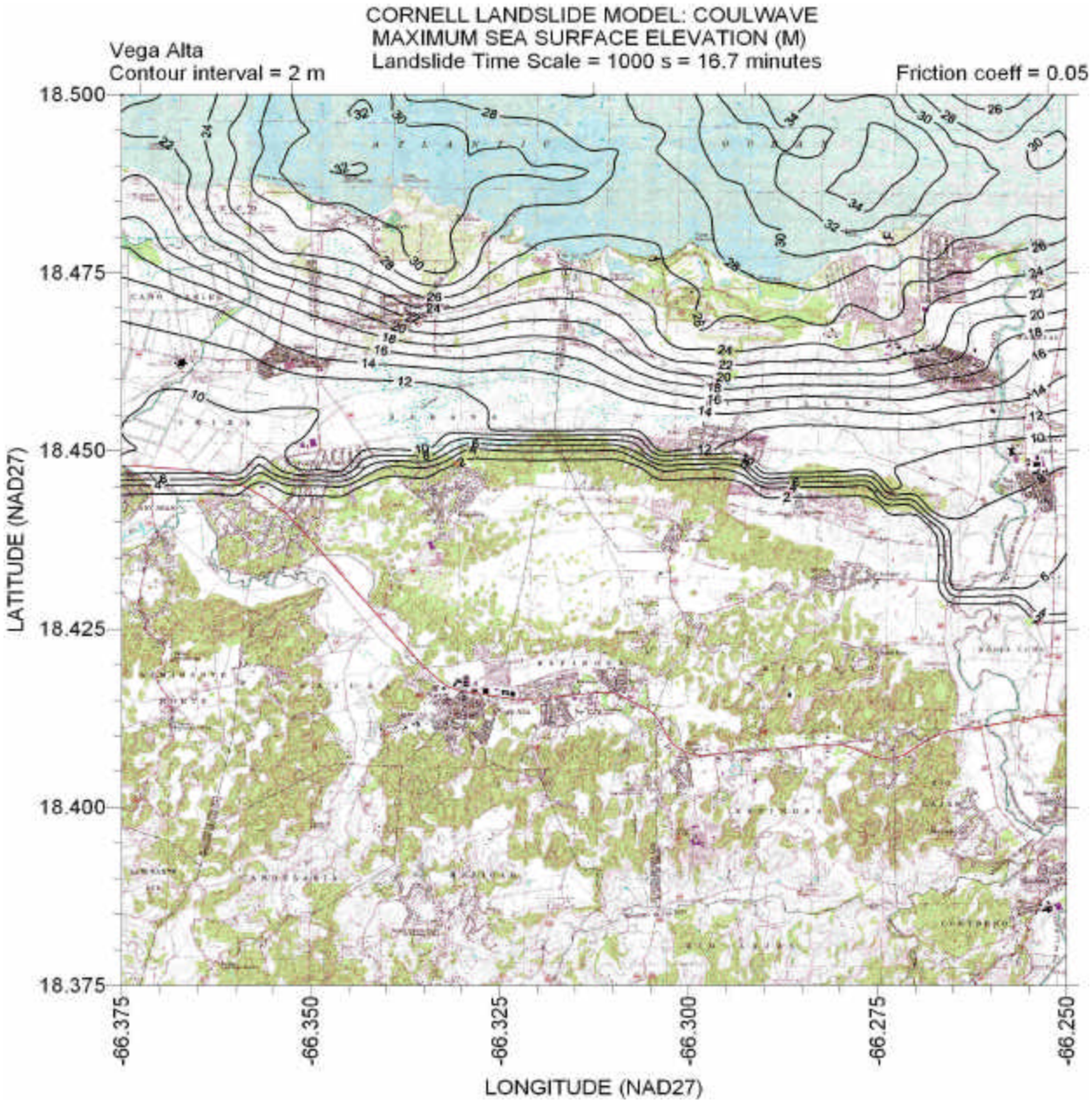


Figure 91– Contours of maximum sea surface elevation for time scale = 1000 s for Vega Alta quadrangle. Friction factor $f$ = 0.05.

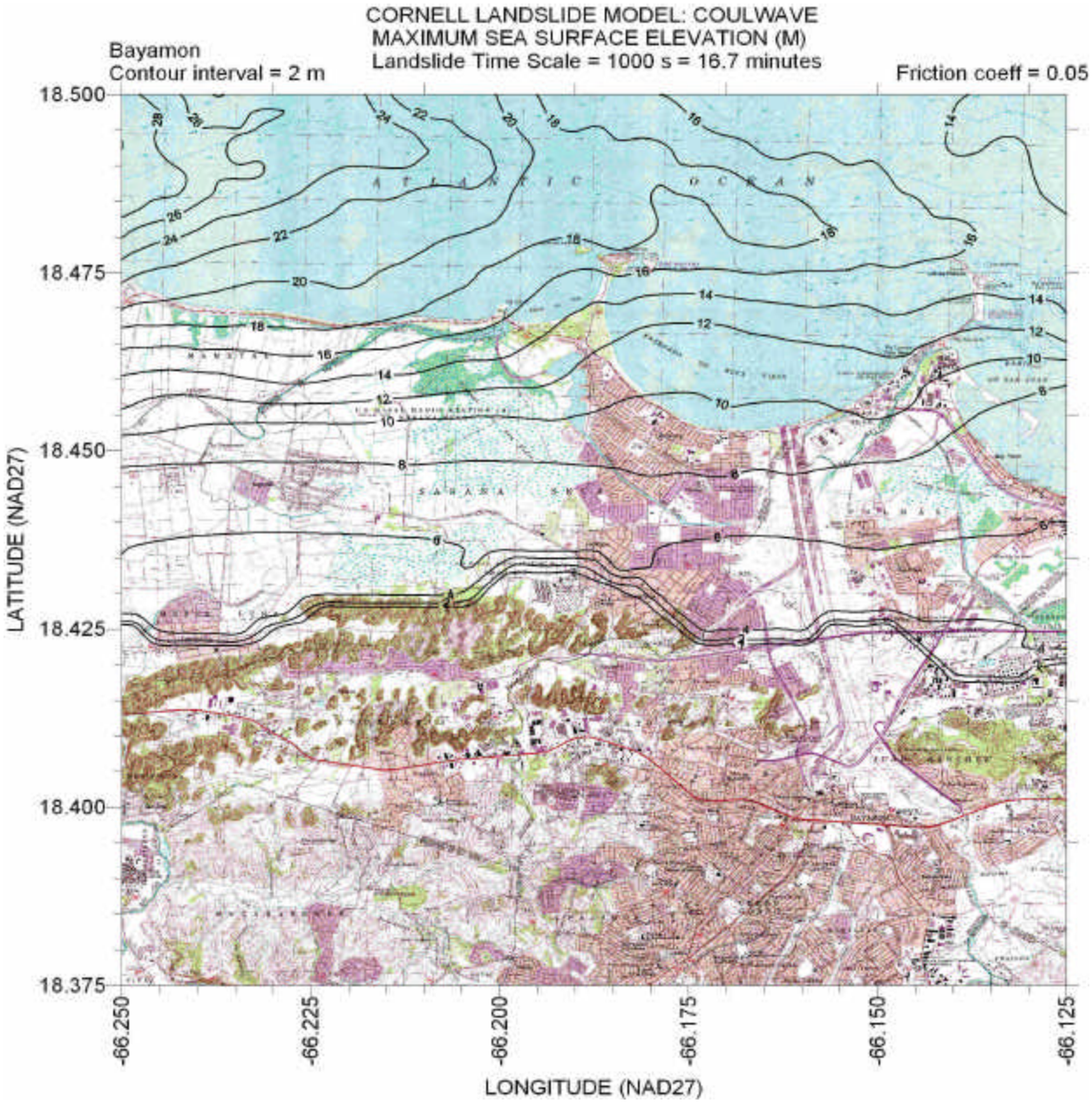


Figure 92– Contours of maximum sea surface elevation for time scale = 1000 s for Bayamon quadrangle. Friction factor $f$ = 0.05.

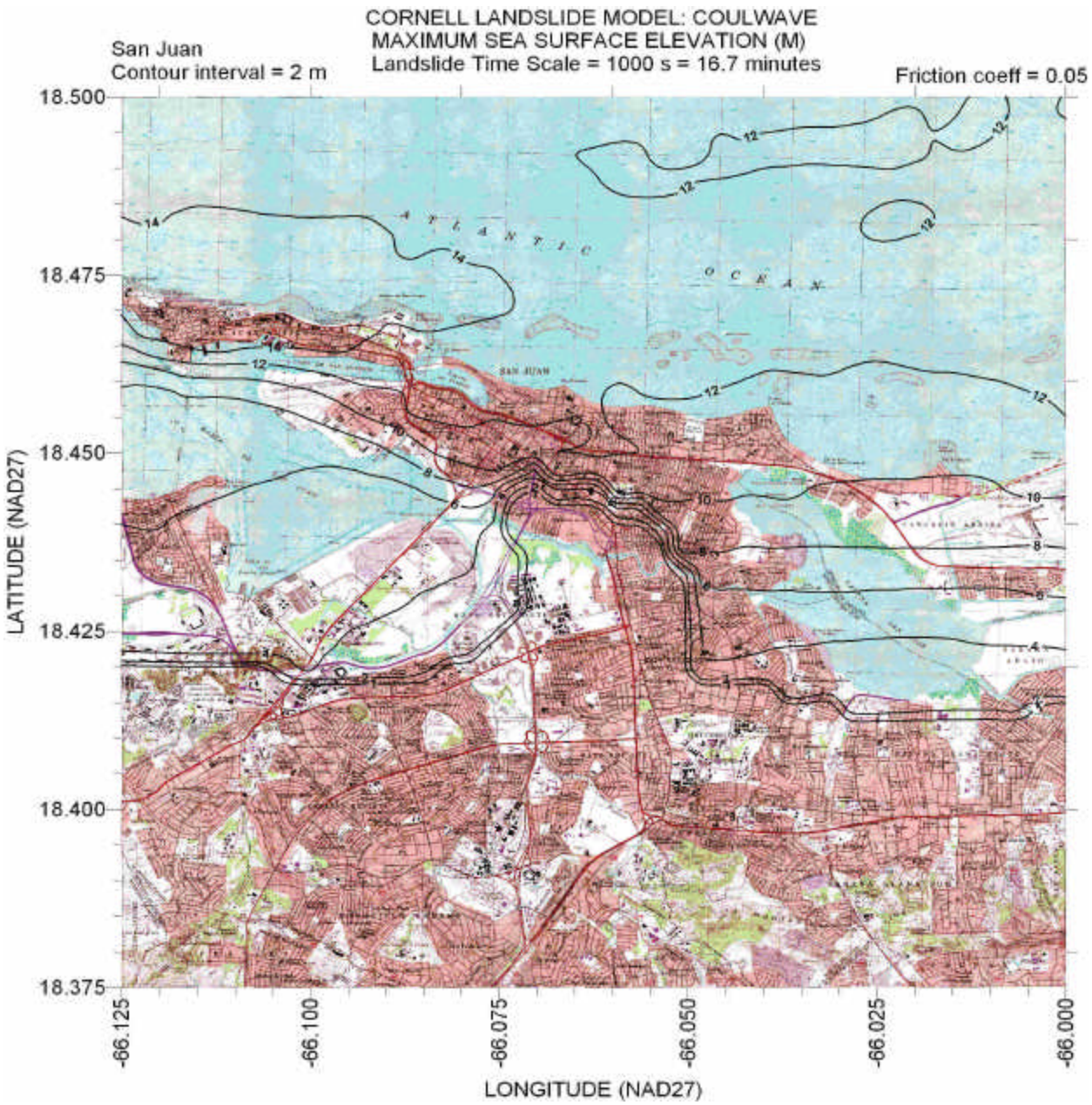


Figure 93– Contours of maximum sea surface elevation for time scale = 1000 s for San Juan quadrangle. Friction factor $f$ = 0.05.

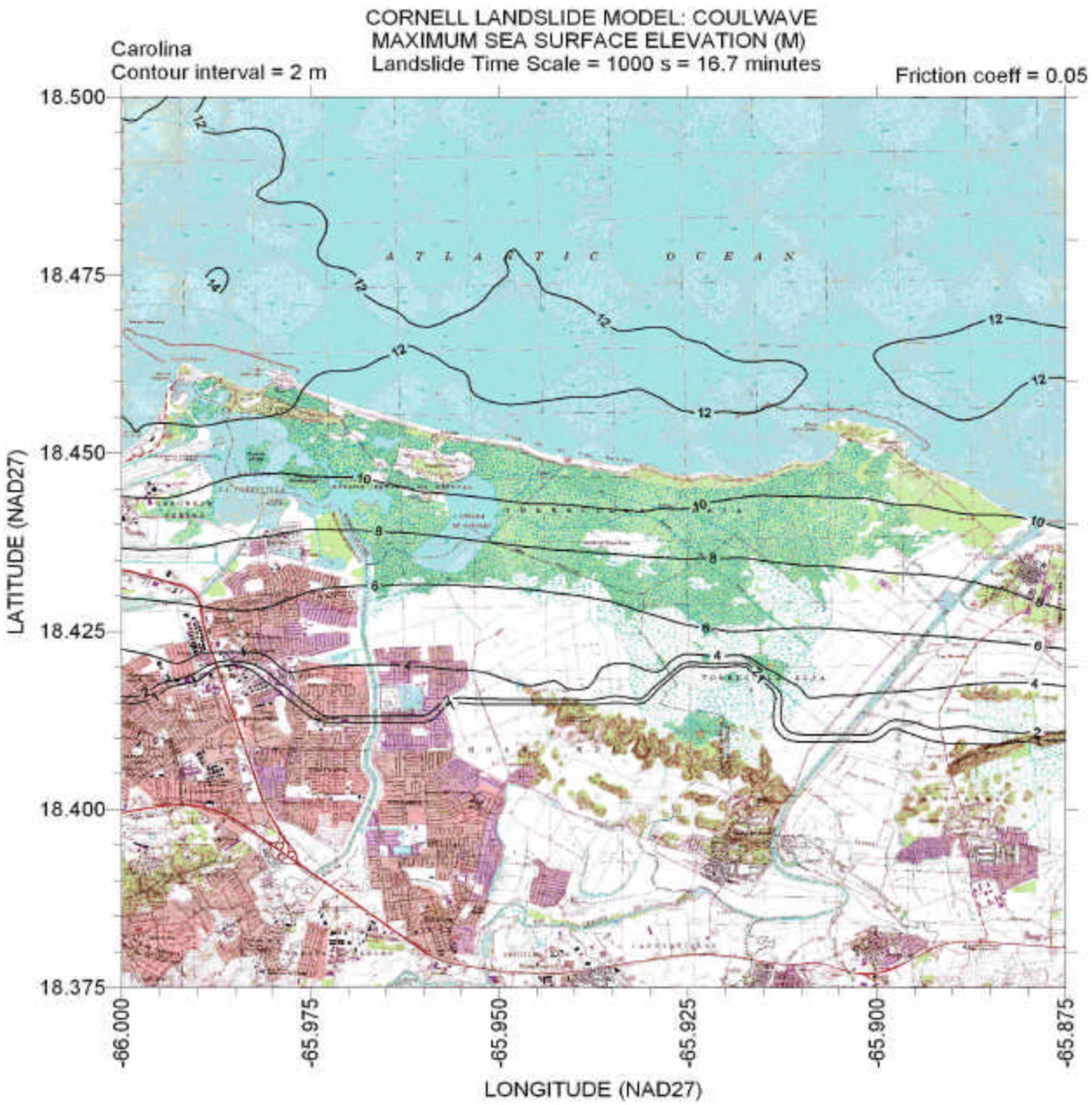


Figure 94– Contours of maximum sea surface elevation for time scale = 1000 s for Carolina quadrangle. Friction factor $f$ = 0.05.

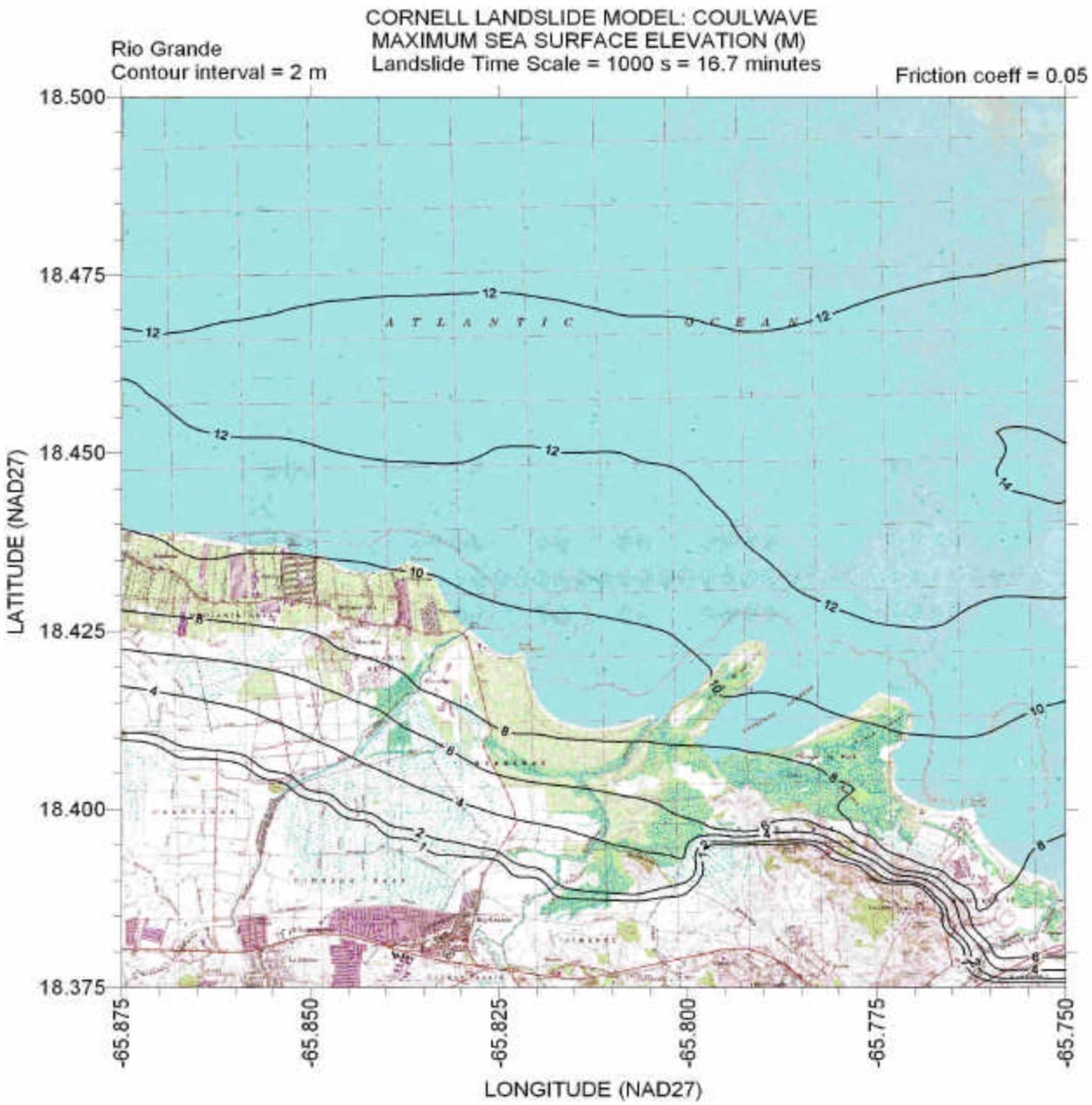


Figure 95– Contours of maximum sea surface elevation for time scale = 1000 s for Rio Grande quadrangle. Friction factor $f$ = 0.05.

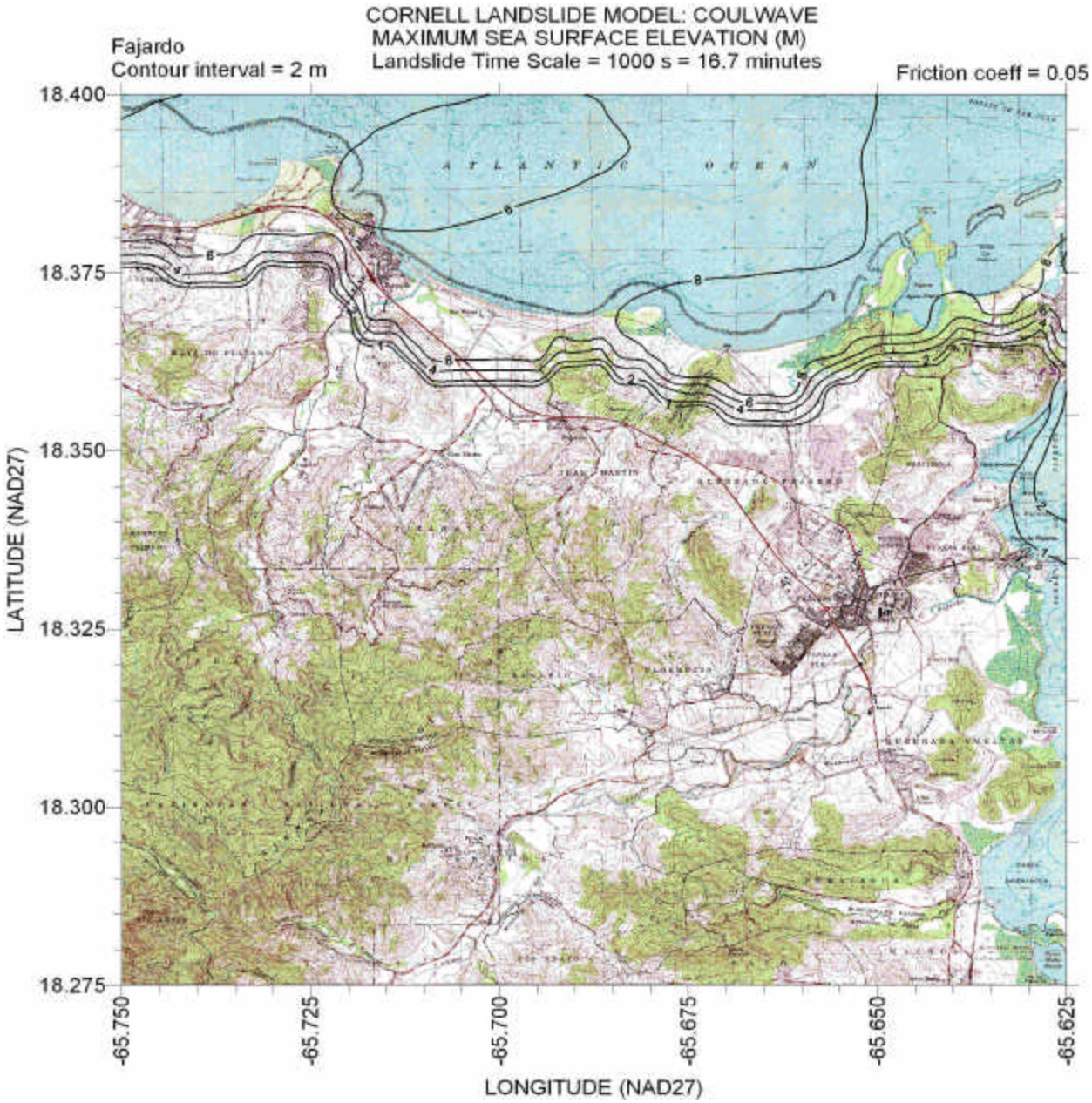


Figure 96– Contours of maximum sea surface elevation for time scale = 1000 s for Fajardo quadrangle. Friction factor $f$ = 0.05.

mismatch cannot be blamed on topographic modifications in the last 40 years, but instead are simply errors in the DEM. But at this moment there is no other source of topographic data for Puerto Rico.

## CONCLUSION

Though the lack of knowledge about the slump time scale is a limiting factor in assessing the credibility of the scenarios we have run, the fact is that model results show that even for slide time scales of 1 to 2 hours the expected coastal flooding along all of the north coast of Puerto Rico is extensive. Recent USGS surveys have documented "cracks' or scarps on the northern insular margin off northern Puerto Rico which have been described as a potential tsunamigenic hazard in Schwab et al (1991, 1993). According to USGS scientists in Woods Hole, MA, the potential tsunami hazard along the northern coast of Puerto Rico is REAL... not hypothetical, as is the case with the recent finding of echelon cracks found off the mid-Atlantic USA shelf region (Driscoll et al., 2000).

According to Schwab (personal communication, 2002), “basically, the "bad" situation in Puerto Rico is set up due to the tectonically controlled rapid tilting of the strata along northern Puerto Rico (there is Pliocene shallow-water limestone at the sea floor in >4,000 m of water....that's a serious elevator ride DOWN!!!). This tilting to the north creates instability of the northern submarine margin. This is not a good situation in an area of high seismicity, in that, in Puerto Rico you have both static (tectonic tilting) and dynamic (earthquake acceleration) triggering mechanisms operating in an area where a bunch of US Citizens live along the coast. By the way, a few of the cracks on the insular margin are only ~20 km seaward of San Juan, one of the largest population centers in the Caribbean!!!!”

In this study an attempt has been made to quantify the order of magnitude of what can be expected based on slide time scales starting from relatively fast slides all the way to relatively slow slides. The results show that the repetition of another such event would be catastrophic for Puerto Rico. But even more important, it shows that even smaller-scale events could be catastrophic. With the quantification of what is at stake like it has been done here, it is imperative that both scientists and emergency management personnel, both at state and federal levels, work towards the goal of making our political leaders comprehend what is at risk such that funding is made available towards monitoring what is going on along the Puerto Rico Trench. Because at present there is no monitoring at all. If we don’t do this, it would be an irresponsible act on our part.

## ACKNOWLEDGMENTS

Aurelio Mercado would like to acknowledge the support of Mr. Mariano Vargas, Director of the Hazard Mitigation Office of the Puerto Rico State Emergency Management Agency, and of the Sea Grant Program of the University of Puerto Rico. It is also desired to acknowledge the hard work of Mr. Patrick Lynett , and his fast response time when asked for additional data. The help of Mr. Harry Justiniano, Department of Marine Sciences, is also recognized.

REFERENCES

Bea, R. G., Wright, S. G., Sicar, P., and Niedoroda, A. W., 1983. Wave-induced slides in South Pass Block 70, Mississippi delta. *J. Geotech. Eng*., v. 109, pp. 619-644.

Bondevik, S., Svendsen, J. I., Johnsen, G., Mangerud, J., and Kaland, P. E., 1997b. The Storegga tsunami along the Norwegian coast, its age and run-up. Boreas, v.26, pp. 29-53.

Bondevik, S., Svendsen, J. I., and Mangerud, J., 1997b. Tsunami sedimentary facies deposited by the Storegga tsunami in shallow marine basins and coastal lakes, western Norway. Sedimentology, v.44, pp. 1115-1131.

Brundsen, D., and Prior, D. B., 1984. Slope Instability. Wiley-Interscience Publication, N.Y.

Bryant, E., 2001. Tsunami, the Underrated Hazard. Cambridge University Press.

Carlson, P. R., 1978. Holocene slump on continental shelf off Malaspina Glacier, Gulf of Alaska. *Amer. Assoc. Petro. Geol. Bull*., v.62, pp. 2412-2426.

Carracedo, J. C., Day, S., Guillou, H., Rodrigues-Badiola, E., Canas, J. A., and Perez Torrado, F. J., 1998. Hotspot volcanism close to a passive continental margin: The Canary Islands, *Geological Magazine*, v. 135, pp. 591-604.

Chernicoff, S., and Venkatakrishnan, R., 1995. Geology. Worth Publishers, N.Y.

Crandell, D. R., Miller, C. D., Christiansen, R. L., Glicken, H. X., and Newhall, C. G., 1984. Catastrophic debris avalanche from an ancestral Mount Shasta volcanoe, California. In Geology of the Upper Cretaceous Hornbrook Formation, Oregona and California, edited by T. H. Nilsen, pp. 197-201, Soc. of Econ. Paleontol. And Mineral., Tulsa, Okla.

Dawson, A. G., Long, D., and Smith, D. E., 1988. The Storegga Slides: evidence from eastern Scotland for a possible tsunami. *Marine Geology*, v.82, pp. 271-276.

Dawson, A. G., 1994. Geomorphological effects of tsunami runup and backwash. *Geomorphology*, v.10, pp. 83-94.

Driscoll, N. W., Weissel, J. K., and Goff, J. A., 2000. Potential for large-scale submarine slope failure and tsunami generation along the U.S. mid-Atlantic coast. *Geology*, v.28, pp. 407-410.

Elverhoi, A., Harbitz, C. B., Dimakis, P., Mohrig, D., Marr, J., and Parker, G., 2000. On the dynamics of subaqueous debris flows. *Oceanography*. v.13, pp. 109-117.

Filed, M. E., Gardner, J. V., Jennings, A. E., and Edwards, B. D., 1982. Earthquake-induced sediment failures on a 0.25° slope, Klamath River delta, California. *Geology*, v.10, pp. 542-546.

Goldfinger, C., Kulm, L. V. D., McNeill, L. C. and Watts, P., 2000. Super-scale failure of the

southern Oregon Cascadia Margin. Pure and Applied Geophys., v.157, pp. 1189-1226.

Grindlay, N. P.. Mann, J. Dolan, 1997. Researchers Investigate Submarine Faults North of Puerto Rico, *EOS, Trans. AGU*, Vol 78, p. 404

Grindlay, N., 1998. Volume and Density Approximations of Material Involved in a Debris Avalanche on the South Slope of the Puerto Rico Trench. Sea Grant College Program, University of Puerto Rico

Hampton, M. A., Lee, H. J., and Locat, J., 1996. Submarine slides. *Rev. Geophys*., v.34, pp. 33-59.

Hansom, J. D., and Briggs, D. J., 1991. Sea-level change in Vestfirdir, northwest Iceland, environmental change in Iceland: Past, present and future. Glacial Quaternary Geology, V.7, pp. 79-91.

Harbitz, C. B., 1992. Model simulations of tsunami generated by the Storegga Slides. *Marine Geology*, v. 105, pp. 21.

Henkel, D. J., 1970. The role of waves in causing submarine landslides. Geotechnique, v.20, pp. 75-80.

Henry, R. E., and Murty, T. S., 1992. Model studies of the effects of the Storegga slide tsunami. *Science of Tsunami Hazards*, v.10, pp. 51-62.

Kulikov, E. A., Rabinovich, A. B., Thomson, R. E., and Bornhold, B. D., 1996. The landslide tsunami of November 3, 1994, Skagway Harbor, Alaska. *J. Geophys. Res*., v. 101, No. C3, pp. 6609-6615.

Lipman, P. W., Normark, W. R., Moore, J. G., Wilson, J. B., and Gutmacher, C. E., 1988. The giant submarine Alika Debris Slide, Mauna Loa, Hawaii. *J. of Geophysical Res*., v. 93, pp. 4279-4299.

Long, D., Smith, D. E., and Dawson, A. G., 1989. A Holocene tsunami deposit in eastern Scotland. J. of Quaternary Science, v.4, pp. 61-66.

Masson, D. G., 1996. Catastrophic collapse of the volcanic island of Hierro 15 ka ago and the history of landslides in the Canary Islands. *Geology*, v. 24, pp. 231-234.

Mercado, A., 1994. Digitization of National Ocean Survey Hydrographic "Smooth" Sheets for Puerto Rico and the U.S. Virgin Islands. Submitted to Sea Grant College Program, University of Puerto Rico. 116 p.

Moore, G. W., and Moore, J. G., 1988. Large-scale bedforms in boulder gravel produced by giant waves in Hawaii. *Geological Soc. of America Special Paper* No. 229, pp. 101-110.

Moore, J. G., Bryan, W. B., and Ludwig, K. R., 1994a. Chaotic deposition by a giant wave, Molokai, Hawaii. *Geological Soc. of America Bulletin*, v. 106, pp. 962-967.

Moore, J. G., Clague, D. A., Holcomb, R. T., Lipman, P. W., Normark, W. R., and Torresan, M. E., 1989. Prodigious submarine landslides on the Hawaiian Ridge. J. Geophys. Res., v. 94, pp. 17465-17484.

Moore, J. G., Normark, W. R., and Holcomb, R. T., 1994b. Giant Hawaiian landslides. *Annual Rev of Earth and Planetary Sciences*, v. 22, pp. 119-144.

Prior, D. B., and Coleman, J. M., Disintegrative retrogressive landslides on very-low-angle subaqueus slopes, Mississippi delta. *Mar. Geotechnol*., v.3, pp. 37-60.

Scanlon, K., D. Masson and R. Rodriguez, GLORIA sidescan-sonar survey of the EEZ of Puerto Rico and US Virgin Islands, Trans. Caribb. Conf., 11th, Barbados, 32:1-32:9, 1988

Schwab, W. C., W. W. Danforth, K. Scanlon, and D. Masson, 1991. A Giant Submarine Slope Failure on the Northern Insular Slope of Puerto Rico, *Marine Geology*, Vol. 96, 237-246

Schwab, W.C., Danforth, W.W., and Scanlon, K.M., 1993, Tectonic and stratigraphic control on submarine slope failure on a lithospheric plate boundary: Puerto Rico insular slope, in Schwab, W.C., Lee, H.J., and Twichell, D.C., eds., Submarine Landslides: Selected Studies in the U.S. Exclusive Economic Zone: U.S. Geological Survey Bulletin 2002, p. 60-68.

Smith, D. L., 2000. Of landslides, couch potatoes, and pocket tsunamis. *Engineering and Science*, No. 1, pp. 27-30.

Varnes, D. J., 1978. Slope movement types and processes, in *Landslides – Analysis and Control*, edited by R. L. Schuster and R. J. Krizek, Spec. Rep. 176, pp. 12-33. Transp. Res. Board, Natl. Res. Council, Washington, D. C.

Ward, S. N., 2000. Landslide tsunami. Submitted to *J. Geophys. Res*.

# APPENDIX 1

## PAPER BY

Schwab, W.C., W.W. Danforth, K. Scanlon, and D. Masson

A giant submarine slope failure on the northern insular slope of Puerto Rico, Marine Geology, 96, 237-246, 1991.

*Marine Geology*, 96 (1991) 237–246
Elsevier Science Publishers B.V., Amsterdam



# A giant submarine slope failure on the northern insular slope of Puerto Rico

W.C. Schwab[a], W.W. Danforth[a], K.M. Scanlon[a] and D.G. Masson[b]
[a]*U.S. Geological Survey, Quissett Campus, Woods Hole, MA 02543, U.S.A.*
[b]*Institute of Oceanographic Sciences, Wormley, Surrey GU8 5UB, U.K.*

(Received January 22, 1990; revision accepted June 28, 1990)

ABSTRACT

Schwab, W.C., Danforth, W.W., Scanlon, K.M. and Masson, D.G., 1991. A giant submarine slope failure on the northern insular slope of Puerto Rico. Mar. Geol., 96: 237–246.

A large amphitheater-shaped scarp, approximately 55 km across, was imaged on the northern insular slope of Puerto Rico using long-range sidescan sonar and bathymetric data. This scarp results from the removal of more than 1500 km$^3$ of Tertiary strata. A review of seismic-reflection profiles, stratigraphic data, and subsidence models of the northern insular margin of Puerto Rico were used to infer that large-scale slope failure was induced by the tectonic oversteepening of the insular slope and was responsible for the formation of the scarp. The oversteepening probably was caused by the most recent episode of convergence of the Caribbean and North American plates, which began between approximately 4 and 2.5 m.y. ago. The Tertiary strata have been tilted approximately 4.5° to the north in the last 4 m.y.

## Introduction

During a 30 day cruise aboard the R.V. *Farnella* in November and December 1985, GLORIA (Geologic Long-Range Inclined Asdic) sidescan-sonar coverage was obtained over the EEZ of Puerto Rico and the U.S. Virgin Islands in water depths greater than 500 m (EEZ-SCAN '85 Scientific Staff, 1987). One of the more spectacular features revealed by the GLORIA imagery was a large amphitheater-shaped scarp on the northern insular slope of Puerto Rico (Figs.1 and 2) representing the removal of approximately 1500 km$^3$ of strata (Scanlon et al., 1988). A review of regional onshore and offshore stratigraphy, subsidence models, offshore dredging surveys, and Caribbean tectonic-framework models all indicate that the scarp formed as a result of slope failure and subsequent mass movement. This study documents the slope failure, evaluates the factors that may have led to failure, and considers the significance to the relative stability of the northern insular slope of Puerto Rico.

## Geologic setting

The study area is located on the northern insular slope of Puerto Rico (Fig.1). Puerto Rico lies within the plate boundary zone between the North American and Caribbean plates, an area of high seismicity (Sykes et al., 1982; Mann and Burke, 1984). Basement rocks of Puerto Rico are folded and faulted metamorphic, sedimentary, and volcanic rocks of Late Jurassic to Eocene age intruded by plutons of intermediate composition and of Late Cretaceous to late Eocene age. Flanking the basement rocks on the north and south are parallel-bedded, seaward dipping, relatively undeformed strata of middle Eocene to Pliocene age. Tertiary strata on the north flank of the island lie in the Arecibo basin (Meyerhoff et al., 1983), a 300 km long 55 km wide structure (Fig.1). The southern flank of the Arecibo basin is subaerially exposed and ranges in age from middle Oligocene to early Pliocene and in thickness from a few hundred meters to more than 1800 m (Briggs and Gordon, 1961). The northern flank of the Arecibo basin is

0025-3227/91/$03.50 

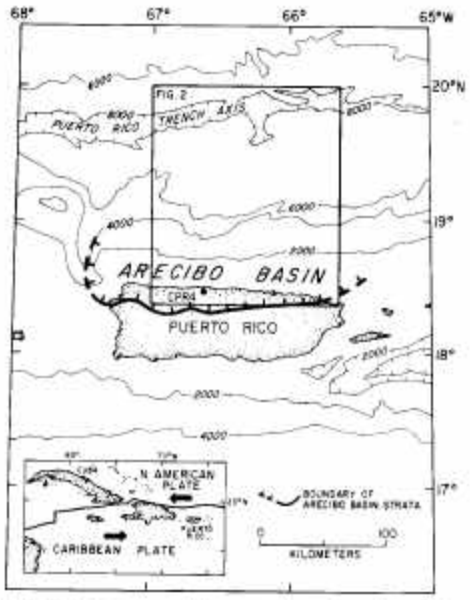


Fig.1. Location map and the general tectonic setting of the study area. The boundary of the Arecibo basin and location of exploratory well CPR4 is from Meyerhoff et al. (1983). Bathymetry is in meters and is from EEZ-SCAN '85 Scientific Staff (1987). Arrows in the inset indicate relative motion of the North American and Caribbean plates (from Klitgord et al., 1986).

exposed along the northern insular slope of Puerto Rico in water depths ranging from 3200 to 6000 m (see Meyerhoff et al., 1983). A more complete and thicker Tertiary section is present offshore (from middle Eocene to early Pliocene; Meyerhoff et al., 1983), the maximum offshore thickness being about 4000 m.

Seismic-reflection profiles (unpublished) collected over the northern insular slope of Puerto Rico show that the offshore stratigraphy can be divided into three units (Fig.3; Meyerhoff et al., 1983). The lowest unit, unit 1, consists of basement rocks which, based on subaerial exposures and samples dredged offshore (Fox and Heezen, 1975; Perfit et al., 1980), are of Late Jurassic to middle Eocene age (Meyerhoff et al., 1983). The upper surface of unit 1 is offset by several large normal faults. The middle unit, unit 2, forms the lower part of the Arecibo basin strata. The ages and compositions of unit 2 rocks are poorly constrained by samples dredged offshore, but Meyerhoff et al. (1983) have inferred them to be shallow-water limestones of late middle Eocene to middle Oligocene age. The uppermost part of the Arecibo basin strata, unit 2, outcrops in northern Puerto Rico (Monroe, 1976) and was penetrated by exploratory well CPR4 (Fig.1; Briggs, 1961). Unit 3 rocks consist of middle Oligocene to early Pliocene age reef and shallow-water limestone (Briggs and Gordon, 1961; Monroe, 1980; Meyerhoff et al., 1983). Similar rocks have been dredged from the insular slope down to water depths of approximately 6800 m (Fox and Heezen, 1975; Perfit et al., 1980).

During late middle Eocene to middle Oligocene, the northern part of Puerto Rico subsided because of crustal thinning and sediment loading (Birch, 1986) and unit 2 was deposited. By this time, southward subduction of the North American plate under the island had stopped (Mattson, 1984; Duncan and Hargraves, 1984; Burke et al., 1984), resulting in an oblique strike-slip plate boundary (Sykes et al., 1982; Mattson, 1984) or a strike-slip boundary (Duncan and Hargraves, 1984).

Unit 3 was deposited along a strike-slip plate boundary from middle Oligocene to early Pliocene time (Sykes et al., 1982; Burke et al., 1984; Duncan and Hargraves, 1984; Mattson, 1984). Meyerhoff et al. (1983), using unpublished seismic-reflection data, reported that the uppermost part of the Arecibo basin strata, unit 3, is characterized by continuous parallel reflectors, by constant thickness, and by constant dip that persists throughout much of the basin offshore. Also, little structure is present in the offshore unit 3 strata with the exception of drape structures and a few faults which cut the section. Meyerhoff et al. (1983) suggest that this stratigraphic setting is a representation of the tectonic stability of the region from late Oligocene to early Pliocene time.

Sykes et al. (1982) suggested that slight convergence between the Caribbean and North American plates in Pliocene time caused renewed subduction. Subduction-induced tectonic erosion may have thinned the island-arc crust from underneath, causing the northern insular margin of Puerto Rico to tilt rapidly to the north (Birch,

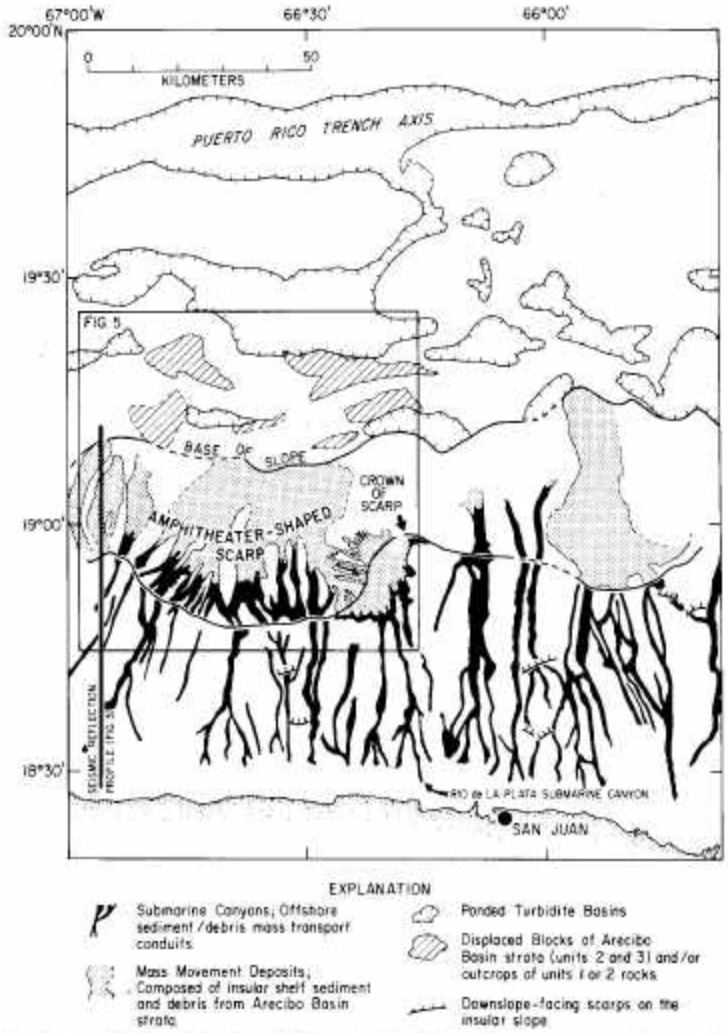


Fig.2. Interpretive sketch (modified from Scanlon and Masson, 1989) of the GLORIA imagery of the northern insular margin of Puerto Rico (EEZ-SCAN '85 Scientific Staff, 1987). The location of this interpretive sketch is shown on Fig.1. The location of the seismic-reflection profile is from Meyerhoff et al. (1983).

1986). As a result, the southern part of unit 3 has been uplifted a few hundred meters within the past 4 m.y., whereas the northern part has subsided more than 4000 m, thus generating a 4.5° regional slope on the Arecibo basin strata (Birch, 1986). The insular slope of Puerto Rico to a water depth of approximately 3000 m is essentially the upper surface of unit 3. This subduction-induced tectonic erosion has been suggested to mark the formation of the present Puerto Rico Trench (Alonso-Harris et al., 1983) and may be related to a reorganization of spreading direction and rate along the entire mid-Atlantic sea-floor-spreading system at approximately 2.5 m.y. (Klitgord and Schouten, 1986).

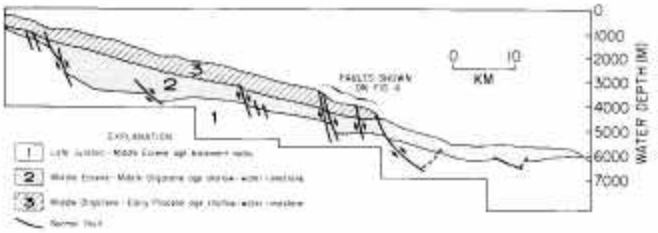


Fig.3. Interpretation of a seismic-reflection profile showing stratigraphic units 1, 2 and 3 (from Meyerhoff et al., 1983). See Fig.2 for location.

## Methods

GLORIA is a shallow-towed (water depth 50 m) long-range sidescan-sonar system designed for deep-ocean reconnaissance mapping. A total swath width of 35 km was achieved in the deepest areas of the Caribbean survey (EEZ SCAN '85 Scientific Staff, 1987). For a detailed description of the GLORIA system, see Somers et al. (1978). Navigation for the Caribbean GLORIA survey was provided by transit satellites and the Global Positioning System (GPS). Bathymetric data were subsequently collected in April 1988 over the amphitheater-shaped scarp using a 12 kHz acoustic profiler aboard the R.V. *Starella*. Navigational control for the bathymetric survey was based on STARFIX, a satellite system similar to GPS.

GLORIA acoustic backscattering intensity data are recorded in digital format with each pixel in the data set representing a rectangular area of the sea floor that is directly dependent on the sonar beam geometry, the speed of the towfish over the sea floor, and the trigger interval of the sonar pulse. Distortions inherent in raw backscatter data due to the sonar beam geometry and other variables, such as towfish altitude and ship speed, were corrected by post-cruise digital processing using the U.S. Geological Survey Mini-Processing System (MIPS) (Chavez, 1986) resulting in imagery that is geometrically and radiometrically correct.

A sidescan-sonar image is an approximate model of the interaction of sound with the sea floor that uses a two-dimensional display of pixels, each with an associated backscattering intensity. The level of acoustic backscattering is a function of, among other things (Reed and Hussong, 1989 and references therein), the sea-floor topography, roughness, and composition. Sonograph interpretation is therefore greatly improved if accurate bathymetric data are available, so that the topographic element can be eliminated. In this study, bathymetry data (Fig.4) were digitized from 12 kHz echosounder profiles collected in the area of the amphitheater scarp and merged with the GLORIA imagery (Fig.5) in order to aid in the sonograph interpretation. The digitized 12 kHz data were subdivided into geographic coordinates with corresponding water depths. The bathymetric data were then gridded in an Albers Equal Area map projection at a scale equal to that of the GLORIA image of the amphitheater-shaped scarp. Bathymetric data were mapped by gradually enlarging the pixels representing each bathymetric value by way of a filtering process until a smooth raster image of the sea-floor topography was produced. The topographic image was then digitally merged with the GLORIA image and projected into three dimensional space (Fig.6).

## Description of the study area

The insular slope above the amphitheater-shaped scarp (water depth < 3000 m) has a regional slope of approximately 4.5° (Fig.4). This section of the slope is cut by a number of nearly straight, downslope trending canyons from 1 to 3 km wide and up to 400 m deep. These submarine canyons are areas of high acoustic backscattering intensity on the GLORIA imagery (Figs.5 and 6), probably representative of outcropping Tertiary

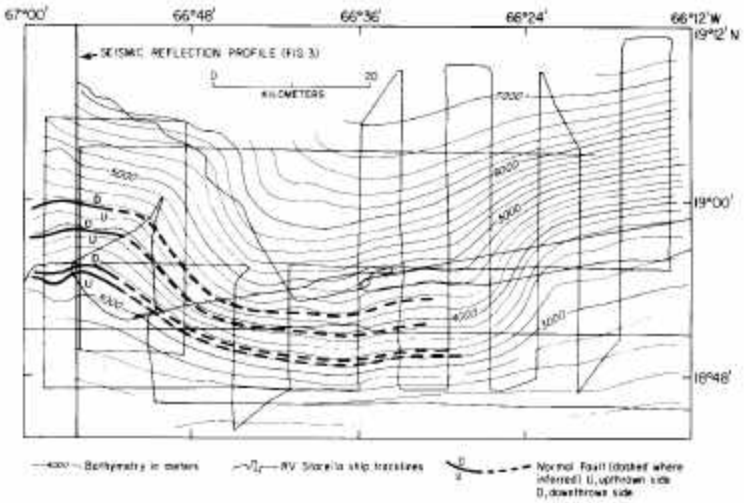


Fig.4. Bathymetry of the amphitheater-shaped scarp from the R.V. *Starella* 12 kHz acoustic-profiler survey. The location of the seismic-reflection line is from Meyerhoff et al. (1983) and its interpretation is shown in Fig.3.

limestone and/or carbonate mass movement deposits (Gardner et al., 1980). These canyons are thought to act as offshore transport conduits for shelf sediments probably in the form of turbidity currents (Schneiderman et al., 1976; Grove et al., 1982). For example, the Rio de La Plata submarine canyon (Fig.2) cuts well onto the shelf off the mouth of the La Plata River, which drains about 537 km$^2$ of the island's interior. The Rio de La Plata canyon terminates downslope in an area of high backscatter on the insular slope immediately east of the amphitheater-shaped scarp (Figs.2 and 5). This area of high backscatter is interpreted to represent mass movement deposits composed of a mixture of terrigenous sediment from the La Plata River, calcareous sediments from the insular shelf, and carbonate material from the canyon itself. These mass movement deposits can be seen on the GLORIA imagery to have spilled over the eastern crown of the amphitheater-shaped scarp down to its base (Fig.6).

The amphitheater-shaped scarp is approximately 55 km across, has it crown in a water depth of about 3000 m (Fig.4), and extends to a water depth of about 6700 m (described on Fig.2 as "base of slope"). The average declivity of the amphitheater-shaped scarp is 8.5°. A system of submarine canyons or talus chutes, recognized as linear areas of high backscatter on the GLORIA imagery (Figs.2, 5, and 6) with little bathymetric expression (Fig.4), has developed on the scarp. Most of these headwall canyons appear to have little relation to the submarine canyons that stripe the insular slope above the crown of the amphitheater-shaped scarp and thus can be viewed as related to the mass wasting developed on the scarp itself.

Subaerial mapping and marine seismic-reflection data show that unit 3 strata, both onshore and offshore, have approximately the same dip (3.5° to 5°) and are, in general, little disturbed by faults (Meyerhoff et al., 1983). Unit 3 is stratigraphically continuous to a water depth of 3300 m, where the section is downfaulted and exposed to a water depth of about 4300 m (Fig.3). These faults are interpreted by Meyerhoff et al. (1983) to be growth faults that were active at least as long ago as the time of deposition of unit 2 (middle Eocene to middle Oligocene). Reactivation of this fault zone due to tectonic stress has caused them to cut early Pliocene-age (Unit 3) strata (Meyerhoff et al., 1983). Extrapolation of this fault zone eastward from the seismic-reflection profile (Fig.3) to the amphitheater (Fig.4) shows that most, if not all, of the parallel-bedded seaward dipping Tertiary


Fig.5. GLORIA imagery of the amphitheater-shaped scarp (EEZ-SCAN '85 Scientific Staff, 1987). The location of this imagery with further interpretation is shown on Fig.2 with north toward the top of the figure.

section has been removed from the amphitheater downslope from the projected line of the fault zone and suggests a causal relation with the amphitheater-shaped scarp.

The sea floor below the amphitheater-shaped scarp, between the base of slope (water depth 6700 m) and the Puerto Rico Trench (water depth 8000 m), exhibits several hundred meters of local relief while displaying a regional slope of only 1.7°. The GLORIA imagery of this 50 km wide area of sea floor displays areas of high and low acoustic backscattering intensity (Fig.5). The areas of low backscatter have been interpreted from high-resolution seismic-reflection profiles and cores to be ponded turbidite basins (Fig.2; Scanlon et al., 1988) and provide a less reflective material. Areas of high backscatter on the GLORIA imagery from the area of sea floor near the base of the slope have been identified based on dredged samples as Cretaceous basement (unit 1) and Tertiary (unit 2) outcrops and displaced carbonate debris (units 2 and 3) from upslope (Scanlon and Masson, 1989), thus substantiating an inference that strata from the insular slope have moved downslope.

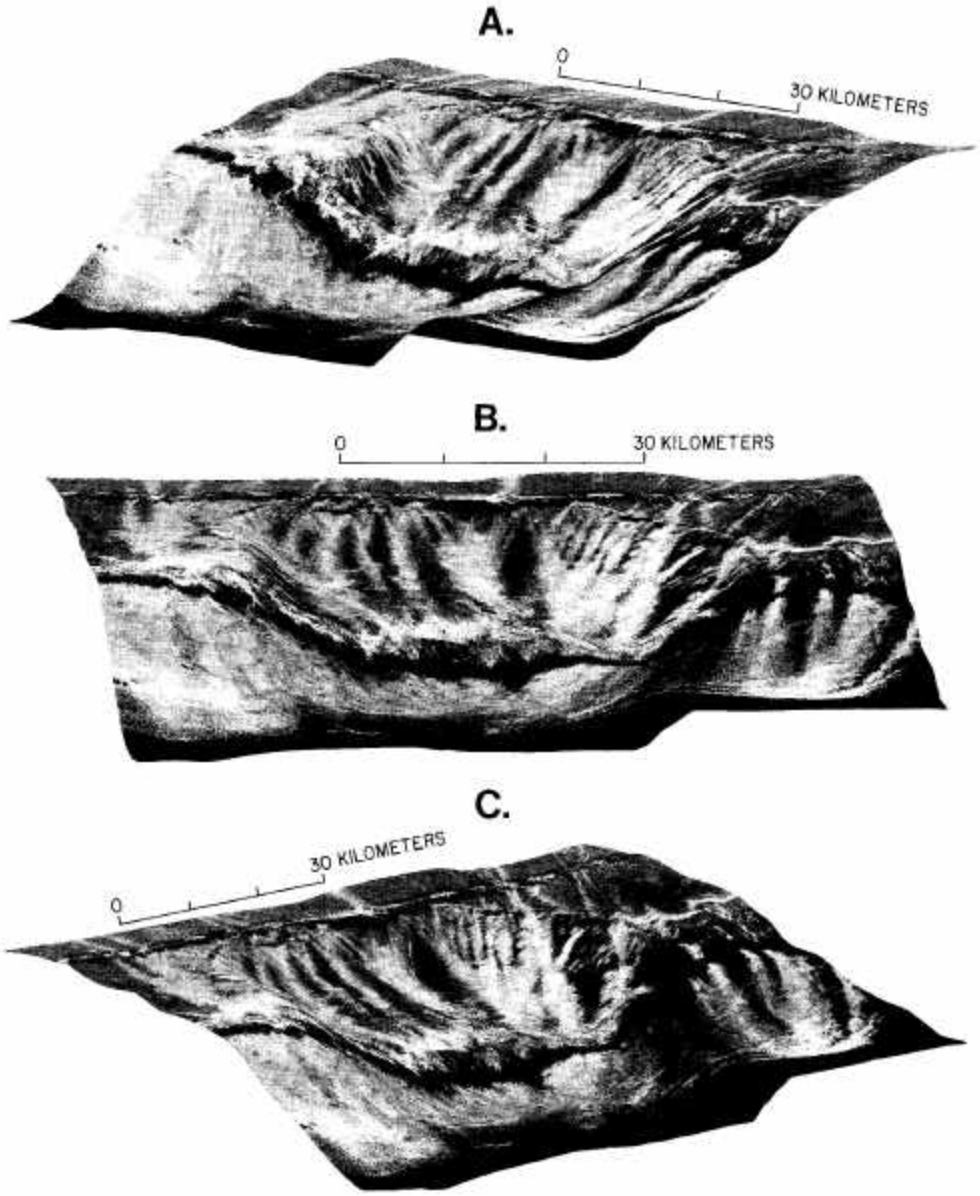


Fig.6. Three-dimensional sonograph perspective views of the amphitheater-shaped scarp. (A) Viewed from the northwest. (B) Viewed from the north. (C) Viewed from the northeast. See Figs.2 and 5 for interpretation.

## Discussion

It is unlikely that slope failure of the Arecibo basin strata is the sole process responsible for the present morphology of the amphitheater-shaped scarp. Other processes, such as the effects of dissolution of carbonate strata below the calcite compensation depth, erosion by abyssal currents or turbidity currents, and bioerosion are also known to be active on lower continental margins. However, it is reasonable to suggest that slope failure was the principal causative factor because of: (1) the tectonic setting of the study area, a plate boundary and region of high seismicity; (2) the general morphology of the scarp, a distinct embayment having a radius of a circle fitting the failure surface (Hansen, 1984); (3) the presence of shallow-water carbonate debris (similar to the rock of units 2 and 3) downslope and near the base of the slope (Fox and Heezen, 1975; Perfit et al., 1980); and (4) the analysis of seismic-reflection data (Meyerhoff et al., 1983) that show truncation of sedimentary strata (unit 3) by faults.

Recently described as a new type of carbonate bank margin (Mullins and Hine, 1989), "scalloped bank margins that are distinctly embayed" (margins containing amphitheater-shaped scarps) also have been identified and verified as the consequence of slope failure in various subaerial and submarine settings (e.g., Brunsden, 1979; Lee, 1989 and references therein). For example, a scalloped margin along the west Florida carbonate platform has been shown, using seismic-reflection profiles, to be the result of a catastrophic slope failure of Miocene age which formed an embayment approximately 100 km long and 30 km wide that represents the removal of about 300 m of stratigraphic section (Mullins et al., 1986). Although the amphitheater-shaped scarp north of Puerto Rico represents the removal of about 1500 $km^3$ of strata, submarine slope failures of this scale may not be particularly unusual. Recent surveys using modern remote sensing instruments show that some of the world's largest slope failures have occurred on submarine slopes (Lee, 1989). These include slides on the steep submerged volcanic slopes of the Hawaiian Islands (Moore et al., 1989), the continental slope of Norway (Bugge et al., 1987) and along the middle and lower slopes of convergent margins (Lewis et al., 1988; Von Huene et al., 1989).

We do not know if the slope failure that resulted in the amphitheater-shaped scarp off Puerto Rico was catastrophic (the entire mass disintegrating rapidly) or took place over a substantial period of time (block by block). In general, slope failure occurs when resistance to deformation offered by the strata (shearing strength) is overcome by the environmental stresses acting downslope. The two principal downslope stresses applicable to the study area result from gravity and earthquake-induced accelerations (Lee, 1989). An important property of strata is that the shearing strength decreases as excess pore-water pressure (i.e., in excess of hydrostatic) increase (Morgenstern, 1967; Sangrey, 1977; Seed, 1979; Lee, 1985). Excess pore-water pressure can be caused by repeated loading from earthquakes (Lee, 1985). The declivity of the insular slope and therefore the downslope gravitational shear stress has been steadily increased due to the northward tilting (tectonic oversteepening) of the Arecibo basin strata since Pliocene time. Furthermore, the strength of the strata was probably significantly reduced by pre-existing faults (Fig.3) that are seen to lead into the headwall of the amphitheater-shaped scarp (Fig.4). The increase in the downslope gravitational shear stress, when coupled with earthquake accelerations and possible strength reduction during major earthquakes, can be expected to exceed the shear strength of the carbonate strata, particularly along the fault-induced pre-existing zones of weakness. The result would be slope failure; such that the northern section of the Arecibo basin strata would have broken off, disintegrated, and slid into the area between the base of slope and the Puerto Rico Trench. Subsequent mass wasting of the exposed failure plane resulted in the formation of the headwall canyons (Fig.5), and turbidite deposits, originating from the headwall of the amphitheater-shaped scarp, the upper insular slope, and insular shelf, partially buried the foot and toe of the failed mass.

Further east along the insular slope near longitude 66°W (Fig.2), a smaller area of high backscattering intensity on the GLORIA imagery has

also been interpreted to be an amphitheater-shaped scarp (Scanlon et al., 1988), suggesting that the entire northern margin of the Arecibo basin is failing due to the present tectonic regime. However, the bathymetric data over this area are poor, making definitive interpretation of the GLORIA sonographs difficult.

## Implications and conclusions

It appears that the slope failure of the northern margin of the Arecibo basin strata results from oversteepening and high seismicity, characteristic of this tectonic setting. It is of note that this oversteepening has occurred within the last 4 m.y. (minimum age of the unit 3 strata) and is probably representative of the present tectonic regime which has existed for approximately 2.5 m.y. (Klitgord and Schouten, 1986). Thus, the slope failure(s) which formed the amphitheater-shaped scarp probably have occurred within the last 2.5 m.y. As this oversteepening continues, the relative stability of the insular slope decreases. In addition to the amphitheater-shaped scarp and its smaller counterpart to the east (Fig.2), several smaller downslope-facing scarps have been identified on the insular slope of Puerto Rico in water depths less than 3000 m (Fig.2; Scanlon et al., 1988). These smaller scarps may represent incipient slope failures, and they may indicate that the slope failure represented by the amphitheater-shaped scarp is retrogressive upslope and will continue to be active.

Knowledge of slope failure and mass movement along the boundary of convergent plates has significance for the understanding of tsunami generation. Although tsunami are commonly caused by large earthquakes [e.g., the 1964 Alaska earthquake (Plafker et al., 1969; Von Huene and Cox, 1972) and the 1960 Chilean earthquake (Kajiura, 1979)], they also can be generated by other mechanisms, including submarine slope failure (McCulloch, 1985; Von Huene et al., 1989). If the amphitheater-shaped scarp was the result of a catastrophic slope failure, it was of sufficient size to have generated a large tsunami that must have had major impact on the nearby (35 km) northern coastal areas of prehistoric Puerto Rico (e.g., von Huene et al., 1989 and references therein). Because the condition of slope instability that allowed an extremely large landslide continues to develop north of Puerto Rico (assuming the mass slid in a single event), and because the seismic risk remains the same as that when the slide took place, a repetition of the event is quite possible, with potential for generation of a catastrophic tsunami.

## Acknowledgments

We thank the captain and the crews of the R.V. *Farnella* and R.V. *Starella* for their excellent cooperation at sea and members of the Deep Submergence Laboratory, Woods Hole Oceanographic Institution for their operational support. Discussions and critical reviews of the manuscript by Kim Klitgord, William Dillon, Elizabeth Winget, D.J. Stanley, and an anonymous reviewer were extremely helpful. All illustrations and photography were provided by Sarah Griscom, Dann Blackwood, and Jeff Zwinakis. Any use of trade names is for descriptive purposes only and does not imply endorsement by the U.S. Geological Survey.

## References

Alonso-Harris, R., Krieg, E.A. and Meyerhoff, A.A., 1983. Post-early Pliocene age of the Puerto Rico trench. Caribb. Geol. Conf., 10th (Catagena de Indias, Colombia), pp.17–18 (Abstr.).

Birch, F.S., 1986. Isostatic, thermal, and flexural models of the subsidence of the north Coast of Puerto Rico. Geology, 14: 427–429.

Briggs, R.P., 1961. Geology of Kewannee Interamerican Oil Company test well number 4CPR, northern Puerto Rico. In: R.P. Briggs and W.A. Gordon, Oil and Gas Possibilities of Northern Puerto Rico: Puerto Rico Min. Comm, San Juan, p.23.

Briggs, R.P., and Gordon, W.A., 1961. Oil and gas possibilities of northern Puerto Rico. Puerto Rico Min. Comm., San Juan, 40 pp.

Brunsden, D., 1979. Mass movements. In: C.E. Embelton and J.B. Thornes (Editors), Progress in Geomorphology. Arnold, New York, pp.130–186.

Bugge, T., Befring, S., Belderson, R.H., Eidvin, T., Jansen, E., Kenyon, N.H., Holtedahl, H. and Sejrup, H.P., 1987. A giant three-stage submarine slide off Norway. Geo-Mar. Lett., 7: 191–198.

Burke, K., Cooper, C., Dewey, J.F., Mann, P. and Pindell, J.L., 1984. Caribbean tectonics and relative plate motions. In: W.E. Bonini et al. (Editors), The Caribbean-South American Plate Boundary and Regional Tectonics. Geol. Soc. Am. Mem., 162: 31–64.

Chavez Jr., P.S., 1986. Processing techniques for digital sonar images from GLORIA. Photogramm. Eng. Remote Sensing, 52: 1133–1145.

Duncan, R.A. and Hargraves, R.B., 1984. Plate tectonic evolution of the Caribbean region in the mantle reference frame. In: W.E. Bonini et al. (Editors), The Caribbean–South American Plate Boundary and Regional Tectonics. Geol. Soc. Am. Mem., 162: 81–93.

EEZ-SCAN '85 Scientific Staff, 1987. Atlas of the U.S. Exclusive Economic Zone, Eastern Caribbean. U.S. Geol. Surv. Misc. Invest. Ser. I–1864 B, 59 pp.

Ewing, M. and Heezen, B.C., 1955. Puerto Rico Trench topographic and geophysical data. Geol. Soc. Am. Spec. Pap., 62: 255–268.

Fox, P.J. and Heezen, B.C., 1975. Geology of the Caribbean crust. In: A.E.M. Nairn and F.G. Stehli (Editors), The Ocean Basins and Margins. Plenum, New York, Vol. 3, 706 pp.

Gardner, W.D., Glover, L.K. and Hollister, C.D., 1980. Canyons off northwest Puerto Rico: studies of their origin and maintenance with the nuclear research submarine NR-1. Mar. Geol. 37: 41–70.

Grove, K.A., Pilkey, O.H. and Trumbull, J.V.A., 1982. Mud transportation on a steep shelf, Rio de La Plata shelf, Puerto Rico. Geo-Mar. Lett., 2: 71–75.

Hansen, M.J., 1984. Strategies for classification of landslides. In: D. Brunsden and D.B. Prior (Editors), Slope Instability. Wiley-Interscience, New York, pp.1–26.

Kajiura, K., 1979. Tsunami generation. In: L.S. Hwang and Y.K. Lee (Editors), Tsunami. Proc. Nat. Sci. Found. Workshop (Coto de Caza, California), pp.15–36.

Klitgord, K.D. and Schouten, H., 1986. Plate kinematics of the central Atlantic. In: P.R. Vogt and B.E. Tucholke (Editors), The Western North Atlantic Region. Vol. M, The Geology of North America. Geol. Soc. Am., Boulder, Colo., pp.341–350.

Lee, H.J., 1985. State of the art: laboratory determination of the strength of marine soils. In: R.C. Chaney and K.R. Demars (Editors), Strength Testing of Marine Sediment: Laboratory and In Situ Measurements, ASTM STP883. Am. Soc. Test. Mater., Philadelphia, Pa., pp.181–250.

Lee, H.J., 1989. Undersea landslides: extent and significance in the Pacific Ocean. In: E.E. Brabb (Editor), Landslides: Extent and Economic Significance: Proc. Int. Geol. Congr., 28th, Symp. Landslides. Balkema, Rotterdam, pp.361–374.

Lewis, S.D., Ladd, J.W. and Bruns, T.R., 1988. Structural development of an accretionary prism by thrust and strike-slip faulting: Shumagin region, Aleutian Trench. Geol. Soc. Am. Bull., 100: 767–782.

Mann, P. and Burke, K., 1984. Neotectonics of the Caribbean. Rev. Geophys. Space Phys., 22: 309–362.

Mattson, P.H., 1984. Caribbean structural breaks and plate movements: In: W.E. Bonini et al. (Editors), The Caribbean–South American Plate Boundary and Regional Tectonics. Geol. Soc. Am. Mem., 162: 131–152.

McCulloch, D.S., 1985. Evaluating tsunami potential. In: J.I. Ziony (Editor), Evaluating Earthquake Hazards in the Los Angeles Region. U.S. Geol. Surv. Prof. Pap., 1360: 325–382.

Meyerhoff, A.A., Krieg, E.A., Cloos, J.D. and Tanner, I., 1983. Petroleum potential of Puerto Rico. Oil Gas J., Dec.: 113–120.

Monroe, W.H., 1976. The karst landforms of Puerto Rico. U.S. Geol. Surv. Prof. Pap., 899, 69 pp.

Monroe, W.H., 1980. Geology of the Middle Tertiary formations of Puerto Rico. U.S. Geol. Surv. Prof. Pap., 953, 93pp.

Moore, J.G., Clague, D.A., Holcomb, R.T., Lipman, P.W., Normark, W.R. and Torresan, M.E., 1989. Prodigious submarine slides on the Hawaiian Ridge. J. Geophys. Res. 94: 17, 465–17, 484.

Morgenstern, N.R., 1967. Submarine slumping and the initiation of turbidity currents. In: A.F. Richards (Editor), Marine Geotechnique. Univ. Illinois Press, Chicago, Ill., pp.189–220.

Mullins, H.T. and Hine, A.C., 1989. Scalloped bank margins: Beginning of the end for carbonate platforms? Geology, 17: 30–33.

Mullins, H.T., Gardulski, A.F. and Hine, A.C., 1986. Catastrophic collapse of the west Florida carbonate platform margin. Geology, 14: 167–170.

Northrop, J., 1954. Bathymetry of the Puerto Rico Trench. Am. Geophys. Union Trans., 35: 221–225.

Perfit, M.R., Heezen, B.C., Rawson, M. and Donnelly, T.W., 1980. Chemistry, origin and tectonic significance of metamorphic rocks from the Puerto Rico trench. Mar. Geol. 34: 125–166.

Plafker, G., Kachadoorian, R., Eckel, E.B. and Mayo, L.R., 1969. Effects of the earthquake of March 27, 1964 on various communities. U.S. Geol. Surv. Prof. Pap., 542-G, 53 pp.

Reed, T.B. and Hussong, D., 1989. Digital image processing techniques for enhancement and classification of SeaMARC II side scan sonar imagery. J. Geophys. Res., 94: 7469–7490.

Sangrey, D.A., 1977. Marine geotechnology — state of the art. Mar. Geotechnol., 2: 45–80.

Scanlon, K.M. and Masson, D.G., 1989. Sedimentary processes in deep ocean areas of Puerto Rico and Virgin Islands. Int. Geol. Congr. 28th, Abstr. 3, p.35.

Scanlon, K.M., Masson, D.G. and Rodriguez, R.W., 1988. GLORIA sidescan-sonar survey of the EEZ of Puerto Rico and the U.S. Virgin Islands. Trans. Caribb. Conf., 11th (Barbados, 1986), pp.32:1–32:9.

Schneidermann, N., Pilkey, O.H. and Saunders, C., 1976. Sedimentation on the Puerto Rico insular shelf. J. Sediment. Petrol., 46: 167–173.

Seed, H.B., 1979. Soil liquefaction and cyclic mobility evaluation for level ground during earthquakes. J. Geotech. Eng. Div., Proc. Am. Soc. Civ. Eng., 105: 201–253.

Somers, M.L., Carson, R.M., Revie, J.A., Edge, R.H., Barrow, B.J. and Andrews, A.G., 1978. GLORIA II — an improved long-range sidescan sonar. In: Proceedings of the IEE/IERE Subconference on Ocean Instruments and Communication. Oceanol. Int., London, pp.16–24.

Sykes, L.R., McCann, W.R. and Kafka, A.L., 1982. Motion of the Caribbean plate during the last 7 million years and implications for earlier Cenozoic movements. J. Geophys. Res. 87: 10656–10676.

Von Huene, R. and Cox, C., 1972. Locally Generated Tsunami and other Local Waves in the Great Alaska Earthquake of 1964; Oceanography and Coastal Engineering. Nat. Acad. Sci., Washington, D.C., pp.211–222.

Von Huene, R., Bourgois, J., Miller, J. and Pautot, G., 1989. A large tsunamogenic landslide and debris flow along the Peru Trench. J. Geophys. Res. 94: 1703–1714.

# APPENDIX 2

Paper by

N. Grindlay, P. Mann, and J. Dolan

Researchers Investigate Submarine Faults North of Puerto Rico

# Researchers Investigate Submarine Faults North of Puerto Rico

A 23-day marine geophysical expedition in the summer of 1996 revealed a previously unidentified strike-slip fault zone within 60–100 km of the densely populated northern coast of Puerto Rico. The purpose of the expedition, which was held aboard the U.S. research vessel *Maurice Ewing*, was to map the northeastern portion of the North America Caribbean plate boundary.

The 3000-km-long North America-Caribbean plate boundary stretches from Guatemala to the Lesser Antilles arc. The dominantly left-lateral strike-slip boundary accommodates slow (1–2.6 cm/yr) eastward motion of the Caribbean plate relative to North America. Distributed interplate motion in the region generates large earthquakes (Figure 1, inset). In 1976, an M 7.5 left-lateral, strike-slip earthquake in Guatemala killed approximately 23,000 people and left a quarter of the nation's population homeless.

The heavily populated Puerto Rico-Hispaniola segment of the plate boundary is complicated by the presence of both strike-slip and subduction-related tectonics and the interaction of these structures with the obliquely colliding Bahama Platform (Figure 1, inset). The main strike-slip feature is the Septentrional fault zone, which is located west of the study area in the Dominican Republic. Fault trenching studies of this fault segment in the Domini-

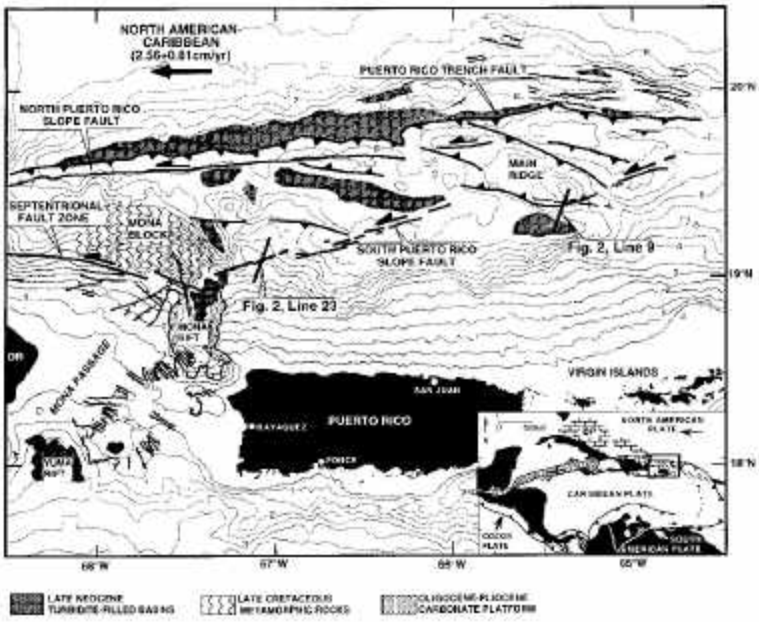


*Fig. 1. (Left) Bathymetric and tectonic map of the Puerto Rico/Virgin Islands study area. Bathymetry consists of integrated Hydrosweep bathymetry, ETOPO5 digital terrain map, and National Ocean Survey hydrographic data sets [Mercado, 1994]. Tectonic features identified from side-scan imagery, single-channel seismic profiles and Hydrosweep bathymetry. North America-Caribbean plate motion vector from* DeMets et al. *[1996]. Inset shows regional tectonic setting and location of recent large (M 7.1–8.0) magnitude earthquakes (open circles) near Guatemala, Puerto Rico, and the Dominican Republic. BP = Bahama Platform.*

*Fig. 2. (Below) Plots of migrated single-channel seismic data across the South Puerto Rico Slope fault zone (locations shown in Figure 1); true dip in line 23 and line 9 is ~ 63°. In line 23, seismic Unit 1 is interpreted to be shallow-water Lower Oligocene to Lower Pliocene clastic and carbonate shelf. Unit 2 is Eocene-Cretaceous volcanic and sedimentary rocks that form the basement of the island of Puerto Rico. In line 9 the South Puerto Rico Slope fault zone shows a component of thrust and defines the southern boundary of the submerged forearc high, the Main Ridge, which is interpreted to be an uplifted block of disrupted sediments and arc substrata.*

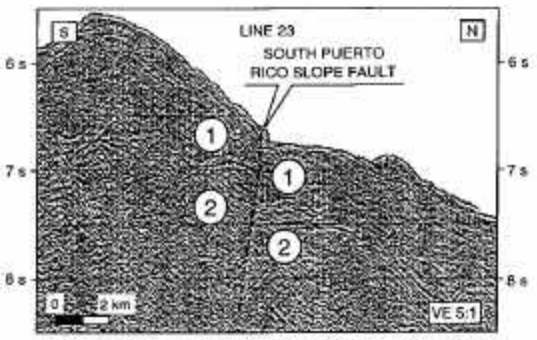


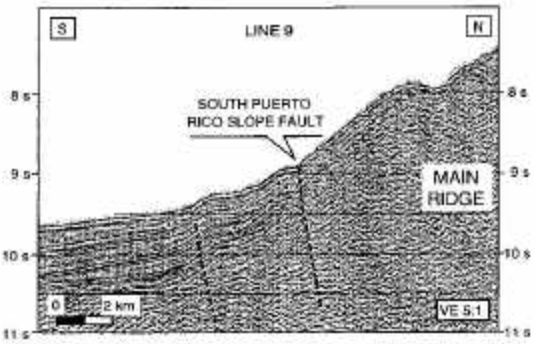



0096/3941/7838/404/$03.00

can Republic by *Prentice et al.* [1993] have shown that its last strike-slip, ground-breaking rupture occurred approximately 700 years ago. The main subduction-related feature is the Puerto Rico Trench, which is located 65–70 km north of the Septentrional fault zone. The Puerto Rico Trench is the surface trace of a southward-dipping Benioff Zone that most recently ruptured during an M 8.0 Hispaniola earthquake [*Dolan and Wald*, 1997].

To better understand the complex relationship between strike-slip and subduction tectonics north of Puerto Rico, U.S. and Spanish researchers acquired close to 50,000 $km^2$ of bathymetric and backscatter data and ~5600 km of along-track single channel seismic, gravity, and magnetic data along the Puerto Rico Trench and northern Puerto Rico/Virgin Island margins. Several major features were observed (Figure 1):

- the outer rise of the obliquely subducting Cretaceous-age Atlantic oceanic crust of the North American plate;
- the 7–8.4-km-deep trace of the subduction zone at the Puerto Rico Trench and the flanking North Puerto Rico Slope strike-slip fault, previously identified by *Masson and Scanlon* [1991];
- a submerged "forearc" where the South Puerto Rico Slope strike-slip fault, observed for the first time, strikes subparallel to the plate vector and to the North Puerto Rico Slope fault 40–60 km to the north;
- the northern Puerto Rico platform/slope area occupied by a drowned Oligocene to lower Pliocene carbonate platform; and
- the Mona Passage, where the Mona Rift was mapped in greater detail and the Yuma Rift was identified for the first time (Figure 1).

New side-scan, bathymetric and single-channel seismic data indicate that two anomalous highs in the northern Puerto Rico and Hispaniola slopes are restraining bends formed between the subparallel North and South Puerto Rico Slope fault zones. The Mona Block restraining bend exhibits more than 4 km of bathymetric relief, is bounded to the south by the Septentrional fault zone, and is known by dredging to consist of blueschist and other high-grade metamorphic rocks. Uplift of the block is attributed to both the bend in the South Puerto Rico Slope fault zone-Septentrional fault zone and underthrusting of the southeastern extension of the Bahama Platform [*Dolan and Wald*, 1997].

The Main Ridge restraining bend exhibits 2 km of bathymetric relief with thrust faults actively uplifting its southern margin (Figure 2, Line 9). The Main Ridge is associated with higher than average crustal seismicity. At the western end of the Main Ridge restraining bend, the South Puerto Rico Slope fault zone exhibits a well-developed pull-apart basin. To the west, the fault dips steeply to the south, offsetting Eocene basement by ~0.5 s (Figure 2, Line 23).

The survey also revealed extensive normal faulting of the Oligocene to early Pliocene carbonate platform in the Mona Passage, indicating a significant amount of recent east-west regional extension. This localized extension of the platform strata reflects the differential eastward relative motions of the Puerto Rico and Hispaniola microplates. Details of the deformational features of these faults, along with answers to more complex questions—such as what is the relation between crustal faulting and the subducted slab of North America beneath Puerto Rico—will require additional processing and integration of these newly acquired side-scan, bathymetry, and geophysical data sets.

*Acknowledgments:* We thank the EW96-05 shipboard science party for their contributions to this report, UTIG contribution no. 1283.

A cruise report for EW96-05 is available from N. Grindlay at the Department of Earth Sciences, tel. 1-910-962-7421, fax 1-910-962-7077.—*N. Grindlay, University of North Carolina, Wilmington; P. Mann, Institute for Geophysics, University of Texas, Austin; J. Dolan, University of Southern California, Los Angeles.*

## References

DeMets, C., T. Dixon, F. Farina, E. Calais, F. Jansma, and P. Mann, GPS-derived velocities in the northeastern Caribbean: Implications for Caribbean-North America motion and the NUVEL-1A model (abstract), *Eos, Trans. AGU, Fall Meet. Suppl.*, *77*(46), F143, 1996.

Dolan, J., and D. Wald, Comment on "The 1946 Hispaniola earthquake and the tectonics of the North America-Caribbean plate boundary zone, northeastern Hispaniola," by R. M. Russo and A. Villasenor, *J. Geophys. Res.*, *102*, 785–792, 1997.

Masson, D., and K. Scanlon, The neotectonic setting of Puerto Rico, *GSA Bull.*, *103*, 144–154, 1991.

Mercado, A., *Digitization of National Ocean Survey Hydrographic Survey "Smooth" Sheets for Puerto Rico and the U.S. Virgin Islands*, University of Puerto Rico, Sea Grant College Program, Mayaguez, Puerto Rico, p. 116, 1994.

Prentice, C. S., P. Mann, F. W. Taylor, G. Burr, and S. Valastro, Jr., Paleoseismicity of the North American-Caribbean Plate Boundary (Septentrional Fault), Dominican Republic, *Geology*, *21*, 49–52, 1993.

# APPENDIX 3

# REPORT BY

Nancy Grindlay, Ph.D.

# VOLUME AND DENSITY APPROXIMATIONS OF MATERIAL INVOLVED IN A DEBRIS AVALANCHE ON THE SOUTH SLOPE OF THE PUERTO RICO TRENCH

# VOLUME AND DENSITY APPROXIMATIONS OF MATERIAL INVOLVED IN A DEBRIS AVALANCHE ON THE SOUTH SLOPE OF THE PUERTO RICO TRENCH

A Report to the Puerto Rico Civil Defense
and the University of Puerto Rico Sea Grant College Program

by

Nancy Grindlay, Ph.D.
Associate Professor
Department of Earth Sciences
University of North Carolina at Wilmington

October, 1998

# VOLUME AND DENSITY APPROXIMATIONS OF MATERIAL INVOLVED IN A DEBRIS AVALANCHE ON THE SOUTH SLOPE OF THE PUERTO RICO TRENCH

## Project Summary

Analysis of recently collected bathymetric, sidescan sonar and single-channel seismic reflection data, together with onshore well and outcrop data are used to estimate the volume and density of material involved in a debris avalanche that generated the 57 km wide amphitheater-shaped scarp centered at approximately 66° 40' W on the northern insular slope of Puerto Rico. It is believed that the Oligocene-Pliocene megasequence of carbonates (PR1) was the major unit involved in the debris avalanche. Studies indicate that this unit, which extends across the entire north coast of Puerto Rico, has a relatively uniform thickness and ranges from 1500-1300 km in the vicinity of the landslide headwall scarp. Measurements of surface area assuming a pre-failure morphology of a straight, slope-parallel shelf break rather than the observed scalloped morphology, estimate that ~700 $km^2$ of material was involved in the failure. On the basis of onshore well logs the density of this unit is estimated to be approximately 2.2 $g/cm^3$. Assuming that the failure was catastrophic, volume estimates of material involved in the landslide range from 910 $km^3$ to 1050 $km^3$.

## Project Description

A recent marine geophysical expedition (Grindlay et al., 1997) of the Puerto Rico Trench and northern insular margin of Puerto Rico and the Virgins Islands was conducted to investigate the seismogenic potential of the region. The Puerto Rico trench represents a tectonically active plate boundary zone, where the north American plate is being subducted obliquely beneath the Caribbean plate. Grindlay et al., (1997) identified several active fault zones within the trench, including one on the south slope of the trench which lies within 60-100 km of the north coast of Puerto Rico. In addition, Grindlay et al., (1997) corroborated the existence of a major submarine slide first reported by Scanlon et al., (1988) and Schwab et al., (1991) on the south slope of the Puerto Rico trench, located about 37 km north of the city of Arecibo on the island of Puerto Rico (Figure 1). Although rarely documented directly, earthquakes are often inferred to be the triggering mechanisms of submarine slides (Hampton and Lee, 1996) and that under certain circumstances submarine slides can be accompanied by large and destructive tsunamis (Moore and Moore, 1984; von Huene et al., 1989; Jiang and Le Blond, 1992; Hampton and Lee, 1996). The presence of active fault zones in the Puerto Rico trench implies that there is a potential threat of repeat submarine slides and accompanying tsunamis.

In this study, geophysical data collected during the June-July 1996 cruise on board the R/V Maurice Ewing (Chief Scientist Grindlay, Co-Chiefs Paul Mann and James Dolan) and existing onshore well and outcrop data are used to provide estimates of the volume and density of material involved in the debris avalanche that formed the large amphitheater-shaped scarp. These data include sidescan sonar imagery (HMR1-system) which provides information about the reflectivity and nature of seafloor material and structures. High-resolution multibeam sonar bathymetric data (Krupps-Atlas Hydrosweep system) provide vertical depth resolutions on the order of 10-15m and swath widths up to 2.5 the water depth. Accurate bathymetric maps are used to estimate the surface area of the material involved in the slide. Single-channel seismic

(SCS) profiles provide information about the subsurface structures, including location of headwall scarps and extent and thickness of units that pre- and post-date the slide. Onshore well data from CPR-4 (Briggs, 1961) and Toa Baja wells (Anderson, 1991) are used to make lithologic and age correlations of seismic reflection data and determine physical properties of these units. The volume and density estimates of the material involved in the submarine landslide provided in this report will be used in numerical models to estimate potential tsunami propagation and runup.

## Results

*Classification and morphologic description of submarine landslide*

On the basis of the geophysical data the landslide that generated the amphitheater-shaped scarp on the south slope of Puerto Rico trench was most likely a debris avalanche. Varnes (1978) define a debris avalanche as a landslide that involves the failure of hundreds to thousands of cubic kilometers of rock and sediment that have disintegrated into relatively smaller pieces (compared to the large slump blocks but can include blocks of many cubic kilometers) and have clearly moved rapidly. Each debris avalanche is thought to represent a single episode of catastrophic slope failure. The bathymetric and sidescan imagery clearly show a giant amphitheater-shaped scarp that is approximately 57 km across (Figures 2 A, B, and 3). The crown of the headwall scarp lies at depths of 2500 m to 3500 m. The debris deposit shown as dark, highly reflective material in the sidescan imagery extends more than 25 km down the slope to depths of approximately 7000 m (Figures 2A &B). The seismic profile 20 shows a thin layer characterized by chaotic returns and a hummocky surface that is the uppermost unit on the amphitheater-shaped scarp (Figure 4).

*Description of the stratigraphic units on the south slope of the PR trench*

Seismic profiles that extend across the northern insular margin of Puerto Rico show that the offshore stratigraphy of the platform can be divided into three megasequences (Meyerhoff et al., 1983; van Gestel et al., in review)(Figure 4, SCS profile 20). On the basis of well data from CPR-4 and Toa Baja wells these sequences can be correlated with lithologic units of defined ages (Figure 5) (Meyerhoff et al., 1983; van Gestel et al., in review). The lowest unit, PR1 consists of island arc basement rocks which based on subaerial exposures and samples dredged offshore (Fox and Heezen, 1975; Perfit et al. 1980) are of Cretaceous to Eocene age. The middle unit, PR2, does not correlate to any major formation or group of formations on Puerto Rico (Meyerhoff et al., 1983) but is speculated to be of Eocene age and formed as a basinal fill in a deep marine setting. Meyerhoff et al., (1983) and van Gestel et al., (in review) note that this unit is offset by large normal faults that extend upward into the overlying unit. It is possible that reactivation of these faults due to recent tectonic activity has resulted in their growth into the overlying unit PR3. The uppermost unit, PR3, consists of Oligocene-Pliocence shallow marine limestones deposited during a tectonically quiescence period (Moussa et al, 1987; Meyerhoff et al., 1983, Reflectors within PR3 can be subdivided in five individual sequences that are conformable with reflectors in the underlying PR2 (van Gestal et al., in review) (Figure 5). Overall, unit PR3 is characterized by continuous parallel reflectors, constant thickness and constant dip that persists through the offshore units. During the past 2.5 m.y. the submarine part of PR3 has subsided more than 4000 m generating a 4.5° regional slope (Birch, 1986).

At the base of south slope SCS profile 20 shows thick onlapping deposits of stratified material characteristic of turbidites. Core and dredge samples show the top portion of this unit to consist of turbidites (Conolly and Ewing, 1967; Fox and Hezzen 1975, Perfit et al. 1980). The source of these deposits is unknown, although it is likely that some portion consists of sediments transported across the shelf and down the scarp face through the submarine canyons. These deposits have been offset vertically and most likely laterally by the South Puerto Rico slope fault. In addition a small, lower headwall scarp is observed cutting these deposits at 7500m.

*Estimates of volume and density of material involved in the landslide*

SCS Profile 20 suggests that only unit PR3 was involved in the submarine landslide, as it is the only unit to be truncated abruptly at the upper headwall scarp (Figure 5). Unit PR2 appears to vary little in thickness, although the seismic data do not provide enough penetration to clearly delineate the interface between units PR2 and PR1. On the basis of systematically collected SCS profiles over the platform, van Gestel et al., in press, estimate that the thickness of unit PR3 ranges from 1500 km to 1300 km (assuming a velocity of 2.75 km/s) at the upper headwall scarp. Given the surface area of failure calculated to be ~ 700 $km^2$ (Figure 6) a volume of ~ 910-1050 $km^3$ material is estimated to be involved in the landslide. Geophysical logs from the Toa Baja well (Anderson, 1991) indicate that unit PR3 has a density of 2.2 $g/cm^3$.

**Figures**

Figure 1. Shaded relief of regional bathymetry (1 min grid interval). Contour interval is 500m. Box indicates location of study area. The location of CPR-4 and Toa Baja wells on the north coast of Puerto Rico are indicated by filled white circles.

Figure 2A. Side scan sonar imagery (HMR1) of amphitheater-shaped scarp cut into the northern Puerto Rico insular margin and debris deposit downslope. Highly reflective areas such as fault scarps, bare rock surfaces, appear as dark gray to black; areas with limited backscatter such as heavily sedimented surfaces and shadowed areas appear as light gray. Also identified: a possible lower headwall scarp at the base of the slope, the South Puerto Rico Slope Fault Zone and submarine canyons cut into the Oligocene-Miocene carbonate platform. The north coast of Puerto Rico is shown in black, areas of no data are in white. Location of seismic profile shown in Figure 5 is marked by dashed white line.

Figure 2B. Bathymetric map (250m grid-interval) of the study area at the same scale as the side scan sonar imagery. Contour interval is 100 m. The crown of the amphitheater-shaped scarp ranges from 2500-3500 m. The base of the upper scarp lies at approximately 7000m water depth. Location of the seismic profile 20 shown in Figure 4 is indicated by the dashed white line. The north coast of Puerto Rico is shown in black; areas of no data are in white.

Figure 3. A three-dimensional perspective view of the amphitheater-shaped scarp. View from the northeast. Modified from Grindlay et al., in prep.

Figure 4. Interpretation of main seismic megasequences of the northern margin of Puerto Rico from EW96-05 SCS line 20. This line is considered representative of several lines which extend across the margin. This figure shows the head-wall scarp of the amphitheater-shape scarp, debris deposits associated with scarp, the location of South Puerto Rico Slope Fault Zone, recent turbidite deposits within the trench and the lower-head wall scarp and associated debris deposit at the base of the slope.

Figure 5. CPR-4 and Toa Baja well logs from Briggs (1961) and (Anderson, 1991) and correlation of seismic sequences PR1 and PR3 identified in SCS profile 20 (Figure 5). Eustatic sea level curve of Haq et al., (1987) also shown. After van Gestel et al., in review.

Figure 6. Shaded surface area ~700 $km^2$ of estimated material involved in submarine slide assuming a slope-parallel shelf break rather than the observed scalloped morphology. Contour interval is 100 m.

## References


Anderson, R., Geophysical logs from the Toa Baja Scientific Drill hole, Puerto Rico, Geophys. Res. Lett., 18, 497-500, 1991.

Birch, F, Isostatic, thermal and flexural models of the subsidence of the north coast of Puerto Rico, Geology, 14, 427-429, 1986.

Briggs, R.P., Geology of Kewanne Interamerican Oil Company test well number CPR-4 northern Puerto Rico in Oil and Gas Possibilities of Northern Puerto Rico, pp 1-23, 1961.

Conolly, F. and M. Ewing, Sedimentation in the Puerto Rico Trench, Jour. Sed. Petrology, 37, 44-59, 1967.

Fox, J. and B. Heezen, Geology of the Caribbean crust, in The Ocean Basins and Margins, eds. A Nairn and F. Stehli, pp. 421-466, New York, NY, 1975.

Grindlay, N., P. Mann, and J. Dolan, Researchers investigate submarine faults north of Puerto Rico, Eos, Trans. AGU, 78, 404, 1997.

Grindlay, N., P. Mann, J. Dolan, and J-P van Gestal, Oblique collision of the Bahamas Platform in the Hispaniola-Puerto Rico area, northeastern Caribbean 2: Puerto Rico trench and northern Puerto Rico Island Slope, J. Geophys. Res., in prep.

Hampton, M., H. Lee and J. Locat, Submarine landslides, Rev. of Geophys, 34, 33-59, 1996.

Haq, B., J. Hardenbol and P.R. Vail, Chronology of fluctuating sea levels since the Triassic, Science, 235, 1156-1167, 1987.

Jiang, L., and P.H. LeBlond, The coupling of a submarine slide and the surface waves which it generates, J. Geophys. Res., 97, 12,731-12,744, 1992.

Meyerhoff, A., E.A. Krieg, J.D. Cloos, and I. Taner, Petroleum potential of Puerto Rico, Oil and Gas Jour., 81, 113-120, 1983.

Monroe, W., Stratigraphy and petroleum possibilities of middle Tertiary rocks in Puerto Rico, AAPG Bull., 57, 1086-1099, 1973.

Moore, G. and J.G. Moore, Deposit from a giant wave on the island of Lanai, Science, 226, 1312-1315, 1984.

Moussa, M.T., G.A. Seiglie, A.A. Meyerhoff and I. Taner, The Quebradillas Limestone (Miocen-Pliocene), northern Puerto Rico and tectonics of the northeastern Caribbean margin, GSA Bull, 99, 427-439, 1987.

Perfit, M.R., B.C. Heezen, M. Rawson and T. Donnelly, Chemistry, origin and tectonic significance of metamorphic rocks from the Puerto Rico trench, Marine Geology, 34, 125-156, 1980.

Scanlon, K., D. Masson and R. Rodriguez, GLORIA sidescan-sonar survey of the EEZ of Puerto Rico and US Virgin Islands, Trans. Caribb. Conf., 11th, Barbados, 32:1-32:9, 1988.

Submarine Landslides: Selected Studies in the U.S. Exclusive Economic Zone, ed. W. Schwab, H. Lee, D. Twichell, US Geological Survey Bull., 2002, 1993.

Schwab, W.C., W.W. Danforth, K. Scanlon, and D. Masson, A giant submarine slope failure on the northern insular slope of Puerto Rico, Marine Geology, 96, 237-246, 1991.

van Gestel, J-P, P. Mann, J. Dolan and N. Grindlay, Structure and tectonics of the upper Cenozoic Puerto Rico-Virgin Islands carbonate platform as determined from seismic reflection studies, J. Geophys. Res., in press.

van Gestel, J-P., P. Mann, N. Grindlay, and J. Dolan, Three-phase tectonic evolution of the northern margin of Puerto Rico as inferred from an integration of seismic reflection, well and outcrop data, Marine Geology, in review.

Varnes, D.J. , Slope movement types and processes, in Landslides--Analysis and Control, eds. R.L. Schuster and R.J. Krizek, Spec. Rep. 176, pp. 12-33, Transp. Res. Board, Natl. Res. Counc., Washington, DC, 1978.

von Huene, R. , J. Bourgois, J. Miller, and G. Pautot, A large tsunamogenic landslide and debris flow along the Peru Trench, J. Geophys. Res., 94, 1703-1714, 1989.

Figure 1

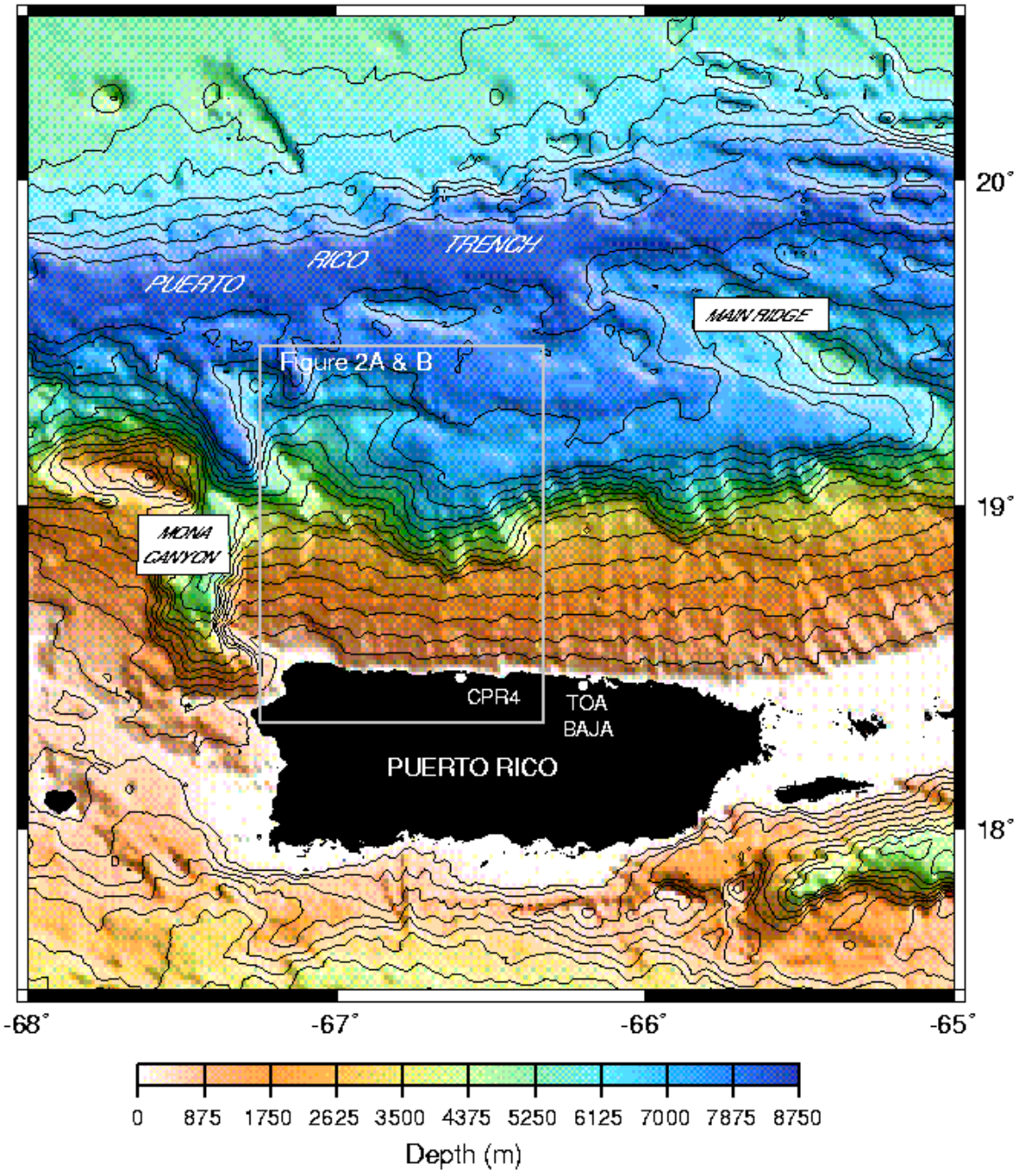
PUERTO
RICO
TRENCH
MAIN RIDGE
Figure 2A & B
MONA
CANYON
CPR4
TOA
BAJA
PUERTO RICO
20˚
19˚
18˚
-68˚
-67˚
-66˚
-65˚
0
875
1750
2625
3500
4375
5250
6125
7000
7875
8750
Depth (m)

Figure 2A

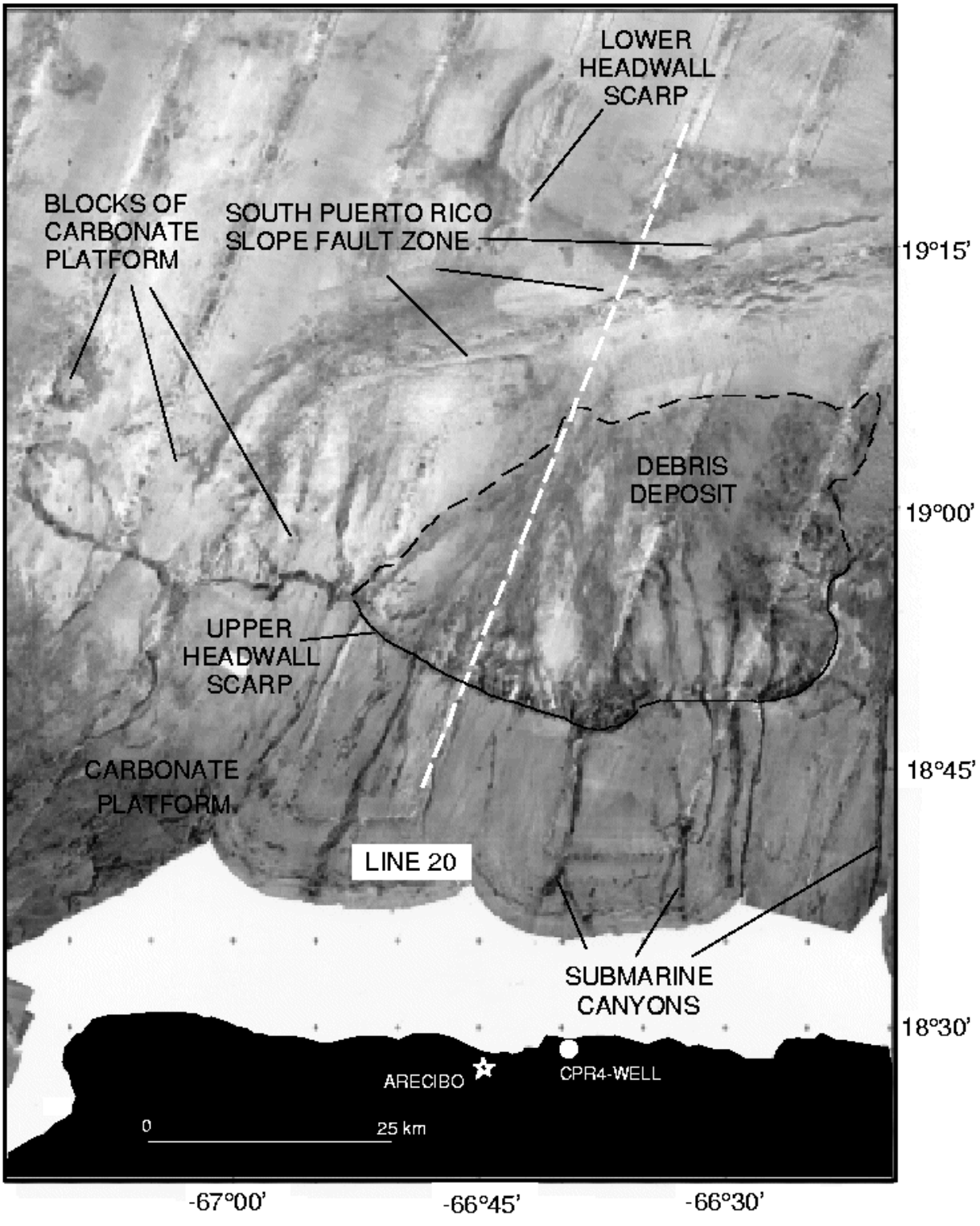
LOWER
HEADWALL
SCARP
BLOCKS OF
CARBONATE
PLATFORM
SOUTH PUERTO RICO
SLOPE FAULT ZONE
19°15'
DEBRIS
DEPOSIT
19°00'
UPPER
HEADWALL
SCARP
CARBONATE
PLATFORM
18°45'
LINE 20
SUBMARINE
CANYONS
18°30'
ARECIBO
CPR4-WELL
0
25 km
-67°00'
-66°45'
-66°30'

Figure 2B

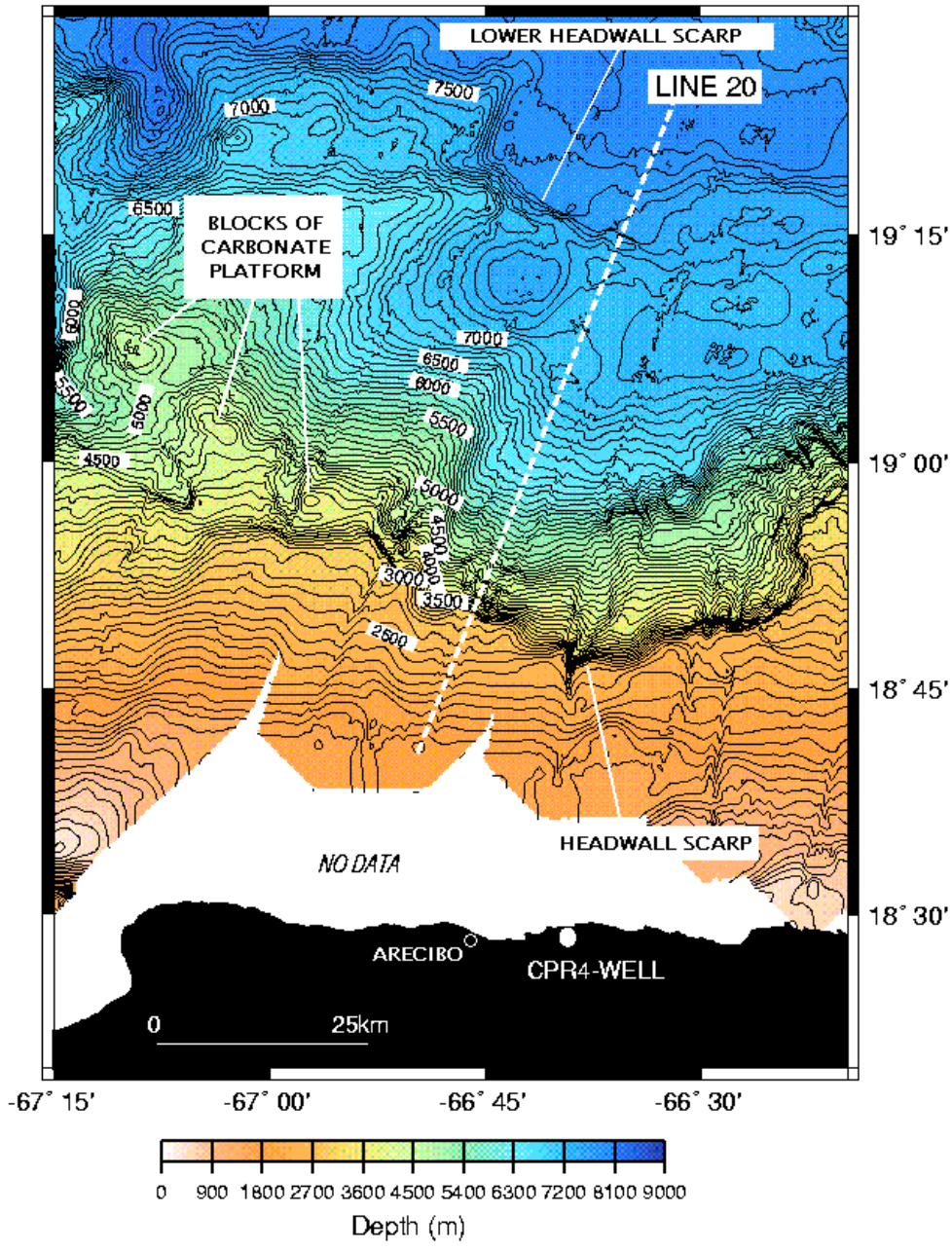
LOWER HEADWALL SCARP
LINE 20
BLOCKS OF CARBONATE PLATFORM
HEADWALL SCARP
NO DATA
ARECIBO
CPR4-WELL
0
25km
19° 15'
19° 00'
18° 45'
18° 30'
-67° 15'
-67° 00'
-66° 45'
-66° 30'
0 900 1800 2700 3600 4500 5400 6300 7200 8100 9000
Depth (m)

FIGURE 3

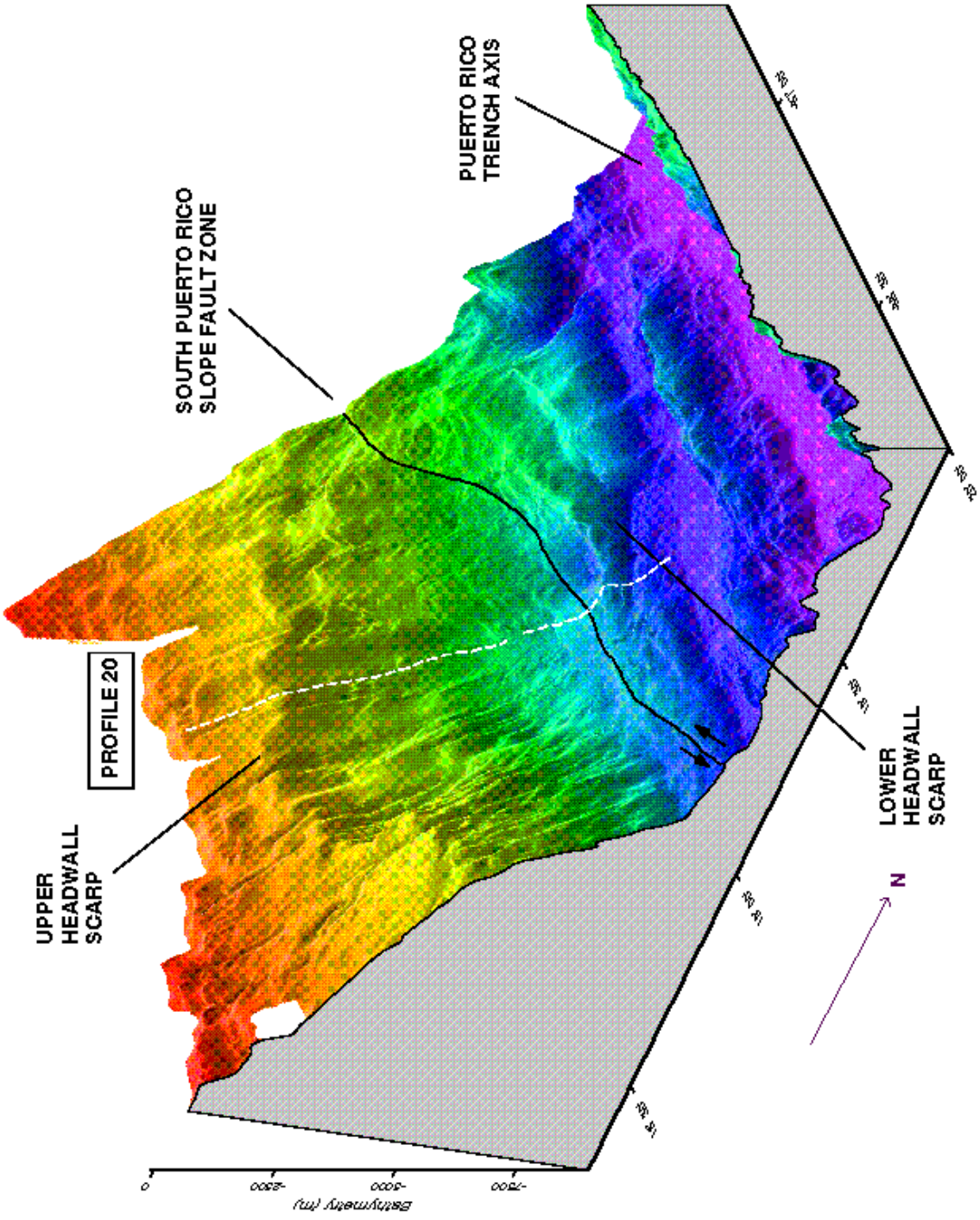
PUERTO RICO
TRENCH AXIS
SOUTH PUERTO RICO
SLOPE FAULT ZONE
PROFILE 20
UPPER
HEADWALL
SCARP
LOWER
HEADWALL
SCARP
N
Bathymetry (m)
0
-2500
-5000
-7500
18°N
18°30'N
19°N
19°30'N
20°N
67°W
66°30'W
66°W
65°30'W
65°W

FIGURE 4

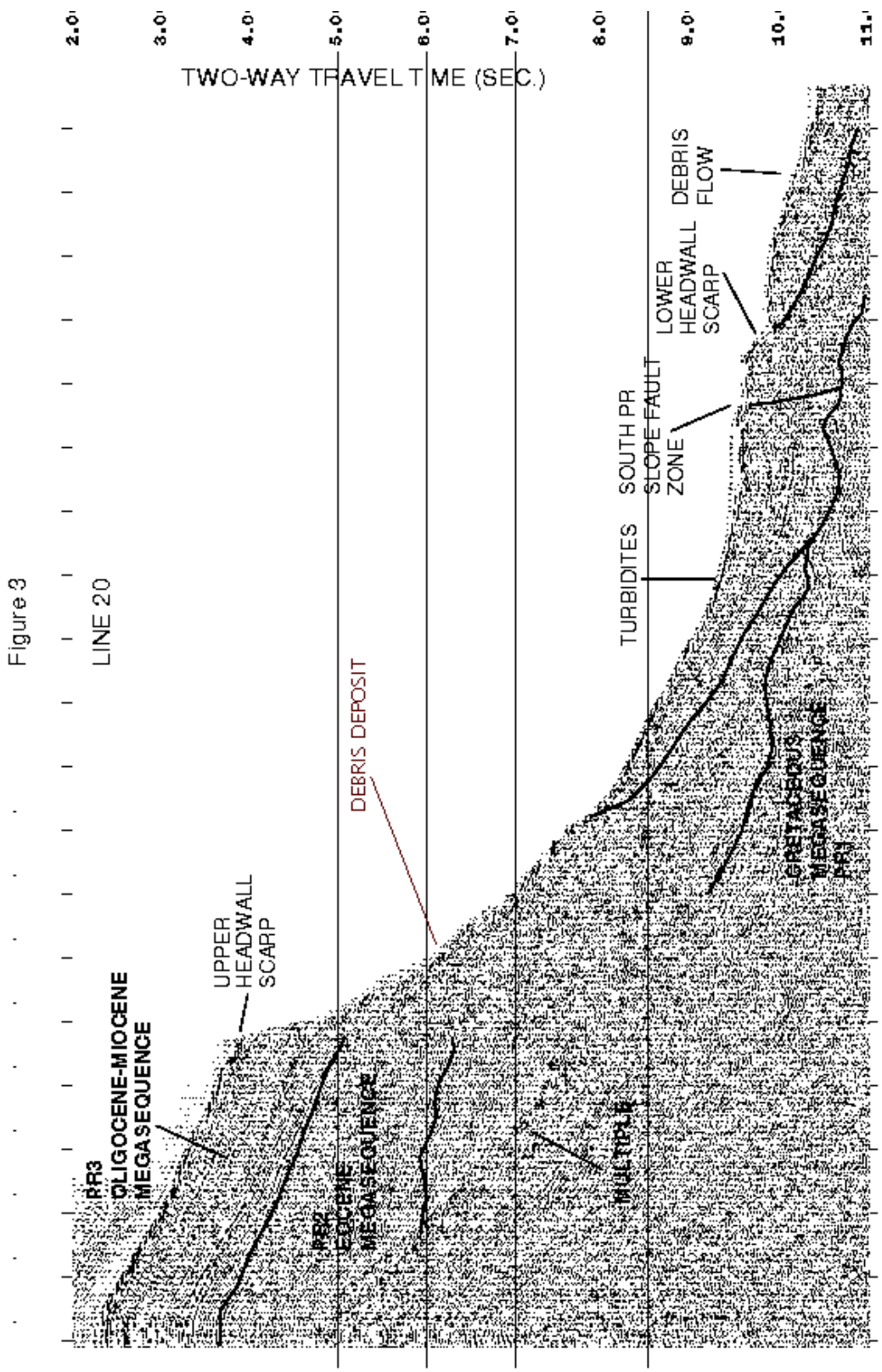
Figure 3
LINE 20
TWO-WAY TRAVEL TIME (SEC.)
2.0
3.0
4.0
5.0
6.0
7.0
8.0
9.0
10.
11.
RR3
OLIGOCENE-MIOCENE
MEGASEQUENCE
UPPER
HEADWALL
SCARP
RR2
EOCENE
MEGASEQUENCE
DEBRIS DEPOSIT
MULTIPLE
TURBIDITES
SOUTH PR
SLOPE FAULT
ZONE
LOWER
HEADWALL
SCARP
DEBRIS
FLOW
CRETACEOUS
MEGASEQUENCE
AR3

FIGURE 5

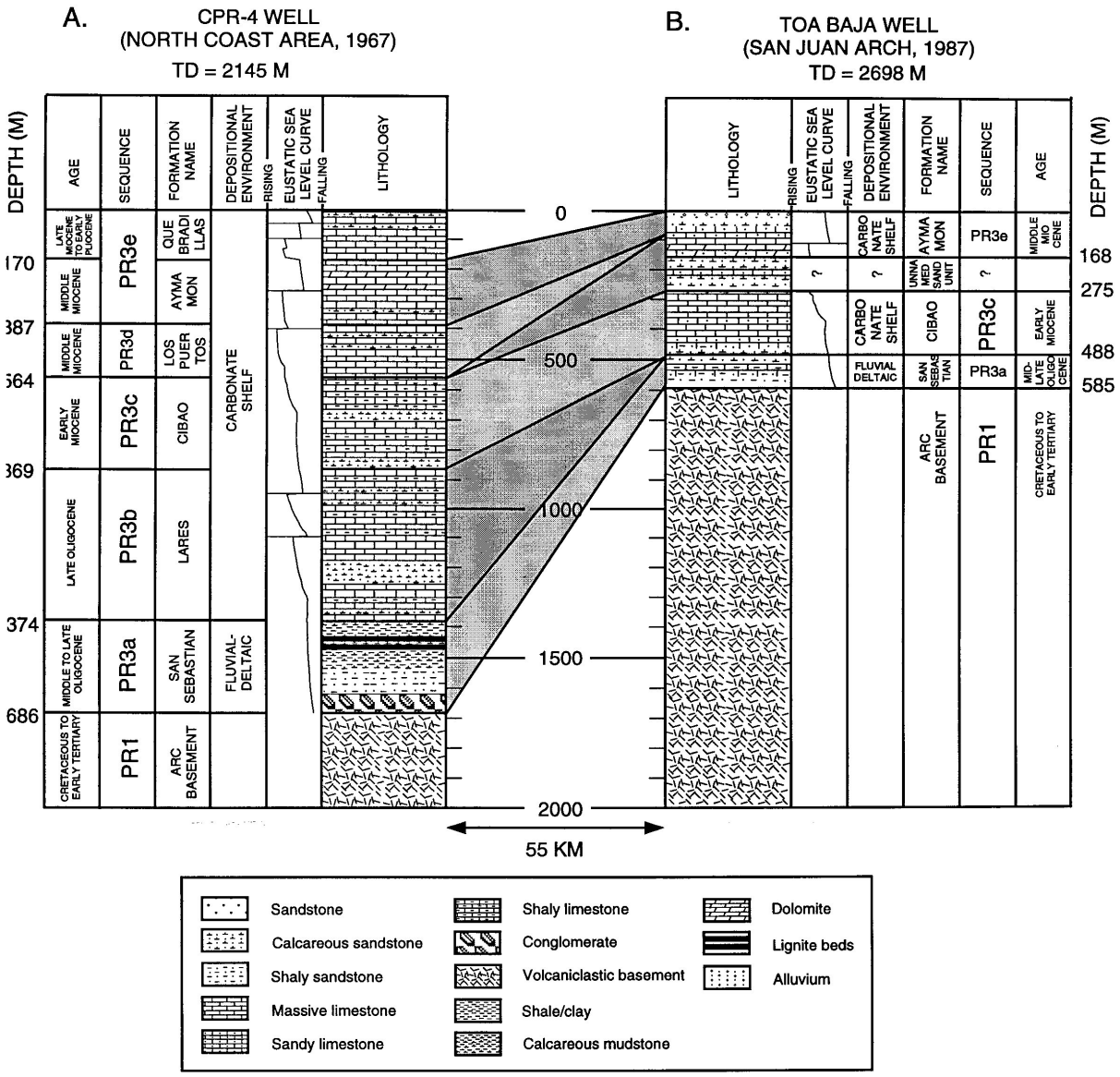
A.
CPR-4 WELL
(NORTH COAST AREA, 1967)
TD = 2145 M
B.
TOA BAJA WELL
(SAN JUAN ARCH, 1987)
TD = 2698 M
DEPTH (M)
AGE
SEQUENCE
FORMATION NAME
DEPOSITIONAL ENVIRONMENT
RISING
EUSTATIC SEA LEVEL CURVE
FALLING
LITHOLOGY
LATE MIOCENE TO EARLY PLIOCENE
MIDDLE MIOCENE
MIDDLE MIOCENE
EARLY MIOCENE
LATE OLIGOCENE
MIDDLE TO LATE OLIGOCENE
CRETACEOUS TO EARLY TERTIARY
PR3e
PR3d
PR3c
PR3b
PR3a
PR1
QUE BRADI LLAS
AYMA MON
LOS PUER TOS
CIBAO
LARES
SAN SEBASTIAN
ARC BASEMENT
CARBONATE SHELF
FLUVIAL-DELTAIC
170
387
564
369
374
686
0
500
1000
1500
2000
55 KM
CARBO NATE SHELF
UNNA MED SAND UNIT
FLUVIAL DELTAIC
SAN SEBAS TIAN
MIDDLE MIOCENE
EARLY MIOCENE
MID-LATE OLIGO CENE
CRETACEOUS TO EARLY TERTIARY
168
275
488
585
Sandstone
Calcareous sandstone
Shaly sandstone
Massive limestone
Sandy limestone
Shaly limestone
Conglomerate
Volcaniclastic basement
Shale/clay
Calcareous mudstone
Dolomite
Lignite beds
Alluvium

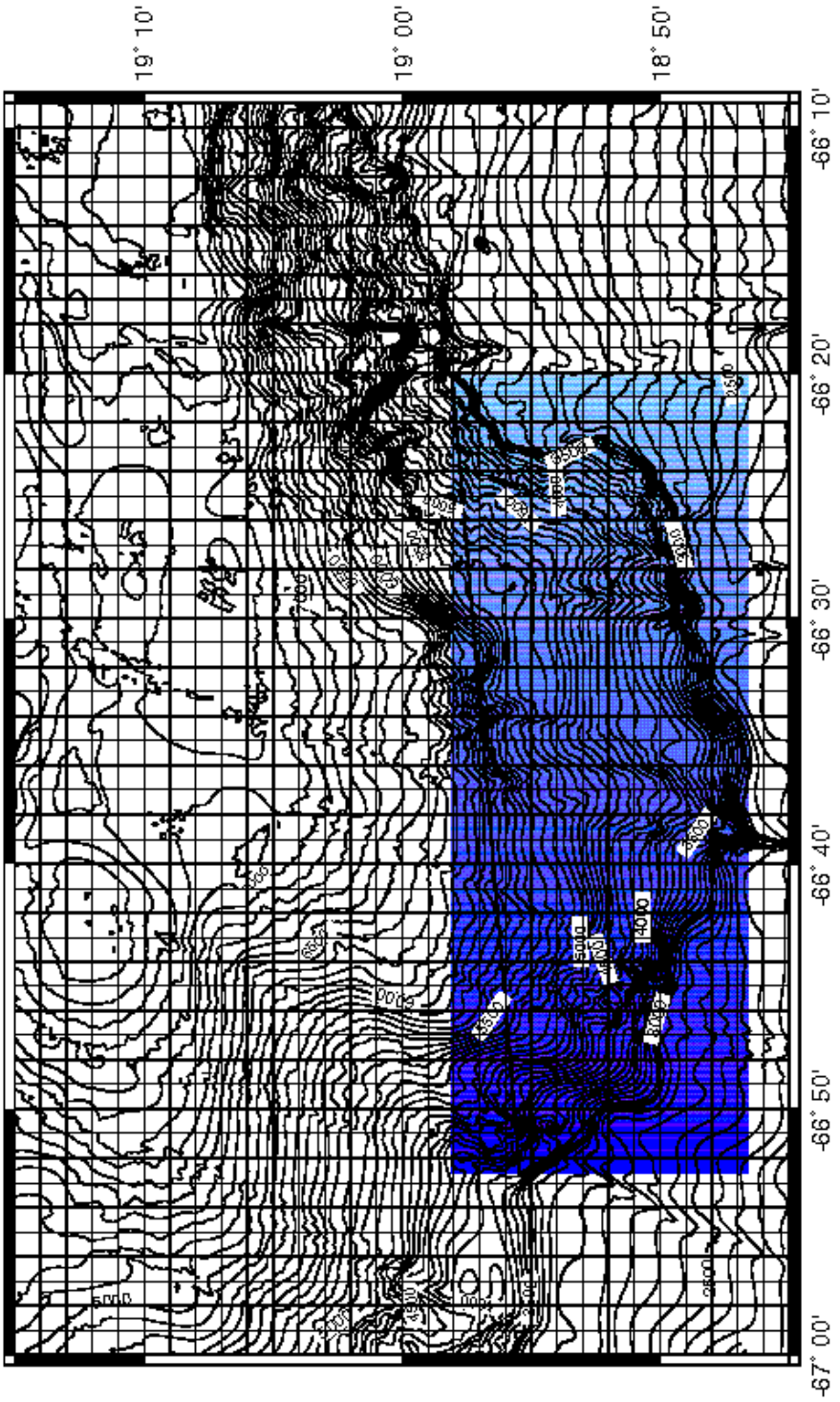


FIGURE 6

# APPENDIX 4

Manuscripts by

Patrick Lynett, Ph.D. Candidate
Philip L-F. Liu, Professor
Department of Civil and Environmental Engineering
Cornell University

# Modeling Wave Runup with Depth-Integrated Equations

Patrick J. Lynett, Tso-Ren Wu, and Philip L.-F. Liu
School of Civil and Environmental Engineering, Cornell University
Ithaca, NY 14853

In this paper, a moving boundary technique is developed to investigate wave runup and rundown with depth-integrated equations. Highly nonlinear and weakly dispersive equations are solved using a high-order finite difference scheme. An eddy viscosity model is adopted for wave breaking so as to investigate breaking wave runup. The moving boundary technique utilizes linear extrapolation through the wet-dry boundary and into the dry region. Nonbreaking and breaking solitary wave runup is accurately predicted by the proposed model, yielding a validation of both the wave breaking parameterization and the moving boundary technique. Two dimensional wave runup in a parabolic basin and around a conical island is investigated, and agreement with published data is excellent. Finally, the propagation and runup of a solitary wave in a trapezoidal channel is examined.

Keywords: wave runup, breaking waves, Boussinesq equations

## Introduction

The past decade saw the advent and wide spread applications of Boussinesq-type equation models for studying wave propagation in one and two horizontal dimensions. The conventional Boussinesq equations (Peregrine, 1967) had two major limitations: (1) The depth-averaged model poorly described the frequency dispersion of wave propagation in intermediate depths, and (2) the weakly nonlinear assumption limited the largest wave height that could accurately be modeled. The dispersion properties of the conventional Boussinesq equation model have been improved by modifying the dispersive terms (Madsen and Sorensen, 1992) or using a reference velocity at a specified depth (Nwogu, 1993). These techniques yield a set of equations whose linear dispersion relation can be adjusted such that the resulting intermediate-depth dispersion characteristics are close to the true linear solution. Liu (1994) and Wei *et al.* (1995) presented a set of highly nonlinear Boussinesq-type equations that not only can be applied to intermediate water depth but also are capable of simulating wave propagation with strong nonlinear interaction. Wei *et al.* (1995) have also developed a high-order numerical scheme to solve these equations. All of these efforts successfully extended the usage of the Boussinesq-type equation model, such that wave evolution from relatively deep water to the breaking point could be accurately captured.

Wave propagation using Boussinesq-type equations is now well simulated and understood, but the process of runup and rundown is not. Shoreline boundaries may move significantly under the temporal influence of incident waves. A numerical model should be able to take into account such variations correctly in order to obtain realistic flow patterns.

Researchers generally use a fixed grid, finite difference or finite element method to solve the Boussinesq-type equations. Using a fixed grid numerical model to solve a moving boundary problem can lead to difficulties related to the loss of mass conservation and instabilities in the computations (Leendertse, 1987) as a result of imposing discrete

fixed increments to the extent of wetting and drying areas (Balzano, 1998). To reduce the computational instabilities near the wet-dry interface, some researchers added bottom friction into the momentum equations. However, a numerical model should be stable even without using bottom friction dissipation.

Zelt (1991) used a Lagrangian form of the Boussinesq-type equations to simulate shoreline movement. This model produced maximum runup values that compared well with experimental values, but the shape of the wave as it traveled up the slope did not compare as favorably. A handful of others have utilized Lagragian techniques with depth-integrated equation models to simulate a moving shoreline (e.g., Petera and Nassehi, 1996: Gopalakrishnan, 1989). Another treatment of moving boundary problem is employing a slot or permeable-seabed technique (Tao, 1983, 1984). The first application of the permeable slot with a Boussinesq-type model (Madsen *et al.*, 1997) yielded runup errors on the order of ten percent of the maximum. Modifications have been made to this permeable slot technique (Kennedy *et al.*, 2000), increasing the accuracy, but it was also shown that the empirical coefficients that govern the technique can not be universally determined, due to numerical stability problems (Chen *et al.*, 2000).

In this paper, we present a new moving boundary treatment for wave propagation models. The moving boundary algorithm is conceptually simple, easy to implement, and can be employed by different numerical schemes (i.e., finite difference and finite element) utilizing depth-integrated equations. The moving boundary technique utilizes linear extrapolation near the wet-dry boundary, thereby allowing the real boundary location to exist in-between nodal points. The model is compared with the classic Carrier and Greenspan (1958) solution for monochromatic long wave runup on a constant slope. As another one horizontal dimension test, the solitary wave runup experiments of Synolakis (1986,1987), which range from non-breaking to breaking waves, are recreated numerically. To test the accuracy of two horizontal dimension moving boundary

problems, three cases are examined: wave oscillations in a parabolic basin, solitary wave interaction with a conical island, and wave evolution in a trapezoidal channel.

## Model Equations and Numerical Scheme

The model equations to be utilized in this paper are the highly nonlinear, weakly dispersive wave equations, given in dimensional form (e.g., Liu, 1994):

$$\zeta_t + E = 0, \quad \boldsymbol{u}_{\alpha t} + \boldsymbol{F} = 0 \tag{1}$$

where

$$E = \nabla \cdot [(h+\zeta)\boldsymbol{u}_\alpha] - \nabla \cdot \left\{ (h+\zeta) \left[ \left( \frac{1}{6}(\zeta^2 - \zeta h + h^2) - \frac{1}{2} z_\alpha^2 \right) \nabla(\nabla \cdot \boldsymbol{u}_\alpha) + \left[ \frac{1}{2}(\zeta - h) - z_\alpha \right] \nabla \left[ \nabla \cdot (h\boldsymbol{u}_\alpha) \right] \right] \right\} \tag{2}$$

$$\begin{aligned} \boldsymbol{F} = {} & \boldsymbol{u}_\alpha \cdot \nabla \boldsymbol{u}_\alpha + g\nabla\zeta + \left\{ \frac{1}{2} z_\alpha^2 \nabla(\nabla \cdot \boldsymbol{u}_{\alpha t}) + z_\alpha \nabla \left[ \nabla \cdot (h\boldsymbol{u}_{\alpha t}) \right] \right\} \\ & + \{ [\nabla \cdot (h\boldsymbol{u}_\alpha)] \nabla [\nabla \cdot (h\boldsymbol{u}_\alpha)] - \nabla [\zeta(\nabla \cdot (h\boldsymbol{u}_{\alpha t})] + (\boldsymbol{u}_\alpha \cdot \nabla z_\alpha) \nabla [\nabla \cdot (h\boldsymbol{u}_\alpha)] \} \\ & + \left\{ z_\alpha \nabla [\boldsymbol{u}_\alpha \cdot \nabla(\nabla \cdot (h\boldsymbol{u}_\alpha)] + z_\alpha (\boldsymbol{u}_\alpha \cdot \nabla z_\alpha) \nabla(\nabla \cdot \boldsymbol{u}_\alpha) + \frac{z_\alpha^2}{2} \nabla [\boldsymbol{u}_\alpha \cdot \nabla(\nabla \cdot \boldsymbol{u}_\alpha)] \right\} \\ & + \nabla \left\{ -\frac{\zeta}{2}^2 \nabla \cdot \boldsymbol{u}_{\alpha t} - \zeta \boldsymbol{u}_\alpha \cdot \nabla [\nabla \cdot (h\boldsymbol{u}_\alpha) +] + \zeta [\nabla \cdot (h\boldsymbol{u}_\alpha)] \nabla \cdot \boldsymbol{u}_\alpha \right\} \\ & + \nabla \left\{ \frac{\zeta^2}{2} \left[ (\nabla \cdot \boldsymbol{u}_\alpha)^2 - \boldsymbol{u}_\alpha \cdot \nabla(\nabla \cdot \boldsymbol{u}_\alpha) \right] \right\} \end{aligned} \tag{3}$$

where $\zeta$ is the free surface elevation, $h$ is the local water depth, and $\boldsymbol{u}_\alpha = (u_\alpha, v_\alpha)$ is the reference horizontal velocity. The velocity is evaluated at the elevation $z_\alpha = -0.531h$, as recommended by Nwogu (1993), based on optimum agreement of the governing equations with the linear dispersion relation. Wherever $h$ is negative (initially dry land), this relationship is set to $z_\alpha = -h$, so as to avoid the evaluation of $\boldsymbol{u}_\alpha$ under the seafloor. Two dimensionless, characteristic coefficients can be given as

$$\varepsilon = a/h, \quad \mu = h/\lambda \tag{4}$$

where $a$ is the wave amplitude and $\lambda$ is the horizontal length scale. $\varepsilon$ is indicative of the importance of nonlinearity and is assumed to be $O(1)$ in (1)-(3): $\mu$ represents frequency dispersion and $O(\mu^2) << 1$. The order of magnitude of accuracy of these equations is $O(\mu^4)$. Note that the above momentum equation,(3), is slightly different from that presented by Wei *et al.* (1995). This difference is caused by the omission of some $O(\mu^2)$ terms in Wei *et al.* in their conversion of $\frac{1}{2}\nabla(\boldsymbol{u}_\alpha^2)$ to $\boldsymbol{u}_\alpha \cdot \nabla \boldsymbol{u}_\alpha$. These neglected terms vanish only if $\nabla \times \boldsymbol{u}_\alpha = 0$, which, however, does not imply the irrotationality of the flow field. In fact, $\nabla \times \boldsymbol{u}_\alpha$ is of $O(\mu^2)$. A more mathematically detailed explanation can be found in Hsiao and Liu (2002).

The parameterizations, $\boldsymbol{R}_f$ and $\boldsymbol{R}_b$, account for the effects of bottom friction and wave breaking, respectively. Bottom friction is described in the quadratic form:

$$\boldsymbol{R}_f = \frac{f}{h+\zeta}\boldsymbol{u}_\alpha|\boldsymbol{u}_\alpha| \tag{5}$$

where $f$ is a bottom friction coefficient, typically in the range of $10^{-3}$ to $10^{-2}$, depending on the Reynolds number and seafloor condition. To simulate the effects of wave breaking, the eddy viscosity model (Zelt, 1991: Kennedy *et al.*, 2000) is used here. Readers are directed to Kennedy *et al.* (2000) for a thorough description and validation of the breaking model, and the coefficients and thresholds given therein are used for all the simulations presented in this paper.

The model used for all the simulations in this paper is nicknamed COULWAVE, for Cornell University Long and Intermediate Wave Modeling Package. This model has the ability to simulate a wide range of long wave problems, including interaction with porous coastal structures (Lynett *et al.*, 2000), wave generation by seafloor movements such as landslides (Lynett and Liu, 2002a), and internal wave propagation and evolution (Lynett and Liu, 2002b). The numerical model utilizes a predictor-corrector time-stepping scheme, accurate to $(\Delta t^4)$, where $\Delta t$ is the time step. Similar numerical schemes have been successfully employed by Wei *et al.* (1995) for modeling surface wave phenomena.

Assume now that the numerical simulation is at time $n$, where all physical values (free surface and velocity) at time $n$, and previous times, are known. To determine the physical values at the next time step $n+1$, the explicit predictor is first applied:

$$\zeta_{i,j}^{n+1} = \zeta_{i,j}^{n} - \frac{\Delta t}{12}(23E_{i,j}^{n} - 16E_{i,j}^{n-1} + 5E_{i,j}^{n-2}) \tag{6}$$

$$(\boldsymbol{u}_\alpha)_{i,j}^{n+1} = (\boldsymbol{u}_\alpha)_{i,j}^{n} - \frac{\Delta t}{12}(23\boldsymbol{F}_{i,j}^{n} - 16\boldsymbol{F}_{i,j}^{n-1} + 5\boldsymbol{F}_{i,j}^{n-2}) \tag{7}$$

where $n$ represents the time index, $i$ the $x$-space index, and $j$ the $y$-space index ($x$ and $y$ make up the horizontal plane). Thus, in order to start a simulation, initial conditions from three time levels are required. Now, with an initial estimate of the physical values at the new time level, the implicit corrector equations can be applied:

$$\zeta_{i,j}^{n+1} = \zeta_{i,j}^{n} - \frac{\Delta t}{24}(9E_{i,j}^{n+1} + 19E_{i,j}^{n} - 5E_{i,j}^{n-1} + E_{i,j}^{n-2}) \tag{8}$$

$$(\boldsymbol{u}_\alpha)_{i,j}^{n+1} = (\boldsymbol{u}_\alpha)_{i,j}^{n} - \frac{\Delta t}{24}(9\boldsymbol{F}_{i,j}^{n+1} + 19\boldsymbol{F}_{i,j}^{n} - 5\boldsymbol{F}_{i,j}^{n-1} + \boldsymbol{F}_{i,j}^{n-2}) \tag{9}$$

These equations are solved with Jacobi iteration, so the calculation of $E^{n+1}$ and $\boldsymbol{F}^{n+1}$ is performed with the free surface and velocity values from the previous iteration. To implement the algorithm, an additional grouping of the mixed space and time derivatives in the dispersive terms is required. Wei *et al.*'s (1995) paper gives a good description and justification of this grouping procedure.

Spatial differencing in the numerical model employs centered finite differences. All first order spatial derivatives are differenced with fourth order ($\Delta x^4 = \Delta y^4$) accurate equations, which are five-point differences. Second order spatial derivatives are approximated with three-point centered finite difference equations, which are second order accurate. The second order spatial derivatives are taken to lower order accuracy because these derivatives only appear in dispersive terms. The "combined" dispersive-numerical error for the second order derivatives is $O(\Delta x^2\mu^2)$, which is less than the error associated with first order spatial derivatives, $O(\Delta x^4)$, for all the grid spacings and wavelengths modeled in this paper.

## Moving Boundary Algorithm

The development of the moving boundary algorithm presented in this paper began with a search for a scheme that allows for the wet-dry boundary to exist at any location, not restrictively at a node on a fixed grid. One method of achieving this is through dynamic regridding, using a Lagrangian approach. Methods such as this have been used in finite difference and finite element nonlinear shallow water (NLSW) and Boussinesq equation models (e.g., Petera and Nasshei, 1996: Zelt, 1991). Lagrangian moving boundary techniques require numerical flexibility, in terms of utilizing constantly changing space and time steps, to be implemented in conjunction with a Eulerian-type model. This flexibility is not present in the current numerical scheme, and is difficult to achieve due to the nature of the required high-order derivatives, and so a different approach is developed in this paper.

Owing to the significant number of derivatives calculated by the numerical model ($\sim 50$ in 2D), it would be advantageous if the moving boundary scheme did not require any sort of special treatment of the derivatives near the wet-dry boundary (i.e., forward, backward, or low order finite differences). To require, for example, directional differences at the boundary leads to abundant conditional statements, making the programming tedious and the runtime longer. Therefore, the five-point centered finite differences that are employed in the numerical model are desired to be used at all locations, including those points near the shoreline, where neighboring nodes may be dry. With this in mind, the moving boundary scheme will employ a linear extrapolation of free surface displacement, $\zeta$, and velocity components, $u_o$ and $v_o$, from the fluid domain, through the wet-dry boundary, and into the dry region. Kowalik and Bang (1987) presented a similar approach of employing a linear extrapolation into the dry region, based on Sielecki and Wurtele's (1970) earlier developments. Their model uses an leap-frog scheme to approximate the NLSW equations, and is limited to one-dimensional, non-breaking problems. This paper will attempt to extend this idea to two horizontal dimension

breaking problems, using a high order numerical model.

An extrapolation through the wet-dry boundary permits this boundary to exist in-between nodal points. Figure 1 gives a numerical example of how the extrapolation is performed in a one-dimensional problem, showing a solitary wave interacting with a 1:20 slope. The free surface locations that are determined using the governing equations, (1)-(3), are shown by the solid line, whereas the linearly extrapolated points are shown by the dots. With extrapolated values of $\zeta$ and velocity components in the dry region, solving the model equations at wet nodes can proceed. When solving the model equations, five-point centered differences are employed to approximate the spatial derivatives. Although no derivatives are calculated at dry (extrapolated) points, the physical values of free surface and velocity at these points are used to evaluate derivatives at neighboring wet points. The determination of the location of the wet-dry boundary is performed once per time step, immediately after the predictor step. The moving boundary technique is numerically stable, and does not require any additional dissipative mechanisms. No filtering in the fluid domain is performed in any of the simulations presented in this paper.

The first step in the extrapolation boundary method is to determine a nodal boundary dividing an area where the model equations are to be solved (i.e., the wet region) and an area to be extrapolated (i.e., the dry region). The criteria employed to determine this dividing point is dependant on the total water depth, $\mathcal{H}$, where $\mathcal{H} = h + \zeta$. If $\mathcal{H} > \delta$, where $\delta$ is some threshold, the model equations will be applied at the node, otherwise the physical variables at the node will be extrapolated from a neighboring node. The value of $\delta$ should be small: a value of $a_o/50$, where $a_o$ is the incident wave amplitude, was used for all simulations presented in this paper. This value is chosen based on stability. It was found that decreasing this value can occasionally cause stability problems, especially for simulations with strong wave breaking or ones that include bottom friction. The instability problems associated with these two

parameterizations are due to the fact that they are inversely proportion to the total water depth. A very small total water depth may create an equally large dissipative momentum flux, which can lead to an overflow in the iterative numerical scheme. However, for non-breaking simulations without bottom friction, a $\delta$ value of $a_\circ/5000$ could be stably employed. A convergence check, by changing $\delta$, will be discussed briefly in the next section.

For the simple one dimensional problem shown in Figure 1, the extrapolation procedure is straightforward. Using the two wet points (where $\mathcal{H} > \delta$) nearest to the wet-dry boundary, a linear extrapolation into the dry (where $\mathcal{H} < \delta$) region is performed. For the two-dimensional case, the procedure is slightly more complex, but the logic is identical. The 2D extrapolation is performed by checking the surrounding eight points of a dry node. For each surrounding node that is wet, a 1D linear extrapolation is used to estimate the free surface at the dry node. Since more than one surrounding node can be wet, the free surface value at the dry node is taken to be the average of the 1D extrapolations. This procedure is simply repeated for the second layer of dry nodes, extrapolating from the just-extrapolated first layer of dry nodes. For both 1D and 2D cases, a four-point filter is passed over the extrapolated region, smoothing $\zeta$, $u_\alpha$, and $v_\alpha$, and eliminating possible slope discontinuities in the extrapolation. Additionally, there is one possible arrangement of wet and dry nodes that can not be allowed to exist. When a wet node is grouped with dry nodes on both sides, i.e., if node $i$ is wet and both $i-1$ and $i+1$ are dry, the extrapolation is impossible for both dry nodes. When this situation is developed, the wet node is no longer considered to be in the fluid domain, and its value will be extrapolated.

As the shoreline moves up and down the slope, the number of wet and dry points changes. For example, at time $n-1$, node $i-1$ is wet and node $i$ is dry, and its free surface value has been extrapolated. Now, at time $n$, the new extrapolation for node $i$ yields a total water depth greater than $\delta$. Node $i$ is therefore now a wet node, and its

value is no longer extrapolated, but calculated by (1)-(3).

As the extrapolated, dry points are soley a function of the neighboring wet points, the finite differences that incorporate these dry points cannot truly be thought of as centered finite differences. Let us consider a one horizontal dimension problem, and focus on 6 grid points, numbered from $i = -3$ to $i = 2$. At the time that we take a snapshot, the shoreline exists somewhere between point $i = 0$ and $i = 1$. Points to the left of this point are wet ($i = -3, -2, -1, 0$), and points to the right are dry ($i = 1, 2$). At the wet points, the governing equations, using the predictor-corrector scheme, are solved. At the dry points, the free surface and velocity are linearly extrapolated, and can be given as:

$$P_1 = 2P_0 - P_{-1} \tag{10}$$

$$P_2 = 3P_0 - 2P_{-1} \tag{11}$$

where $P$ represents both $\zeta$ and $u_\alpha$, and the subscripts represent the $i$-index. Substituting the extrapolated values of points $i = 1$ and $i = 2$ into the $4^{th}$ order first derivative difference equation:

$$\frac{\partial P_0}{\partial x} = \frac{P_{-2} - 8P_{-1} + 8P_1 - P_2}{12\Delta x} \tag{12}$$

yields, after some manipulation:

$$\frac{\partial P_0}{\partial x} = \frac{1}{6}\left[\frac{\partial P_0}{\partial x}\right]_{2B} + \frac{5}{6}\left[\frac{\partial P_0}{\partial x}\right]_{1B} \tag{13}$$

where $2B$ stands for the $2^{nd}$ order backward (or upwind) finite difference:

$$\left[\frac{\partial P_0}{\partial x}\right]_{2B} = \frac{P_{-2} - 4P_{-1} + 3P_0}{2\Delta x} \tag{14}$$

and $1B$ stands for the $1^{st}$ order backward (or upwind) finite difference:

$$\left[\frac{\partial P_0}{\partial x}\right]_{1B} = \frac{-P_{-1} + P_0}{\Delta x} \tag{15}$$

Using the same approach, the derivative at $i = -1$ can be rewritten as:

$$\frac{\partial P_{-1}}{\partial x} = \frac{1}{2}\left[\frac{\partial P_0}{\partial x}\right]_{3T} + \frac{1}{3}\left[\frac{\partial P_0}{\partial x}\right]_{2C} + \frac{1}{6}\left[\frac{\partial P_0}{\partial x}\right]_{1B} \tag{16}$$

where $3T$ stands for the $3^{rd}$ order tilted (in the backward direction) finite difference:

$$\left[\frac{\partial P_{-1}}{\partial x}\right]_{3T} = \frac{P_{-3} - 6P_{-2} + 3P_{-1} + 2P_0}{6\Delta x} \tag{17}$$

and $2C$ stands for the $2^{nd}$ order centered finite difference:

$$\left[\frac{\partial P_{-1}}{\partial x}\right]_{2C} = \frac{-P_{-2} + P_0}{2\Delta x} \tag{18}$$

So clearly, hidden within the linear extrapolation, is leading order dissipation associated with the upwind differencing, even though a $4^{th}$ order centered difference is being taken. Note that the extrapolations are done for both free surface and velocity, so the moving boundary scheme will dissipate both momentum and mass.

The same analysis can be done for the second-order in space derivatives. At the point $i = 0$, the curvature is given as

$$\frac{\partial^2 P_0}{\partial x^2} = \frac{P_{-1} - 2P_0 + P_1}{\Delta x^2} \tag{19}$$

which is, with the linear extrapolation of $P_1$, exactly zero at this point. Therefore, at the first wet point, all second-order differences disappear, and the governing equations (1)-(3), reduce to the nonlinear shallow water wave equations. Now, looking at the whole picture of first and second order spatial derivatives, we see that numerical dissipation is not as great as it might appear. It was shown that the first spatial derivative at the first wet point, $\frac{\partial P_0}{\partial x}$, is in large part approximated by the first order upwind finite difference, $\left[\frac{\partial P_0}{\partial x}\right]_{1B}$. The leading numerical truncation error of the upwind difference is $\frac{\Delta x}{2}\frac{\partial^2 P_0}{\partial x^2}$, which is the source of the numerical dissipation in upwind schemes. However, at this first wet point, the second spatial derivative, $\frac{\partial^2 P_0}{\partial x^2}$, is forced to zero in the numerical model. The leading numerical truncation error of the second spatial derivative taken with a second order centered difference formula is $\frac{\Delta x^2}{12}\frac{\partial^4 P_0}{\partial x^4}$. Therefore,

the leading order, dissipative truncation error of the upwind difference at the first wet point is actually $\frac{\Delta x}{2}\left(\frac{\Delta x^2}{12}\frac{\partial^3 P_0}{\partial x^3}\right)$. At the second wet point, the first spatial derivative, $\frac{\partial P_{-1}}{\partial x}$, also incorporates upwind differencing (although its importance is 5 times less here as compared to the first wet point). As the second spatial derivative at this point is non-zero, there will at this point occur dissipation proportional to the second spatial derivative, equal to $\frac{\Delta x}{10}\frac{\partial^2 P_{-1}}{\partial x^2}$.

It is worth noting that these issues with leading order numerical dissipation associated with the linear extrapolation could be avoided by utilizing a higher order polynomial extrapolation. Unfortunately, these higher order extrapolations created stability problems with breaking and near-breaking wave runup. As these waves approach the beach, typically the curvature of the free surface is large very near the shoreline. The large curvature created rapidly varying extrapolated values, which then led to numerical roundoff problems.

It would seem to be unnecessary to perform the linear extrapolation in the numerical model, as one could simply code a couple conditional statements, where if the current calculation node in the model is near the wet/dry boundary, use upwind differencing, instead of centered differencing. This too was attempted, but always resulted in $2\Delta x$ waves. It was found, through trial and error, that stability comes from the prediction of velocity in the dry region. In this numerical scheme:

$$(\boldsymbol{u}_o)^{n+1} = f\left[(\boldsymbol{u}_o)^{n+1}, (\boldsymbol{u}_o)^{n}, (\boldsymbol{u}_o)^{n-1}, (\boldsymbol{u}_o)^{n-2}\right] \tag{20}$$

as well as a function of numerous other parameters. Let us say that at time $n$, the point $i$ was dry. Now, at time $n+1$, the point $i$ is wet. What are the previous values of velocity, at times $n-2$, $n-1$, and $n$, to use in the predictor-corrector scheme? An answer of zero velocity would be most obvious, because physically, there was no fluid. Using a zero velocity at these times in the numerical model led to $2\Delta x$ waves. So for this type of model, a zero velocity at previous times does not work. Using the linearly extrapolated velocities at the previous times of $n-2$, $n-1$, and $n$ works well. It could

be argued that the velocities at the previous "dry" times should not be zero, in fact they should not be anything - they are undefined. Thus, this model is simply taking a reasonable guess at what the undefined velocity should be in order to yield a stable and accurate numerical model. The linear spatial extrapolation is not just important as a spatial extrapolation (which is equivalent to some combination of upwind differencing) - it is especially important as a temporal extrapolation.

As a primary check of the algorithm, its ability to conserve mass is analyzed. Mass is defined as the integral of the free surface elevation, not the integral of the total water depth. A range of solitary waves, from $0.01 < \varepsilon < 0.4$ propagating up one-dimensional slopes of 1:10, 1:20, and 1:50 were checked for conservation of mass. Note that when referencing solitary waves, $\varepsilon = H/h$, where $H$ is the solitary wave height. The solitary wave is generated using the analytic formulas presented in Wei and Kirby (1995), which are derived from the weakly nonlinear, "extended" Boussinesq equations. Figure 2 summarizes the conservation properties of these cases. Shown in this figure is the fractional change in mass of the soliton, after completely exiting the nearshore region. Thus, these fractions represent the change in mass, scaled by the initial mass, after interaction with the shoreline is over. There are two clear trends: (1) for a given slope, the error in conservation is larger with larger wave heights (2) for a given wave height, the error is larger with milder slopes. Both of these trends are consistent with the expectation that the numerical error is larger when the curvature near the shoreline is larger. For all the simulations shown in Fig. 2 and contained in this paper, the change in mass is less than 1% of the initial mass (or the mass contained in one wavelength for the periodic wave test).

## Validation in One Horizontal Dimension

*Sine Wave Runup*

As a first check of the moving boundary model, a monochromatic wave train is let to runup and rundown a plane beach. This situation has an analytic solution derived by Carrier and Greenspan (1958). Their derivation makes use of the NLSW equations, and thus for consistency the dispersive ($\mu^2$) terms will be ignored in the numerical simulations for this comparison. The wave and slope parameters for this test case are identical to those used by Madsen *et al.* (1997) and Kennedy *et al.* (2000). A wave train with height 0.006 m and period of 10 s travels in a one dimensional channel with a depth of 0.5 m and a slope of 1:25. For the numerical simulation, a grid size of 0.045 m and a time step 0.01 s are used: bottom friction is not included and the wave does not break. It should be noted that the grid size is an order of magnitude smaller than what is required for a convergent solution. This small grid size is used only to make certain that the boundary location travels a significant number of grid points ($> 10$) during runup and rundown.

The results of the numerical simulation are shown in Figure 3. Figure 3a) shows the numerical free surface at various times, along with two profiles of the analytic free surface. The comparison between analytic and numerical horizontal shoreline movement is shown as Figure 3b). The agreement is good. Also, as a check on the convergence properties of $\delta$, an additional simulation with $\delta = a_o/5000$ was run. A comparison between the $\delta = a_o/50$ shows little difference, and is not given in this paper . The maximum deviation in shoreline at any time between the two $\delta$ runs is on the order of 0.01% of the maximum excursion.

*Nonbreaking and Breaking Solitary Wave Runup*

Solitary wave runup and rundown was investigated experimentally by Synolakis (1986,1987). In his work, dozens of experimental trials were performed, encompassing

two orders of magnitude of solitary wave height. The beach slope was kept constant at 1:19.85. Many researchers have used this data set to validate numerical models (e.g., Zelt, 1991: Lin *et al.*, 1999). To compare with this data, solitary waves with heights in the range of $0.005 < \varepsilon < 0.5$ are made to runup and rundown a slope and the maximum vertical runup is calculated. Note that this range includes both non-breaking and breaking waves. For all simulations, $\Delta x/h = 0.3$ and $\Delta t\sqrt{g/h} = 0.03$. As a test of the sensitively of wave runup to bottom friction, three sets of simulations were undertaken with different bottom friction coefficients, $f$. Set 1 was run with no bottom friction, Set 2 with $f = 10^{-3}$, and Set 3 with $f = 10^{-2}$.

The numerical results are compared with the experimental data in Figure 4, where maximum vertical runup is scaled by the water depth. For the smallest solitary waves ($\varepsilon < 0.01$) bottom friction does not affect the runup, as maximum runup is identical for all three numerical sets. This is consistent with previous research (e.g., Liu *et al.* 1995), where it is shown that bottom friction effects are minor for nonbreaking waves, and will typically alter the runup by $< 0.5\%$ of the maximum. For larger wave heights, breaking is initiated, both experimentally and numerically, near $\varepsilon = 0.04$. It is at this point that the numerical runup for Set 1 and Set 2 begins to diverge. Note that due to the log-log scale used in Figure 4, the deviation in maximum runup may not be apparent. As an example, for $\varepsilon = 0.3$, scaled runup with no bottom friction is 1.21, with $f = 10^{-3}$ runup is 0.73, and with $f = 10^{-2}$ is 0.45, which are significantly different. Use of $f = 5 * 10^{-3}$ yields the best agreement with experimental data for this particular case.

It would seem that inclusion of an accurate bottom friction parameterization becomes increasingly important with increasing degree of wave breaking. The probable reason is that as a broken wave runs up a mild slope, it travels up the slope as a fairly thin layer of water. As can be seen from (5), the smaller the total water depth, the more important bottom friction becomes.

Synolakis (1986) also photographed the waves during runup and rundown. One

set of these snapshots, for $\varepsilon = 0.28$, was digitized and compared with the numerical prediction, shown in Figure 5. The numerical simulation shown in this figure uses $f = 10^{-3}$. The wave begins to break between Figs. 5a) and 5b), and the runup/rundown process is shown in Figs. 5c)-d). In Fig 5c), numerical snapshots from three other models are plotted. The comparisons indicate a significant improvement over weakly nonlinear Boussinesq equation results of Zelt (1991) and the NLSW results of Titov and Synolakis (1995). Additionally, the numerical results presented in this paper compare favorably to the two dimensional (vertical plane) results of Lin *et al.* (1999), which makes use of a complex turbulence model.

## Validation in Two Horizontal Dimensions

*Long Wave Resonance in a Parabolic Basin*

Analytic solutions exist for few nonlinear, two horizontal dimension problems. One such solution is that for a long wave resonating in an circular parabolic basin. Thacker (1981) presented a solution to the NLSW equations, where the initial free surface displacement is given as:

$$\zeta(r, t=0) = h_\circ \left[ \frac{(1-A^2)^{1/2}}{1-A} - 1 - \frac{r^2}{a^2} \left\{ \frac{1-A^2}{(1-A^2)^2} - 1 \right\} \right] \tag{21}$$

and the basin shape is given by:

$$h(r) = h_\circ \left( 1 - \frac{r^2}{a^2} \right) \tag{22}$$

where

$$A = \frac{a^\downarrow - r_\circ^\downarrow}{a^\downarrow + r_\circ^\downarrow}, \tag{23}$$

$h_\circ$ is the center point water depth, $r$ is the distance from the center point, $a$ is the

distance from the center point to the zero elevation on the shoreline, and $r_\circ$ is the distance from the center point to the point where the total water depth is initially zero. The numerical values used for this test are : $h_\circ = 1.0m$, $r_\circ = 2,000m$, and $a = 2,500m$. The centerline initial condition and depth profile is shown in Figure 6. Thacker showed the solution to this problem to be:

$$\zeta(r,t) = h_\circ \left[ \frac{(1-A^2)^{1/2}}{1-A\cos wt} - 1 - \frac{r^2}{a^2}\left\{ \frac{1-A}{(1-A\cos wt)^2} - 1 \right\} \right] \tag{24}$$

where

$$w = \frac{1}{a}(8gh_\circ)^{1/2} \tag{25}$$

and g is gravity. Cho (1995) also used this solution as a test for his NLSW moving boundary model. Cho's model, an explicit leap-frog finite-difference scheme which includes numerical frequency dispersion, reproduced the analytical solution very well for roughly one-half of an oscillation, but began to deviate soon after. A simulation using the extrapolation boundary technique presented in this paper was undertaken, truncating the dispersive terms in (2) and (3) to be consistent with the NLSW solution, and using $\Delta x = 28m$ and $\Delta t = 0.9s$. Bottom friction is not included and the wave does not break. The comparison between the numerical and analytic results is shown in Figure 7. The numerical free surfaces shown in Fig 7a)-d) are from the fifth oscillation, and show excellent agreement with the analytic solution. Additionally, a test using the full equations (2) and (3), with dispersive terms, was performed. Interestingly, the wave field in this situation becomes chaotic after the first oscillation, and shows a similar pattern of divergence from the analytical solution as Cho's results. Therefore this parabolic basin comparison would appear to be an ideal test for NLSW models, as the effects of numerical dispersion or dissipation become evident rapidly.

*Runup on a Conical Island*

Briggs *et al.* (1994) presented a set of experimental data for solitary wave interaction around a conical island. The slope of the island is 1:4 and the water depth is $0.32m$. Three cases were simulated, corresponding to solitary wave heights of 0.013 $m$ ($\varepsilon = 0.04$) , 0.028 $m$ ($\varepsilon = 0.09$), and 0.058 $m$ ($\varepsilon = 0.18$). In addition to recording free surface elevation at a half dozen locations, maximum wave runup around the entire island was measured. This data set has been used by several researchers to validate numerical runup models (e.g., Liu *et al.*, 1995: Titov and Synolakis, 1998: Chen *et al.*, 2000). In this paper, free surface elevation is compared at the locations shown in Figure 8. Gages #6 and #9 are located near the front face of the island, with #9 situated very near the initial shoreline position. Gages #16 and #22 are also located at the initial shoreline, where #16 is on the side of the island and #22 on the back face.

Simulations were performed using $\Delta x = 0.15m$ and $\Delta t = 0.02s$: bottom friction is neglected for these numerical tests. A soliton is placed in the numerical domain, as an initial condition. Numerical-experimental time series comparisons are shown in Figure 9. Figures 9a)-d) are for Case 1 ($\varepsilon = 0.04$), 9e)-h) are for Case 2 ($\varepsilon = 0.09$), and 9i)-l) are for Case 3 ($\varepsilon = 0.18$). The gage number is shown in the upper left of each subplot. For all comparisons, the lead wave height and shape is predicted very well with the current model. Also, for all comparisons, the secondary depression wave is not predicted well. The numerical results show less of a depression following the main wave than in the experiments. This deviation is consistent with other runup model tests (e.g., Liu *et al.*, 1995: Chen *et al.*, 2000). The agreement of Case 3 is especially notable, as the soliton breaks along the back side of the island as the trapped waves intersect. This breaking occurs both experimentally, as discussed in Liu *et al.* (1995), and numerically.

As mentioned, maximum runup was also experimentally recorded. The vertical runup heights are converted to horizontal runups, scaled by the initial shoreline radius, and plotted on Figure 10. The crosshairs represents the experimental data, where Fig.

10a) is for Case 1., Fig. 10b) is for Case 2, and Fig. 10c) is for Case 3. The numerical maximum inundation is also plotted, given by the solid line. The agreement for all cases is very good.

*Soliton Evolution in a Trapezoidal Channel*

Peregrine (1969) presented laboratory experiments wherein solitary waves propagated through a trapezoidal channel. To experimentally create the solitons, a piston wavemaker was cut to fit the channel and could slide horizontally along the trapezoidal channel. In the numerical simulations, as it is difficult to implement a piston wavemaker in a trapezoidal channel, the solutions of solitary waves in rectangular channels are used as an initial condition everywhere in the channel.

Once a solitary wave enters a trapezoidal channel, it deforms. Eventually, in certain channels, the leading wave will reach a quasi steady state, and the waveform will not change in time. After reaching this quasi steady state, numerical results of the lead wave height are compared with Peregrine's experimental results. The comparisons are shown in Figure 11. For this comparison, a trapezoidal half - channel (one vertical wall and one sloping side wall) with constant depth width of $1.5h_o$, where $h_o$ is the depth at the non-sloping part the channel, and a sidewall slope of 1:1 is employed. Three different amplitude solitary waves ($a = 0.08h_o$, $a = 0.12h_o$, and $a = 0.18h_o$) are simulated and compared with experimental results. The numerical results show reasonably good agreement with laboratory data, although there is a clear trend of under prediction of wave height near the shoreline.

An interesting property of wave evolution in certain trapezoidal channels is the successive regeneration of the wave front. When the channel is wide enough, with respect to the wavelength, and the side-wall slope is gradual enough, the wave energy

that is reflected off the side walls does not resituate in the original wave, as occurs in the Peregrine (1969) experiments discussed above, but forms a distinct wave behind the original wave front. Wave energy is continually transferred from the original wave front into the new wave behind, until the original wave front virtually disappears. The new front has a smaller height, and a slightly longer wavelength than the original.

One example of the phenomenon is discussed in this section. A half channel is created (one vertical wall at $y = 0$, one sloping side wall), with a constant water depth width of $9h_\circ$ and a length of $250h_\circ$, where $h_\circ$ is the constant water depth along the center of the channel. The side wall is sloped at 1:5. A solitary wave, with wave height $0.1h_\circ$ is placed in the channel as an initial condition. The wave does not break, and bottom friction is not included. For this simulation, $\Delta x/h_\circ = 0.14$ and $\Delta t\sqrt{g/h_\circ} = 0.05$ are used.

Figure 12 shows four snapshots, in plan view, of the wave propagating through the part of channel. The dashed line plotted across the channel is the $x - ct = 0$ line, where $c$ is the linear long wave speed, $\sqrt{gh_\circ}$. Seafloor elevation contours are also shown on each plot. Fig. 12a) shows the wave soon after the simulation has begun, and the front is beginning to arc, due to slower movement in the shallower water. By the time shown in Fig. 12b), wave energy has reflected off the slope, and has formed a second, trailing, wave crest behind the original wave. As this slope-reflected wave crest interacts with the vertical wall (or centerline of channel), a Mach stem forms at the vertical wall, and virtually no wave energy is reflected off the vertical wall. Also at this time, an oscillatory train, trailing the leading wave, forms along the slope. At time = 65, shown in Fig. 12c), most of the wave energy has transferred from the original wave front, to the secondary crest. In the last plot, Fig. 12d), the process has started to repeat itself, evidenced by the lobe growing behind the second front, near a depth of 0.9.

This process can be examined from a different perspective with Figure 13. This figure shows numerous time series, taken along the centerline of the channel ($y = 0$).

Also shown are three characteristic lines. Following the first characteristic, we can see that the lead wave as nearly disappeared by $x = 140h_o$, whereas the secondary wave is clearly defined by this point. The process repeats: at $x = 230h_o$, the secondary wave is vanishing, and a third wave front is beginning to take shape. The phenomenon shown in Figs. 12 and 13 is an interesting one, although not wholly unexpected, and is a demonstration of the interaction between nonlinearity and refraction.

## Conclusion

A moving boundary algorithm is developed for use with depth integrated equations. Used here in conjunction with a fixed grid finite difference model, the moving boundary algorithm could also be employed by a finite element scheme. Founded around the restrictions of the high-order numerical wave propagation model, the moving boundary scheme employs linear extrapolation of free surface and velocity through the wet-dry boundary, into the dry region. The linear extrapolation is simple to implement and can be straightforwardly incorporated into a numerical model. The technique is numerically stable, does not require any sort of additional dissipative mechanisms or filtering, and conserves mass.

The moving boundary is tested for accuracy using one and two dimensional analytical solutions and experimental data sets. Nonbreaking and breaking solitary wave runup is accurately predicted, yielding a validation of both the eddy viscosity breaking parameterization and the runup model. For strongly breaking waves, the proper numerical estimation of bottom friction is shown to be important. Two dimensional wave runup in a parabolic basin and around a conical island is investigated, and comparisons with published data show excellent agreement. Also, solitary wave evolution in a trapezoidal channel is simulated, and an interesting phenomenon is examined.

## Acknowledgement

This research has been supported in part by National Science Foundation grants to Cornell University (CMS-9908392, CTS-9808542).

### References

Balzano, A. (1998). "Evaluation of methods for numerical simulation of wetting and drying in shallow water flow models." *Coast. Engng.*, 34, 83-107.

Briggs, M. J., Synolakis, C. E., and Harkins, G. S. (1994). "Tsunami runup on a conical island." *Proc., Waves-Physical and Numerical Modeling*, 446-455.

Carrier, G. F., and Greenspan, H. P. (1958). "Water waves of finite amplitude on a sloping beach." *Journal of Fluid Mechanics*, 4, 97-109.

Chen, Q., Kirby, J. T., Dalrymple, R. A., Kennedy, A. B., and Chawla, A. (2000). "Boussinesq modeling of wave transformation, breaking, and runup. Part I: 2D." *Journal of Waterway, Port, Coastal and Ocean Engng.*, 126(1), 57-62.

Cho, Y.-S., (1995). "Numerical simulations of tsunami propagation and run-up.", Ph. D. Thesis, Cornell University. 264 pgs.

Gopalakrishnan, T. C. (1989). "A moving boundary circulation model for regions with large tidal flats.", *International Journal for Numerical Methods in Engineering* , 28, 245-260.

Hsiao, S.-C. and Liu, P. L.-F. (2002). "Permeable effects on nonlinear water waves" *Proceedings of the Royal Society of London*, in press.

Kennedy, A. B., Chen, Q., Kirby, J. T., and Dalrymple, R. A. (2000). "Boussinesq modeling of wave transformation, breaking, and runup. Part I: 1D." *Journal of Waterway, Port, Coastal and Ocean Engng.*, 126(1), 39-47.

Kowalik, Z. and Bang, I. (1987). "Numerical computation of tsunami run-up by the upstream derivative method." *Science of Tsunami Hazards*, 5(2), 77-84.

Nwogu, O. (1993). "Alternative form of Boussinesq equations for nearshore wave propagation." *Journal of Waterway, Port, Coastal and Ocean Engng.*, 119(6), 618-638.

Leendertse, J. J. (1987). "Aspects of SIMSYS2D, a system for two-dimensional flow computation." R-3752-USGS. Rand Corp., Santa Monica, CA, 80.

Lin, P., Chang, K.-A., and Liu, P. L.-F. (1999). "Runup and rundown of solitary waves on sloping beaches." *Journal of Waterway, Port, Coastal and Ocean Engng.*, 125(5), 247-255.

Liu, P. L.-F. (1994). "Model equations for wave propagation from deep to shallow water", in *Advances in Coastal Engineering*, Vol. 1, (ed. P. L.-F. Liu), 125-157.

Liu, P. L.-F., Cho, Y.-S., Briggs, M. J., Kanoglu, U., and Synolakis, C. E. (1995). "Runup of solitary waves on a circular island.", *Journal of Fluid Mechanics*, 302, 259-285.

Lynett, P., Liu, P. L.-F., Losada, I., and Vidal, C. (2000). "Solitary wave interaction with porous breakwaters." *Journal of Waterway, Port, Coastal and Ocean Engng.*, 126(6), 314-322.

Lynett, P. and Liu, P. L.-F. (2002a). "A numerical study of submarine landslide generated waves and runup." in review *Proceedings of the Royal Society of London.*

Lynett, P. and Liu, P. L.-F. (2002b). "A two-dimensional, depth-integrated model for internal wave propagation." accepted in final form *Wave Motion.*

Madsen, P. A., and Sorensen, O. R. (1992). "A new form of the Boussinesq equations with improved linear dispersion characteristics. Part II: A slowly varying bathymetry ." *Coast. Engng.*, 18, 183-204.

Madsen, P. A., Sorensen, O. R., and Schaffer, H A. (1997). "Surf zone dynamics simulated by a Boussinesq-type model. Part I: Model description and cross-shore motion of regular waves." *Coast. Engng.*, 32, 255-287.

Peregrine, D. H. (1967). "Long waves on a beach.", *Journal of Fluid Mechanics*, 27, 815-827.

Peregrine, D. H. (1969). "Solitary waves in trapezoidal channels", *Journal of Fluid Mechanics*, 35, 1-6.

Petera, J., and Nassehi, V. (1996). "A new two-dimensional finite element model for the shallow water equations using a Lagrangian framework constructed along fluid particle trajectories.", *International Journal for Numerical Methods in Engineering* , 39,

4159-4182.

Sielecki, A. and Wurtele, M.G. (1970). "The numerical integration of the nonlinear shallow-water equations with sloping boundaries." *Journal of Computational Physics*, 6, 219-236.

Synolakis, C.E. (1986). "The runup of long waves." PhD thesis, California Institute of Technology, Pasadena, Calif.

Synolakis, C.E. (1987). "The runup of solitary waves." *Journal of Fluid Mechanics*, 185, 523-545

Tao, J. (1983). "Computation of wave runup and wave breaking." *Internal Report*, Danish Hydraulics Institute, Denmark.

Tao, J. (1984). "Numerical modeling of wave runup and breaking on the beach." *Acto Oceanologica Sinica*, 6(5), 692-700 (in Chinese).

Thacker, W. C. (1981). "Some exact solutions to the nonlinear shallow water wave equations." *Journal of Fluid Mechanics*, 107, 499-508.

Titov, V. V., and Synolakis, C. E. (1998). "Numerical modeling of tidal wave runup." *Journal of Waterway, Port, Coastal and Ocean Engng.*, 124(4), 157-171.

Wei, G. and Kirby, J. T. (1995). "A time-dependent numerical code for extended Boussinesq equations." *Journal of Waterway, Port, Coastal and Ocean Engng.*, 120, 251-261.

Wei, G., Kirby, J. T., Grilli, S. T., and Subramanya, R. (1995). "A fully nonlinear Boussinesq model for surface waves. Part I. Highly nonlinear unsteady waves." *Journal of Fluid Mechanics*, 294, 71-92.

Zelt, J. A. (1991). "The runup of nonbreaking and breaking solitary waves." *Coast. Engrg.*, 15, 205-246.

**Figure 1.** Runup and rundown of a solitary wave, where extrapolated nodes are shown by the dots.

**Figure 2.** Fractional change in mass for breaking and non-breaking solitary waves interacting with 3 different planar slopes. Simulations where breaking occurs are indicated by the $x$'s, non-breaking results by the $o$'s.

**Figure 3.** Sine wave runup on a planar beach, a) Numerical free surface at various times, analytic free surface is shown by the dashed line ($--$), and is only compared for the maximum and minimum shoreline movement profiles. b) Comparison between analytical ($--$) and numerical ($-$) shoreline movement.

**Figure 4.** Nondimensional maximum runup of solitary waves on a 1:19.85 beach versus nondimensional wave hieght. The points represent experimental data taken from Synolakis (1986), the dotted line is the numerical result with no bottom friction, the solid line is the numerical result with a bottom friction coefficient, $f$, of $10^{-3}$, and the dashed line with $f = 10^{-2}$.

**Figure 5.** Breaking solitary wave runup and rundown on a planar beach at $t(g/h)^{1/2}$ = a) 15, b) 20, c) 25, d) 45. The solid line represents the numerical results and the points experimental data. In c) the dashed line represents numerical results by Lin et al. (1999) (closest to experiment and numerical results presented in this paper), the dotted line represents results by Zelt (1991), and the dashed-dotted line results by Titov and Synolakis (1995).

**Figure 6.** Initial free surface and depth profile for parabolic basin test.

**Figure 7.** Centerline free surface profiles for numerical (——) and analytical (· · ·) bowl oscillation solutions at t= a) $5T$, b) $5\frac{1}{6}T$, c) $5\frac{1}{3}T$ , d) $5\frac{1}{2}T$, where $T$ is the oscillation period.

**Figure 8.** Conical island setup. The gage locations are shown by the dots, and the wave approaches the island from the left.

**Figure 9.** Experimental (- -) and numerical (–) time series for solitary wave interaction with a conical island. Figures a) - d) are for case A, e) - h) are for case B, and i) - l) are for case C. The gage number is shown in the upper left.

**Figure 10.** Maximum horizontal runup, scaled by the initial shoreline radius, for case A a), case B b), and case C c). Experimental values are shown by the stars and the numerical results by the solid line.

**Figure 11.** The transverse profile of a solitary wave in a trapezoidal channel. The continuous line shows the numerical result: the crosses indicate the measured profile digitized from Peregrine's (1969) paper.

**Figure 12.** Evolution of a solitary wave in a trapezoidal channel (half channel shown), at $t(g/h)^{1/2}$ = a) 7.5 b) 35 c) 65 d) 93. Seafloor elevation contours are shown at increments of 0.5 $h_o$, by the solid lines. The line of $x - ct = 0$ is shown by the dashed line.

**Figure 13.** Time series along the centerline of the channel ($y = 0$): location of each time series is note along the right border of the figure. Characteristics are shown by the dashed-dotted lines.

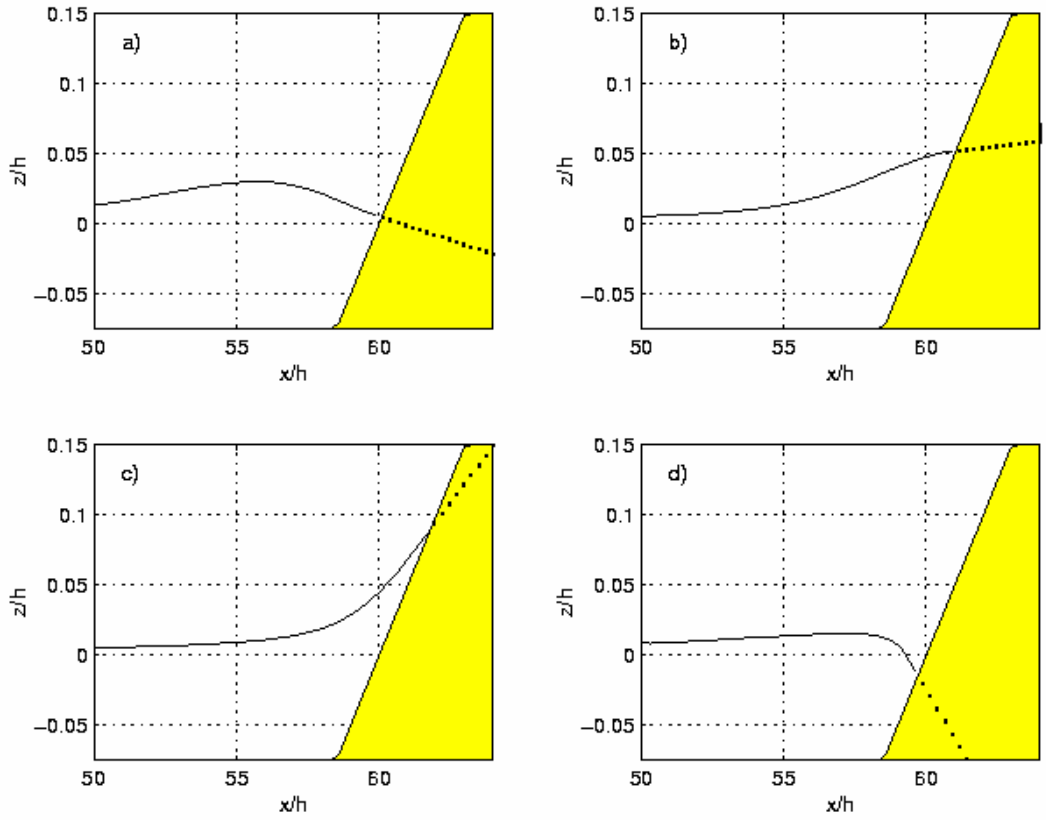


Figure 1, Lynett *et al.*

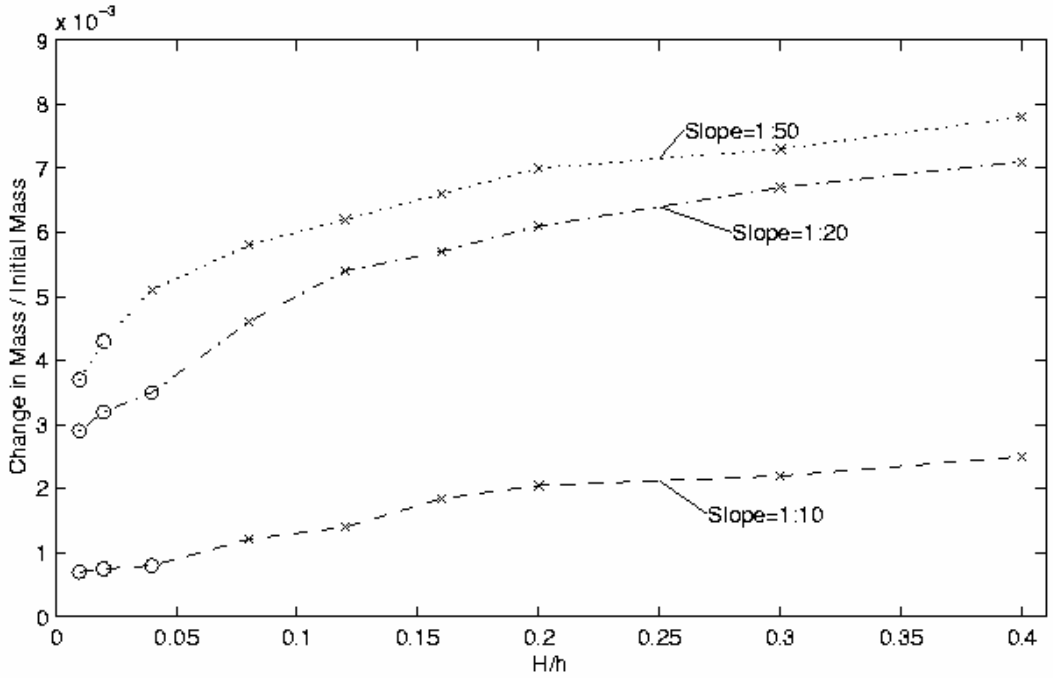


Figure 2, Lynett *et al.*

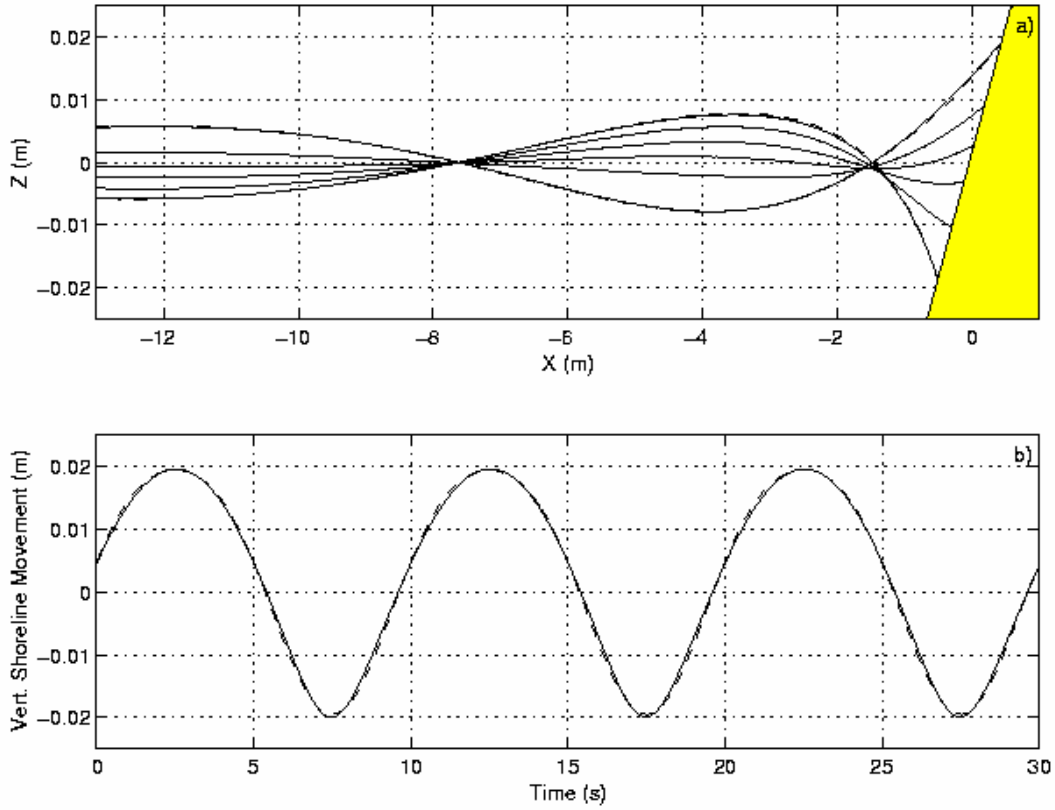


Figure 3, Lynett *et al.*

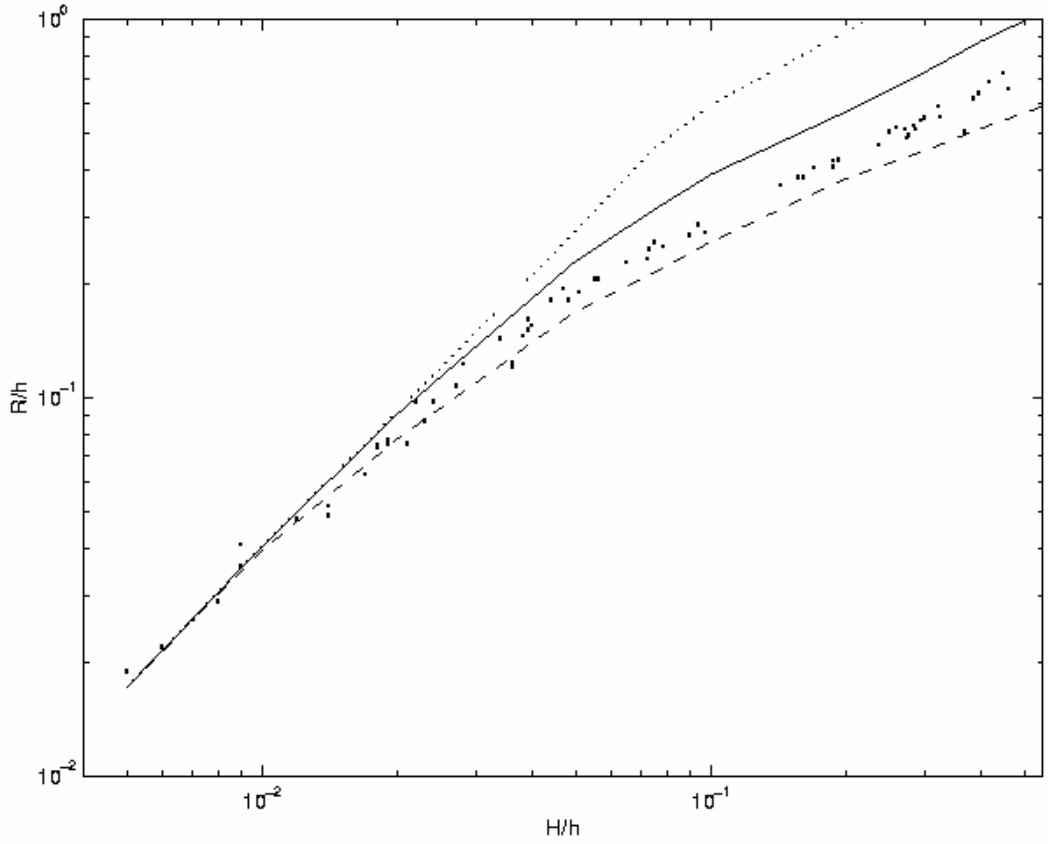


Figure 4, Lynett *et al.*

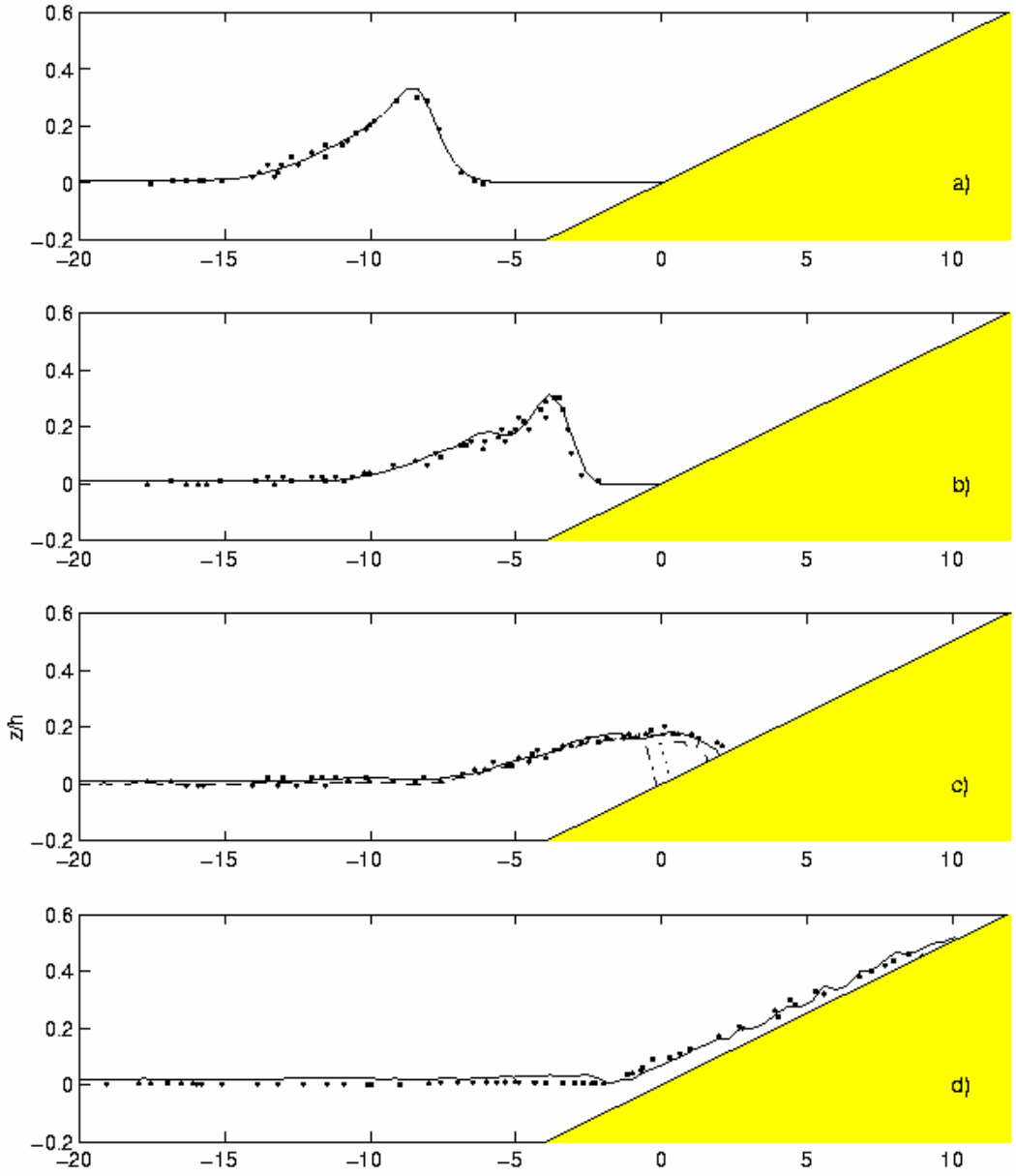


Figure 5, Lynett *et al.*

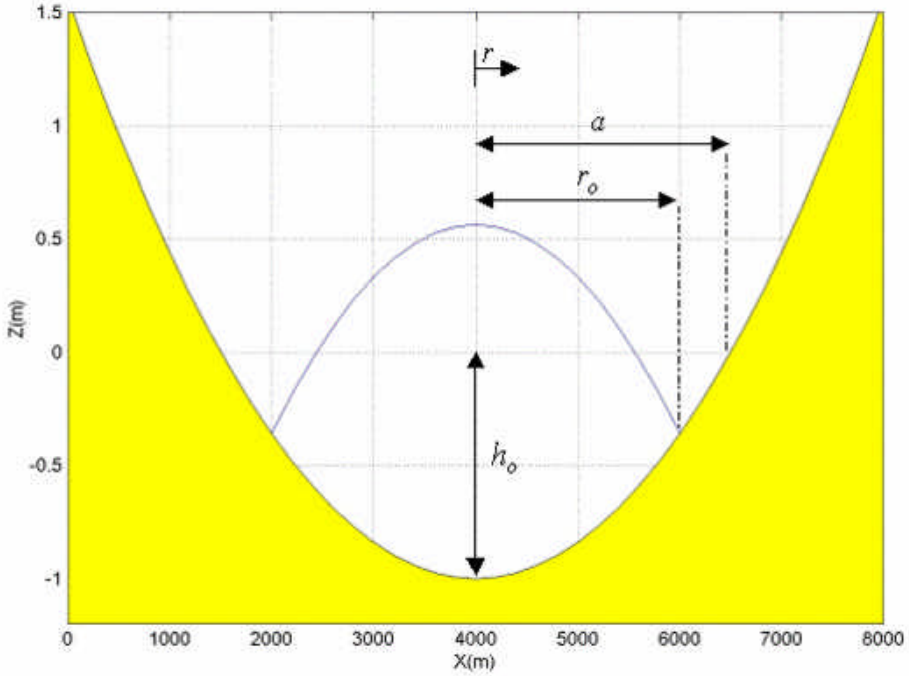


Figure 6, Lynett *et al.*

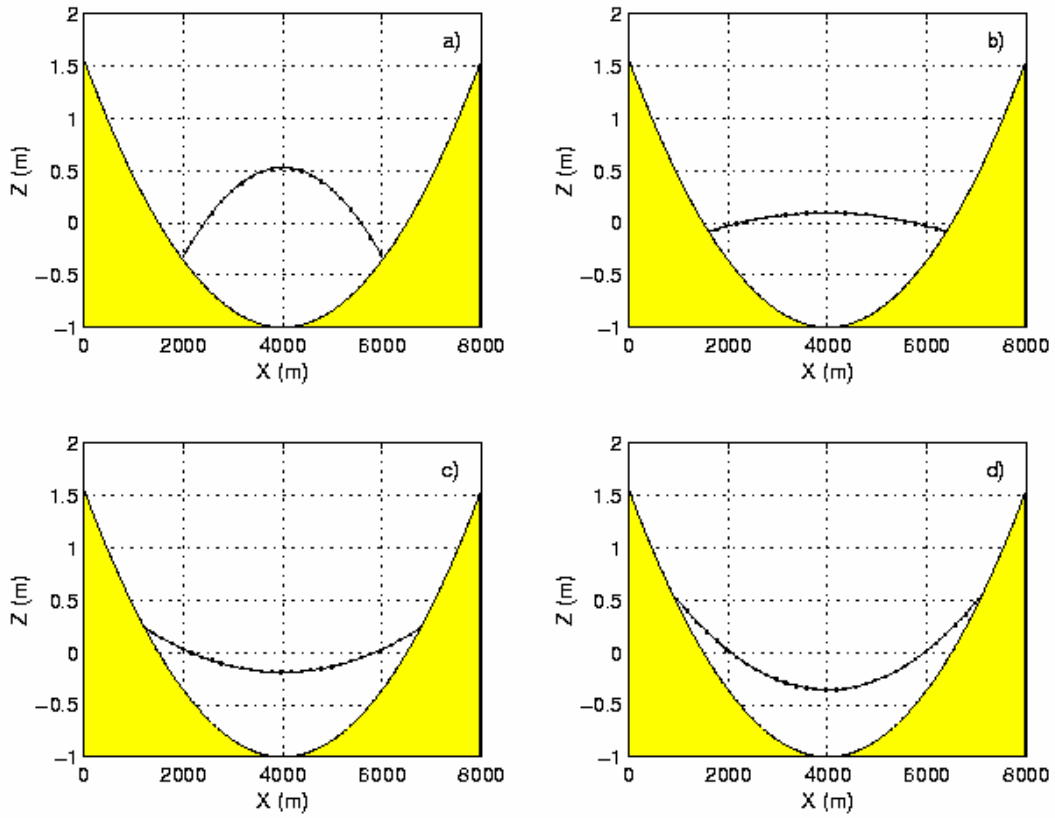


Figure 7, Lynett *et al.*

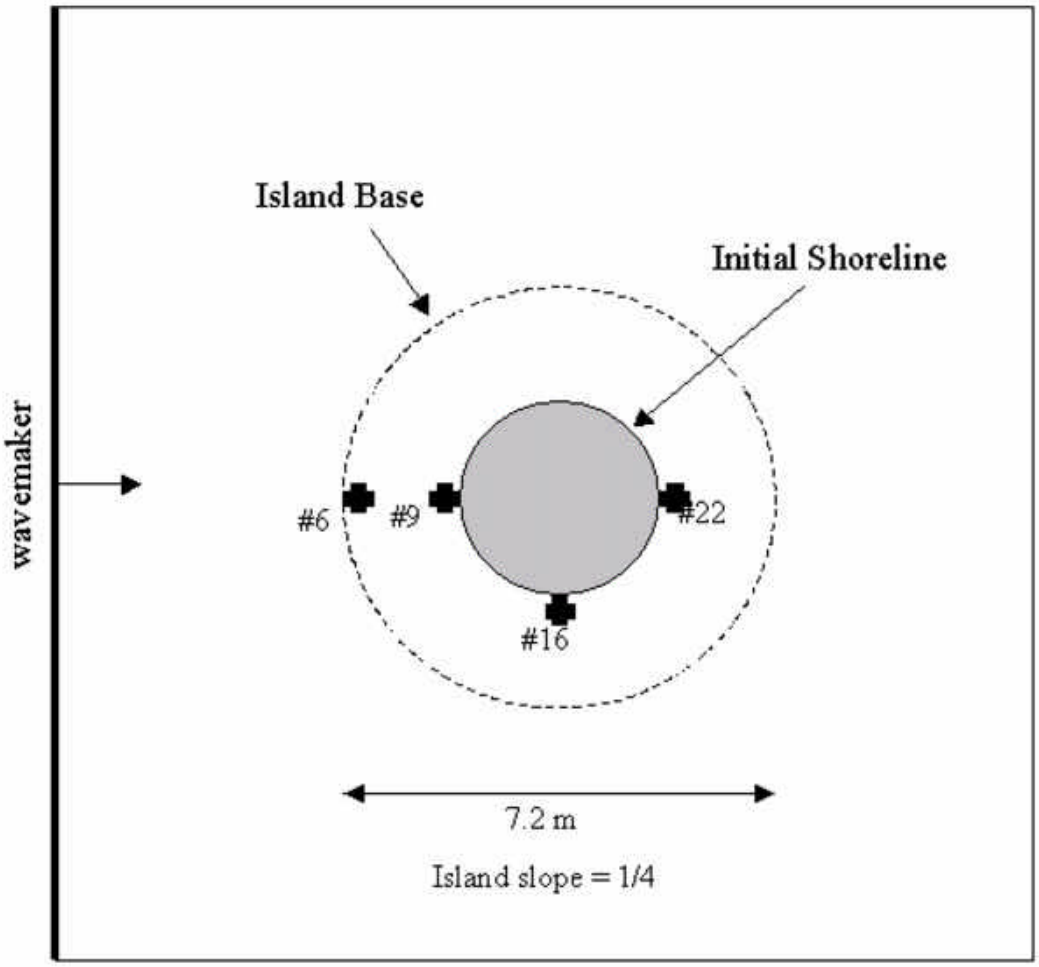


Figure 8, Lynett *et al.*

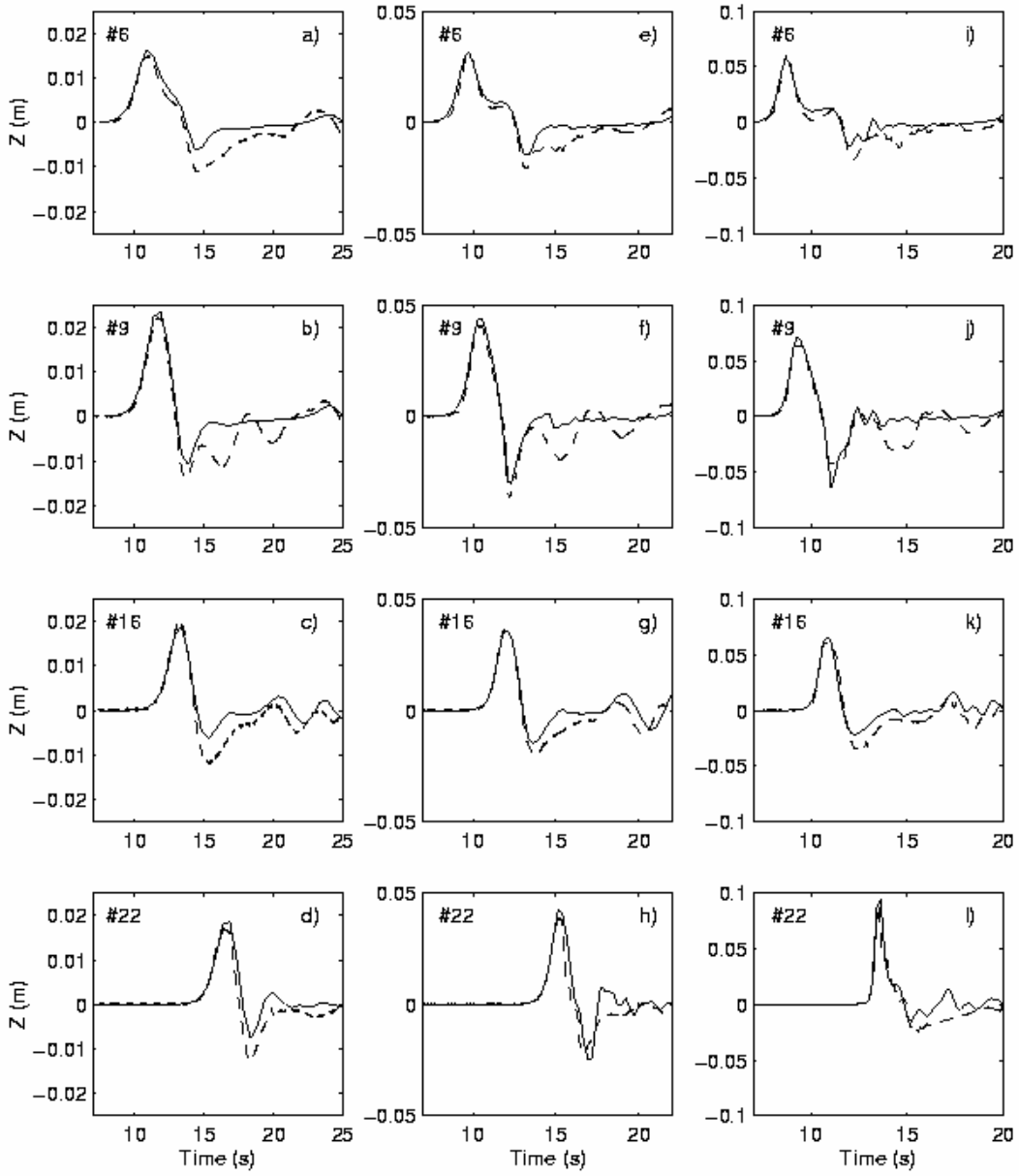


Figure 9, Lynett *et al.*

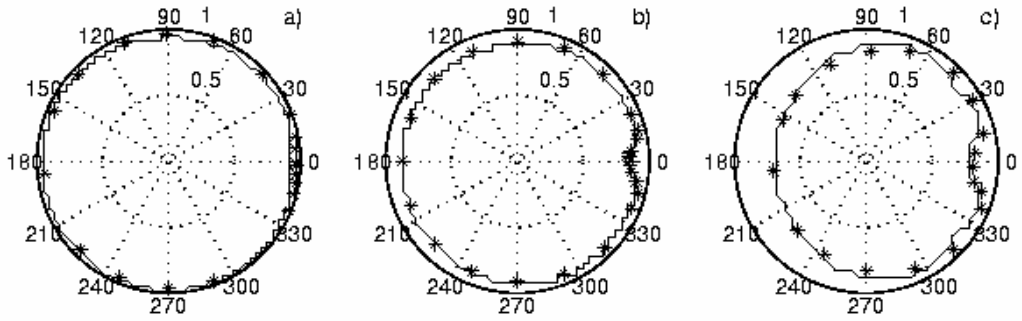


Figure 10, Lynett *et al.*

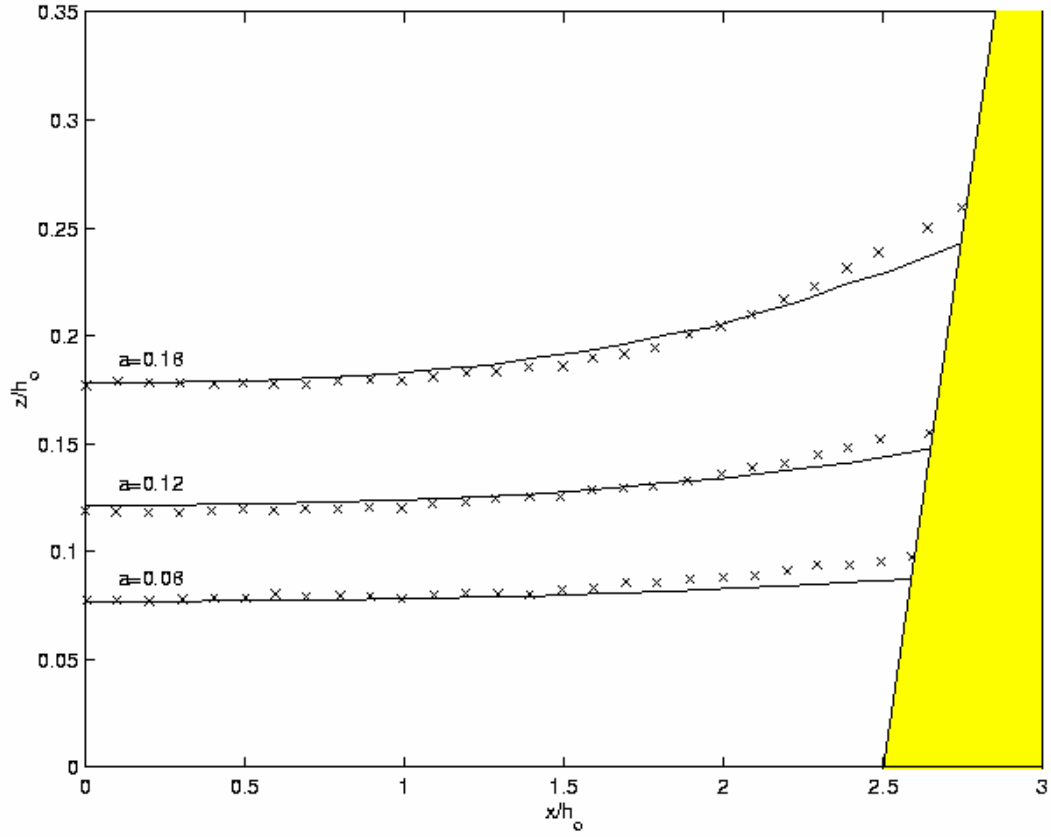


Figure 11, Lynett *et al.*

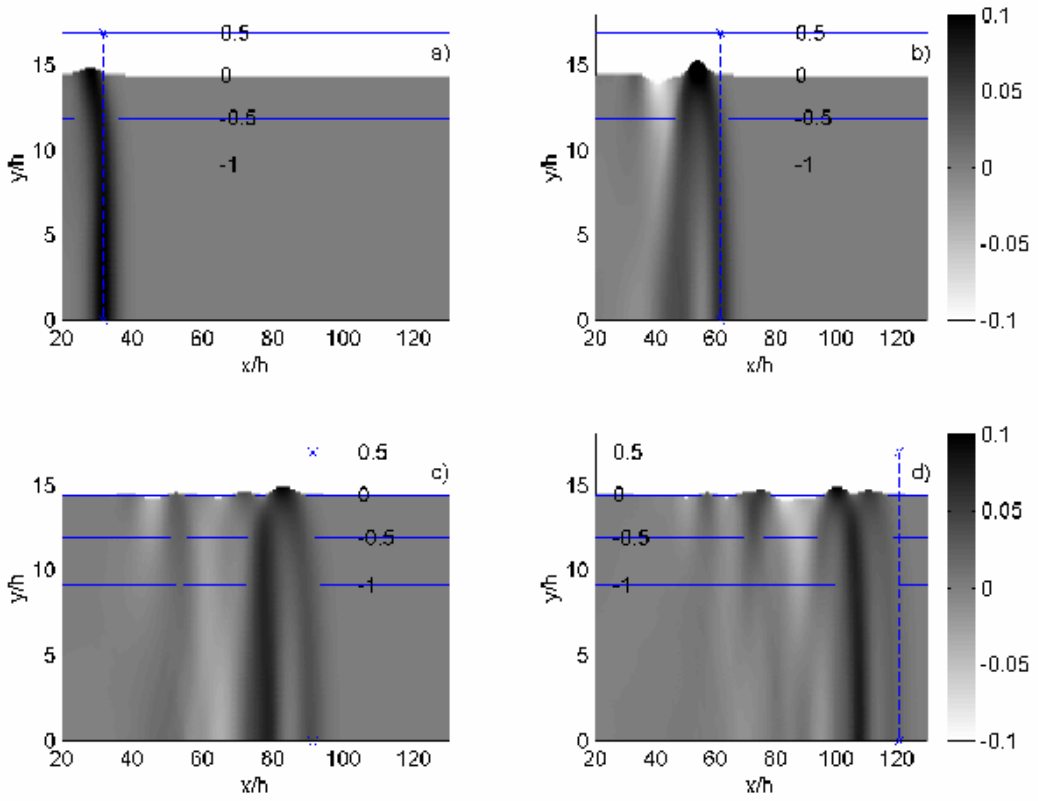


Figure 12, Lynett *et al.*

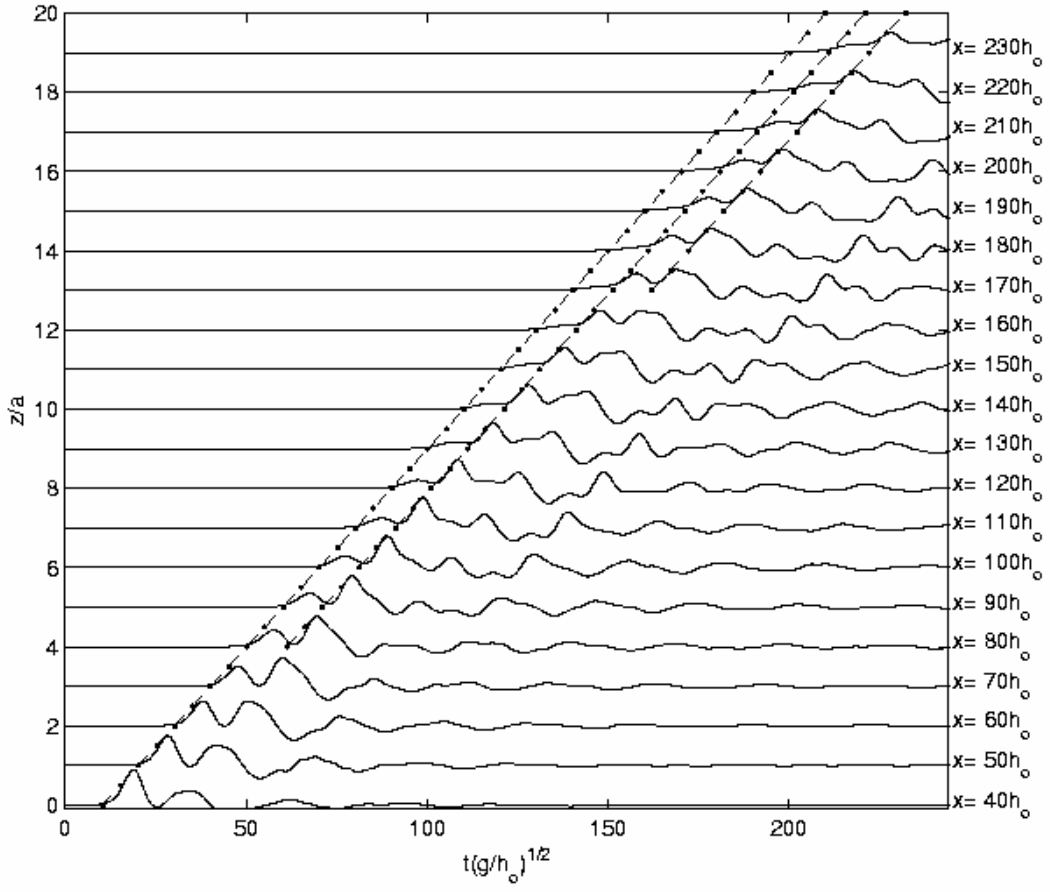


Figure 13, Lynett *et al.*

# A numerical study of submarine landslide generated waves and runup

Patrick Lynett and Philip L.-F. Liu

School of Civil and Environmental Engineering

Cornell University, Ithaca, NY 14853

October, 2001

## Abstract

A mathematical model is derived to describe the generation and propagation of water waves by a submarine landslide. The model consists of depth-integrated continuity equation and momentum equations, in which the ground movement is the forcing function. These equations include full nonlinear, but weak frequency dispersion effects. The model is capable of describing wave propagation from relatively deep water to shallow water. Simplified models for waves generated by small seafloor displacement or creeping ground movement are also presented. A numerical algorithm is developed for the general fully nonlinear model. Comparisons are made with a Boundary Integral Equation Method model, and a deep water limit for the depth-integrated model is determined in terms of a characteristic side length of the submarine mass. The importance of nonlinearity and frequency dispersion in the wave generation region and on the shoreline movement is discussed. As a case study, a tsunami generated by a prehistoric massive submarine slump off the northern coast of Puerto Rico is modeled. Sensitivities of the slump time scale to the generated wave amplitude and wave form are investigated, and two-horizontal dimension effects are also examined.

## Introduction

In recent years, significant advances have been made in developing mathematical models to describe the entire process of generation, propagation and run-up of a tsunami event (e.g. Yeh *et al.* 1996; Geist 1998). These models are based primarily on the shallow-water wave equations and are adequate for tsunamis generated by seismic seafloor deformation. Since the duration of the seismic seafloor deformation is very short, the water surface response is almost instantaneous and the initial water surface profile mimics the final seafloor deformation. The typical wavelength of this type of tsunami ranges from 20 km to 100 km. Therefore, frequency dispersion can be ignored in the generation region. The nonlinearity is also usually not important in the generation region, because the initial wave amplitude is relatively small compared to the wavelength and the water depth. However, the frequency dispersion becomes important when a tsunami propagates for a long distance. Nonlinearity could also dominate as a tsunami enters the runup phase. Consequently, a complete model that can describe the entire process of tsunami generation, evolution, and runup needs to consider both frequency dispersion and nonlinearity.

Tsunamis are also generated by other mechanisms. For example, submarine landslides have been documented as one of possible sources for several destructive tsunamis (Moore & Moore 1984, von Huene *et al.* 1989, Jiang & LeBlond 1992, Tappin *et al.* 1999, Keating & McGuire 1999). On November 29, 1975, a landslide was triggered by a 7.2 magnitude earthquake along the southeast coast of Hawaii. A 60 km stretch of Kilauea's south coast subsided 3.5 m and moved seaward 8 m. This landslide generated a local tsunami with a maximum runup height of 16 m at Keauhou (Cox & Morgan 1977). More recently, the devastating Papua New Guinea tsunami in 1998 is thought to be caused by a submarine landslide (Tappin *et al.* 1999, Keating & McGuire 1999, Tappin *et al.* 2001). In terms of tsunami generation mechanisms, two significant differences exist between submarine landslide and coseismic seafloor deformation. First, the duration of a landslide is much longer and is in the order of magnitude of several minutes. Hence the time history of the seafloor movement will affect the characteristics of the generated wave and needs to be included in the model. Secondly, the effective size of the landslide region is usually much smaller than the coseismic

seafloor deformation zone. Consequently, the typical wavelength of the tsunamis generated by a submarine landslide is also shorter, i.e., about 1 to 10 km. Therefore, the frequency dispersion could be important in the wave generation region. The existing numerical models based on shallow-water wave equations may not be suitable for modeling the entire process of submarine landslide generated tsunami (e.g., Raney & Butler 1976, Harbitz *et al.* 1993).

In this paper, we shall present a new model describing the generation and propagation of tsunamis by a submarine landslide. In this general model only the assumption of weak frequency dispersion is employed, i.e., the ratio of water depth to wavelength is small or $O(\mu^2) \ll 1$. Until the past decade, weakly dispersive models were formulated in terms of a depth-averaged velocity (e.g. Peregrine, 1967). Recent work has clearly demonstrated that modifications to the frequency dispersion terms (Madsen *et al.*, 1992) or expression of the model equations in terms of an arbitrary-level velocity (Ngowu, 1993; Liu, 1994) can extend the validity of the linear dispersion properties into deeper water. The general guideline for dispersive properties is that the "extended" versions of the depth-integrated equations are valid for wavelengths greater than two water depths, whereas the depth-averaged model is valid for lengths greater than five water depths (e.g., Nwogu, 1993). Moreover, in the model presented in this paper, the full nonlinear effect is included, i.e., the ratio of wave amplitude to water depth is of order one or $\varepsilon = O(1)$. Therefore, this new model is more general than that developed by Liu & Earickson (1983), in which the Boussinesq approximation, i.e., $O(\mu^2) = O(\varepsilon) \ll 1$ was used. In the special case where the seafloor is stationary, the new model reduces to the model for fully nonlinear and weakly dispersive waves propagating over a varying water depth (e.g. Liu 1994, Madsen & Schäffer 1998). The model is applicable for both the impulsive slide movement and creeping slide movement. In the latter case the time duration for the slide is much longer than the characteristic wave period.

This paper is organized in the following manner. Governing equations and boundary conditions for flow motions generated by a ground movement are summarized in the next section. The derivation of approximate two-dimensional depth-integrated governing equations follows. The general model equations are then simplified for special cases. A numerical algorithm is presented to solve the general mathematical model. The numerical model is

tested using available experimental data (e.g., Hammack 1973) for one-dimensional situations. Employing a Boundary Integral Equation Model, which solves for potential flow in the vertical plane, a deep water limit for waves generated by submarine slides is determined for the depth-integrated model. The importance of nonlinearity and frequency dispersion is inferred through numerical simulation of a large number of different physical setups. As a case study, a large prehistoric slide off the northern coast of Puerto Rico, whose attributes have been well documented (Grindlay 1998), is examined. Through this analysis, the impact of slide velocity on the free surface is investigated. Additionally, the magnitude of two-dimensional wave energy spreading effects is captured by comparison of one and two dimensional numerical simulations.

## Governing Equations and Boundary Conditions

As shown in Figure 1, $\zeta'(x',\ y',\ t')$ denotes the free surface displacement of a wave train propagating in the water depth $h'(x',\ y',\ t')$. Introducing the characteristic water depth $h_0$ as the vertical length scale, the characteristic length of the submarine slide region $\ell_0$ as the horizontal length scale, $\ell_0/\sqrt{gh_0}$ as the time scale, and the characteristic wave amplitude $a_0$ as the scale of wave motion, we can define the following dimensionless variables:

$$(x,\ y) = (x',\ y')/\ell_0, \quad z = z'/h_0, \quad t = \sqrt{gh_0}t'/\ell_0$$

$$h = h'/h_0, \quad \zeta = \zeta'/a_0, \quad p = p'/\rho g a_0$$

$$(u,\ v) = (u',\ v')/\left(\varepsilon\sqrt{gh_0}\right), \quad w = w'/\left[\frac{\varepsilon}{\mu}\sqrt{gh_0}\right] \tag{2.1}$$

in which $(u, v)$ represent the horizontal velocity components, $w$ the vertical velocity component, $p$ the pressure. Two dimensionless parameters have been introduced in (2.1), which are

$$\varepsilon = a_0/h_0, \quad \mu = h_0/\ell_0 \tag{2.2}$$

Assuming that the viscous effects are insignificant, the wave motion can be described by the

continuity equation and the Euler's equations, i.e.,

$$\mu^2 \nabla \cdot \boldsymbol{u} + w_z = 0 \tag{2.3}$$

$$\boldsymbol{u}_t + \varepsilon \boldsymbol{u} \cdot \nabla \boldsymbol{u} + \frac{\varepsilon}{\mu^2} w \boldsymbol{u}_z = -\nabla p \tag{2.4}$$

$$\varepsilon w_t + \varepsilon^2 \boldsymbol{u} \cdot \nabla w + \frac{\varepsilon^2}{\mu^2} w w_z = -\varepsilon p_z - 1 \tag{2.5}$$

where $\boldsymbol{u} = (u, v)$ denotes the horizontal velocity vector, $\nabla = (\partial/\partial x,\ \partial/\partial y)$ the horizontal gradient vector, and the subscript the partial derivative.

On the free surface, $z = \varepsilon\zeta(x,\ y,\ t)$, the usual kinematic and dynamic boundary conditions apply:

$$w = \mu^2(\zeta_t + \varepsilon \boldsymbol{u} \cdot \nabla \zeta), \quad \text{on } z = \varepsilon\zeta \tag{2.6a}$$

$$p = 0 \tag{2.6b}$$

Along the seafloor, $z = -h$, the kinematic boundary condition requires

$$w + \mu^2 \boldsymbol{u} \cdot \nabla h + \frac{\mu^2}{\varepsilon} h_t = 0, \quad \text{on } z = -h \tag{2.7}$$

For later use, we note here that the depth-integrated continuity equation can be obtained by integrating (2.3) from $z = -h$ to $z = \varepsilon\zeta$. After applying the boundary conditions (2.6a) and (2.7), the resulting equation reads

$$\nabla \cdot \left[ \int_{-h}^{\varepsilon\zeta} \boldsymbol{u} dz \right] + \frac{1}{\varepsilon} H_t = 0 \tag{2.8}$$

where

$$H = \varepsilon\zeta + h \tag{2.9}$$

We remark here that (2.8) is exact.

### Approximate Two-Dimensional Governing Equations

The three-dimensional boundary-value problem described in the previous section will be approximated and projected onto a two-dimensional horizontal plane. In this section, the nonlinearity is assumed to be of $O(1)$. However, the frequency dispersion is assumed to be weak, i.e.,

$$O(\mu^2) \ll 1 \tag{3.1}$$

Using $\mu^2$ as the small parametet, a perturbation analysis is performed on the primitive governing equations. The complete derivation is given in Appendix A. The resulting approximate continuity equation is

$$\frac{1}{\varepsilon}h_t+\zeta_t+\nabla\cdot(H\boldsymbol{u}_\alpha)-\mu^2\nabla\cdot\left\{H\left[\left(\frac{1}{6}(\varepsilon^2\zeta^2-\varepsilon\zeta h+h^2)-\frac{1}{2}z_\alpha^2\right)\nabla(\nabla\cdot\boldsymbol{u}_\alpha)\right.\right.$$
$$\left.\left.+\left(\frac{1}{2}(\varepsilon\zeta-h)-z_\alpha\right)\nabla\left(\nabla\cdot(h\boldsymbol{u}_\alpha)+\frac{h_t}{\varepsilon}\right)\right]\right\}=O(\mu^4) \tag{3.2}$$

Equation (3.2) is one of three governing equations for $\zeta$ and $\boldsymbol{u}_\alpha$. The other two equations come from the horizontal momentum equation, (2.4), and are given in vector form as

$$\boldsymbol{u}_{\alpha t}+\varepsilon\boldsymbol{u}_\alpha\cdot\nabla\boldsymbol{u}_\alpha+\nabla\zeta+\mu^2\frac{\partial}{\partial t}\left\{\frac{1}{2}z_\alpha^2\nabla(\nabla\cdot\boldsymbol{u}_\alpha)+z_\alpha\nabla\left[\nabla\cdot(h\boldsymbol{u}_\alpha)+\frac{h_t}{\varepsilon}\right]\right\}$$
$$+\varepsilon\mu^2\left\{\left[\nabla\cdot(h\boldsymbol{u}_\alpha)+\frac{h_t}{\varepsilon}\right]\nabla\left[\nabla\cdot(h\boldsymbol{u}_\alpha)+\frac{h_t}{\varepsilon}\right]\right.$$
$$-\nabla\left[\zeta\left(\nabla\cdot(h\boldsymbol{u}_\alpha)_t+\frac{h_{tt}}{\varepsilon}\right)\right]+(\boldsymbol{u}_\alpha\cdot\nabla z_\alpha)\nabla\left[\nabla\cdot(h\boldsymbol{u}_\alpha)+\frac{h_t}{\varepsilon}\right]$$
$$\left.+z_\alpha\nabla\left[\boldsymbol{u}_\alpha\cdot\nabla\left(\nabla\cdot(h\boldsymbol{u}_\alpha)+\frac{h_t}{\varepsilon}\right)\right]+z_\alpha(\boldsymbol{u}_\alpha\cdot\nabla z_\alpha)\nabla(\nabla\cdot\boldsymbol{u}_\alpha)+\frac{z_\alpha^2}{2}\nabla[\boldsymbol{u}_\alpha\cdot\nabla(\nabla\cdot\boldsymbol{u}_\alpha)]\right\}$$
$$+\varepsilon^2\mu^2\nabla\left\{-\frac{\zeta^2}{2}\nabla\cdot\boldsymbol{u}_{\alpha t}-\zeta\boldsymbol{u}_\alpha\cdot\nabla\left[\nabla\cdot(h\boldsymbol{u}_\alpha)+\frac{h_t}{\varepsilon}\right]+\zeta\left[\nabla\cdot(h\boldsymbol{u}_\alpha)+\frac{h_t}{\varepsilon}\right]\nabla\cdot\boldsymbol{u}_\alpha\right\}$$
$$+\varepsilon^3\mu^2\nabla\left\{\frac{\zeta^2}{2}\left[(\nabla\cdot\boldsymbol{u}_\alpha)^2-\boldsymbol{u}_\alpha\cdot\nabla(\nabla\cdot\boldsymbol{u}_\alpha)\right]\right\}=O(\mu^4) \tag{3.3}$$

Equations (3.2) and (3.3) are the coupled governing equations, written in terms of $\boldsymbol{u}_\alpha$ and $\zeta$, for fully nonlinear, weakly dispersive waves generated by a seafloor movement. We reiterate here that $\boldsymbol{u}_\alpha$ is evaluated at $z=z_\alpha(x,\ y,\ t)$, which is a function of time. The choice of $z_\alpha$ is made based on the linear frequency dispersion characteristics of the governing equations (e.g., Nwogu 1993, Chen & Liu 1995). Assuming a stationary seafloor, in order to extend the applicability of the governing equations to relatively deep water (or a short wave), $z_\alpha$ is recommended to be evaluated as $z_\alpha=-0.531h$. In the following analysis, the same relationship is employed. These model equations will be referred to as FNL-EXT, for fully-nonlinear, "extended" equations.

**Creeping ground movements**

Up to this point the time scale of the seafloor movement is assumed to be in the same order of magnitude as the typical period of generated water wave, $t_w = \ell_0/\sqrt{gh_0}$ as given in (2.1). When the ground movement is creeping in nature, the time scale of seafloor movement, $t_c$, could be larger than $t_w$. The only scaling parameter that is directly affected by the time scale of the seafloor movement is the characteristic amplitude of the wave motion. After introducing the time scale $t_c$ into the time derivatives of $h$ in the continuity equation, (3.2), along with a characteristic change in water depth $\Delta h$, the coefficient in front of $h_t$ becomes

$$\frac{\delta}{\varepsilon}\frac{t_w}{t_c}$$

where $\delta = \Delta h/h_o$. To maintain the conservation of mass, the above parameter must be of order one. Thus,

$$\varepsilon = \delta\frac{t_w}{t_c} = \frac{\delta l_o}{t_c\sqrt{gh_o}} \tag{3.4}$$

The above relationship can be interpreted in the following way: During the creeping ground movement, over the time period $t < t_c$ the generated wave has propagated a distance $t\sqrt{gh_o}$. The total volume of the seafloor displacement, normalized by $h_o$, is $\delta l_o\frac{t}{t_c}$, which should be the same as the volume of water underneath the generated wave crest, i.e., $\varepsilon t\sqrt{gh_o}$. Therefore, over the ground movement period, $t < t_c$, the wave amplitude can be estimated by (3.4). Consequently, nonlinear effects become important only if $\varepsilon$ defined in (3.4) is $O(1)$. Since, by definition of a creeping slide, the value $\frac{l_o}{t_c\sqrt{gh_o}}$ is always less than one, fully nonlinear effects will be important for only the largest slides. The same conclusion was reached by Hammack (1973), using a different approach. The importance of the fully nonlinear effect when modeling creeping ground movements will be tested in a following section.

## Limiting Cases

In this section the general model is further simplified for different physical conditions.

**Weakly nonlinear waves**

In many situations the seafloor displacement is relatively small in comparison with the local depth, and the seafloor movement can be approximated as

$$h(x,y,t) = h_0(x,y) + \delta\overline{h}(x,y,t), \tag{4.1}$$

in which $\delta$ is considered to be small. In other words, the maximum seafloor displacement is much smaller than the characteristic water depth. Since the free surface displacement is directly proportional to the seafloor displacement, i.e. $O(\varepsilon\zeta) = O(\delta\overline{h})$ or much less than the seafloor displacement in the case of creeping ground movements, we can further simplify the governing equations derived in the previous section by allowing

$$O(\varepsilon) = O(\delta) = O(\mu^2) \ll 1 \tag{4.2}$$

which is the Boussinesq approximation. Thus, the continuity equation, (3.2) can be reduced to

$$\zeta_t + \nabla\cdot(H\boldsymbol{u}_\alpha) + \frac{\delta}{\varepsilon}\overline{h}_t - \mu^2\nabla\cdot\left\{h_0\left[\left(\frac{1}{6}h_0^2 - \frac{1}{2}z_\alpha^2\right)\nabla(\nabla\cdot\boldsymbol{u}_\alpha)\right.\right.$$
$$\left.\left. - \left(\frac{1}{2}h_0 + z_\alpha\right)\nabla\left(\nabla\cdot(h_0\boldsymbol{u}_\alpha) + \frac{\delta}{\varepsilon}\overline{h}_t\right)\right]\right\} = O(\mu^4, \mu^2\varepsilon, \delta\mu^2) \tag{4.3}$$

The momentum equation becomes

$$\boldsymbol{u}_{\alpha t} + \varepsilon\boldsymbol{u}_\alpha\cdot\nabla\boldsymbol{u}_\alpha + \nabla\zeta + \mu^2\frac{\partial}{\partial t}\left\{\frac{1}{2}z_\alpha^2\nabla(\nabla\cdot\boldsymbol{u}_\alpha) + z_\alpha\nabla[\nabla\cdot(h_0\boldsymbol{u}_\alpha) + \frac{\delta}{\varepsilon}\overline{h}_t]\right\}$$
$$= O(\mu^4, \varepsilon\mu^2, \delta\mu^2) \tag{4.4}$$

These model equations will be referred to as WNL-EXT, for weakly-nonlinear, "extended" equations. The linear version of the above will also be utilized in the following analysis, and will be referred to as L-EXT, for linear, "extended" equations.

It is also possible to express the approximate continuity and momentum equations in terms of a depth-averaged velocity. The depth-averaged equations can be derived using the same method presented in Appendix A. One version of the depth-averaged equations will be employed in future sections, which is subject to the restraint (4.2), and is given as

$$\zeta_t + \nabla \cdot (H\overline{\boldsymbol{u}}) + \frac{\delta}{\varepsilon}\overline{h}_t = 0 \tag{4.5}$$

$$\overline{\boldsymbol{u}}_t + \varepsilon\overline{\boldsymbol{u}} \cdot \nabla\overline{\boldsymbol{u}} + \nabla\zeta + \mu^2\frac{\partial}{\partial t}\left\{\frac{h_0^2}{2}\nabla(\nabla\cdot\overline{\boldsymbol{u}}) - \frac{h_0}{6}\nabla[\nabla\cdot(h_0\overline{\boldsymbol{u}}) + \frac{\delta}{\varepsilon}\overline{h}_t]\right\}$$
$$= O(\mu^4, \varepsilon\mu^2, \delta\mu^2) \tag{4.6}$$

where the depth-averaged velocity is defined as

$$\overline{\boldsymbol{u}}(x,y,t) = \frac{1}{h+\varepsilon\zeta}\int_h^{\varepsilon\zeta} \boldsymbol{u}(x,y,z,t)\ dz \tag{4.7}$$

This set of model equations, (4.5) and (4.6), will be referred to as WNL-DA, for weakly-nonlinear, depth-averaged equations.

**Nonlinear shallow-water waves**

In the case that the water depth is very shallow or the wavelength is very long, the governing equations, (3.2) and (3.3), can be truncated at $O(\mu^2)$. These resulting equations are the well-known nonlinear shallow water equations in which the seafloor movement is the forcing term for wave generation. This set of equations will be referred to as NL-SW, for nonlinear, shallow-water equations.

## Numerical Model

In this paper, a finite difference algorithm is presented for the general model equations, FNL-EXT. This model has the robustness of enabling slide-generated surface waves, although initially linear or weakly nonlinear in nature, to propagate into shallow water, where fully nonlinear effects may become important. The structure of the present numerical model is similar to those of Wei & Kirby (1995) and Wei *et al.* (1995). Differences between the model presented here and that of Wei *et al.* exist in the added terms due to a time-dependant water depth and the numerical treatment of some nonlinear dispersive terms, which is discussed in more detail in Appendix B. A high-order predictor-corrector scheme is utilized, employing a third order in time explicit Adams-Bashforth predictor step, and a fourth order in time Adams-Moulton implicit corrector step (Press *et al.*, 1989). The implicit corrector step must be iterated until a convergence criterion is satisfied. All spatial derivatives are differenced

to fourth order accuracy, yielding a model which is numerically accurate to $(\Delta x)^4, (\Delta y)^4$ in space and $(\Delta t)^4$ in time. The governing equations, (3.2) and (3.3), are dimensionalized for the numerical model, and all variables described in this and following sections will be in the dimensional form. Note that the dimensional equations are equivalent to the non-dimensional ones with $\varepsilon = \mu = 1$ and the addition of gravity, $g$, to the coefficient of the leading order free surface derivative in the momentum equation (i.e., the third term on the left hand side of (3.3)). The predictor-corrector equations are given in Appendix B, along with some additional description of the numerical scheme. Runup and rundown of the waves generated by the submarine disturbance will also be examined. The moving boundary scheme employed here is the technique developed by Lynett *et al.* (2001).

In addition to the depth-integrated model numerical results, output from a two dimensional (vertical plane) Boundary Integral Equation Method (BIEM) model will be presented for certain cases. This BIEM model will be primarily used to determine the deep water accuracy limit of the depth-integrated model. The BIEM model solves for inviscid, irrotational flows and converts a boundary value problem into an integral equation along the boundary of a physical domain. Therefore, just as with the depth-integration approach, it reduces the dimension of the problem by one. The BIEM model utilized here solves the Laplace equation in the vertical plane $(x, z)$, and, of course, is valid in all water depths for all wavelengths. Details of this type of BIEM model, when used to model water wave propagation, can be found in Grilli *et al.* (1989), Liu *et al.* (1992), and Grilli (1993) for example. The BIEM model used in this work has reproduced the numerical results presented for landslide generated waves in Grilli & Watts (1999) perfectly.

### Comparisons with Experiment and Other Models

As a first check of the present model, a comparison between Hammack's (1973) experimental data for an impulsive bottom movement in a constant water depth is made. The bottom movement consists of a length, $l_o$= 24.4 water depths, which is pushed vertically upward. The change in depth for this experiment, $\delta$, is 0.1, so nonlinear effects should play a small role near the source region. Figure 2 shows a comparison between the numerical

results using FNL-EXT, experimental data, and the linear theory presented by Hammack. Both the fully nonlinear model and the linear theory agree well with experiment at the edge of the source region (Figure 2a). From Figure 2b, a time series taken at 20 water depths from the edge of the source region, the agreement between all data is again quite good, but the deviation between the linear theory and experiment is slowly growing. The purpose of this comparison is to show that the present numerical model accurately predicts the free surface response to a simple seafloor movement. It would seem that if one was interested in just the wave field very near the source, linear theory is adequate. However, as the magnitude of the bed upthrust, $\delta$, becomes large, linear theory is not capable of accurately predicting the free surface response even very near the source region. One such linear vs. nonlinear comparison is shown in Figure 2 for $\delta = 0.6$. The motion of the bottom movement is the same as in Hammack's case above. Immediately on the outskirts of the bottom movement, there are substantial differences between linear and nonlinear theory, as shown in Figure 2c. Additionally, as the wave propagates away from the source, errors in linear theory are more evident.

A handful of experimental trials and analytic solutions exist for non-impulsive seafloor movements. However, for the previous work that made use of smooth obstacles, such as a semi-circle (e.g., Forbes & Schwartz, 1982) or a semi-ellipse (e.g., Lee *et al.*, 1989), the length of the obstacle is always less than 1.25 water depths, or $\mu \geq 0.8$. Unfortunately, these objects will create waves too short to be modeled accurately by a depth-integrated model.

Watts (1997) performed a set of experiments where he let a triangular block free fall down a planar slope. In all the experiments, the front face (deep water face) of the block was steep, and in some cases vertical. Physically, as the block travels down a slope, water is pushed out horizontally from the vertical front. Numerically, however, using the depth-integrated model, the dominant direction of water motion near the vertical face is vertical. This can be explained as follows. Examining the depth-integrated model equations, starting from the leading order, shallow water wave equations, the only forcing term due to the changing water depth appears in the continuity equation. There is no forcing term in the horizontal momentum equation. Therefore, in the non-dispersive system, any seafloor bottom cannot

directly create a horizontal velocity. This concept can be further illuminated by the equation describing the vertical profile of horizontal velocity:

$$\boldsymbol{u}(x,y,z,t) = \boldsymbol{u}_\alpha(x,y,t) + O(\mu^2) \tag{6.1}$$

Again, the changing seafloor bottom cannot directly create a horizontal velocity component for the non-dispersive system. All of the seafloor movement, whether it is a vertical or translational motion, is interpreted as strictly a vertical motion, which can lead to a very different generated wave pattern.

When adding the weakly dispersive terms, the vertical profile of the horizontal velocity becomes:

$$\boldsymbol{u}(x,y,z,t) = \boldsymbol{u}_\alpha(x,y,t) -$$
$$\mu^2 \left\{ \frac{z^2 - z_\alpha^2}{2} \nabla(\nabla \cdot \boldsymbol{u}_\alpha) + (z - z_\alpha) \nabla \left[ \nabla \cdot (h\boldsymbol{u}_\alpha) + \frac{h_t}{\varepsilon} \right] \right\} + O(\mu^4) \tag{6.2}$$

Now, with the higher-order dispersive formulation, there is the forcing term, $\nabla h_t$, which accounts for the effects of a horizontally moving body. Keep in mind, however, that this forcing term is a second-order correction, and therefore should represent only a small correction to the horizontal velocity profile. Thus, with rapid translational motion and/or steep side slopes of a submarine slide, the flow motion is strongly horizontal locally, and the depth-integrated models are not adequate. In slightly different terms, let the slide mass have a characteristic side length, $L_s$. A side length is defined as the horizontal distance between two points at which $\partial h/\partial t = 0$. This definition of a side length is described graphically in Figure 3. Figure 3a shows a mass that is symmetric around its midpoint in the $x$-plane, where the back (shallow water) and front (deep water) side lengths are equal. Figure 3b shows a mass whose front side is much shorter that the back. An irregular slide mass will have least two different side lengths. In these cases, the characteristic side length, $L_s$, is the shortest of all sides. When $L_s$ is small compared to a characteristic water depth, $h_o$, that side is consider steep, or in deep water, and the shallow-water based depth-integrated model will not be accurate. For the vertical face of Watts' experiments, $L_s = 0$, and therefore $L_s/h_o = 0$ and the situation resembles that of an infinitely deep ocean. The next section will attempt to determine a limiting value of $L_s/h_o$ where the depth-integrated model begins to fail.

### Limitations of the Depth-Integrated Model

Before utilizing the model for practical applications, the limits of accuracy of the depth-integrated model must be determined. As illustrated above, just as there is a short wave accuracy limit (wave should be at least 2 water depths long when applying the "extended" model), it is expected that there is also a slide length scale limitation. By comparing the outputs of this model to those of the BIEM model, a limiting value of $L_s/h_o$ can be inferred. The high degree of BIEM model accuracy in simulating wave propagation is well documented (e.g. Grilli 1989, Grilli *et al.* 1994).

The comparison cases will use a slide mass travelling down a constant slope. The slide mass moves as a solid body, with velocity described following Watts (1997). This motion is characterized by a decreasing acceleration until a terminal velocity is reached. All of the solid body motion coefficients used in this paper are identical to those employed by Grilli & Watts (1999). Note that all of the submarine landslide simulations presented in this paper are non-breaking.

The setup of the slide mass on the slope is shown in Figure 4. The time history of the seafloor is described by

$$h(x,t) = h_o(x) - \frac{\Delta h}{2}\left[1 + tanh\left(\frac{x - x_l(t)}{S}\right)\right]\left[1 - tanh\left(\frac{x - x_r(t)}{S}\right)\right] \qquad (7.1)$$

where $\Delta h$ is the maximum vertical height of the slide, $x_l$ is the location of the $tanh$ inflection point of the left side of the slide, $x_r$ is the location of the inflection point on the right side, and $S$ is a shape factor, controlling the steepness of the slide sides. The right and left boundaries, and steepness factor are given by:

$$x_l(t) = x_c(t) - \frac{b}{2}cos(\theta), \quad x_l(t) = x_c(t) + \frac{b}{2}cos(\theta), \quad S = \frac{0.5}{cos(\theta)}$$

where $x_c$ is the horizontal location of the center point of the slide, and is determined using the equations governing the solid body motion of the slide. The angle of the slope is given by $\theta$. The thickness of the "slideless" water column, or the baseline water depth, at the centerpoint of the slide is defined by $h_c(t) = h_o(x_c(t)) = \Delta h + d(t)$. With a specified depth above the initial center point of the slide mass, $d_o = d(t = 0)$, the initial horizontal location of the slide

center, $x_c(t=0)$, can be found. The length along the slope between $x_l$ and $x_r$ is defined as $b$, and all lengths are scaled by $b$.

For the first comparison, a slide with the parameter set: $\theta$=6°, $d_o/b$=0.2, and $\Delta h/b$=0.05 is modeled with FNL-EXT and BIEM. With these parameters the characteristic horizontal side length of the slide mass, $L_s/b$, is 1.7. $L_s$ is defined as in Figure 3, or specifically, the horizontal distance between two points at which $\partial h/\partial t$ is less than 1% of the maximum $\partial h/\partial t$ value. Note that a 6° slope is roughly 1/10. Figure 5 shows four snapshots of the free surface elevation from both models. The lowest panel in the figure shows the initial location of the slide mass, along with the locations corresponding to the four free surface snapshots. Initially, as shown in Figures 5a and b, where $L_s/h_c$=6.1 and 4.5 respectively, the two models agree, and thus are still in the range of acceptable accuracy of the depth-integrated model. In Figure 5c, as the slide moves into deeper water, where $L_s/h_c$=3.1, the two models begin to diverge over the source region, and by Figure 5d, the free surface responses of the two models are quite different. These results indicate that in the vicinity of $x/b$=5, the depth-integrated model becomes inaccurate. At this location, $h_c/b$=0.5, and $L_s/h_c$=3.4.

Numerous additional comparison tests were performed, and all indicated that the depth-integrated model becomes inaccurate when $L_s/h_c < 3 \sim 3.5$. One more of the comparisons is shown here. Examining a 20° slope and a slide mass with a maximum height $\Delta h/b$=0.1, the initial depth of submergence, $d_o/b$, will be successively increased from 0.4 to 0.6 to 1.0. The corresponding initial $L_s/h_c$ values are 3.4, 2.4, and 1.5, respectively. Time series above the initial centerpoint of the slide masses and vertical shoreline movements are shown in Figure 6. The expectation is that the first case ($L_s/h_c = 3.4$ initially) should show good agreement, the middle case ($L_s/h_c = 2.4$ initially) marginal agreement, and the last case ($L_s/h_c = 1.5$ initially) bad agreement. The time series above the center, Figures 6a, c, and e, do clearly agree with the stated expectation. Various different $z_o$ levels were tested in an attempt to better the agreement with the BIEM model results for the deeper water cases, but $z_o$=-0.531h provided the most accurate output. Rundown, as shown in Figures 6b, d, and f, shows good agreement for all the trials. The explanation is that the wave that creates the rundown is generated from the backface of the slide mass. This wave sees a characteristic

water depth that is less than $h_c$, and thus this backface wave remains in the region of accuracy of the depth-integrated model, whereas the wave motion nearer to the front face of the slide is inaccurate. This feature is also clearly shown in Figure 5. Thus, if one was solely interested in the leading wave approaching the shoreline, the characteristic water depth should be interpreted as the average depth along the backface of the slide, instead of $h_c$. The inaccurate elevation waves created by the front face of the moving mass could be absorbed numerically, such as with a sponge layer, so that they do not effect the simulation.

A guideline that the depth-integrated "extended" model will yield accurate results for $L_s/h_c > 3.5$ is accepted. This restriction would seem to be more stringent than the "extended" model frequency dispersion limitation, which requires that the free surface wave be at least two water depths long. In fact, the slide length scale limitation is more in line with the dispersion limitations of the depth-averaged (conventional) model. The limitations of the various model formulations, i.e. "extended" and depth-averaged, are discussed in the next section.

### Importance of Nonlinearity and Frequency Dispersion

Another useful guideline would be to know when nonlinear effects begin to play an important role. This can be determined by running numerous numerical trials, employing the FNL-EXT, WNL-EXT, and L-EXT equation models. These three equation sets share identical linear dispersion properties, but have varying levels of nonlinearity. The FNL-EXT model will be considered correct, and any difference in output compared to the other models with lesser nonlinearity would indicate that full nonlinear effects are important.

The importance of nonlinearity will be tested through examination of various $\Delta h/d_o$ combinations, using the slide mass described in the previous section. The value of $\Delta h/d_o$ can be thought of as an impulsive nonlinearity, as this value represents the magnitude of the free surface response if the slide motion was entirely vertical and instantaneous. The procedure will be to hold the value $h_{c_o} = h_c(t=0) = \Delta h + d_o$ constant for a given slope angle, while altering $\Delta h$ and $d_o$. Two output values will be compared between all the simulations: maximum depression above the initial centerpoint of the slide and maximum rundown. For all simulations presented in this section $\Delta x/b = 0.003$ and $\Delta t\sqrt{gh_{c_o}}/b = 0.0003$.

| Set # | Slope (degrees) | $h_{c_o}/b$ | $L_s/h_{c_o}$ |
|---|---|---|---|
| 1 | 30 | 0.55 | 3.5 |
| 2 | 15 | 0.55 | 3.5 |
| 3 | 5 | 0.55 | 3.5 |
| 4 | 5 | 0.15 | 13 |

Table 1. Characteristics of the simulations performed for the nonlinearity test.

Figure 7 shows the output from four sets of comparisons, whose characteristics are given in Table 1. Figures 7a & b show the depression above the centerpoint and the rundown for Set 1, Figures 7c & d for Set 2, Figures 7e & f for Set 3, and Figures 7g & h for Set 4. Examining the maximum depression plots for Sets 1,2, & 3, it is clear that the trends between the three sets are very similar, with FNL-EXT predicting the largest depression, and L-EXT predicting the smallest. The difference between FNL-EXT and WNL-EXT is solely due to nonlinear dispersive terms, which are of $O(\varepsilon\mu^2)$, while the difference between WNL-EXT and L-EXT is caused by the nonlinear divergence term in the continuity equation and the convection term in the momentum equation, which are of $O(\varepsilon)$. The relative differences in the maximum depression predicted between FNL-EXT and WNL-EXT are roughly the same as the differences between WNL-EXT and L-EXT for Sets 1,2, & 3. Therefore, in the source region, for $L_s/h_{c_o}$ values near the accuracy limit of the "extended" model (near 3.5), the nonlinear dispersive terms are as necessary to include in the model as the leading order nonlinear terms. As the $L_s/h_c$ value is increased, the slide produces an increasingly longer (shallow water) wave. Frequency dispersion plays a lesser role, and thus the nonlinear dispersive terms become expectedly less important. This can be seen in the maximum depression plot for Set 4. For this set, $L_s/h_{c_o} = 13$, and the FNL-EXT and WNL-EXT results are nearly indistinguishable.

Inspecting the maximum rundown plots for Sets 1, 2, & 3, it seems that the trends between the three different models have changed. Now, WNL-EXT predicts the largest rundown, while L-EXT predicts the smallest. It is hypothesized that the documented over-shoaling of WNL-EXT (Wei *et al.*, 1995) cancels out the lesser wave height generated in the source region compared to FNL-EXT, leading to rundown heights that agree well between the two models. As the slope is decreased, the error in the L-EXT rundown prediction increases. This

is attributed to a longer distance of shoaling before the wave reaches the shoreline. As the slope is decreased, while $h_{c_o}$ is kept constant, the horizontal distance from the shoreline to the initial centerpoint of the slide increases. The slide length is roughly the same for the three sets, therefore the generated wavelength is roughly the same. Thus, with a lesser slope the generated wave shoals for a greater number of wave periods. During this relatively larger distance of shoaling, nonlinear effects, and in particular the leading order nonlinear effects, accumulate and yield large errors in the linear (L-EXT) simulations. This trend is also evident in the rundown plot for Set 4. Also note that in Set 4, where the nonlinear dispersive terms are very small, the FNL-EXT and WNL-EXT rundowns are identical.

A deep water limit has been determined for the "extended" model ($L_s/h_c > 3.5$), but it would also be interesting to know the limits of applicability of the depth-averaged (WNL-DA) and shallow water (NL-SW) models. The only differences between these three models (the weakly nonlinear "extended", weakly nonlinear depth-averaged, and nonlinear shallow-water) are found in the frequency dispersion terms - the nonlinear terms are the same. The testing method to determine the deep water limits of the various model types will be to fix both a slope of 15° and a slide mass, with $\Delta h/b = 0.05$ and $L_s/b = 1.85$, while incrementally increasing the initial water depth above the centerpoint of the slide, $d$. Figure 8 shows a summary of the comparisons of the three models. Figures 8a & d show the maximum free surface depression measured above the initial centerpoint of the slide and the maximum rundown for various $L_s/h_{c_o}$ combinations. WNL-EXT solutions are indicated by solid lines, WNL-DA by dashed lines, and NL-SW by the dotted lines. Also shown in Figures 8b & e are the maximum depression and rundown results from WNL-DA and NL-SW relative to the results from WNL-EXT, thereby more clearly depicting the differences between the models. These figures show WNL-EXT and WNL-DA agreeing nearly exactly, while the errors in NL-SW decrease with increasing $L_s/h_{c_o}$. The NL-SW results do not converge with the WNL-EXT results until $L_s/h_{c_o} >\sim 15$. Figures 8c & f are time series of the free surface elevation above the initial centerpoint of the slide and the vertical movement of the shoreline for the case of $L_s/h_{c_o}$=3.5, respectively. Differences between NL-SW and WNL-EXT are clear, with NL-SW under-predicting the free surface above the slide, but over-predicting the rundown due to over

shoaling in the non-dispersive model. The only significant difference between the WNL-EXT and WNL-DA results come after the maximum depression in Figure 8c, where WNL-DA predicts an oscillatory train following the depression. These results indicate that to the deep water limit that WNL-EXT was shown to be accurate, WNL-DA is accurate as well. As mentioned previously, altering the level on which $z_\alpha$ is evaluated in the "extended" model does not increase the deep water accuracy limit for slide generated waves.

In summary, the nonlinear dispersive terms are important for slides near the deep water limit ($L_s/h_c = 3.5$) whose heights, or $\Delta h/d_o$ values, are large ($> 0.4$). For shallow water slides ($L_s/h_c > 10$), the nonlinear dispersive terms are not important near the source, even for the largest slides. The "extended" formulation of the depth-integrated equations does not appear to offer any benefits over the depth-averaged formulation in regards to modeling the generation of waves in deeper water. The "extended" model would be useful if one was interested in modeling the propagation of shallow-water, slide-generated waves into deeper water, which is not the focus of this paper. The shallow water wave equations are only valid for slides in very shallow water, where $L_s/h_{c_o} > \sim 15$.

### Modeling A Submarine Slump

As a case study to apply this model, a prehistoric, massive submarine slump off the Northern coast of Puerto Rico is investigated. According to Grindlay (1998), the slump was approximately 57 km wide, occurring on a steep slope (roughly 1/10) with a length of about 40 km; the top of the failure slope is at a depth of 3000 meters, the bottom at 7000 meters. The catastrophic failure is estimated to involve over 900 km$^3$ of soil. With this information and the evidence of a circular slip, the maximum decrease in water depth along the slope is estimated at 700 m. Assuming solid body motion of the mass and using the estimated soil density given by Grindlay, the duration of the movement is calculated to be on the order of 10 minutes.

To implement any bottom movement in the model, the evolution of the motion must be completely known beforehand. There are different slide mechanisms, which of course will determine the free surface response. In the previous sections, a solid mass slid down a slope. In this section, a rotational slump is examined. This type of seafloor movement is most likely

the type that occurred off the coast of Puerto Rico, where there is a large circular cut-out of a steep slope (Grindlay 1998). A depth transformation function that approximates this motion is a sine-wave addition. In this approach, a sine wave, whose amplitude is a function of time and wavelength is a constant in time, is added to the initial water depth. In order to numerically model a two horizontal dimension slump, the transverse motion is described with a Gaussian distribution of the centerline profile. The time history of the seafloor for the rotational slump is given by

$$h(x,y,t) = h_o(x,y) + a(t)\ G(y)\ sin\left[2\pi\frac{x-x_c}{l_o}\right] \quad \text{for } -\frac{l_o}{2} \le x - x_c \le \frac{l_o}{2} \tag{9.1}$$

where

$$a(t) = \Delta h\left(1 - e^{-\pi t/t_c}\right),$$

$$G(y) = e^{-(y-y_c)^2/r_o^2},$$

$\Delta h$ is the maximum change in depth due to the slump, $x_c$ is $x$-coordinate of the mid-point of the slump, $y_c$ is the $y$-coordinate, and $r_o$ is the half-width of the slump. Figure 9 shows the evolution of ground movements. The nonlinearity parameter (3.4) for this failure is:

$$\frac{l_o}{t_c\sqrt{g\overline{h}}}\ \frac{\overline{h}}{h_0} = \frac{60000m}{600s\sqrt{9.81m/s^2\ 6000m}}\ \frac{700m}{6000m} = 0.048$$

Thus, nonlinear effects are weak over the source region, but of primary interest will be wave heights in shallow water near the coast. Assuming a characteristic failure side length of half the slump length and a characteristic depth as the depth at the midpoint of the slump, the side length parameter is

$$\frac{L_s}{h_o} = \frac{30000m}{6000} = 5.0$$

and this submarine mass movement is near the deep water limit of FNL-EXT.

### Numerical Results

The first numerical simulation presented is for a one-horizontal dimension (1D) problem. At the top of the slope the water depth is 3000 m, at the bottom it is 7000 m. The slope in the failure region is 1/10. This failure slope is connected to the shallow water by a milder

slope of 1/50, and the depth is constant in the deep water. The maximum change in water depth during the slide, $\Delta h$, is 700 m, and the slump period, $t_c$, is 10 minutes. The numerical results using FNL-EXT are given as Figure 10. In Figure 10a, the slump is 2 minutes old, and very large waves have been created. A large negative wave is created over the region of the slump where the depth increases, and vice-versa. Almost halfway through the slump period, Figure 10b, the waves have begun to propagate away from the slide region. In Figures 10c and 10d, the wave propagating into the shallow water region begins to shorten and amplify, and nonlinear effects begin to become important. In this last subplot, the predicted free surface using L-EXT is also shown, indicating the importance of leading order nonlinearity. Up to the time shown in this figure, there is no difference between FNL-EXT and WNL-EXT simulation results. However, as the wave continues to travel towards the shoreline, the FNL-EXT and WNL-EXT models begin to deviate for a short time before breaking initiates.

Figure 10 and other numerical tests seem to indicate that the leading, and largest amplitude waves are only a function of the initial seafloor motion. A simple physical argument can provide an explanation. Focusing on the slump in Figure 10, the average depth in the region is 5000 m, and the linear long wave speed, $c$, is 220 m/s. The horizontal slump side length, $L_s$, is 30 km, and so the time required for a wave (disturbance) to travel across the half the slump region, $L_s/c$, is about 2 minutes. Therefore, after about 2 minutes of seafloor motion, the leading waves should be exiting the source region. Examination of Figure 10a supports this value, as the leading waves are separating and moving from the failure slope 2 minutes after the slump start. The argument can be further solidified by examining the effects of slumps with different durations. If the arrival times of the leading waves for slumps with different durations are the same, that would indicate that the waves have exited the source region at the same time, and the seafloor movement after about 2 minutes will not affect the leading waves. Figure 11 shows free surface snapshots for slumps of identical geometry, but different durations of motion ($t_c$ values). All the slumps have identical arrival times, but very different amplitudes as each of the leading waves experiences a different two-minute water depth change. Thus, it is shown that for an accurate modeling of the leading waves created by a slump, one only needs to correctly model the first $L_s/c$ seconds of the motion. This

statement is limited to small amplitude waves, where the nonlinear phase speed correction is minor.

Looking back to Figure 10, it is clear that when the waves reach the shoreline, they will be of extremely large amplitude. Realistically, the tsunami created from this event would not be as large, due to spreading effects. To demonstrate this, a two dimensional numerical simulation is performed, with a slide width of 57 km ($r_o$=28.5 km). Numerical profiles are shown in Figure 12. Initially, the wave amplitude is still large, with a maximum depression and elevation of nearly 100 m about 2 minutes after the slide start (Figure 12a). Some of this wave energy spreads, and by the time the slide is over, Figure 12d, the leading depression traveling towards the shoreline has an amplitude of less than 70 m, followed by an elevation wave of about 100 m.

Comparison of spatial profiles with the 1D results gives an estimate of the importance of 2D effects. The comparisons are given as Figure 13. The 2D profiles given in the figure are the centerline free surface displacements. The two sets of numerical simulations have very similar waveforms, but the 1D results are larger in amplitude, especially the leading depression traveling into shallower water. Naturally, the width of the slide ($2r_o$) directly effects the importance of two-dimensional spreading. Figure 14, a plot of the maximum depression recorded at the top of the slide slope ($x$=150 km in Figure 10) as a function of slide width, shows this relationship. The trend very closely resembles an exponential decay, where for an aspect ratio of unity, the maximum depression along the centerline for a 2D simulation is roughly 80% of the corresponding value from a 1D result. Clearly, the 1D model can give highly conservative results, depending on the aspect ratio of the failure region.

## Conclusions

A model for the creation of fully nonlinear long waves by seafloor movement, and their propagation away from the source region, is presented. The general fully nonlinear model can be truncated, so as to only include weakly nonlinear effects, or model a non-dispersive wave system. Rarely will fully nonlinear effects be important above the landslide region, but the model has the advantage of allowing the slide-generated waves to become fully nonlinear in

nature, without requiring a transition among governing equations.

A high-order finite difference model is developed to numerically simulate wave generation by seafloor movement. The numerical generation of waves by both impulsive and creeping movements agrees with experimental data and other numerical models. A deep-water accuracy limit of the model, $L_s/h_c > 3.5$, is adopted. Within this limitation, the "extended" formulation of the depth-integrated equations shows no benefit over the "conventional", depth-averaged approach near the source region. Leading order nonlinear effects were shown to be important for prediction of shoreline movement, and the fully nonlinear terms are important for only the thickest slides with relatively short length scales. Through the numerical examination of an ancient slide off the Puerto Rican coast, it is seen that the leading depression wave traveling towards the coastline is solely a function of the initial slide movement. A comparison between one and two dimension simulations indicates that, due to the neglect of two-dimensional energy spreading effects, the one dimensional model can significantly overpredict wave height.

## Acknowledgment

The research reported here is partially supported by Grants from National Science Foundation (CMS-9528013, CTS-9808542, and CMS 9908392) and a subcontract from University of Puerto Rico. The authors wish to thank Professor Aurelio Mercado, of the University of Puerto Rico at Mayaguez, for providing information describing the slump discussed in the last sections of this work. We also wish to thank Ms. Yin-yu Chen for providing the numerical results based on her BIEM model.

## References

Cox, D. C. & Morgan, J. 1977 "Local Tsunamis and Possible Local Tsunamis in Hawaii", Hawaii Institute of Geophysics, University of Hawaii, Report HIG 77-14.

Chen, Y., & Liu, P. L.-F., 1995. "Modified Boussinesq Equations and Associated Parabolic Model for Water Wave Propagation." J. Fluid Mech., **228**, 351–381.

Forbes, L. K., and Schwartz, L. W., 1982. "Free-Surface Flow over a Semicircular Obstruction," J. Fluid Mech. **114**, 299-314

Geist, E. L. 1998. "Local Tsunami and Earthquake Source Parameters" Advances in Geophysics, **39**, 117-209.

Grilli, S.T. 1993. "Modeling of nonlinear wave motion in shallow water." Chapter 3 in *Computational Methods for Free and Moving Boundary Problems in Heat and Fluid Flows* (eds. I.C. Wrobel and C.A. Brebbia), pps. 37-65, Computational Mechanics Publication, Elsevier Applied Sciences, London, UK.

Grilli, S.T, Skourup, J., and Svendsen, I.A. 1989. "An Efficient Boundary Element Method for Nonlinear Waves ." Engng. Analysis with Boundary Elements , **6**, 97-107.

Grilli, S.T, Subramanya, R., Svendsen, I.A., and Veeramony, J. 1995. "Shoaling of Solitary Waves on Plane Beaches." Journal of Waterway, Port, Coastal and Ocean Engng., **120**, 74-92.

Grilli, S.T, and Watts, P. 1999. "Modeling of Waves Generated by a Moving Submerged Body. Applications to Underwater Landslides" Engng. Analysis with Boundary Elements , **23**, 645-656.

Grindlay, N. 1998 "Volume and Density Approximations of Material Involved in a Debris Avalanche on the South Slope of the Puerto Rico Tench", Puerto Rico Civil Defense Report.

Harbitz, C. B., Pedersen, G., & Gjevik, B. 1993 "Numerical Simulation of Large Water Waves

due to Landslides", J. Hydraulic Engineering, ASCE **119**, 1325-1342.

Hammack, H. L., 1973. "A Note on Tsunamis: Their Generation and Propagation in an Ocean of Uniform Depth," J. Fluid Mech. **60**, 769-799.

Jiang, L., Ren, X., Wang, K.-H., & Jin, K.-R. 1996. "Generalized Boussinesq Model for Periodic Non-Linear Shallow-Water Waves," Ocean Engng, **23**, 309-323.

Jiang, L. & LeBlond, P. H., 1992 "The Coupling of a Submarine Slide and the Surface Waves Which It Generates", J. Geophys. Res., **97**, 12,731-12,744.

Kirby, J.T., Wei, G., Chen, Q., Kennedy, A.B. & Dalrymple, R.A., 1998. "FUNWAVE 1.0: Fully Nonlinear Boussinesq Wave Model Documentation and User's Manual," Center for Applied Coastal Research, University of Delaware.

Keating, B. H. & McGuire, W. J. 1999 "Island Edifice Failures and Associated Hazards". In Pure and Applied Geophysics, Special Issue: Landslide and Tsunamis. In press.

Kennedy, A. B., Kirby, J. T., Chen, Q. & Dalrymple, R. A., 2001. "Boussinesq-type Equations with Improved Nonlinear Behaviour," Wave Motion, **33**, 225-243.

Lee, S.-J., Yates, G. T., and Wu, T. Y., 1989. "Experiments and analyses of upstream-advancing solitary waves generated by moving disturbances," J. Fluid Mech. **199**, 569-593.

Liu, P. L.-F., 1994. "Model Equations for Wave Propagations From Deep to Shallow Water," in *Advances in Coastal and Ocean Engineering*, Vol. **1** (ed. P.L.-F. Liu), 125–158.

Liu, P. L.-F., Hsu, H.-W., and Lean, M.H. 1992. "Applications of Boundary Integral Equation Methods for Two-Dimensional Non-Linear Water Wave Problems," Int. J. for Numer. Meth. in Fluids, **15**, 1119-1141.

Liu, P. L.-F. & Earickson, J. 1983 "A Numerical Model for Tsunami Generation and Propagation," in *Tsunamis: Their Science and Engineering* (eds. J. Iida and T. Iwasaki),

Terra Science Pub. Co., 227-240.

Lynett, P., Wu, T-W., & Liu, P. L.-F., 2001. "Modeling Wave Runup with Depth-Integrated Equations," *submitted to* Coast. Engng.

Madsen, P. A., and Sorensen, O. R., 1992. "A new form of the Boussinesq equations with improved linear dispersion characteristics. Part II: A slowly varying bathymetry," Coast. Engng., **18**, 183-204.

Madsen, P.A. & Schäffer, H.A., 1998. "Higher-Order Boussinesq-type Equations for Surface Gravity Waves: Derivation and Analysis," Phil. Trans. R. Soc. Lond. A, **356**, 2123–3184.

Moore, G. & Moore, J. G. 1984 "Deposit from Giant Wave on the Island of Lanai," Science, **222**, 1312-1315.

Nwogu, O., 1993 "Alternative Form of Boussinesq Equations for Nearshore Wave Propagation," J. Wtrwy, Port, Coast and Ocean Engtg., ASCE, 119(6), 618-638.

Peregrine, D. H., 1967. "Long Waves on a Beach," J. Fluid Mech. **27**, 815-827

Press, W.H., Flannery, B.P., & Teukolsky, S.A. 1989. "Numerical Recipes," Cambridge University Press, 569-572.

Raney, D. C. & Butler, H. L. 1976 "Landslide Generated Water Wave Model," J. Hydraulic Div., ASCE **102**, 1269-1282.

Tappin, D. R., *et al.* 1999 "Sediment Slump Likely Caused 1998 Papua New Guinea Tsunami," EOS, **80(30)**, 329.

Tappin, D. R., Watts, P., McMurtry, G. M., Lafoy, Y., and Matsumoto, T. 2001 "The Sissano, Papau New Guinea Tsunami of July 1998 - Offshore Evidence on the Source Mechanism," Marine Geology, **175**, 1-23.

von Huene, R. Bourgois, J. Miller, J. & Pautot, G. 1989 "A Large Tsunamigetic Landslide and Debris Flow Along the Peru Trench," J. Geophys. Res., **94**, 1703-1714.

Wang, K-H. 1993. "Diffraction of Solitary Waves by Breakwaters," Journal of Waterway, Port, Coastal and Ocean Engng., **119**, 49-69.

Watts, P. 1997. Water Waves Generated by Underwater Landslides. Ph. D. Thesis, California Institute of Technology, 1997

Wei, G. & Kirby, J. T. 1995. "A Time-Dependent Numerical Code for Extended Boussinesq Equations," Journal of Waterway, Port, Coastal and Ocean Engng., **120**, 251-261.

Wei, G., Kirby, J.T., Grilli, S.T., & Subramanya, R., 1995. "A Fully Nonlinear Boussinesq Model for Surface Waves. Part 1. Highly Nonlinear Unsteady Waves," J. Fluid Mech. **294**, 71–92.

Yeh, H., Liu, P. L.-F. & Synolakis, C. (Eds) 1996 "Long-wave Runup Models," Proc. 2nd Int. Workshop on Long-wave Runup Models, World Scientific Publishing Co., Singapore.

## Appendix A. Derivation of Approximate Two-Dimensional Governing Equations

In deriving the two-dimensional, depth-integrated governing equations, the frequency dispersion is assumed to be weak, i.e.,

$$O(\mu^2) \ll 1 \tag{A.1}$$

We can expand the dimensionless physical variables as power series of $\mu^2$.

$$f = \sum_{n=0}^{\infty} \mu^{2n} f_n; \quad (f = \zeta,\ p,\ \boldsymbol{u}) \tag{A.2}$$

$$w = \sum_{n=1}^{\infty} \mu^{2n} w_n; \tag{A.3}$$

Furthermore, we will adopt the following assumption on the vorticity field. We assume that the vertical vorticity component, $(u_y - v_x)$, is of $O(1)$, while the horizontal vorticity components are weaker and satisfy the following conditions

$$\frac{\partial}{\partial z}\boldsymbol{u}_0 = 0, \tag{A.4}$$

$$\frac{\partial}{\partial z}\boldsymbol{u}_1 = \nabla w_1. \tag{A.5}$$

Consequently, from (A.4), the leading order horizontal velocity components are independent of the vertical coordinate, i.e.,

$$\boldsymbol{u}_0 = \boldsymbol{u}_0(x,\ y,\ t), \tag{A.6}$$

Substituting (A.2) and (A.3) into the continuity equation (2.3) and the boundary condition (2.7), we collect the leading order terms as

$$\nabla \cdot \boldsymbol{u}_0 + w_{1z} = 0, \quad -h < z < \varepsilon\zeta \tag{A.7}$$

$$w_1 + \boldsymbol{u}_0 \cdot \nabla h + \frac{h_t}{\varepsilon} = 0 \quad \text{on } z = -h \tag{A.8}$$

Integrating (A.7) with respect to $z$ and using (A.8) to determine the integration constant, we obtain the vertical profile of the vertical velocity components:

$$u_1 = -z\nabla\cdot\boldsymbol{u}_0 - \nabla\cdot(h\boldsymbol{u}_0) - \frac{h_t}{\varepsilon} \tag{A.9}$$

Similarly, integrating (A.5) with respect to $z$ with information from (A.8), we can find the corresponding vertical profiles of the horizontal velocity components:

$$\boldsymbol{u}_1 = -\frac{z^2}{2}\nabla(\nabla\cdot\boldsymbol{u}_0) - z\nabla\left[\nabla\cdot(h\boldsymbol{u}_0) + \frac{h_t}{\varepsilon}\right] + \boldsymbol{C}_1(x,\ y,\ t) \tag{A.10}$$

in which $\boldsymbol{C}_1$ is a unknown function to be determined. Up to $O(\mu^2)$, the horizontal velocity components can be expressed as

$$\boldsymbol{u} = \boldsymbol{u}_0(x,\ y,\ t) + \mu^2\left\{-\frac{z^2}{2}\nabla(\nabla\cdot\boldsymbol{u}_0) - z\nabla\left[\nabla\cdot(h\boldsymbol{u}_0) + \frac{h_t}{\varepsilon}\right] + \boldsymbol{C}_1(x,\ y,\ t)\right\}$$
$$+O(\mu^4),\ -h < z < \varepsilon\zeta \tag{A.11}$$

Now, we can define the horizontal velocity vector, $\boldsymbol{u}_\alpha(x,\ y,\ z_\alpha(x,\ y,\ t),\ t)$ evaluated at $z = z_\alpha(x,\ y,\ t)$ as

$$\boldsymbol{u}_\alpha = \boldsymbol{u}_0 + \mu^2\left\{-\frac{z_\alpha^2}{2}\nabla(\nabla\cdot\boldsymbol{u}_0) - z_\alpha\nabla\left[\nabla\cdot(h\boldsymbol{u}_0) + \frac{h_t}{\varepsilon}\right] + \boldsymbol{C}_1(x,\ y,\ t)\right\} + O(\mu^4) \tag{A.12}$$

Subtracting (A.12) from (A.11) we can express $\boldsymbol{u}$ in terms of $\boldsymbol{u}_\alpha$ as

$$\boldsymbol{u} = \boldsymbol{u}_\alpha - \mu^2\left\{\frac{z^2 - z_\alpha^2}{2}\nabla(\nabla\cdot\boldsymbol{u}_\alpha) + (z - z_\alpha)\nabla\left[\nabla\cdot(h\boldsymbol{u}_\alpha) + \frac{h_t}{\varepsilon}\right]\right\} + O(\mu^4) \tag{A.13}$$

Note that $\boldsymbol{u}_\alpha = \boldsymbol{u}_0 + O(\mu^2)$ has been used in (A.13).

The exact continuity equation (2.8) can be rewritten approximately in terms of $\zeta$ and $\boldsymbol{u}_\alpha$. Substituting (A.13) into (2.8), we obtain

$$\frac{1}{\varepsilon}H_t + \nabla\cdot(H\boldsymbol{u}_\alpha) - \mu^2\nabla\cdot\left\{H\left[\left(\frac{1}{6}(\varepsilon^2\zeta^2 - \varepsilon\zeta h + h^2) - \frac{1}{2}z_\alpha^2\right)\nabla(\nabla\cdot\boldsymbol{u}_\alpha)\right.\right.$$
$$\left.\left. + \left(\frac{1}{2}(\varepsilon\zeta - h) - z_\alpha\right)\nabla\left(\nabla\cdot(h\boldsymbol{u}_\alpha) + \frac{h_t}{\varepsilon}\right)\right]\right\} = O(\mu^4) \tag{A.14}$$

in which $H = h + \varepsilon\zeta$.

Equation (A.14) is one of three governing equations for $\zeta$ and $\boldsymbol{u}_\alpha$. The other two equations come from the horizontal momentum equation, (2.4). However, we must find the pressure field first. This can be accomplished by approximating the vertical momentum equation (2.5) as

$$\varepsilon p_z = -1 - \mu^2(\varepsilon u_{1t} + \varepsilon^2\boldsymbol{u}_0\cdot\nabla u_1 + \varepsilon^2 u_1 u_{1z}) + O(\mu^4),\ -h < z < \varepsilon\zeta \tag{A.15}$$

We can integrate the equation above with respect to $z$ to find the pressure field as

$$p=(\zeta-\frac{z}{\varepsilon})+\mu^2\left\{\frac{1}{2}(z^2-\varepsilon^2\zeta^2)\nabla\cdot\boldsymbol{u}_{0t}+(z-\varepsilon\zeta)[\nabla\cdot(h\boldsymbol{u})_{0t}+\frac{h_{tt}}{\varepsilon}]\right.$$
$$+\frac{\varepsilon}{2}(z^2-\varepsilon^2\zeta^2)\boldsymbol{u}_0\cdot\nabla(\nabla\cdot\boldsymbol{u}_0)+\varepsilon(z-\varepsilon\zeta)\boldsymbol{u}_0\cdot\nabla\left[\nabla\cdot(h\boldsymbol{u}_0)+\frac{h_t}{\varepsilon}\right]+\frac{\varepsilon}{2}(\varepsilon^2\zeta^2-z^2)(\nabla\cdot\boldsymbol{u}_0)^2$$
$$\left.+\varepsilon(\varepsilon\zeta-z)[\nabla\cdot(h\boldsymbol{u}_0)+\frac{h_t}{\varepsilon}]\nabla\cdot\boldsymbol{u}_0\right\}+O(\mu^4),\ \ -h<z<\varepsilon\zeta \tag{A.16}$$

We remark here that (A.11) has been used in deriving (A.16). To obtain the governing equations for $\boldsymbol{u}_\alpha$, we first substitute (A.13) and (A.16) into (2.4) and obtain the following equation, up to $O(\mu^2)$,

$$\boldsymbol{u}_{\alpha t}+\varepsilon\boldsymbol{u}_\alpha\cdot\nabla\boldsymbol{u}_\alpha+\nabla\zeta+\mu^2\left\{\frac{1}{2}z_\alpha^2\nabla(\nabla\cdot\boldsymbol{u}_{\alpha t})+z_\alpha\nabla\left[\nabla\cdot(h\boldsymbol{u}_\alpha)_t+\frac{h_{tt}}{\varepsilon}\right]\right\}$$
$$+\mu^2 z_{\alpha t}\left\{z_\alpha\nabla(\nabla\cdot\boldsymbol{u}_\alpha)+\nabla\left[\nabla\cdot(h\boldsymbol{u}_\alpha)+\frac{h_t}{\varepsilon}\right]\right\}$$
$$+\varepsilon\mu^2\left\{\left[\nabla\cdot(h\boldsymbol{u}_\alpha)+\frac{h_t}{\varepsilon}\right]\nabla\left[\nabla\cdot(h\boldsymbol{u}_\alpha)+\frac{h_t}{\varepsilon}\right]\right.$$
$$-\nabla\left[\zeta(\nabla\cdot(h\boldsymbol{u}_\alpha)_t+\frac{h_{tt}}{\varepsilon})\right]+(\boldsymbol{u}_\alpha\cdot\nabla z_\alpha)\nabla\left[\nabla\cdot(h\boldsymbol{u}_\alpha)+\frac{h_t}{\varepsilon}\right]$$
$$\left.+z_\alpha\nabla\left[\boldsymbol{u}_\alpha\cdot\nabla(\nabla\cdot(h\boldsymbol{u}_\alpha)+\frac{h_t}{\varepsilon})\right]+z_\alpha(\boldsymbol{u}_\alpha\cdot\nabla z_\alpha)\nabla(\nabla\cdot\boldsymbol{u}_\alpha)+\frac{z_\alpha^2}{2}\nabla\left[\boldsymbol{u}_\alpha\cdot\nabla(\nabla\cdot\boldsymbol{u}_\alpha)\right]\right\}$$
$$+\varepsilon^2\mu^2\nabla\left\{-\frac{\zeta^2}{2}\nabla\cdot\boldsymbol{u}_{\alpha t}-\zeta\boldsymbol{u}_\alpha\cdot\nabla\left[\nabla\cdot(h\boldsymbol{u}_\alpha)+\frac{h_t}{\varepsilon}\right]+\zeta\left[\nabla\cdot(h\boldsymbol{u}_\alpha)+\frac{h_t}{\varepsilon}\right]\nabla\cdot\boldsymbol{u}_\alpha\right\}$$
$$+\varepsilon^3\mu^2\nabla\left\{\frac{\zeta^2}{2}\left[(\nabla\cdot\boldsymbol{u}_\alpha)^2-\boldsymbol{u}_\alpha\cdot\nabla(\nabla\cdot\boldsymbol{u}_\alpha)\right]\right\}=O(\mu^4) \tag{A.17}$$

Equations (A.14) and (A.17) are the coupled governing equations, written in terms of $\boldsymbol{u}_\alpha$ and $\zeta$, for fully nonlinear, weakly dispersive waves generated by a submarine landslide.

## Appendix B. Numerical Scheme

To simplify the predictor-corrector equations, the velocity time derivatives in the momentum equations are grouped into the dimensional form:

$$U=u+\frac{z_\alpha^2-\zeta^2}{2}u_{xx}+(z_\alpha-\zeta)(hu)_{xx}-\zeta_x\left[\zeta u_x+(hu)_x\right] \tag{B.1}$$

$$V=v+\frac{z_\alpha^2-\zeta^2}{2}v_{yy}+(z_\alpha-\zeta)(hv)_{yy}-\zeta_y\left[\zeta v_y+(hv)_y\right] \tag{B.2}$$

where subscripts denote partial derivatives. Note that this grouping is different from that given in Wei *et al.* (1995). The grouping given above in $B.1$ and $B.2$ incorporates nonlinear terms, which is not done in Wei *et al.*. These nonlinear time derivatives arise from the nonlinear dispersion terms $\nabla\left[\zeta(\nabla\cdot(h\boldsymbol{u}_\alpha)_t+\frac{hu_t}{\varepsilon})\right]$ and $\nabla\left(\frac{\zeta}{2}^2\nabla\cdot\boldsymbol{u}_{\alpha t}\right)$, which can be reformulated using the relation:

$$\nabla\left[\zeta(\nabla\cdot(h\boldsymbol{u}_\alpha)_t+\frac{h_{tt}}{\varepsilon})\right]=\nabla\left[\zeta(\nabla\cdot(h\boldsymbol{u}_\alpha)+\frac{h_t}{\varepsilon})\right]_t-\nabla\left[\zeta_t(\nabla\cdot(h\boldsymbol{u}_\alpha)+\frac{h_t}{\varepsilon})\right]$$

$$\nabla\left(\frac{\zeta}{2}^2\nabla\cdot\boldsymbol{u}_{\alpha t}\right)=\nabla\left(\frac{\zeta}{2}^2\nabla\cdot\boldsymbol{u}_\alpha\right)_t-\nabla(\zeta\zeta_t\nabla\cdot\boldsymbol{u}_\alpha)$$

The authors have found that this form is more stable and requires less iterations to converge for highly nonlinear problems, as compared to the Wei *et al.* formulation. The predictor equations are

$$\eta_{i,j}^{n+1}=\eta_{i,j}^n+\frac{\Delta t}{12}(23E_{i,j}^n-16E_{i,j}^{n-1}+5E_{i,j}^{n-2}) \tag{B.3}$$

$$U_{i,j}^{n+1}=U_{i,j}^n+\frac{\Delta t}{12}(23F_{i,j}^n-16F_{i,j}^{n-1}+5F_{i,j}^{n-2})+2(F_1)_{i,j}^n-3(F_1)_{i,j}^{n-1}+(F_1)_{i,j}^{n-2} \tag{B.4}$$

$$V_{i,j}^{n+1}=V_{i,j}^n+\frac{\Delta t}{12}(23G_{i,j}^n-16G_{i,j}^{n-1}+5G_{i,j}^{n-2})+2(G_1)_{i,j}^n-3(G_1)_{i,j}^{n-1}+(G_1)_{i,j}^{n-2} \tag{B.5}$$

where

$$\begin{aligned}E=&-h_t-[(\zeta+h)u]_x-[(\zeta+h)v]_y\\&+\left\{(h+\zeta)\left[\left(\frac{1}{6}\left(\zeta^2-\zeta h+h^2\right)-\frac{1}{2}z_\alpha^2\right)S_x+\left(\frac{1}{2}(\zeta-h)-z_\alpha\right)T_x\right]\right\}_x\\&+\left\{(h+\zeta)\left[\left(\frac{1}{6}\left(\zeta^2-\zeta h+h^2\right)-\frac{1}{2}z_\alpha^2\right)S_y+\left(\frac{1}{2}(\zeta-h)-z_\alpha\right)T_y\right]\right\}_y\end{aligned} \tag{B.6}$$

$$\begin{aligned}F=&-[(u^2)_x+(v^2)_x]-g\zeta_x-z_\alpha h_{xtt}-z_{\alpha t}h_{xt}\\&+(\zeta h_{tt})_x-[E(\zeta S+T)]_x-\left[\frac{1}{2}\left(z_\alpha^2-\zeta^2\right)(uS_x+vS_y)\right]_x\end{aligned}$$

$$-\left[\left(z_\alpha-\zeta\right)\left(uT_x+vT_y\right)\right]_x-\frac{1}{2}\left[\left(T+\zeta S\right)^2\right]_x \tag{B.7}$$

$$F_1=\frac{z_\alpha^2-\zeta^2}{2}v_{xy}+(z_\alpha-\zeta)(hv)_{xy}-\zeta_x[\zeta v_y+(hv)_y] \tag{B.8}$$

$$\begin{aligned}G=&-[(u^2)_y+(v^2)_y]-g\zeta_y-z_\alpha h_{ytt}-z_{\alpha t}h_{yt}\\&+(\zeta h_{tt})_y-[E(\zeta S+T)]_y-\left[\frac{1}{2}\left(z_\alpha^2-\zeta^2\right)\left(uS_x+vS_y\right)\right]_y\\&-\left[\left(z_\alpha-\zeta\right)\left(uT_x+vT_y\right)\right]_y-\frac{1}{2}\left[\left(T+\zeta S\right)^2\right]_y\end{aligned} \tag{B.9}$$

$$G_1=\frac{z_\alpha^2-\zeta^2}{2}u_{xy}+(z_\alpha-\zeta)(hu)_{xy}-\zeta_y[\zeta u_x+(hu)_x] \tag{B.10}$$

and

$$S=u_x+v_y \qquad\qquad T=(hu)_x+(hv)_y+h_t \tag{B.11}$$

All terms are evaluated at the local grid point $(i,j)$, and $n$ represents the current time step, when values of $\zeta, u$ and $v$ are known. The above expressions, (B.6) - (B.11), are for the fully nonlinear problem; if a weakly nonlinear or non-dispersive system is to be examined, the equations should be truncated accordingly. The fourth-order implicit corrector expressions for the free surface elevation and horizontal velocities are

$$\eta_{i,j}^{n+1}=\eta_{i,j}^n+\frac{\Delta t}{24}(9E_{i,j}^{n+1}+19E_{i,j}^n-5E_{i,j}^{n-1}+E_{i,j}^{n-2}) \tag{B.12}$$

$$U_{i,j}^{n+1}=U_{i,j}^n+\frac{\Delta t}{24}(9F_{i,j}^{n+1}+19F_{i,j}^n-5F_{i,j}^{n-1}+F_{i,j}^{n-2})+(F_1)_{i,j}^{n+1}-(F_1)_{i,j}^n \tag{B.13}$$

$$V_{i,j}^{n+1}=V_{i,j}^n+\frac{\Delta t}{24}(9G_{i,j}^{n+1}+19G_{i,j}^n-5G_{i,j}^{n-1}+G_{i,j}^{n-2})+(G_1)_{i,j}^{n+1}-(G_1)_{i,j}^n \tag{B.14}$$

The system is solved by first evaluating the predictor equations, then $u$ and $v$ are solved via (B.1) and (B.2), respectively. Both (B.1) and (B.2) yield a diagonal matrix after finite

differencing. The matrices are diagonal, with a bandwidth of five (due to five point finite differencing), and an efficient LU decomposition can be utilized. At this point in the numerical system, we have predictors for $\zeta$, $u$, and $v$. Next, the corrector expressions are evaluated, and again $u$ and $v$ are determined from (B.1) and (B.2). The relative errors in each of the physical variables is found, in order to determine if the implicit correctors need to be reiterated. This relative error is given as:

$$\frac{u^{n+1} - u_*^{n+1}}{u^{n+1}} \tag{B.15}$$

where $u$ represents $\zeta$, $u$, and $v$, and $u_*$ is the previous iterations value. The correctors are recalculated until all errors are less than $10^{-4}$. Note that inevitably there will be locations in the numerical domain where values of the physical variables are close to zero, and applying the above error calculation to these points may lead to unnecessary iterations in the corrector loop. Thus it is required that $|\frac{\zeta}{a}|, |\frac{u,v}{\epsilon\sqrt{gh}}| > 10^{-4}$ for the corresponding error calculation to proceed, where $a$ is determined from equation (3.4) for a creeping slide. For the model equations, linear stability analysis gives that $\Delta t < \frac{\Delta x}{2c}$, where $c$ is the wave celerity in the deepest water. Note that when modeling highly nonlinear waves, a smaller $\Delta t$ is usually required for stability. In this analysis, $\Delta t = \frac{\Delta x}{4c}$ produced stable and convergent results for all trails.

For the numerical exterior boundaries, two types of conditions are applied: reflective and radiation. The reflective, or no-flux, boundary condition for the Boussinesq equations has been examined by previous researchers (Wei & Kirby, 1995), and their methodology is followed here. For the radiation, or open, boundary condition, a sponge layer is utilized. The sponge layer is applied in the manner recommended by Kirby *et al.* (1998). Runup and rundown is modeled with the "extrapolation" moving boundary algorithm described in Lynett *et al.* (2001).

## Appendix C. Notation

$a$ = wave amplitude

$b$ = length along the slope between $x_l$ and $x_r$ for the $tanh$ slide

$c$ = wave celerity

$d$ = depth of water above the centerpoint of the slide, function of time

$d_o$ = initial depth of water above the centerpoint of the slide, *i.e.* at $t = 0$

$g$ = gravity

$G$ = transverse water depth function for the two-horizontal dimension slump

$h_o$ = characteristic water depth or baseline water depth, function of space

$h$ = water depth profile, function of space and time

$\overline{h}$ = the changing part of the water depth profile $= (h - h_o)/\delta$

$h_c$ = baseline water depth at the centerpoint of the slide $= \Delta h + d$

$h_{c_o}$ = initial baseline water depth at the centerpoint of the slide $= \Delta h + d_o$

$H$ = total water depth $= h + \varepsilon\zeta$

$l_o$ = characteristic horizontal lengthscale of the submarine slide

$L_s$ = characteristic horizontal side length of the submarine slide

$p$ = depth dependant pressure

$r_o$ = half-width of the slump profile

$S$ = shape factor for $tanh$ slide

$t$ = time

$t_c$ = time scale of seafloor motion

$t_w$ = typical period of wave generated by a specified seafloor motion

$u, v, w$ = depth dependant components of velocity in $x, y, z$

$u_o, v_o$ = magnitude of horizontal velocity components, $u, v$, evaluated on $z_o$

$\overline{u}, \overline{v}$ = depth-averaged horizontal velocity components

$\boldsymbol{u}$ = horizontal velocity vector $= (u, v)$

$x_c, y_c$ = horizontal coordinates of the midpoint of the seafloor movement

$x_l, x_r$ = locations of the left and right inflection points for the $tanh$ slide profile

$z_o$ = arbitrary level on which the "extended" equations are derived

$\delta$ = scaled characteristic change in water depth due to seafloor motion $= \Delta h / h_o$

$\Delta h$ = characteristic, or maximum, change in water depth due to seafloor motion

$\Delta t$ = time step in numerical model

$\Delta x, \Delta y$ = space steps in numerical model

$\varepsilon$ = nonlinearity parameter, $= a/h_o$

$\nabla$ = horizontal gradient vector

$\rho$ = density of water

$\theta$ = slope angle

$\mu$ = frequency dispersion parameter, $= h_o/l_o$

$\zeta$ = free surface displacement

(1)

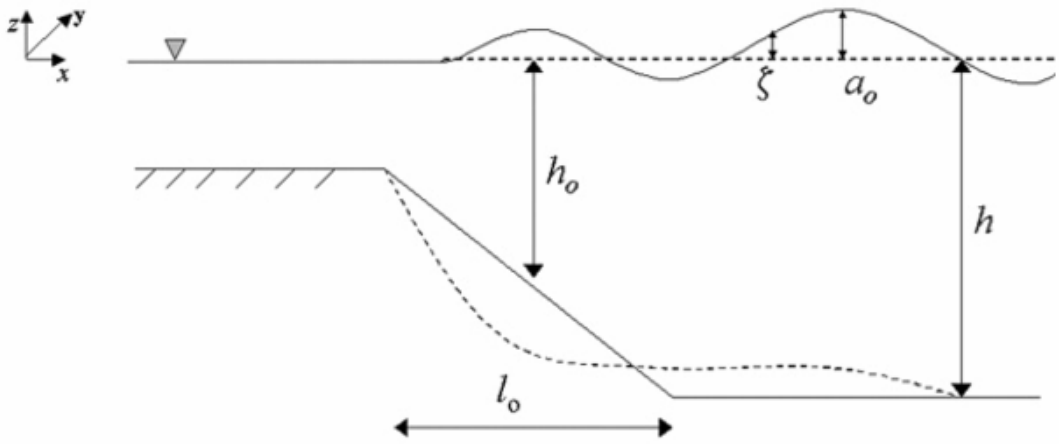


**Figure 1.** Basic formulational setup.

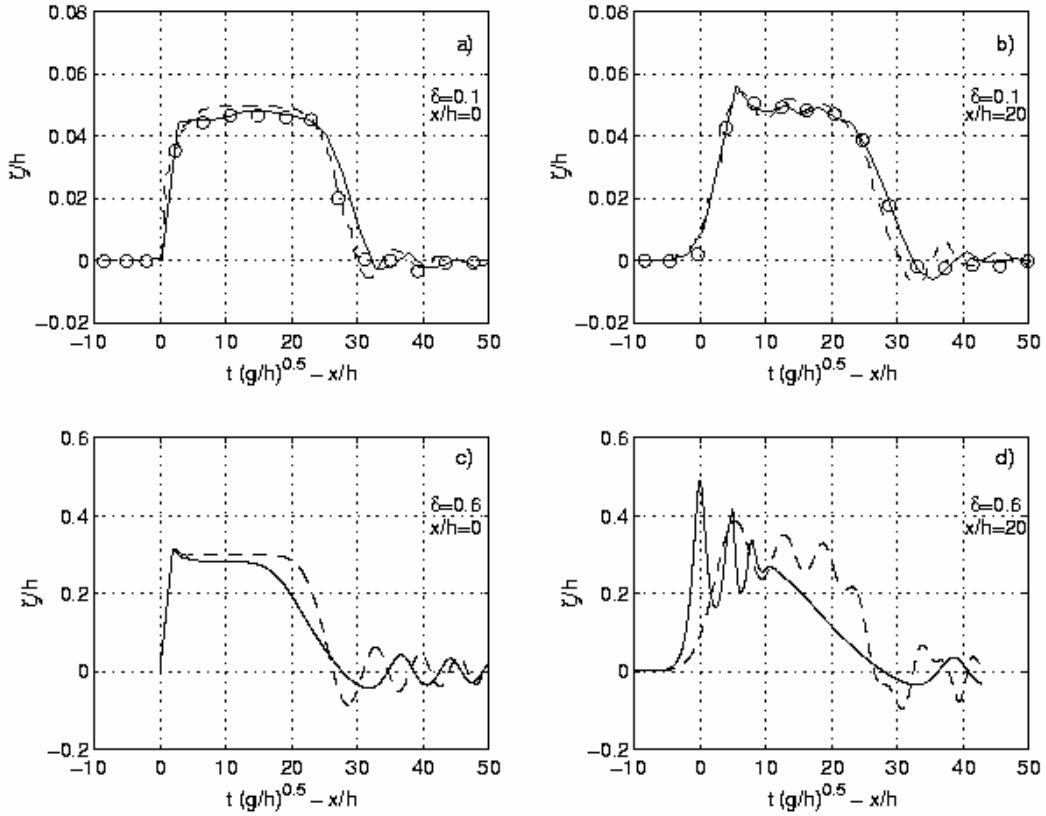


**Figure 2.** Shown in subplots a) and b), a comparison between Hammack's (1973) experimental data (dots) for an impulsive seafloor upthrust of $\delta$=0.1, FNL-EXT numerical simulation (solid line), and linear theory (dashed line): a) is a time series at x/h=0 and b) is at x/h=20, where x is the distance from the edge of the impulsive movement. Subplots c) and d) show FNL-EXT (solid line) and L-EXT (dashed line) numerical results for Hammack's setup, except with $\delta$=0.6.

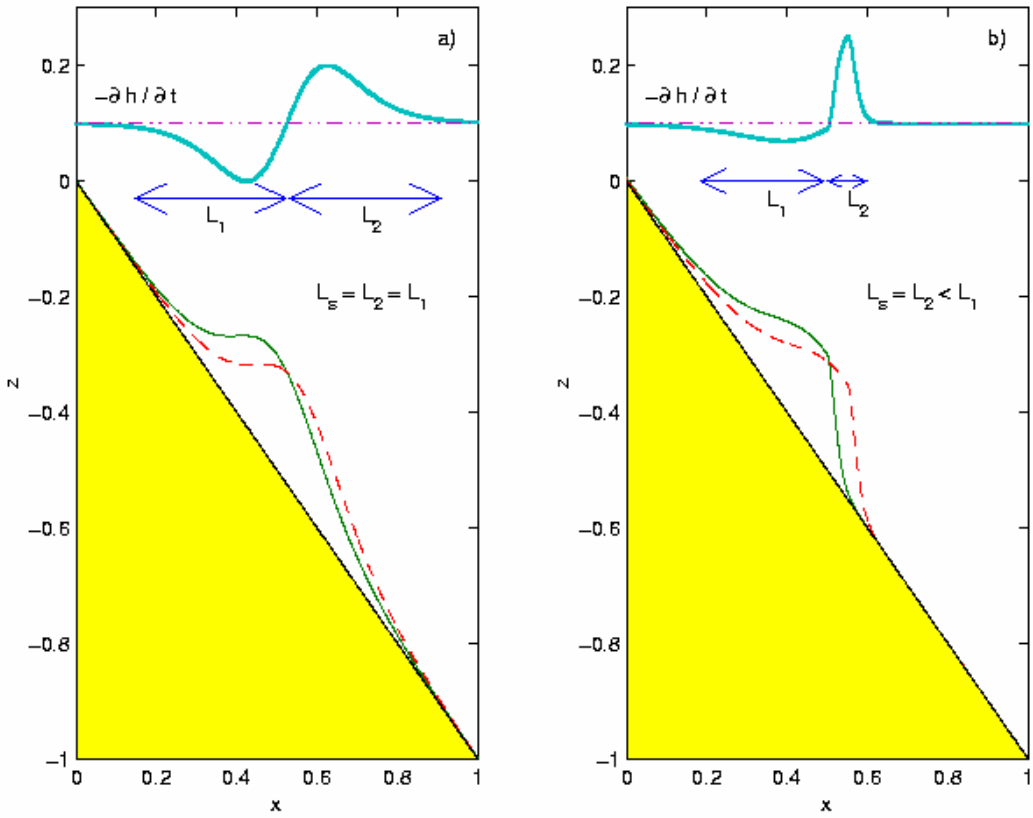


**Figure 3.** Graphical definition of the characteristic side length of a slide mass. The slide mass at time=$t_o$ is shown by the solid line, while the profile at some time=$t > t_o$ is shown by the dashed line. The negative of the change in water depth (or the approximate free surface response in the non-dispersive equation model) during the increment $t - t_o$ is shown by the thick line plotted on $z$=0.1.

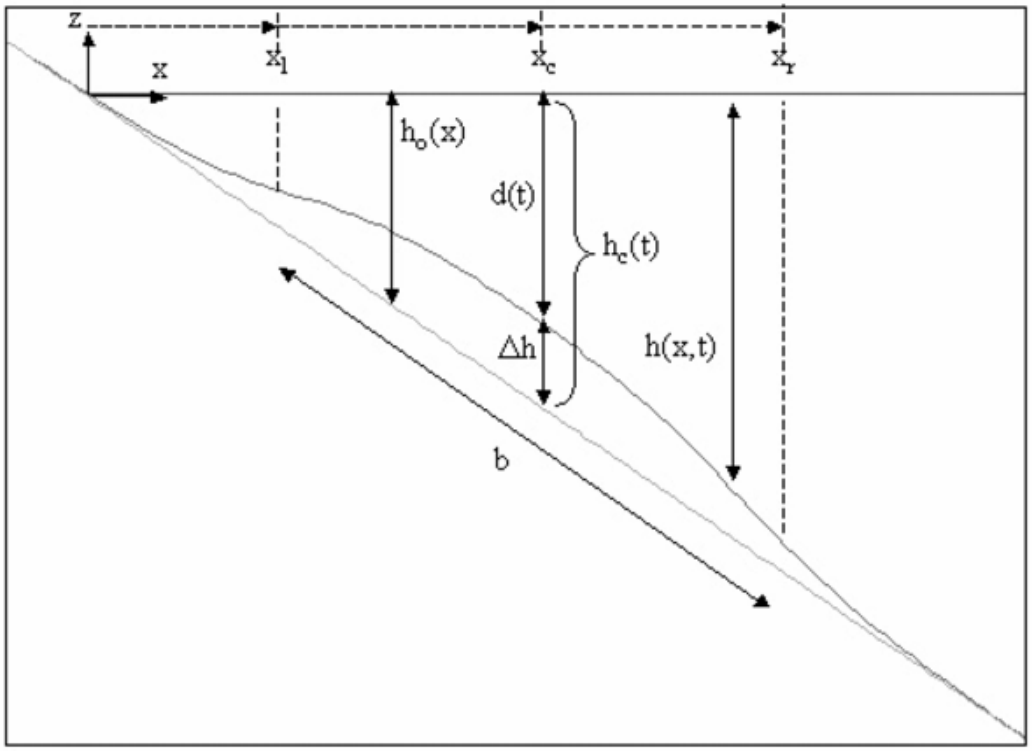


**Figure 4.** Setup for submarine landslide comparisons.

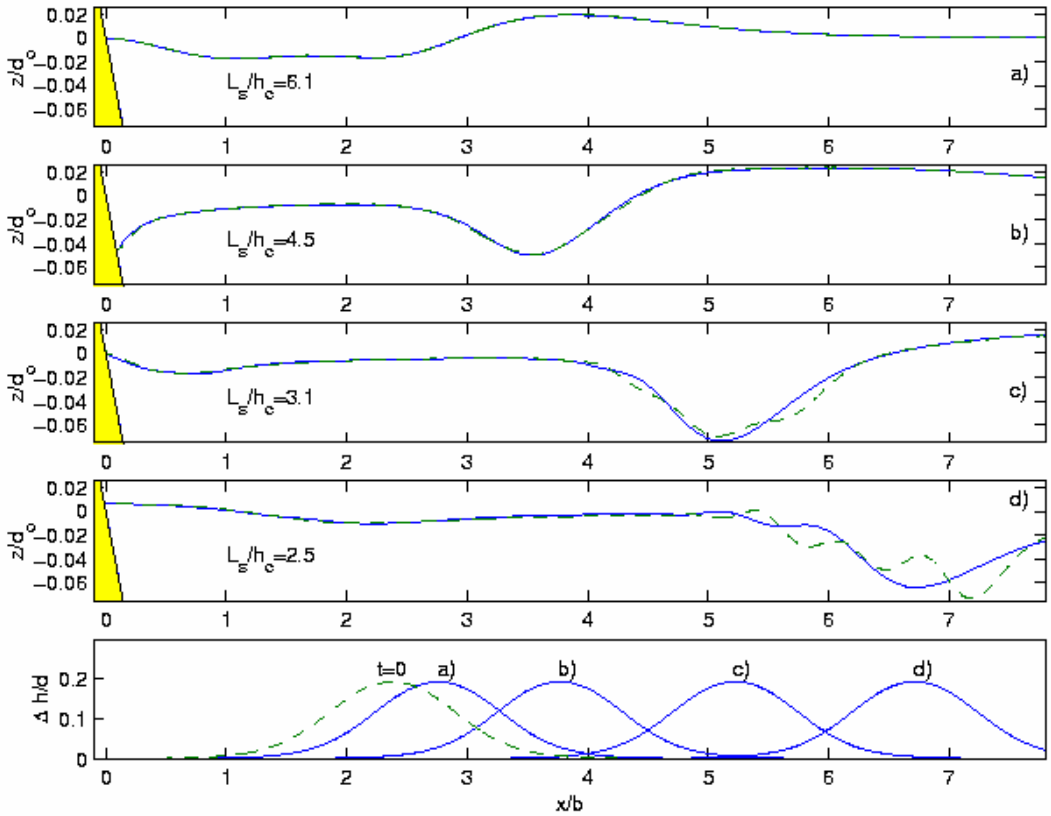


**Figure 5.** Free surface snapshots for BIEM (solid line) and depth-integrated (dashed line) results at $t(g/d_o)^{1/2}$ = a) 10.6, b) 21, c) 31.6, and d) 41. The lower subplot shows the location of the slide mass in each of the above four snapshots.

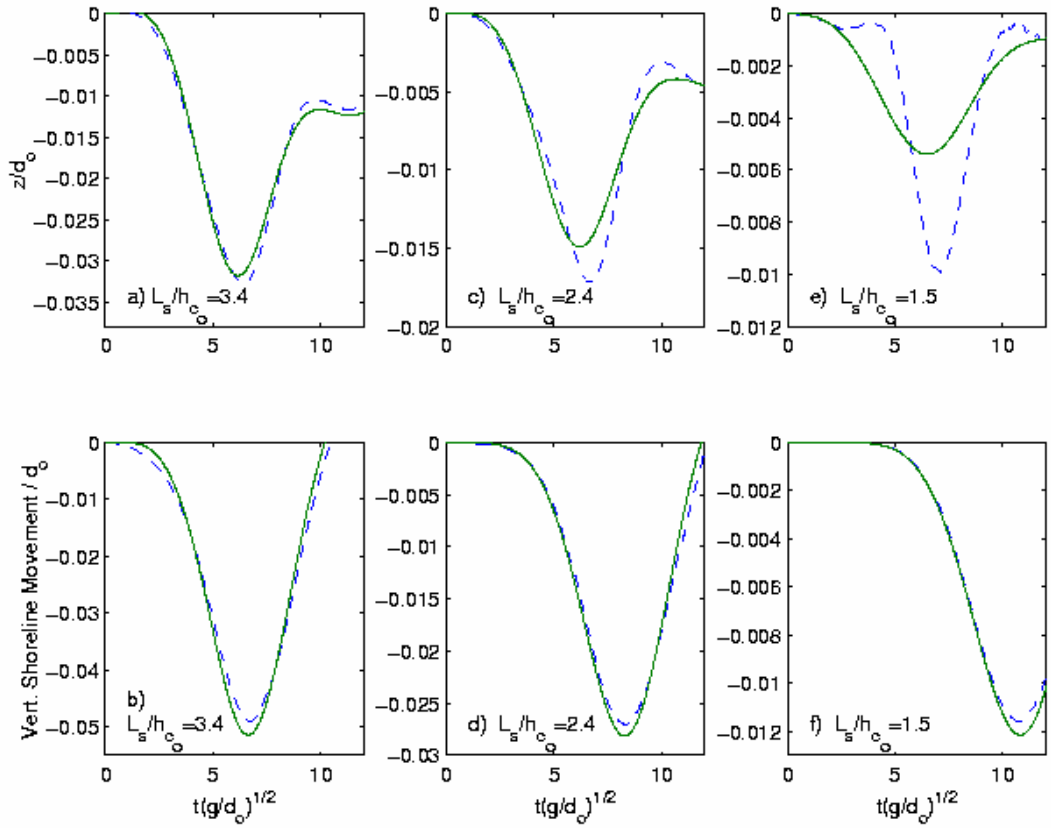


**Figure 6.** Time series above the initial centerpoint of the slide (top row) and vertical movement of the shoreline (bottom row) for a 20° slope and a slide mass with a maximum height $\Delta h$=0.1. BIEM results are shown by the solid line, depth-integrated results by the dashed line. Subplots a & b are for $d_o/b$=0.4, c & d for $d_o/b$=0.6, and e & f for $d_o/b$=1.0.

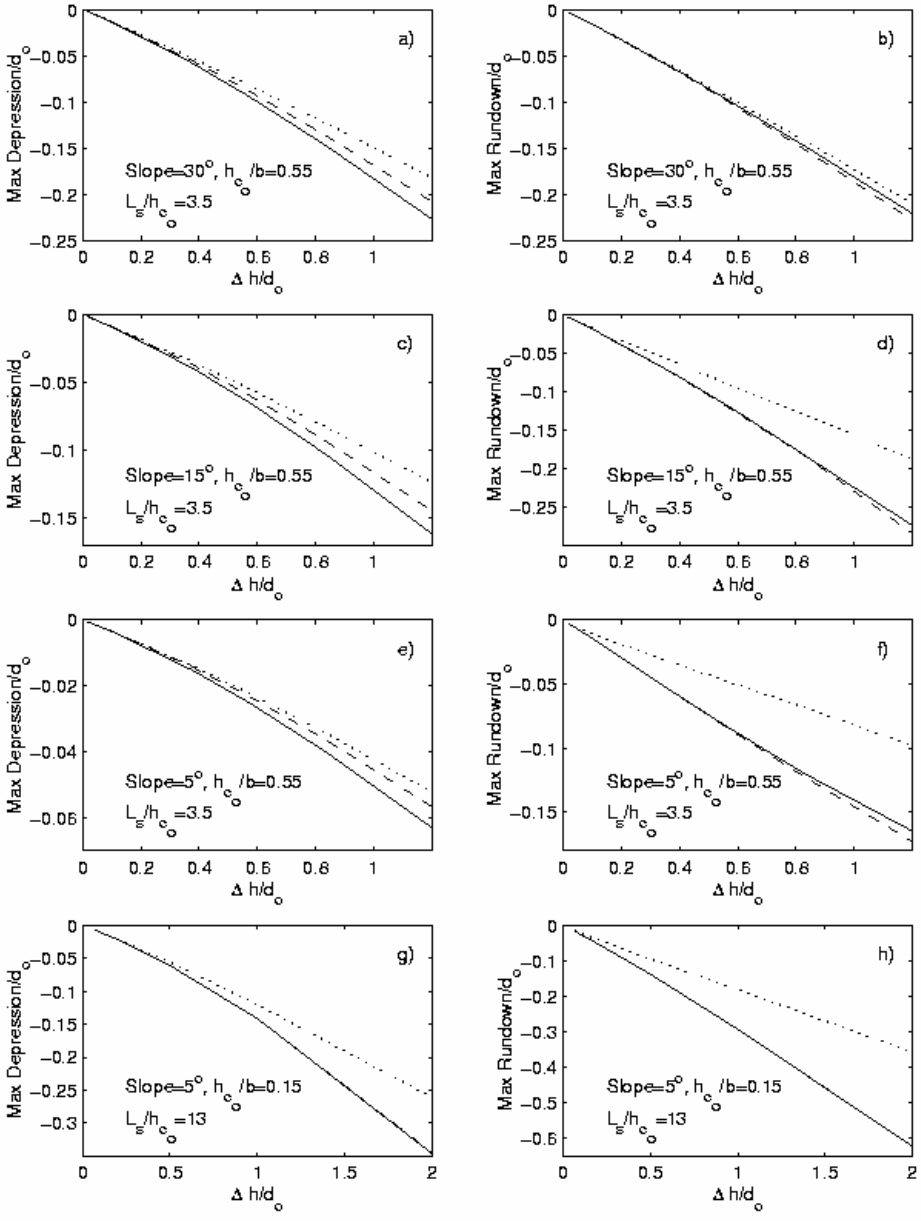
a)
Max Depression/d$_o$
Slope=30°, h$_{c_o}$/b=0.55
L$_s$/h$_{c_o}$=3.5
Δ h/d$_o$
b)
Max Rundown/d$_o$
Slope=30°, h$_{c_o}$/b=0.55
L$_s$/h$_{c_o}$=3.5
Δ h/d$_o$
c)
Max Depression/d$_o$
Slope=15°, h$_{c_o}$/b=0.55
L$_s$/h$_{c_o}$=3.5
Δ h/d$_o$
d)
Max Rundown/d$_o$
Slope=15°, h$_{c_o}$/b=0.55
L$_s$/h$_{c_o}$=3.5
Δ h/d$_o$
e)
Max Depression/d$_o$
Slope=5°, h$_{c_o}$/b=0.55
L$_s$/h$_{c_o}$=3.5
Δ h/d$_o$
f)
Max Rundown/d$_o$
Slope=5°, h$_{c_o}$/b=0.55
L$_s$/h$_{c_o}$=3.5
Δ h/d$_o$
g)
Max Depression/d$_o$
Slope=5°, h$_{c_o}$/b=0.15
L$_s$/h$_{c_o}$=13
Δ h/d$_o$
h)
Max Rundown/d$_o$
Slope=5°, h$_{c_o}$/b=0.15
L$_s$/h$_{c_o}$=13
Δ h/d$_o$

**Figure 7.** Maximum depression above the initial centerpoint of the slide mass and maximum rundown for four different trial sets. FNL-EXT results indicated by the solid line, WNL-EXT by the dashed line, and L-EXT by the dotted line.

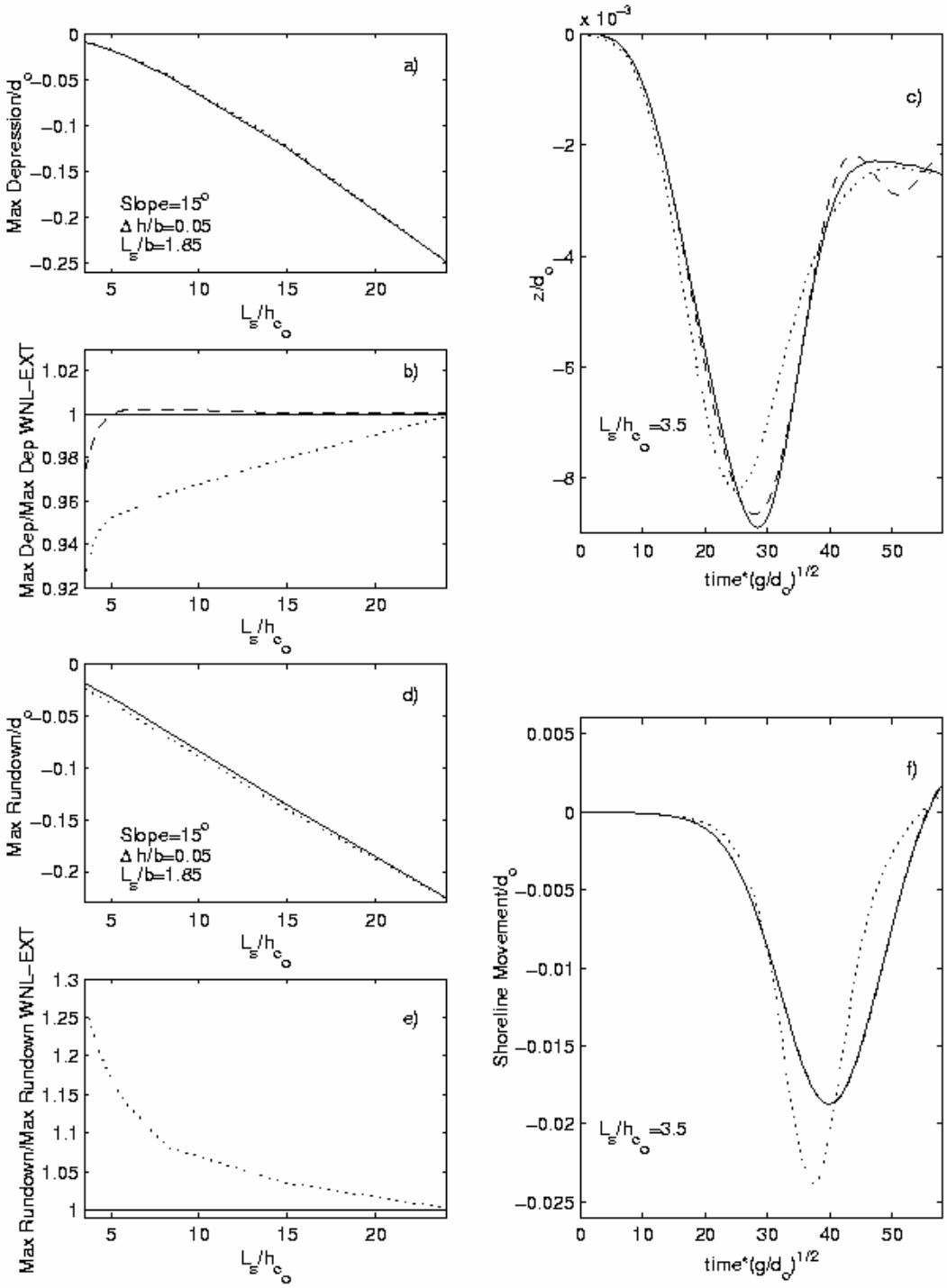
a)
Max Depression/d$_o$
Slope=15°
Δ h/b=0.05
L$_s$/b=1.85
L$_s$/h$_{c_o}$
b)
Max Dep/Max Dep WNL−EXT
L$_s$/h$_{c_o}$
c)
x 10$^{-3}$
z/d$_o$
L$_s$/h$_{c_o}$=3.5
time*(g/d$_o$)$^{1/2}$
d)
Max Rundown/d$_o$
Slope=15°
Δ h/b=0.05
L$_s$/b=1.85
L$_s$/h$_{c_o}$
e)
Max Rundown/Max Rundown WNL−EXT
L$_s$/h$_{c_o}$
f)
Shoreline Movement/d$_o$
L$_s$/h$_{c_o}$=3.5
time*(g/d$_o$)$^{1/2}$

**Figure 8.** Maximum depression above the initial centerpoint of the slide mass a) and maximum rundown d) for a set of numerical simulations on a 15° slope. Shown in b) and e) are the maximum depression and maximum rundown scaled by the corresponding values from the WNL-EXT model. Time series comparisons for $L_s/h_{c_o} = 3.5$ showing the free surface elevation above the centerpoint c) and vertical shoreline movement f) are given on the right. WNL-EXT results indicated by the solid line, WNL-DA by the dashed line, and NL-SW by the dotted line.

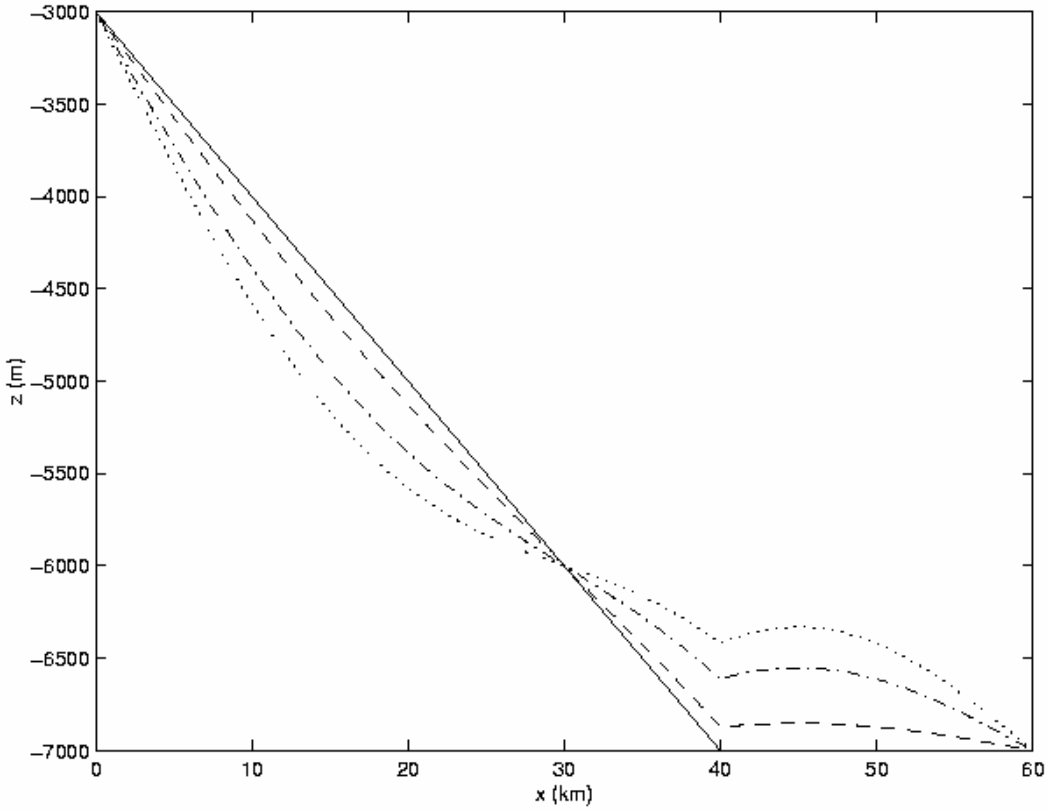


**Figure 9.** Submarine slump modeled using a sine wave transformation, where the solid line is the initial water depth, the dashed line at $t = t_c/12$, the dashed-dotted line at $t = t_c/3$, and the dotted line at $t = t_c$.

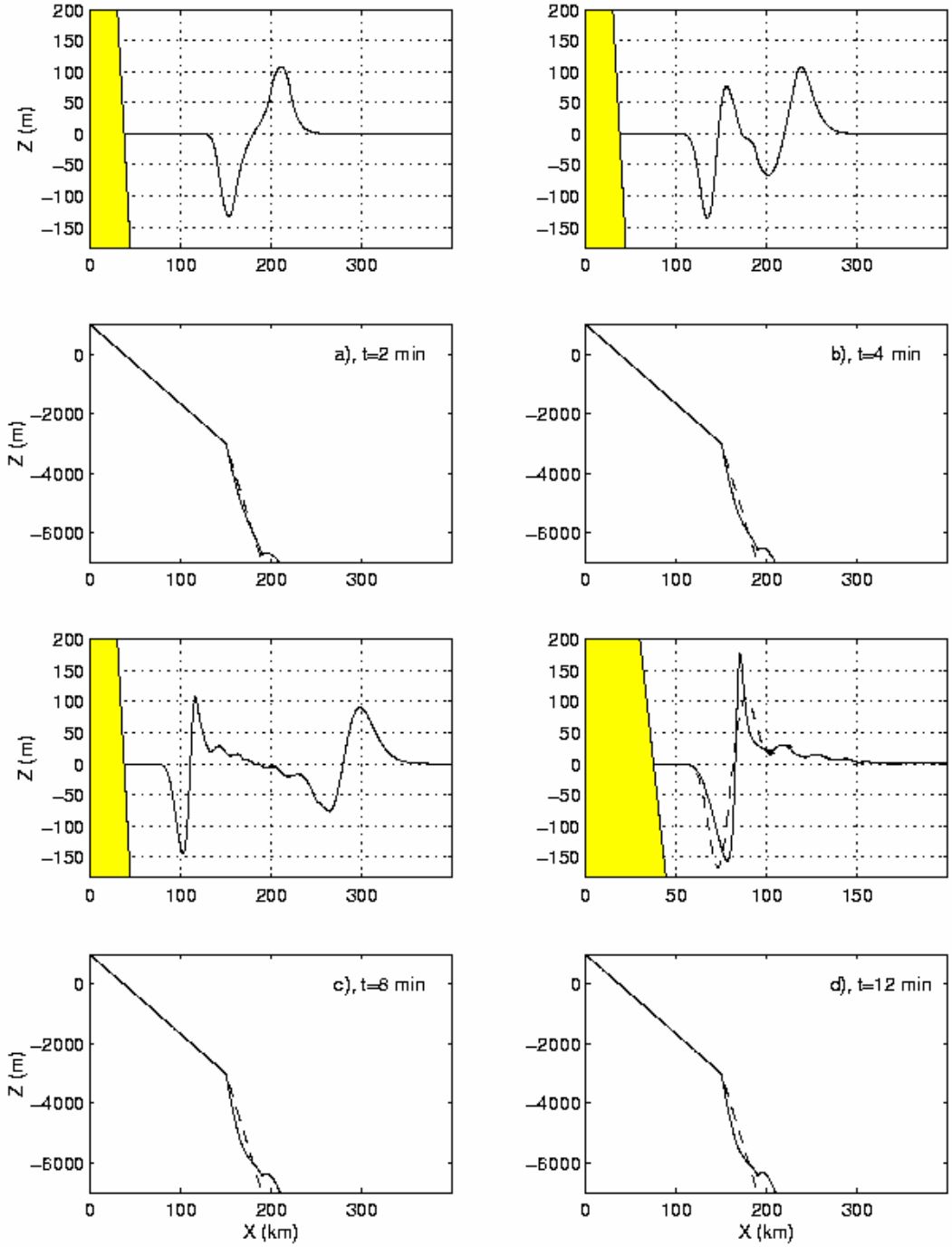


**Figure 10.** 1D simulation of a submarine slump using FNL-EXT. Numerical free surface results from L-EXT are also shown by the dotted line for the last time.

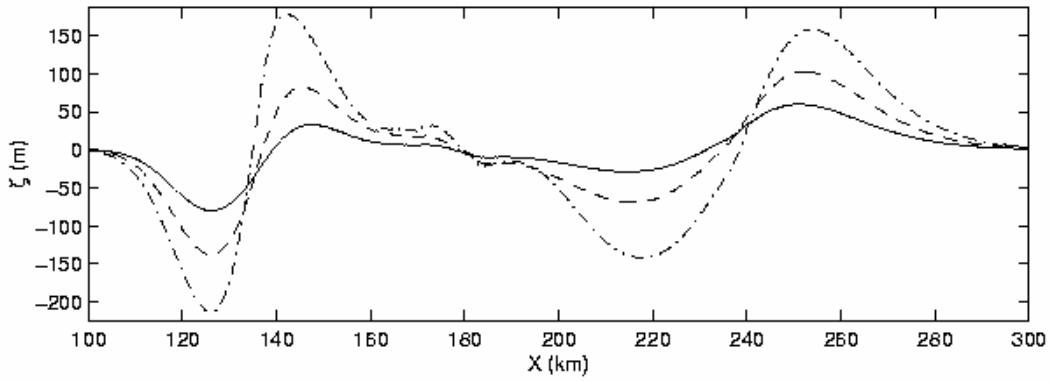


**Figure 11.** Effect of slump duration, comparing free surface response due to slumps of the same geometry, but different periods, for $t_c$=20 min (—), $t_c$=10 min (– –), $t_c$=5 min(– ·). Profiles are taken 5 minutes after the start of the movement.

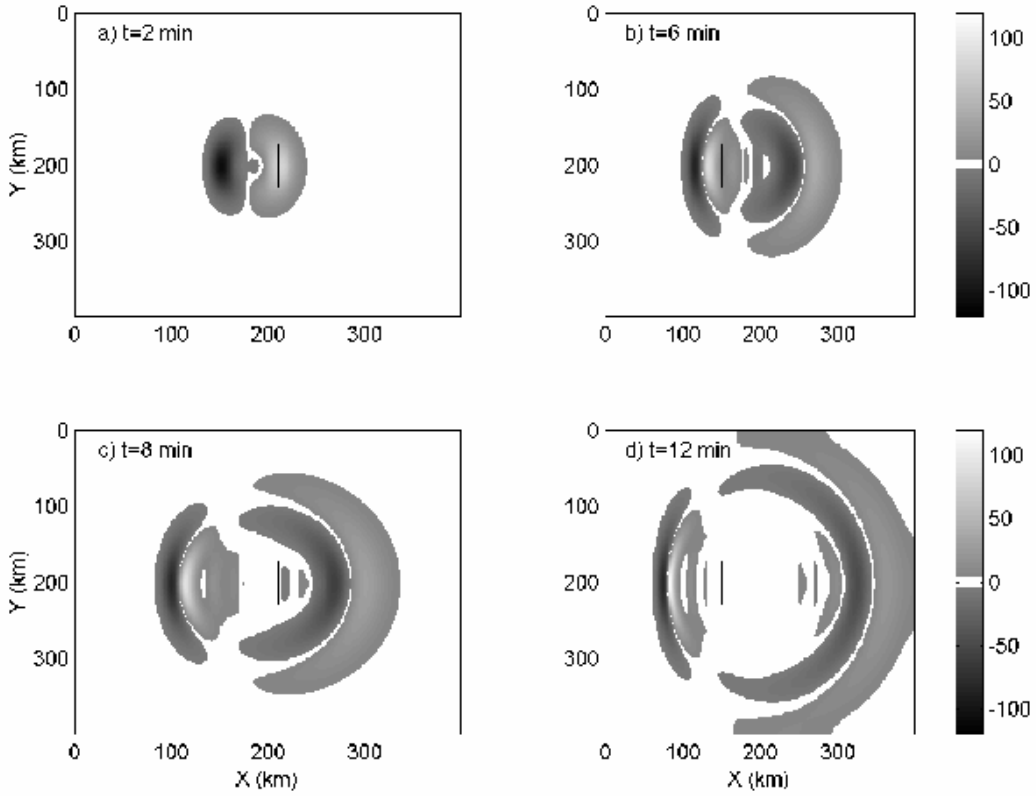


**Figure 12.** 2D free surface response to a submarine slump.

**Figure 13.** Comparison between 1D (—) and 2D centerline (– –) spatial profiles.

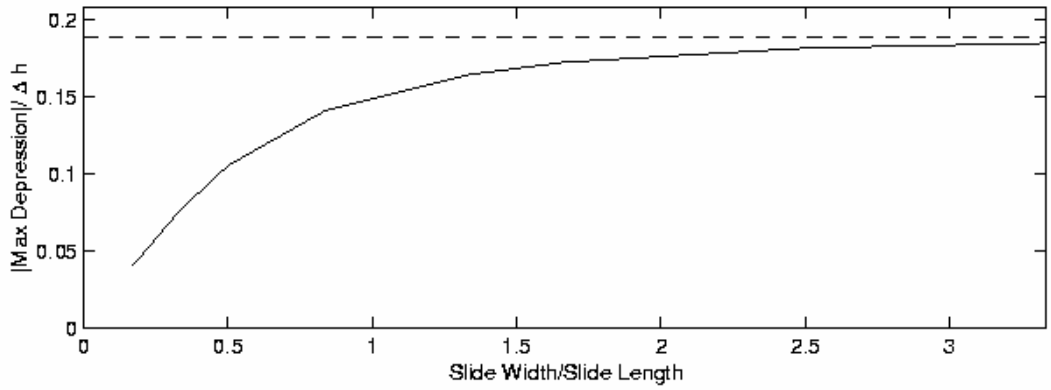


**Figure 14.** Dependence of the maximum depression generated at the top of the failure slope on the aspect ratio of the slump region. The dashed line represents the maximum depression predicted by a 1D simulation.